



## City Research Online

### City, University of London Institutional Repository

---

**Citation:** Ho, D. (2000). On the Influence of Lateral Boundaries in Nonlinear Convection. (Unpublished Doctoral thesis, City, University of London)

This is the accepted version of the paper.

This version of the publication may differ from the final published version.

---

**Permanent repository link:** <https://openaccess.city.ac.uk/id/eprint/30796/>

**Link to published version:**

**Copyright:** City Research Online aims to make research outputs of City, University of London available to a wider audience. Copyright and Moral Rights remain with the author(s) and/or copyright holders. URLs from City Research Online may be freely distributed and linked to.

**Reuse:** Copies of full items can be used for personal research or study, educational, or not-for-profit purposes without prior permission or charge. Provided that the authors, title and full bibliographic details are credited, a hyperlink and/or URL is given for the original metadata page and the content is not changed in any way.

ON THE INFLUENCE OF LATERAL  
BOUNDARIES IN NONLINEAR  
CONVECTION

By  
Diep Ho

A THESIS SUBMITTED TO CITY UNIVERSITY  
FOR THE DEGREE OF DOCTOR OF PHILOSOPHY  
IN THE DEPARTMENT OF MATHEMATICS

October 2000

# Contents

<b>Abstract</b>	<b>11</b>
<b>Declaration</b>	<b>12</b>
<b>Copyright</b>	<b>13</b>
<b>Acknowledgements</b>	<b>14</b>
<b>1 Introduction</b>	<b>15</b>
<b>2 Solutions of the One Dimensional Swift-Hohenberg Equation</b>	<b>23</b>
2.1 Introduction . . . . .	23
2.2 Initial Value Computations . . . . .	23
2.3 Periodic Steady-state Solutions . . . . .	32
2.3.1 Linear Analysis . . . . .	33
2.3.2 Weakly Nonlinear Analysis . . . . .	34
2.4 Numerical Methods for Finding Periodic Solutions . . . . .	37
2.4.1 Shooting Method . . . . .	37
2.4.2 Boundary Value Problem: Finite Difference Method . . . . .	41
2.5 Numerical Results . . . . .	43
2.6 Mode Interactions . . . . .	56
2.6.1 Mode-1-2 Interaction . . . . .	56
2.6.2 Mode-1-3 Interaction . . . . .	62
2.7 Summary . . . . .	69
<b>3 Floquet Theory for the One-Dimensional Swift-Hohenberg Equation</b>	<b>71</b>
3.1 Introduction . . . . .	71
3.2 Asymptotic Solution . . . . .	72

3.3	Weakly Nonlinear Analysis . . . . .	75
3.4	Numerical Results . . . . .	79
3.5	Summary . . . . .	80
<b>4</b>	<b>Steady Solutions of the One-Dimensional Swift-Hohenberg Equation in a Semi-infinite Domain</b>	<b>89</b>
4.1	Introduction . . . . .	89
4.2	Weakly Nonlinear Analysis . . . . .	90
4.3	Approximate Theory for General $\epsilon$ . . . . .	101
4.4	Nonlinear Theory for General $\epsilon$ . . . . .	110
4.5	Summary . . . . .	111
<b>5</b>	<b>Solutions of the Two Dimensional Swift-Hohenberg Equation</b>	<b>118</b>
5.1	Introduction . . . . .	118
5.2	Linear Analysis . . . . .	119
5.2.1	Even and Odd Solutions . . . . .	122
5.3	Two Dimensional Periodic Solutions . . . . .	128
5.4	Summary . . . . .	132
<b>6</b>	<b>Floquet Theory for the Two Dimensional Swift-Hohenberg Equation</b>	<b>141</b>
6.1	Introduction . . . . .	141
6.2	Floquet-Fourier Method . . . . .	141
6.3	Numerical Results . . . . .	145
6.4	Summary . . . . .	162
<b>7</b>	<b>Solutions of the Two-Dimensional Swift-Hohenberg Equation in a Semi-infinite Channel</b>	<b>163</b>
7.1	Introduction . . . . .	163
7.2	Approximate Theory for General $\epsilon$ . . . . .	164
7.3	Summary . . . . .	165
<b>8</b>	<b>Discussion</b>	<b>167</b>
8.1	Conclusions . . . . .	167
8.2	Further Work . . . . .	168
	<b>Bibliography</b>	<b>170</b>

# List of Figures

1.1	A schematic diagram of an experimental set up used to study Rayleigh Bénard convection. . . . .	15
1.2	Diagram illustrating convective rolls formed by upward- and downward-moving regions of fluid. . . . .	16
1.3	Evolution for rolls beyond the Eckhaus instability. . . . .	18
2.1	An example of a periodic solution at $\epsilon = 0.65$ . . . . .	26
2.2	An example of a quasi-periodic solution at $\epsilon = 0.5$ . . . . .	26
2.3	An example of an unbounded solution at $u'(0) = 0.02722$ and $u'''(0) = 0.05$ with $\epsilon = 0.1$ . Our adaptive numerical algorithm has stopped due to numerical overflow. . . . .	27
2.4	A bounded solution at $\epsilon = 0.1$ with $a = 0.02721$ and $b = 0.05$ . . . . .	27
2.5	An example of a solution with $\epsilon = -0.0001$ . . . . .	28
2.6	A solution with $\epsilon = -0.001$ . . . . .	28
2.7	A solution with $\epsilon = -0.01$ . . . . .	29
2.8	A solution with $\epsilon = -0.05$ . . . . .	29
2.9	An example of a solution with $\epsilon = 1.01$ , $a = 0.1$ and $b = 0.1$ . . . . .	30
2.10	An example of a solution with $\epsilon = 1.01$ , $a = 0.1$ and $b = -0.1$ . . . . .	30
2.11	An example of a solution with $\epsilon = 1.01$ , $a = 0.01$ and $b = -0.01$ . . . . .	31
2.12	An example of a solution with $\epsilon = 1.1$ . . . . .	31
2.13	Marginal curves for individual modes. . . . .	34
2.14	A solution at the point $(L, \epsilon) = (\pi, 0.1)$ . At this parameter point $(\alpha, \beta) = (0.365814, -0.370378)$ . We have extended the solution by plotting the solution for $x \in (0, 40)$ . . . . .	44
2.15	Plots of the parameters $\alpha$ and $\beta$ as a function of $L$ for $\epsilon = 0.01, 0.1, 0.3, 0.4$ and $0.6$ . . . . .	45
2.16	Profiles of the solution $u$ for fixed $L = \pi$ and increasing $\epsilon$ . . . . .	46
2.17	Profiles of the solution $u$ for fixed $L = \pi$ and higher $\epsilon$ . . . . .	46

2.18	Profiles of the solution $u$ obtained from the numerical scheme for fixed $\epsilon = 0.65$ and $L = \pi, \pi + 0.1, \pi + 0.2, \dots, \pi + 3.9$ . A more detailed examination of all possible solutions (displayed in Figure 2.21 below) reveals that the final profile is on the red branch of Figure 2.21, whilst the other profiles are on the green branch. . . . .	48
2.19	Profiles of the solution $u$ for fixed $\epsilon = 0.65$ and finer increments of $L$ near $\pi + 3.9$ . The final two profiles are on the red branch of Figure 2.21 below, whilst the other profiles are on the green branch.	49
2.20	Plot showing multiple steady-state solutions in the region $(L, \epsilon) = (L _{L \in (4.9, 5.2)}, 0.4)$ . Also shown is the profile of the solution at various points. . . . .	50
2.21	Plot showing multiple steady-state solutions in the region $(L, \epsilon) = (L _{L \in (7, 7.2)}, 0.65)$ . Also shown is the profile of the solution at various points. Note that the bifurcation point of the dark blue ( <i>mode 1</i> ) solution obtained numerically at $L = 7.13677273$ is consistent with the value $L = \pi(1 - \epsilon^{\frac{1}{2}})^{-\frac{1}{2}} = 7.13677275$ predicted by linear theory. . . . .	51
2.22	An example of a <i>mixed-1-2-mode</i> solution at $L = 4.9495, \epsilon = 0.4$ . . . . .	52
2.23	An example of a <i>mixed-1-2-mode</i> solution at $L = 4.9673, \epsilon = 0.4$ . . . . .	52
2.24	An example of a <i>mixed-1-2-mode</i> solution at $L = 4.9867, \epsilon = 0.4$ . . . . .	53
2.25	An example of a <i>pure-3-mode</i> solution at $L = 7.0248, \epsilon = 0.65$ . . . . .	53
2.26	An example of a <i>mixed-1-3-mode</i> solution at $L = 7.0248, \epsilon = 0.65$ . . . . .	54
2.27	An example of a <i>mixed-1-3-mode</i> solution at $L = 7.0248, \epsilon = 0.65$ . . . . .	54
2.28	An example of a <i>mixed-1-3-mode</i> solution at $L = 7.0203, \epsilon = 0.65$ . . . . .	55
2.29	Another example of a <i>mixed-1-3-mode</i> solution at $L = 7.0307, \epsilon = 0.65$ . . . . .	55
2.30	An amplitude plot at $\delta = 0.01$ , showing the bifurcation structure of the mode-1-2 interaction. . . . .	60
2.31	A plot showing the bifurcation set for the mode-1-2 interaction. . . . .	63
2.32	An amplitude plot at $\delta = 0.01$ , showing the bifurcation structure of the mode-1-3 interaction. . . . .	67
2.33	A plot showing the bifurcation loci for the mode-1-3 interaction. . . . .	70
3.1	Plot displaying regions of spatially decaying/growing and spatially oscillatory solutions for $\epsilon \ll 1$ . The Eckhaus boundary separates the two regions. . . . .	77

3.2	Plot of the real and imaginary part of the <i>Floquet multipliers</i> for fixed $\epsilon = 0.01$ and for $\lambda$ such that $(\lambda, \epsilon)$ lies above the neutral curve.	82
3.3	Plot of the real and imaginary part of the <i>Floquet multipliers</i> for fixed $\epsilon = 0.1$ and for $\lambda$ such that $(\lambda, \epsilon)$ lies above the neutral curve.	83
3.4	Plot of the real and imaginary part of the <i>Floquet multipliers</i> for fixed $\epsilon = 0.4$ and for $\lambda$ such that $(\lambda, \epsilon)$ lies above the neutral curve.	84
3.5	Plot of the real and imaginary part of the <i>Floquet multipliers</i> for fixed $\epsilon = 0.6$ and for $\lambda$ such that $(\lambda, \epsilon)$ lies above the neutral curve.	85
3.6	Plot of the real and imaginary part of the <i>Floquet exponent</i> , $c$ for $\epsilon \in \{0.01, 0.1, 0.4, 0.6\}$ and for $\lambda$ such that $(\lambda, \epsilon)$ lies above the neutral curve. The blue and green lines represent the real and imaginary parts respectively. . . . .	86
3.7	Plot of the functions $u_p(x)$ , $P_1(x)$ , $P_2(x)$ , $P_3(x)$ and $P_4(x)$ at the parameter point $(\lambda, \epsilon) = (2\pi, 0.1)$ where $P_1$ , $P_2$ , $P_3$ and $P_4$ correspond to the $c$ values $c_1 = -0.21956$ , $c_2 = 0.21956$ , $c_3 = 0$ and $c_4 = 0$ respectively. . . . .	87
3.8	Plot comparing the numerical results from the <i>Floquet</i> method and the weakly-nonlinear approximation of the <i>Eckhaus</i> boundary. . .	88
4.1	Diagram illustrating the inner and outer approximation regions and the matching that is required. The inner solution is formulated in equation (4.45) below. . . . .	91
4.2	The solution for $r$ . . . . .	95
4.3	Plots of the wavenumber restriction, equation (4.60), together with the neutral curve and the Eckhaus boundary. . . . .	98
4.4	The figure shows the two possible values of $\theta$ as the intersections of the blue and green lines. The red arrow indicates the possible positions that the green line can take. . . . .	99
4.5	The red and blue lines are plots of $F(\phi)$ for a fixed $\epsilon = 0.1$ and different values of $\lambda$ . Their positions in the $(\lambda, \epsilon)$ space are represented respectively by the red and blue crosses in Figure 4.8. . . .	102
4.6	The red and blue lines are plots of $F(\phi)$ for a fixed $\epsilon = 0.5$ and different values of $\lambda$ . Their positions in the $(\lambda, \epsilon)$ space are represented respectively by the red and blue crosses in Figure 4.8. . . .	103

4.7	The red and blue lines are plots of $F(\phi)$ for a fixed $\epsilon = 1$ and different values of $\lambda$ . Their positions in the $(\lambda, \epsilon)$ space are represented respectively by the red and blue crosses in Figure 4.8. . . . .	103
4.8	The blue and green curves are the marginal curve and the Eckhaus boundary respectively. The red lines represent the weakly-nonlinear result for the wavenumber restriction (from Section 4.2). The red and blue crosses are the solutions determined by the zeros of $F$ in Figures 4.5–4.7. . . . .	104
4.9	An example of an iterative scheme used for the evaluation of $\bar{x}^*$ and $\bar{k}^*$ , where $m = 5$ and $\bar{k}_0 = 0$ . . . . .	106
4.10	Results of the approximate method at $\epsilon = 0.1$ . . . . .	107
4.11	Results of the approximate method at $\epsilon = 0.5$ . . . . .	108
4.12	Results of the approximate method at $\epsilon = 1$ . . . . .	108
4.13	Plot comparing the approximate theory for the wavenumber restriction (crosses) with the weakly-nonlinear results (red line). The top graph shows the wavelength, $\lambda$ , and the lower graph shows the wavenumber, $q$ . . . . .	109
4.14	Results of the nonlinear method at $\epsilon = 0.1$ . . . . .	112
4.15	Results of the nonlinear method at $\epsilon = 0.5$ . . . . .	112
4.16	Results of the nonlinear method at $\epsilon = 1$ . . . . .	113
4.17	Plots comparing the results of the nonlinear method (crosses) and the weakly nonlinear approximation (lines) of $k$ , $u''(0)$ and $u'''(0)$ at $\epsilon = 0.1$ . Notice that we have used $\lambda = 2\pi/q$ , (4.44) and (4.58) to get an expression in $\lambda$ . . . . .	114
4.18	Plots comparing the results of the nonlinear method (crosses) and the weakly nonlinear approximation (lines) of $k$ , $u''(0)$ and $u'''(0)$ at $\epsilon = 0.5$ . . . . .	115
4.19	Plots comparing the results of the nonlinear method (crosses) and the weakly nonlinear approximation (lines) of $k$ , $u''(0)$ and $u'''(0)$ at $\epsilon = 1$ . . . . .	116
4.20	Plot comparing the nonlinear results for the wavenumber restriction (crosses) with the weakly-nonlinear result (red line). The top graph shows the wavelength, $\lambda = 2L$ , and the lower graph shows the wavenumber, $q$ . . . . .	117

5.1	Diagram illustrating the geometry of the equivalent Rayleigh-Bénard problem. . . . .	119
5.2	The lowest even and odd solution branches. The critical point, $(K_c, \bar{\epsilon}_c)$ , is also shown, along with the locus of the <i>1D-neutral-curve</i> (red curve). . . . .	124
5.3	The two lowest solution branches scaled back to the $(q, \epsilon)$ -parameter space for the case $L_y = 2\pi$ . The critical point corresponds to $(q_c, \epsilon_c) = (0.82374, 0.22056)$ in this case, and the <i>1D-neutral-curve</i> is also shown (red curve). . . . .	125
5.4	Profile of $U(Y)$ in the lower region of the <i>even-solution</i> branch. . . . .	126
5.5	Profile of $U(Y)$ in the lower region of the <i>odd-solution</i> branch. . . . .	126
5.6	Profile of $U(Y)$ showing rolls developing at the channel wall which then grow in amplitude and move inwards as we decrease $K$ . . . . .	127
5.7	The first four even and odd solution branches. The crosses and circles show the intersection of the even and odd branches with the <i>1D-neutral-curve</i> . . . . .	134
5.8	The geometry and boundary conditions of the two-dimensional problem. . . . .	135
5.9	Profiles of $a_j(y)$ for $j = 1, 2, \dots, 9$ with $\epsilon = 1$ (blue profile) and decreasing in steps of 0.02 (green profiles). The solution is for a channel of width $L_y = 2\pi$ , wavenumber $q = 1$ and discretisation parameter $M = 50$ . . . . .	136
5.10	The top row shows the contour plots of $a_j(y)$ , $j = 1, 3, \dots, 9$ for $L_y = 2\pi$ , $\epsilon = 0.5$ and discretisation parameter $M = 50$ . The bottom row shows plots of the maximum values of $a_j(y)$ , $j = 1, 3, \dots, 9$ with the same parameters. . . . .	137
5.11	Profiles of $a_1(y)$ for different wavenumbers $q$ with $L_y = 2\pi$ , $\epsilon = 0.5$ and the discretisation parameter $M = 50$ . . . . .	138
5.12	Plot comparing the 2D neutral curve derived in Section 5.2 with the neutral curve derived from the fully nonlinear finite difference method. The results are for a fixed channel width $L_y = 2\pi$ . The small kink should be ignored, being an artifact introduced by the numerical procedure used to solve equation (5.20) which has a non-meaningful solution $\alpha = 0$ , equivalent to the one-dimensional neutral curve. . . . .	139

5.13	The solution $u(x, y) = \sum_{j=1}^9 a_j(y) \sin jqx$ for a channel width $L_y = 2\pi$ , wavenumber $q = 1$ and $\epsilon = 0.5$ . . . . .	140
6.1	The two plots show the zeros of $\min  (\text{eig } \mathcal{M}_1^{fd}) $ . The upper and the lower plots are of the identical region and differ by representing values of $\min  (\text{eig } \mathcal{M}^{fd}) $ as shades and contours respectively. The zeros (examples are indicated by the arrows) correspond to different eigenvalues becoming zero. Notice that there are three zero-eigenvalues on the real axis. . . . .	148
6.2	Diagram illustrating the geometry of the 2D problem and showing the coefficient $a_1$ of the periodic solution $u_p$ and the eigenfunctions $b_1$ and $c_1$ at $(L_y, q, \epsilon) = (2\pi, 0.82374, 0.4)$ corresponding to the characteristic exponent $\mathcal{C}_+ = 0.3533$ . . . . .	149
6.3	Shading plot of the functions $u_p(y) = a_1(y) \sin qx$ and $[b_1(y) \cos qx + c_1(y) \sin qx]$ at the parameter values $(L_y, q, \epsilon) = (2\pi, 0.82374, 0.4)$ and $\mathcal{C}_+ = 0.3533$ . . . . .	150
6.4	Contour plots of $\min  (\text{eig } \mathcal{M}_1^{fd}) $ for the fixed parameter values $(L_y, \epsilon) = (2\pi, 0.45)$ and $q \in \{0.5, 0.6, 0.7, 0.8, 0.82374, 0.85, 0.9, 1\}$ . . . . .	151
6.5	Plots of $ \mathcal{C} $ for parameter values $L_y = 2\pi$ and $\epsilon \in \{0.5, 0.6, 0.7, 0.8\}$ . The circles marking a kink on the curves indicate that the numerical algorithm may be converging to another nearby solution branch. The investigation of such solution branches is left for future work. . . . .	152
6.6	Plots showing the neutral curve (green curve) and the Eckhaus boundary (blue curves) for a channel of width $L_y = 2\pi$ . The red crosses indicate points at which the plots in Figure 6.4 are evaluated and the red pluses indicate points at which the plots in Figure 6.7 are evaluated. . . . .	153
6.7	Contour plot of $\min  (\text{eig } \mathcal{M}_1^{fd}) $ for the fixed parameter values $(L_y, q) = (2\pi, 0.82374)$ and $\epsilon \in \{0.25, 0.35, 0.45, 0.5, 0.55, 0.75\}$ . . . . .	154
6.8	Plots showing the profiles of $a_1, b_1$ and $c_1$ at fixed $(L_y, \epsilon) = (2\pi, 0.4)$ and $q_c = 0.82374 \leq q \leq 0.95374$ . The green profiles represent the profiles at $q_c = 0.82374$ . The cyan arrow points in the direction of increasing values of $q$ . . . . .	155
6.9	Plots of the profiles of $a_1, b_1$ and $c_1$ ; and the functions $b_1 \cos qx + c_1 \sin qx$ and $e^{\mathcal{C}x}[b_1 \cos qx + c_1 \sin qx]$ at $q = 0.82374$ . . . . .	156

6.10	Plots of the profiles of $a_1$ , $b_1$ and $c_1$ ; and the functions $b_1 \cos qx + c_1 \sin qx$ and $e^{Cx}[b_1 \cos qx + c_1 \sin qx]$ at $q = 0.84874$ . . . . .	157
6.11	Plots of the profiles of $a_1$ , $b_1$ and $c_1$ ; and the functions $b_1 \cos qx + c_1 \sin qx$ and $e^{Cx}[b_1 \cos qx + c_1 \sin qx]$ at $q = 0.89874$ . . . . .	158
6.12	Plots of the profiles of $a_1$ , $b_1$ and $c_1$ ; and the functions $b_1 \cos qx + c_1 \sin qx$ and $e^{Cx}[b_1 \cos qx + c_1 \sin qx]$ at $q = 0.92374$ . . . . .	159
6.13	Plots of the profiles of $a_1$ , $b_1$ and $c_1$ ; and the functions $b_1 \cos qx + c_1 \sin qx$ and $e^{Cx}[b_1 \cos qx + c_1 \sin qx]$ at $q = 0.94874$ . . . . .	160
6.14	Plots of the profiles of $a_1$ , $b_1$ and $c_1$ ; and the functions $b_1 \cos qx + c_1 \sin qx$ and $e^{Cx}[b_1 \cos qx + c_1 \sin qx]$ at $q = 0.96874$ . . . . .	161
7.1	The top plot shows the neutral curve, the Eckhaus boundary and the wavenumber restriction (red lines) for the channel of width $L_y = 2\pi$ . The lower plot shows the functions $(B_1^2 + C_1^2)^{\frac{1}{2}}$ and $ 2qC^{-1}B_1 + C_1 $ for values of $\epsilon = 0.25, 0.3, 0.35, 0.4, 0.45$ and $0.5$ .	166

# Abstract

This thesis is concerned with solutions of the one-dimensional and two-dimensional Swift-Hohenberg equation as a model of nonlinear convection. In particular it is concerned with the influence of lateral boundaries on nonlinear solutions.

We start by giving a linear stability analysis for the one-dimensional case and use this as a basis for finding one-dimensional nonlinear periodic solutions. We also study the bifurcation structure and stability of nonlinear mode interactions.

We use Floquet theory to analyse, in a spatial sense, the departure of the nonlinear solutions from their periodic form and locate the Eckhaus boundary for the one-dimensional case.

We then use the Floquet analysis to find nonlinear solutions of the Swift-Hohenberg equation in the presence of a lateral boundary and determine the restriction imposed by the boundary on wavenumber selection.

In the two-dimensional case, we obtain linear stability results for the solution in a channel of finite width and use this as a basis for finding nonlinear solutions which are periodic along the channel.

We then use Floquet theory to analyse, in a spatial sense, the departure of nonlinear solutions from their periodic form and to locate the two-dimensional equivalent of the Eckhaus boundary.

Finally, the Floquet theory is used as the basis of an approximate method of finding the restriction on wavenumber selection imposed by the presence of a lateral boundary across the channel.

# Declaration

No portion of the work referred to in this thesis has been submitted in support of an application for another degree or qualification of this or any other university or other institution of learning.

# Copyright

Copyright in text of this thesis rests with the Author. Copies (by any process) either in full, or of extracts, may be made **only** in accordance with instructions given by the Author. This page must form part of any such copies made. Further copies (by any process) of copies made in accordance with such instructions may not be made without the permission (in writing) of the Author.

The ownership of any intellectual property rights which may be described in this thesis is vested in City University, subject to any prior agreement to the contrary, and may not be made available for use by third parties without the written permission of the University, which will prescribe the terms and conditions of any such agreement.

# Acknowledgements

I would like to express my appreciation to Professor P.G. Daniels and Dr. A.C. Skelton for all their guidance and support throughout the research and preparation of this thesis. I would also like to acknowledge the financial support provided by EPSRC.

I would like to thank my family for all the support that they have given me over the years. Also, special thanks to all the friends that I have made in City University who have made my stay an enjoyable one.

# Chapter 1

## Introduction

There are many examples of systems that spontaneously develop a periodic cellular pattern through a continuous bifurcation from a structureless state. Such patterns have been observed in hydrodynamic instabilities of simple fluids, in electro-hydrodynamic instability of liquid crystals, in crystal growth and in buckling of plates. In this thesis we will be considering hydrodynamic instabilities of simple fluids. In particular, we will be considering the problem of thermal convection in a fluid contained between horizontal plates (an example of such an experimental apparatus is shown in Figure 1.1). For a critical temperature gra-

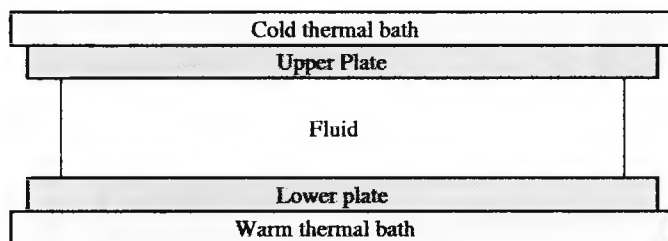


Figure 1.1: A schematic diagram of an experimental set up used to study Rayleigh Bénard convection.

dient between the upper and the lower plates, buoyancy forces overcome the dissipative effects of viscous shear and thermal conduction, and the motionless fluid spontaneously breaks up into convective rolls of upward- and downward-moving regions of fluid (see Figure 1.2). This problem was first considered in Bénard's work (1900, [3]; 1901, [4]) and later in Rayleigh's theoretical analysis (1916, [43]); and it is commonly known as Rayleigh-Bénard convection or simply

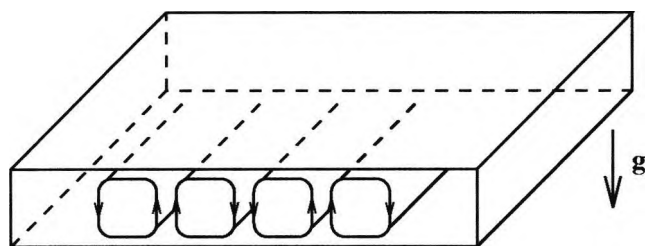


Figure 1.2: Diagram illustrating convective rolls formed by upward- and downward-moving regions of fluid.

as Bénard convection<sup>1</sup>.

Amplitude equations, also known as envelope equations, have been derived and used in a variety of cases to obtain, for example, bifurcation diagrams and small amplitude stationary solutions. In the context of convection, amplitude equations were first introduced, nearly simultaneously, by Segel (1969, [45]), and Newell and Whitehead (1969, [40]). The fact that their derivation had overlooked the role of large scale horizontal flow allowed by stress-free boundaries was pointed out by Siggia and Zippelius (1981, [48]).

Many of the early investigations of Rayleigh-Bénard convection are concerned with the unconfined problem (the problem with no lateral walls). Later, the need for a realistic comparison with experimental investigations led to studies of Rayleigh-Bénard convection in a confined box. The earliest study of the confined problem was provided by Davis (1967, [23]). He found that convection rolls line-up so that the axes are parallel with the shorter sides of the rectangular box. Davies-Jones (1970, [22]), in his study of convection in an infinite channel with no-slip sidewalls, shows that the preferred configuration at the onset of convection is with the axes of the convection rolls perpendicular to the sidewalls. Cross (1982, [13]) recognises that these are two competing effects, i.e., a sidewall effect that favours rolls perpendicular to the sidewalls, and so tends to produce  $O(1)$  rotation of the roll orientation over the cell, and the bulk effects that favour straight parallel rolls. He uses the notion of a Lyapunov functional (which is used

<sup>1</sup>Historically, the name is inaccurate; Bénard's pioneering work, although for long believed to be related to the description above, was mostly of another phenomenon (Marangoni convection) that gives rise to similar effects. However, the name, Rayleigh-Bénard convection, is so well established that its usage does not cause any confusion. Note that some authors still use Bénard convection to refer to Marangoni convection.

to order the stability of various patterns) to examine the role of the competing effects on textural transitions. Segel (1969, [45]) was the first to consider the boundary conditions which the amplitude equation must satisfy when the fluid layer is confined laterally by rigid, perfectly insulating sidewalls. His analysis was later corrected by Brown and Stewartson (1977, [6]) in their study of thermal convection in a large box. Their study was an extension of the investigation by Daniels (1977, [19]), who had studied the effect of distant sidewalls on the transition to finite amplitude convective rolls. He showed that if there is a small heat transfer through the walls the bifurcation is in general replaced by a smooth transition to finite amplitude convection. Other work on the confined problem includes the well referenced work by Pomeau and Manneville (1981, [41]) and Cross, Daniels, Hohenberg and Siggia (1980, [14]; 1983, [15]), who studied the wave-number selection mechanism in a confined box. In their papers they showed that the allowable band of wave-vectors which can occur in the bulk of the container is reduced if the system has sidewalls (i.e., greatly reducing the number of steady states).

Many experimental investigations have been undertaken with different geometries and thermal conditions. The first detailed experimental investigation of convection in rectangular and cylindrical planforms was made by Koschmieder (1966, [32]). He found with rectangular planforms that straight rolls formed whose axes were parallel to the shorter side of the container in agreement with the theory of Davis (1967, [23]). With cylindrical planforms circular concentric rolls were found. This is one of many possible configurations. Croquette, Mory and Schosseler (1983, [11]) also experimented on cylindrical planforms and they found fields of disordered rolls whose axes tend to be perpendicular to the circular wall. Their results were verified by Ahlers, Cannell and Steinberg (1985, [1]) in their work on flow patterns in cylindrical planforms. A detailed review of much of the experimental work is given by Koschmieder (1993, [33]).

An important question in the context of Rayleigh-Bénard convection already referred to above is concerned with the selection of the wavenumber,  $q$  (where  $q$  may be dependent on initial conditions, boundary conditions, and external noise) and the evolution mechanism towards the steady state defined by  $q$ . Several different mechanisms have been proposed to answer this question

- If the equation has a Lyapunov functional we have the notion of minimising this functional to order the stability of various patterns.

- The second mechanism (containing the first as a special case), is based on a balance of forces between solutions of different  $q$  value. This is not restricted to systems with a potential function.
- The third idea assumes that the system selects the mode most susceptible to external noise, i.e., via external forcing.
- The last mechanism deals with the resultant periodic patterns via front propagation. This mechanism includes the effects observed by Cross (1982, [13]), and does not relate to any of the previous mechanisms.

Beyond the primary bifurcation, i.e., transition from a structureless base state to a pattern formed of convective rolls of upward- and downward-moving regions of the fluid, it is commonly observed (experimentally by Lowe and Gollub (1985, [37]); analytically by Clever and Busse (1974, [9]) and Kramer and Zimmerman (1985, [35]); and numerically by Hernández-García et al. (1992, [30])) that these rolls become unstable by the Eckhaus instability. The Eckhaus instability or compression/dilatation instability was first analysed by Eckhaus (1965, [26]). It takes place for rolls with wavenumber,  $q$ , sufficiently larger or smaller than the optimal wavenumber (known as the critical wavenumber),  $q_c$ . Let us assume for example a roll configuration with  $q$  sufficiently larger than  $q_c$ . The modulation<sup>2</sup> within the bulk of the system produces both compression and dilation regions, but the dilation regions are unstable and are suitable for a collapse of a pair of rolls. This collapse results in a decrease in the average wavenumber, or equivalently,  $q$  approaches the optimal value,  $q_c$ . Figure 1.3 illustrates this transformation. A theoretical treatment for Rayleigh-Bénard convection in large

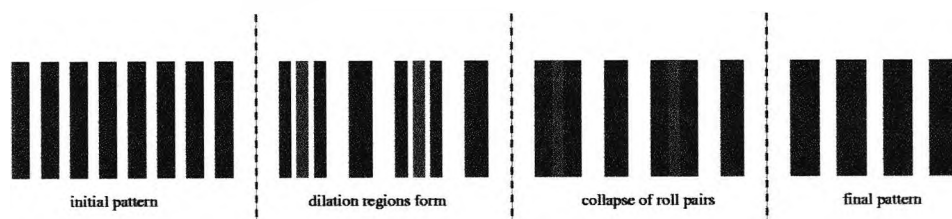


Figure 1.3: Evolution for rolls beyond the Eckhaus instability.

aspect ratio containers was provided by Clever and Busse (1974, [9]) and Kramer and Zimmerman (1985, [35]). It has been studied experimentally by Lowe and

<sup>2</sup>Modulation to some ideal periodic solution with wavenumber  $q_c$ .

Gollub (1985, [37]) by preparing a state with the wavenumber in the stable region and lowering the temperature gradient until it falls into the Eckhaus bands. The rolls are then too narrow or too wide and the system abruptly gains or loses one or more rolls. Lowe and Gollub (1985, [37]) also initialised the system in an unstable wavenumber state by spatially-periodic forcing.

A number of phenomenological models have been studied as a means of gaining insight into the Rayleigh-Bénard phenomenon (see, for example, Manneville (1990, [38]) and Cross and Hohenberg (1993, [16])). The following relaxational model equation was first derived by Swift and Hohenberg (1977, [49]):

$$\frac{\partial u}{\partial t} = (\epsilon - [1 + \Delta]^2) u - u^3, \quad (1.1)$$

where  $t$  is time,  $u = u(x, y, t)$  is a two-dimensional scalar field,  $\epsilon = (R - R_c)/R_c$  is the reduced Rayleigh number,  $R$  is the Rayleigh number<sup>3</sup>,  $R_c = (27\pi^4)/4$  is the critical Rayleigh number<sup>4</sup>, and  $\Delta = \nabla^2$  is the two dimensional Laplacian. The function  $u$  represents the rescaled fluid field in a given horizontal plane, e.g., the vertical velocity component in the mid-plane of the convective rolls. Swift and Hohenberg (1977, [49]) used this model which they derived in an appendix to their paper, to discuss the role of fluctuations close to the onset of convection. They derived the model from the Boussinesq approximation<sup>5</sup> in the limit of infinite Prandtl number<sup>6</sup>, corresponding to an infinitely viscous fluid. This limit is well approximated in practice by certain fluids such as oils (fluids with large Prandtl number). Certainly, the Swift-Hohenberg (SH) equation is an immense simplification of the Boussinesq approximation that was considered in detail in Chandrasekhar (1961, [8]). The SH equation contains the essential ingredients of cubic nonlinearity and diffusion which are also a feature of the Rayleigh-Bénard system. It is expected to be quantitatively accurate only for temperature differentials close to threshold, and only in the limit of large domains.

The derivation of the amplitude equation for the SH model equation leads

---

<sup>3</sup>The Rayleigh number is a ratio of the temperature gradient to the damping due to viscosity and thermal diffusion. It is a measure of the driving force on the system.

<sup>4</sup>The critical Rayleigh number (for stress-free upper and lower boundaries) corresponds to the critical temperature gradient, mentioned in the first paragraph, when the motionless fluid spontaneously breaks up into convective rolls.

<sup>5</sup>Hydrodynamic equations that describe Rayleigh-Bénard convection in a simple fluid. For a detailed study refer to the references Chandrasekhar (1961, [8]) and Drazin and Reid (1981, [25]).

<sup>6</sup>The Prandtl number is a ratio of viscosity to the thermal diffusion coefficient. It characterises the fluid.

to the same type of amplitude equation as the hydrodynamic equations (in the Boussinesq approximation). In the latter case the systematic expansion to non-trivial order for a two-dimensional amplitude function was first considered by Newell and Whitehead (1969, [40]) and was further reviewed by Cross (1980, [12]) who compiled the values of the coefficients for convection with no-slip boundary conditions. Derivation of the one-dimensional amplitude equations for the SH equation at leading and higher orders is described by Cross *et al* (1983, [15]), with applications to the wavelength selection problem in a finite container. In more recent work, Daniels and Weinstein (1992, [20]; 1996, [21]) used the two-dimensional SH amplitude equations to consider the role of orthogonal roll patterns in describing the features of the finite-amplitude motion near an imperfect<sup>7</sup> lateral boundary and within a general rectangular domain.

Even phenomenological models of the type mentioned above cannot be completely solved by analytical techniques; thus numerical simulations are of fundamental importance in gaining an understanding of some of these problems. Simulations of the SH equation in a rectangular geometry were performed by Greenside, Coughran and Schryer (1982, [28]) and subsequently by Greenside and Coughran (1984, [29]); and simulations in a cylindrical cell were performed by Morris, Bodenschatz, Cannell and Ahlers (1993, [39]). These works have all relied on an operator-splitting approach based on the fast direct constant-coefficient biharmonic solver described by Bjorstad (1983, [5]). However, this method has several drawbacks: it does not support large time-steps due to numerical stability; it is not easily parallelised; and it can not be easily adjusted to take account of different boundary conditions or coordinate systems. Anderson (1996, [2]) has implemented a nonlinear finite-difference, Newton-Krylov scheme that overcomes each of the above drawbacks, successfully pursuing a time-dependent trajectory over a large spatial grid and large time-steps, and resulting in a time-independent Newton solution; it is easily parallelisable; and equally effective for rigid or periodic boundary conditions and for rectangular or polar coordinate systems.

Our work is motivated partly by the work of Cross, Daniels, Hohenberg and Siggia (1980, [14]; 1983, [15]), who studied the wave-number selection mechanism in a confined box both for the Rayleigh-Bénard system and for the SH model. In their papers they showed that in the weakly nonlinear regime the band of

---

<sup>7</sup>The imperfection could be used to represent a finite porosity or thermal conductivity of the sidewall.

allowed wave-vectors which can occur in the bulk of the container is reduced if the system has sidewalls. Our work aims to extend these results to the fully nonlinear regime and to do this we must first classify all the possible steady state solutions that can occur in the bulk of a semi-infinite container (Cross *et al* (1983, [15]) showed that for weakly nonlinear motion this number is greatly reduced because of the lateral wall). Once these solutions are found the lateral walls can be incorporated by finding how they adjust to satisfy the relevant boundary conditions. Our classifying problem turned out to be more complicated than we had first thought. There are a myriad of bifurcation structures that exist even for the simplified Swift-Hohenberg model. This thesis will concentrate on identifying some of these bifurcation structures and classifying the periodic solutions of the Swift-Hohenberg equation in the fully nonlinear regime for both one- and two-dimensional situations. We will also consider how the relevant solutions are modified in a semi-infinite domain by the introduction of a lateral wall. In the case of the one-dimensional SH equation, this problem has been considered numerically by Kramer and Hohenberg (1984, [34]) who have obtained some isolated results in the nonlinear regime.

Other work on the Swift-Hohenberg equation includes that by Tsiveriotis and Brown (1989, [50]) who investigate the bifurcation structure and the Eckhaus instability. They show that the Eckhaus diagram is destroyed with simple mode coupling such as in a coupled pair of Swift-Hohenberg equations. Hernández-García *et al* (1992, [30]) consider the influence of noise in pattern selection and show that noise destroys long-range order in the long-time patterns. Kuwamura (1996, [36]) considers the stability of roll solutions of the two-dimensional equation. He used spectral analysis and found that the system size can affect the stability of the roll solutions.

The plan of the thesis is as follows. In Chapter 2 we investigate the one-dimensional SH equation in an infinite domain, identifying nonlinear periodic steady-state solutions. In fact, we find that the Swift-Hohenberg equation has solutions that are spatially periodic, quasi-periodic and unbounded. We study the linear stability of the trivial solution to different Fourier modes. Restricting our investigation to periodic solutions we perform a multiple-scale analysis to determine their weakly nonlinear form. Then, we describe numerical methods which we used to follow the nonlinear solutions as a function of  $\epsilon$  and  $L$ , where  $L$  is used to denote the half-wavelength of the periodic solution. Various nonlinear

bifurcations and mode interaction solutions are identified and are investigated analytically and numerically.

In Chapter 3 we study the perturbation of periodic solutions (at finite  $\epsilon$ ) to spatial disturbances by using Floquet theory. We analyse their *Floquet exponents* and obtain the Eckhaus boundary (the locus that separates the regions where the perturbations are spatially decaying or growing from perturbations that are oscillatory). We extend the weakly nonlinear analysis of Chapter 2 to analyse the Eckhaus boundary for small  $\epsilon$  and compare it with the numerical results for arbitrary  $\epsilon$ .

In Chapter 4 we consider solutions of the SH equation in a semi-infinite domain. This is done by introducing no-slip boundary conditions at a lateral wall  $x = 0$ . Using numerical and analytical methods for general  $\epsilon$  and the results of the Floquet theory we find that the choice of the wavenumber  $q$  at large distances from the boundary is restricted by the presence of the boundary (we shall call this restriction the  $q$ -restriction). We compare numerical results for general  $\epsilon$  with the weakly nonlinear result of Cross *et al* (1983, [15]) for small  $\epsilon$  and find that the weakly-nonlinear result agrees remarkably well, even up to  $\epsilon = 1$ .

In Chapter 5 we investigate the spatially periodic solutions of the two-dimensional SH equation in a channel with no-slip sidewalls at  $y = 0$  and  $y = L_y$ . First we consider the linear stability of the trivial solution in the two-dimensional domain by using a scaling in the channel width  $L_y$ . Then we use a numerical method to calculate nonlinear solutions which are periodic in  $x$  along the channel.

In Chapter 6 we investigate further the steady two-dimensional SH equation for a channel of width  $L_y$ . Using Floquet theory, we perturb the two dimensional periodic solution and classify regions where the perturbation is spatially decaying or growing and regions where the perturbation is spatially oscillatory. The boundary separating the two regions is analogous to the Eckhaus stability boundary for the one-dimensional case. Our aim, as in the one dimensional theory of Chapter 3, is to determine the asymptotic form of the solution which applies in a semi-infinite channel at large distances from a lateral wall at  $x = 0$ .

In Chapter 7 we consider solutions of the steady two-dimensional SH equation for a channel of width  $L_y$  with the presence of a lateral boundary at  $x = 0$ . We use the Floquet theory of Chapter 6 to determine an estimate of the wavenumber restriction at general  $\epsilon$ .

We conclude with a discussion of our findings in Chapter 8.

## Chapter 2

# Solutions of the One Dimensional Swift-Hohenberg Equation

### 2.1 Introduction

In this chapter we obtain steady-state solutions of the one-dimensional SH equation. In Section 2.2 a shooting method is used to find solutions corresponding to a range of different initial conditions at  $x = 0$ . Periodic solutions are considered in Section 2.3 and are obtained analytically in both linear form and in weakly nonlinear form for values of  $\epsilon$  close to zero. Nonlinear periodic solutions are found in Sections 2.4 and 2.5 using a modified version of the shooting method. A Newton iteration is used to adjust the starting values at  $x = 0$  for a given wavelength  $2L$ . The results indicate the existence of further bifurcations of the solution which are discussed in Section 2.6.

### 2.2 Initial Value Computations

One approach to finding steady-state solutions  $u(x)$  of the one-dimensional SH equation is to simply compute solutions from specified initial conditions at  $x = 0$ . However, it is readily shown that in general these do not approach a periodic form as  $x \rightarrow \infty$ . Indeed, in this section we show that the steady-state one-dimensional SH equation has many solutions other than periodic solutions—solutions that also exist include quasi-periodic and unbounded solutions. This is investigated by imposing the free boundary conditions,  $u(0) = u''(0) = 0$ , and solving for various values of  $u'(0)$  and  $u'''(0)$ , where primes are used to denote  $\frac{d}{dx}$ .

Consider the initial value problem (IVP)

$$u'''' + 2u'' + (1 - \epsilon)u + u^3 = 0, \quad (2.1)$$

with

$$u(0) = 0, \quad u'(0) = a, \quad u''(0) = 0 \quad \text{and} \quad u'''(0) = b, \quad (2.2)$$

where  $a, b \in \mathbb{R}$ . Equation (2.1) belongs to a general class of reversible fourth order systems whose local and global properties have been reviewed recently by Champneys (1998, [7]). A conserved first integral can be obtained by multiplying by  $u'$  and integrating with respect to  $x$  to give

$$2u'u''' - (u'')^2 + 2(u')^2 + (1 - \epsilon)u^2 + \frac{1}{2}u^4 = R, \quad (2.3)$$

where  $R$  is an arbitrary constant. Using the conditions (2.2) we get

$$2a(b + a) = R. \quad (2.4)$$

By setting  $v = 1/u'$  equation (2.3) can be written as a second order equation for  $v$  as a function of  $u$ :

$$-2v \frac{d^2v}{du^2} + 5 \left( \frac{dv}{du} \right)^2 + (-R + (1 - \epsilon)u^2 + \frac{1}{2}u^4)v^6 + 2v^4 = 0. \quad (2.5)$$

In the terminology of Champneys, equation (2.1) falls within the *focus* case (see [7], Section 3.4) in which there are families of periodic orbits and consequent resonant subharmonic bifurcations. Such solutions are considered in detail in Section 2.3–2.6 below.

Now we formulate the numerical problem so that we can solve equation (2.1) for various values of  $(a, b)$  in the domain  $\mathbb{R} \times \mathbb{R}$ . The fourth order ordinary differential equation (2.1) is written as a system of first order differential equations

$$u'_1 = u_2, \quad (2.6)$$

$$u'_2 = u_3, \quad (2.7)$$

$$u'_3 = u_4, \quad (2.8)$$

$$u'_4 = -2u_3 - (1 - \epsilon)u_1 - u_1^3, \quad (2.9)$$

where  $u_1, u_2, u_3$  and  $u_4$  denote  $u, u', u''$  and  $u'''$  respectively. Then the initial

conditions, equation (2.2), become

$$u_1(0) = 0, \quad u_2(0) = a, \quad u_3(0) = 0 \quad \text{and} \quad u_4(0) = b, \quad (2.10)$$

where  $a, b \in \mathbb{R}$ . The nonlinear system (2.6)–(2.10) can be efficiently solved by an ODE solver such as ODE45, a solver from the Matlab's *ODESUITE* (1996, [46]). The solver is an implementation of the explicit Runge-Kutta (4, 5) pair by Dormand and Prince. It has also been called variously *RK5(4)7FM*, *DOPRI5*, *DP(4, 5)* and *DP54*. The code uses adaptive and free interpolation techniques to speed up the calculations. This particular version was designed and documented by Shampine and Reichelt (1994, [47]).

We have solved the problem for various values of  $(a, b) \in \mathbb{R} \times \mathbb{R}$  and found that there are regions where the numerical solutions are periodic, quasi-periodic or unbounded. Figures 2.1, 2.2 and 2.3 show examples of periodic, quasi-periodic and unbounded solutions respectively. The top left-hand plot of each figure shows the profile of the solution. The top right-hand plot is a projection of the solution's phase diagram (i.e., the plot of  $u$  against its derivative  $u'$ ). The bottom two plots show the discrete Fourier decomposition of the solution. The first plot shows the decomposition between zero wavenumber,  $q$ , and the Nyquist number, and the second plot is a magnification of the region of interest. Notice that Figure 2.4 shows that there are bounded solutions near<sup>1</sup> to unbounded solutions. More exotic solutions for values of  $\epsilon < 0$  and  $\epsilon > 1$  can be found as shown in Figures 2.5–2.12.

Figures 2.1–2.12 are representative of the types of solutions that occur. For a fixed value of  $\epsilon$ , our simulations indicate that the parameter space,  $(a, b)$ , divides into regions in which the solution is bounded and regions in which it is unbounded. We have also found that there were difficulties in identifying bounded solutions by this approach, especially when  $\epsilon > 1$ . Within our region of integration the solution might seem to be periodic or quasi-periodic but at higher values of  $x$  becomes unbounded. An alternative approach (to be described below) was adopted in order to identify the periodic steady-state solutions.

---

<sup>1</sup>The term 'near' is used to indicate proximity in our parameter space of  $a = u'(0)$  and  $b = u'''(0)$ .

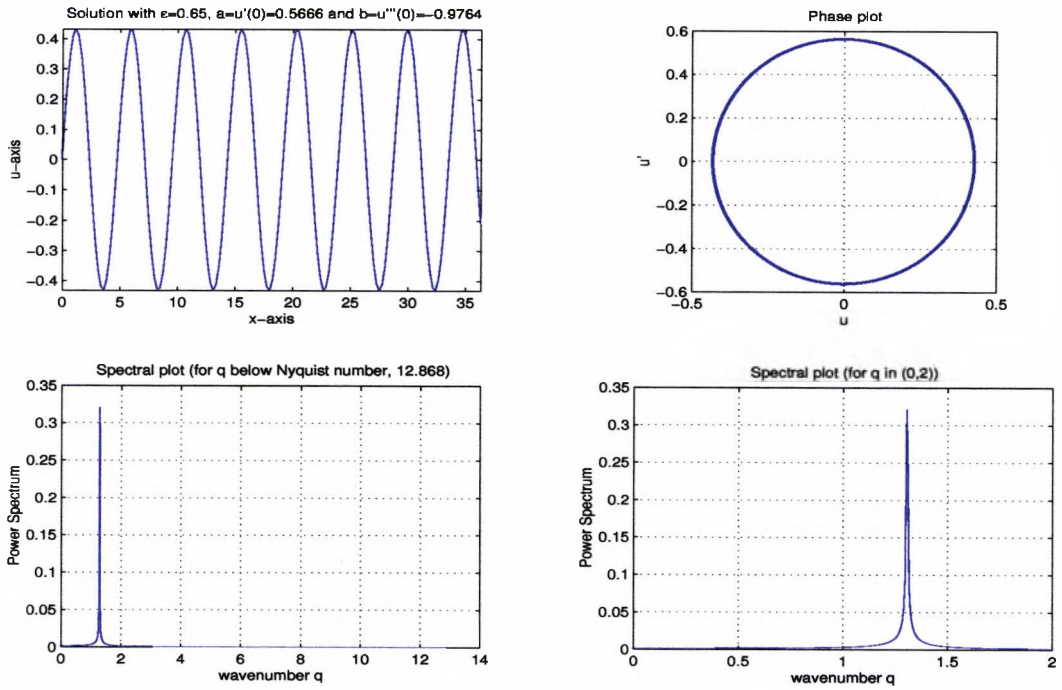


Figure 2.1: An example of a periodic solution at  $\epsilon = 0.65$ .

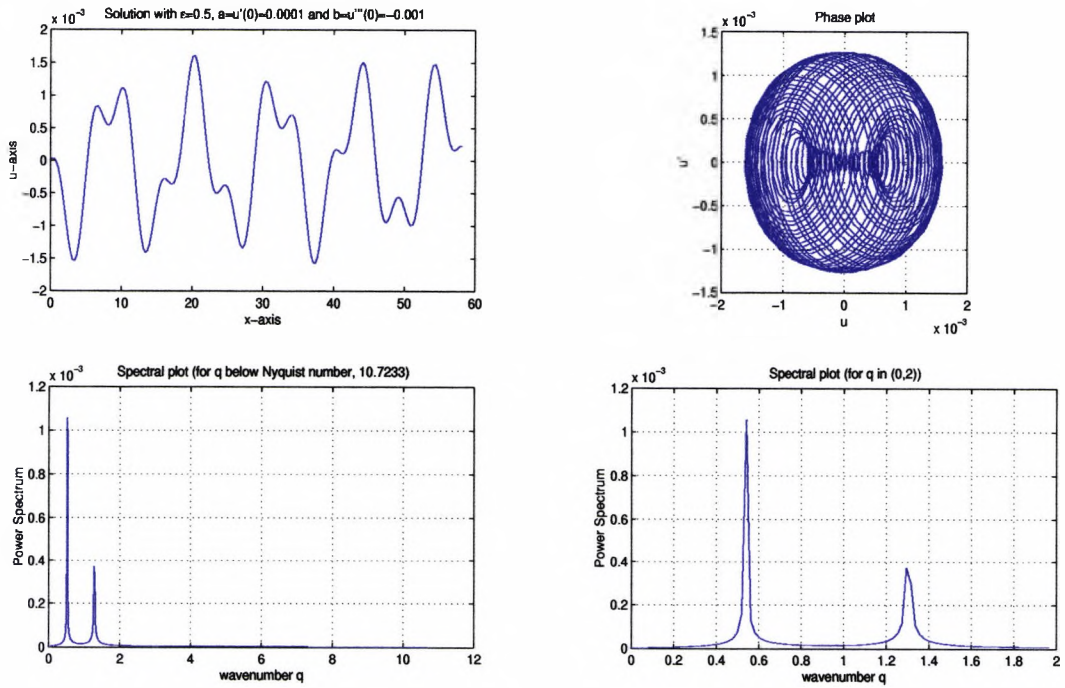


Figure 2.2: An example of a quasi-periodic solution at  $\epsilon = 0.5$ .

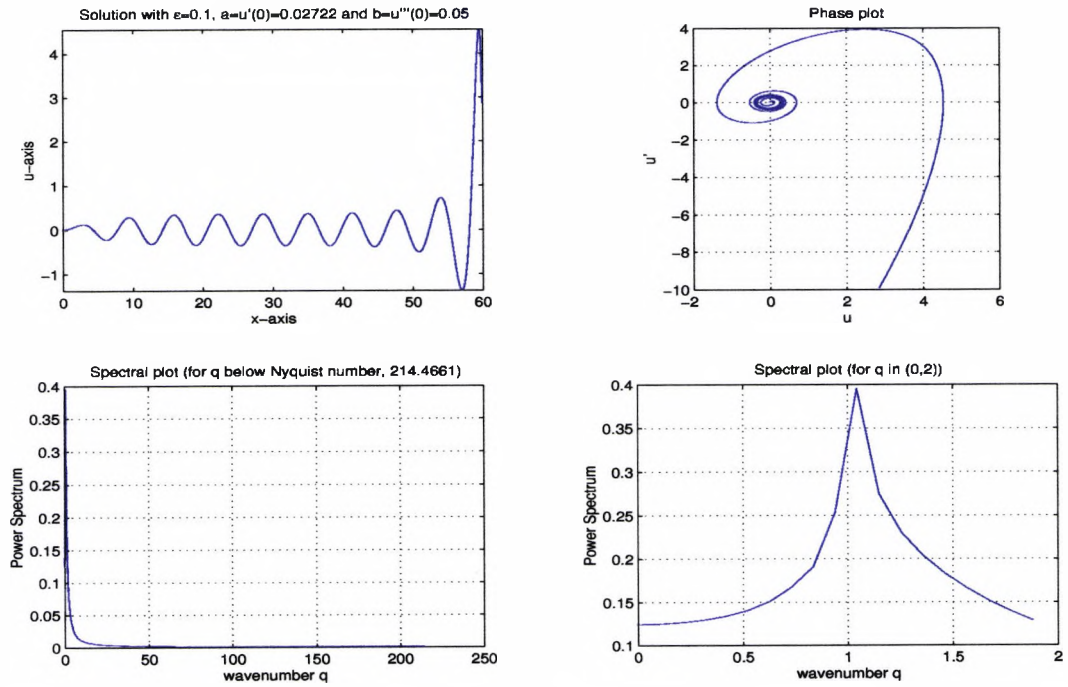


Figure 2.3: An example of an unbounded solution at  $u'(0) = 0.02722$  and  $u'''(0) = 0.05$  with  $\epsilon = 0.1$ . Our adaptive numerical algorithm has stopped due to numerical overflow.

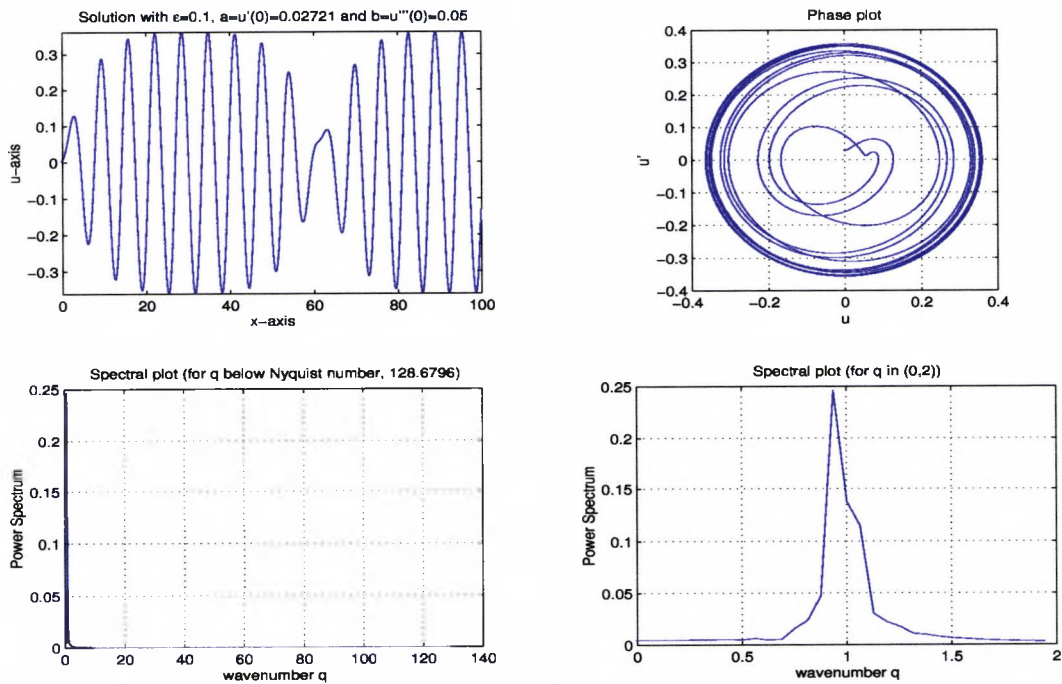


Figure 2.4: A bounded solution at  $\epsilon = 0.1$  with  $a = 0.02721$  and  $b = 0.05$ .

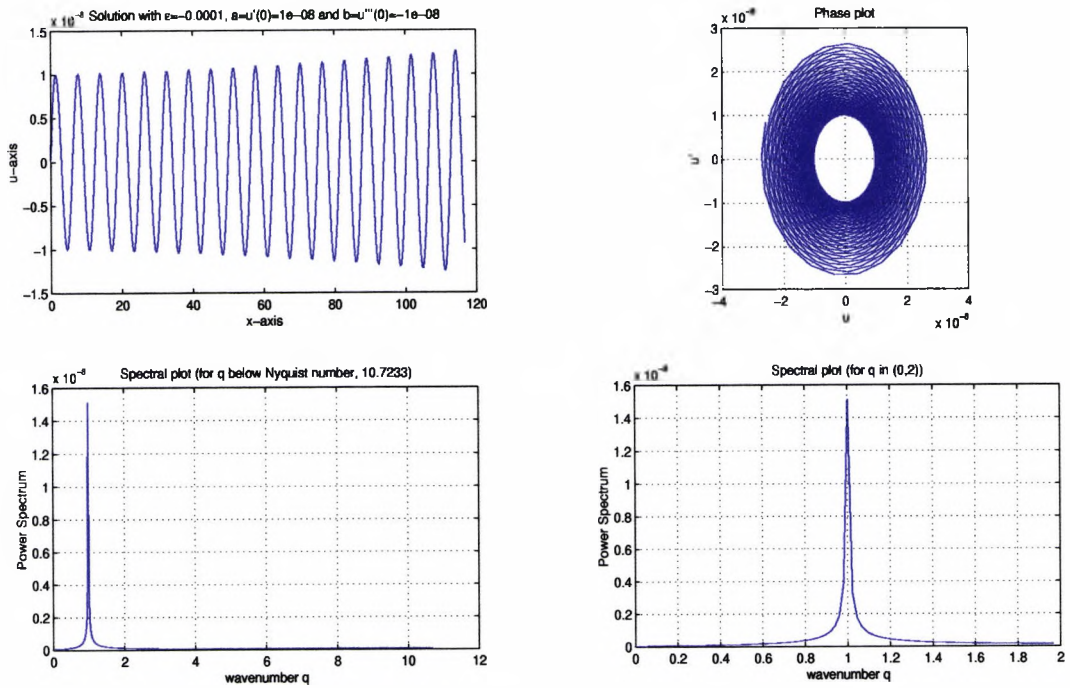


Figure 2.5: An example of a solution with  $\epsilon = -0.0001$ .

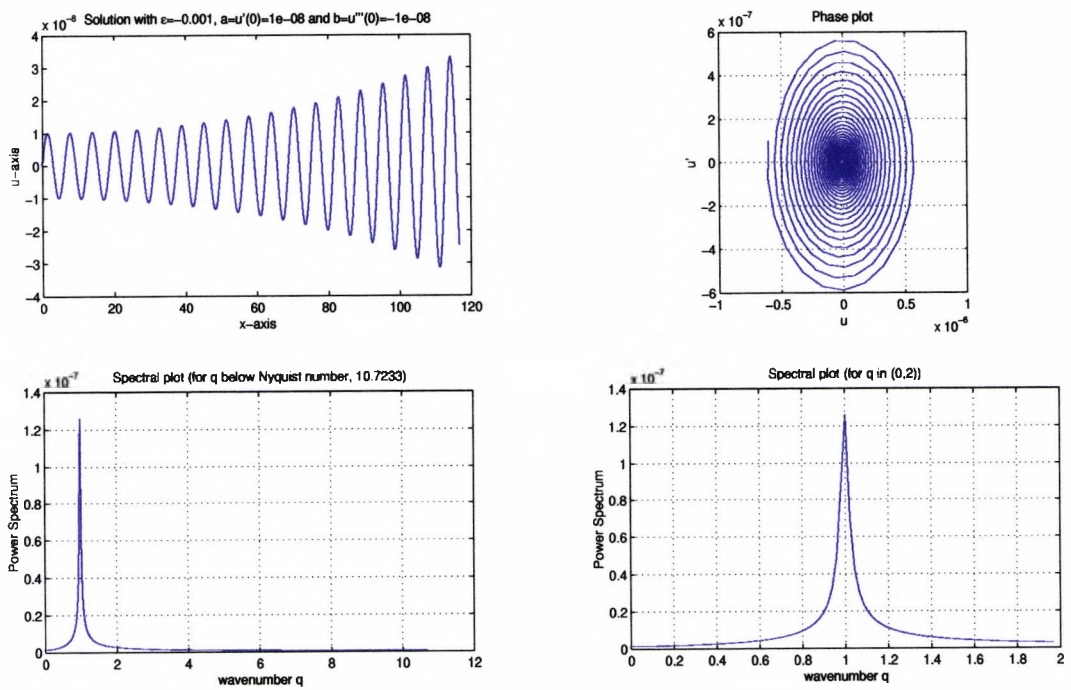


Figure 2.6: A solution with  $\epsilon = -0.001$ .

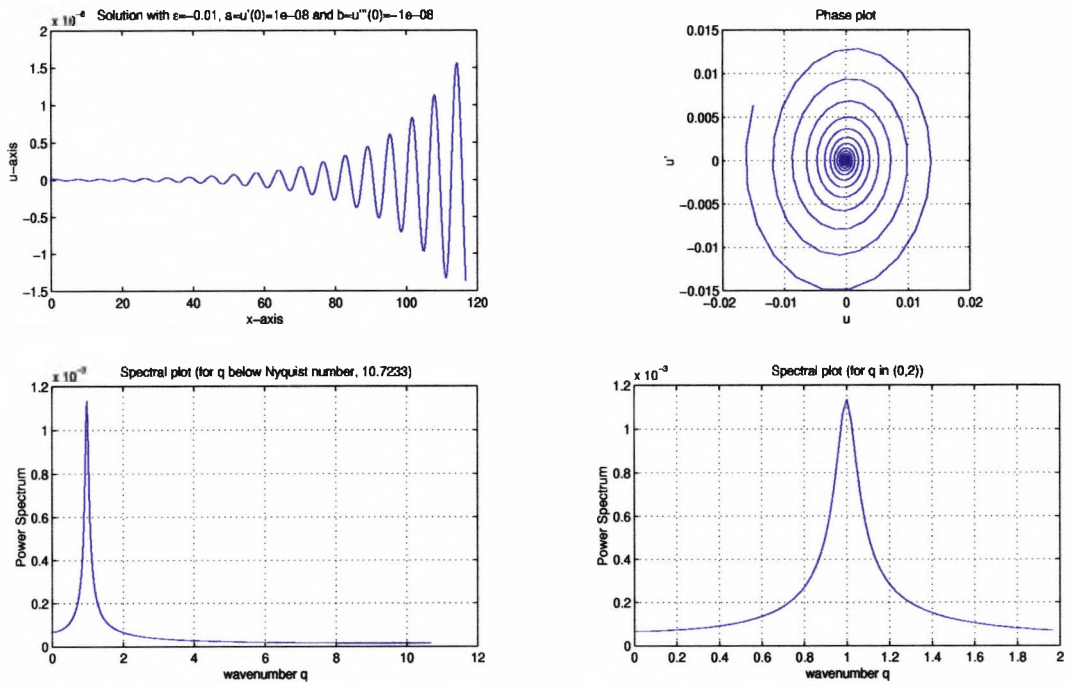


Figure 2.7: A solution with  $\epsilon = -0.01$ .

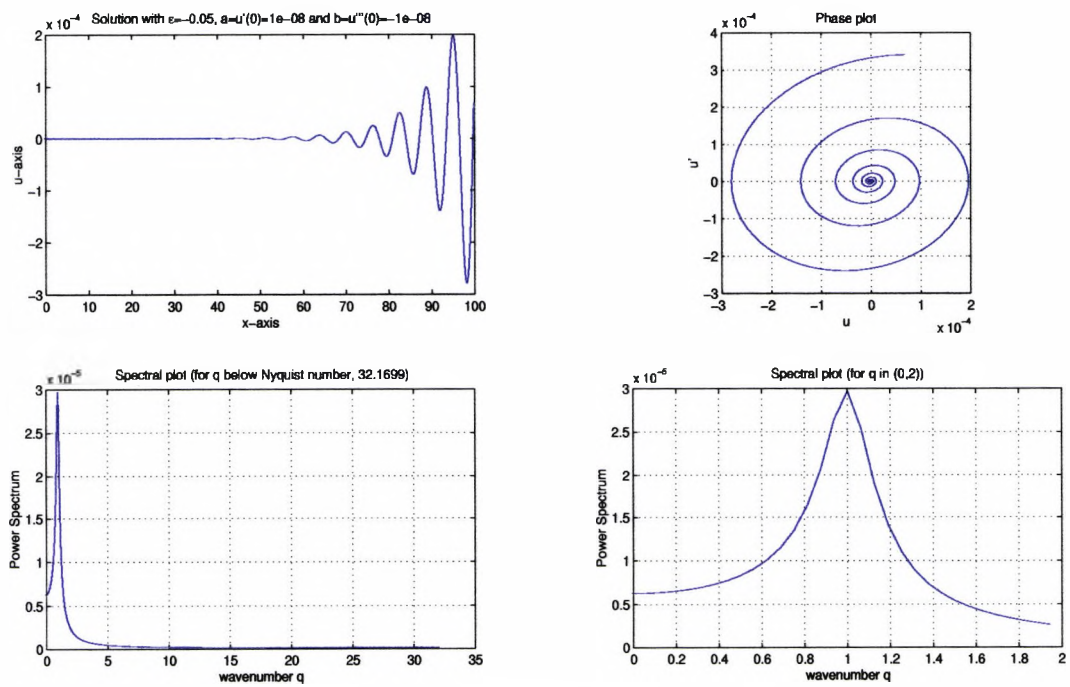


Figure 2.8: A solution with  $\epsilon = -0.05$ .

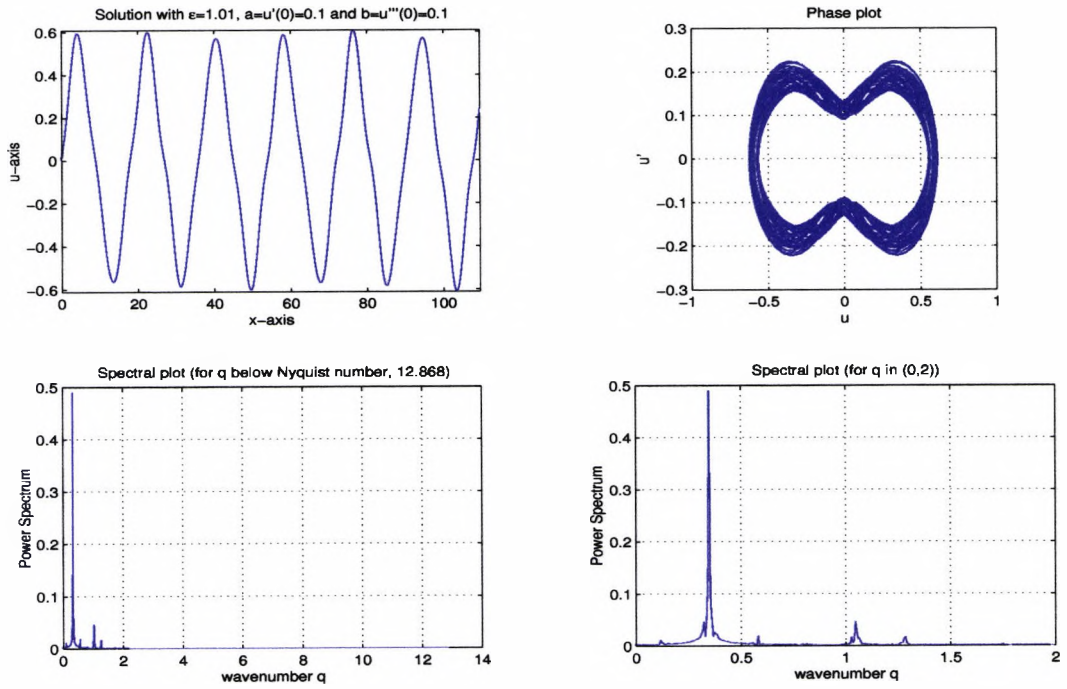


Figure 2.9: An example of a solution with  $\epsilon = 1.01$ ,  $a = 0.1$  and  $b = 0.1$ .

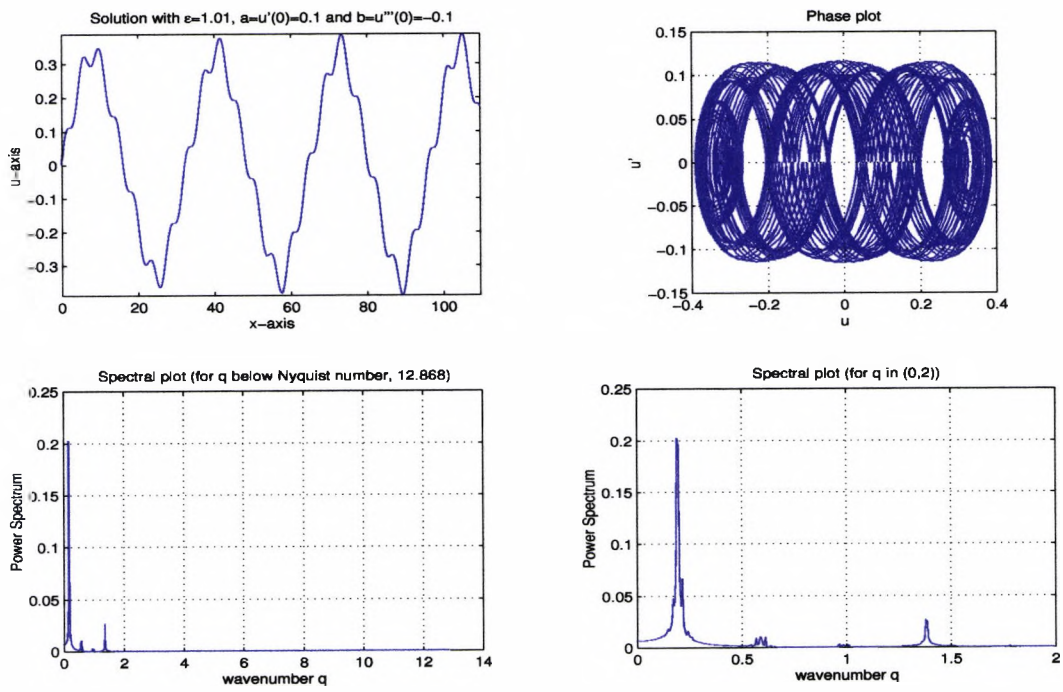


Figure 2.10: An example of a solution with  $\epsilon = 1.01$ ,  $a = 0.1$  and  $b = -0.1$ .

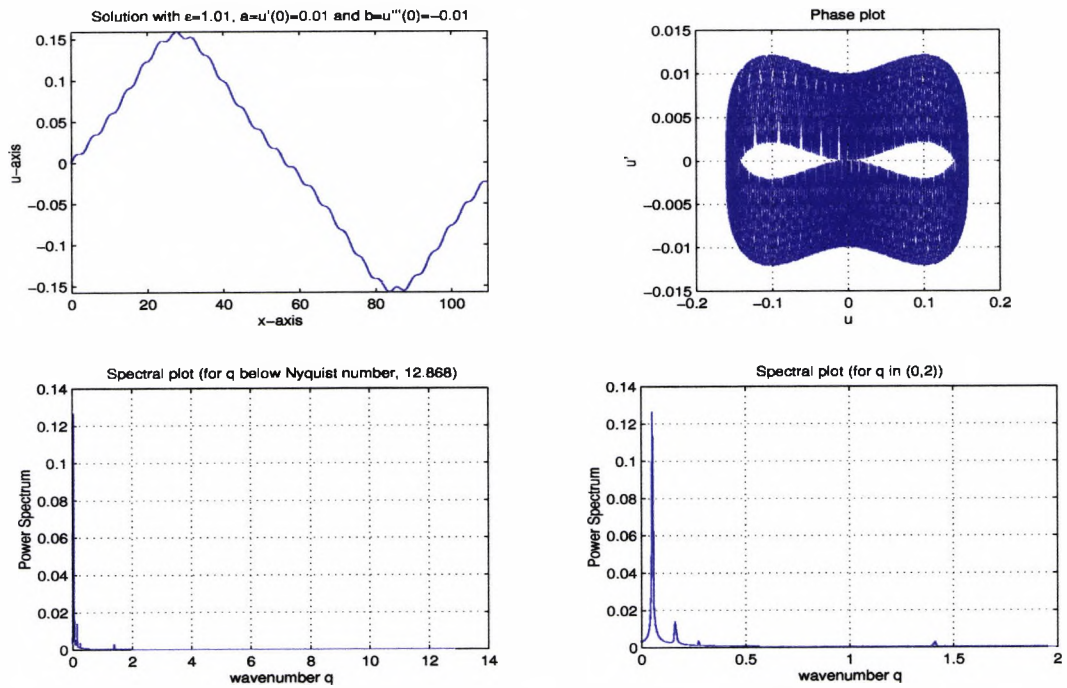


Figure 2.11: An example of a solution with  $\epsilon = 1.01$ ,  $a = 0.01$  and  $b = -0.01$ .

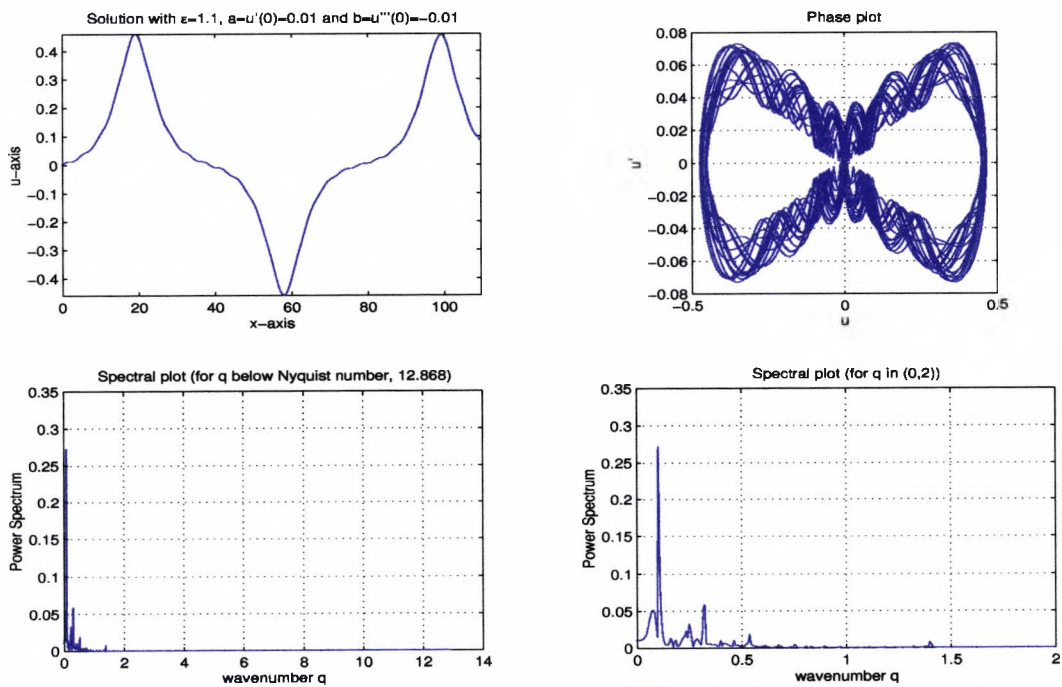


Figure 2.12: An example of a solution with  $\epsilon = 1.1$ .

## 2.3 Periodic Steady-state Solutions

We want to investigate periodic steady-state solutions of wavenumber,  $q$ . Such solutions can be expressed in the form (Kramer and Hohenberg (1984, [34]))

$$u_p(x) = \sum_{m=1}^{\infty} A_m \sin(mqx), \quad (2.11)$$

where the coefficients  $A_m$  correspond to the amplitudes of the fundamental and its harmonics. We believe that such solutions will be relevant within the bulk of a large system with lateral walls, i.e., between and away from the lateral walls. The coefficients can be computed by substituting (2.11) into (2.1) and solving the resulting set of coupled nonlinear equations (1984, [34]; [30], 1992; [44], 1986). However, this involves truncation of the system, and it is more convenient here to find the periodic solutions by numerical integration of the steady-state version of the boundary value problem

$$\frac{\partial u}{\partial t} = \left( \epsilon - \left[ 1 + \frac{\partial^2}{\partial x^2} \right]^2 \right) u - u^3, \quad (2.12)$$

subject to the stress-free boundary conditions

$$u = \frac{\partial^2 u}{\partial x^2} = 0 \quad \text{at} \quad x = 0, L, \quad (2.13)$$

for some finite  $L \in \mathbb{R}$ . This problem contains all periodic solutions of the form (2.11) through the correspondence  $L = n\pi/q$  where  $n$  is an integer. By adding the extra stress-free boundary conditions at  $x = L$  we restrict the solution set of the initial value problem, (2.1)–(2.2), to bounded solutions with finite period.

We shall proceed with our analysis of periodic solutions as follows. In Section 2.3.1 we shall perform a linear analysis of our problem. This will provide us with solutions that are infinitesimal perturbations from the trivial state,  $u = 0$ , equivalent to the conduction state in the Rayleigh-Bénard problem. Then in Section 2.3.2 we look for weakly nonlinear solutions by performing a perturbation analysis for  $\epsilon \ll 1$ . From this we obtain information about the nature of weakly nonlinear periodic solutions. These results assist in finding numerical steady-state solutions of the full nonlinear problem (2.12)–(2.13) in Sections 2.4 and 2.5.

### 2.3.1 Linear Analysis

First consider the linear analysis of the time dependent SH equation (2.12) with boundary conditions (2.13). Certainly, the trivial state,  $u = 0$ , is a solution to the system (2.12)–(2.13). Any infinitesimal perturbations from the trivial state are governed by the linearised version of (2.12), i.e., by neglecting the nonlinear term to obtain

$$\frac{\partial u}{\partial t} = \left( \epsilon - \left[ 1 + \frac{\partial^2}{\partial x^2} \right]^2 \right) u. \quad (2.14)$$

We want to look for normal modes in the form  $u = U(x) \exp(st)$ , and by substituting into (2.14) and (2.13) we get the homogeneous linear differential equation for  $U$ ,

$$U'''' + 2U'' + (1 + s - \epsilon)U = 0,$$

to be solved subject to

$$U = U'' = 0 \quad \text{at} \quad x = 0, L.$$

Solving the boundary value problem we obtain solutions

$$U = A \sin(q_n x) \quad \text{and} \quad q_n = \frac{n\pi}{L},$$

where  $n = 1, 2, 3, \dots$ , with

$$s = s_n = \epsilon - (q_n^2 - 1)^2.$$

Individual modes are marginally stable when  $s_n = 0$ , i.e., when

$$\epsilon = (q_n^2 - 1)^2 = ((n\pi/L)^2 - 1)^2. \quad (2.15)$$

Figure 2.13 shows the first ten marginal curves for the different modes. Notice that when  $L$  is small the most unstable mode is well isolated from its immediate neighbours. In contrast, when  $L$  becomes larger, the first eigenmodes (say  $n = 1, 2, \dots, 5$  for  $L = 4\pi$ ) stay well grouped. In this chapter we shall focus attention on the modes  $n = 1$ ,  $n = 2$  and  $n = 3$ . It should be stressed that at a given value of  $\epsilon$  the separate modes shown in Figure 2.13 actually represent just one periodic solution, the higher values of  $L$  simply accommodating additional oscillations in the interval  $(0, L)$ . However, we shall see below that the representation is useful

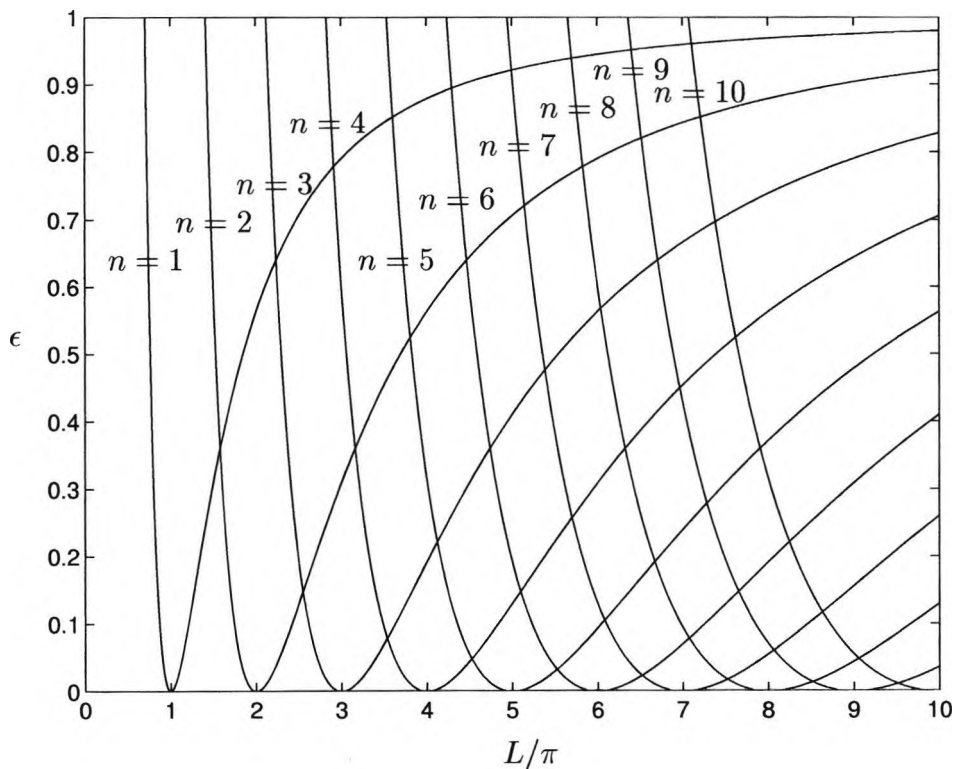


Figure 2.13: Marginal curves for individual modes.

in identifying further periodic forms which arise in the nonlinear spectrum of solutions.

### 2.3.2 Weakly Nonlinear Analysis

The linear analysis shows that steady-state periodic solutions of small amplitude exist in the neighbourhood of the marginal curves shown in Figure 2.13, and that as  $\epsilon$  increases these are first encountered when  $\epsilon$  reaches zero and  $L = n\pi$ , i.e., at a critical wavenumber  $q_n = 1$ . Here we shall consider how nonlinear periodic steady-state solutions (i.e. weakly nonlinear solutions) emerge from this point.

Thus we consider (2.12)–(2.13) and assume that  $\epsilon$  is small and positive. Balancing the terms in the partial differential equation suggests that  $u(x, t)$  develops

with terms of order,  $\epsilon^{1/2}, \epsilon, \epsilon^{3/2}, \dots$ , so that

$$u = \epsilon^{1/2}u_0 + \epsilon u_1 + \epsilon^{3/2}u_2 + \dots, \quad \epsilon \rightarrow 0. \quad (2.16)$$

In order to analyse equation (2.12) we shall let the solution contain modulations on the scales  $X = \sqrt{\epsilon}x$  and  $T = \epsilon t$  so that in (2.16) we assume that  $u_i = u_i(x, X, T)$ . After substitution into (2.12) we collect and compare coefficients of powers of  $\epsilon$ . We obtain

$$\frac{\partial^4 u_0}{\partial x^4} + 2 \frac{\partial^2 u_0}{\partial x^2} + u_0 = 0, \quad (2.17)$$

$$\frac{\partial^4 u_1}{\partial x^4} + 2 \frac{\partial^2 u_1}{\partial x^2} + u_1 = -4 \left[ \frac{\partial^4 u_0}{\partial x^3 \partial X} + \frac{\partial^2 u_0}{\partial x \partial X} \right], \quad (2.18)$$

$$\begin{aligned} \frac{\partial^4 u_2}{\partial x^4} + 2 \frac{\partial^2 u_2}{\partial x^2} + u_2 = & - \left[ 4 \frac{\partial^4 u_1}{\partial X \partial x^3} + 4 \frac{\partial^2 u_1}{\partial X \partial x} + 6 \frac{\partial^4 u_0}{\partial X^2 \partial x^2} \right. \\ & \left. + \frac{\partial u_0}{\partial T} + 2 \frac{\partial^2 u_0}{\partial X^2} + u_0^3 - u_0 \right], \end{aligned} \quad (2.19)$$

at orders  $\epsilon^{1/2}, \epsilon$  and  $\epsilon^{3/2}$  respectively. Solving equation (2.17), the relevant periodic form is

$$u_0(x, X, T) = A_0(X, T) \exp(ix) + \text{c.c.}, \quad (2.20)$$

where  $A_0$  is a complex amplitude function and c.c. denotes the complex conjugate. Substitution for  $u_0(x, X, T)$  into equation (2.18) then gives

$$\frac{\partial^4 u_1}{\partial x^4} + 2 \frac{\partial^2 u_1}{\partial x^2} + u_1 = 0,$$

so that

$$u_1(x, X, T) = A_1(X, T) \exp(ix) + \text{c.c.}, \quad (2.21)$$

where  $A_1$  is a further complex amplitude function. We now substitute for  $u_0(x, X, T)$  and  $u_1(x, X, T)$  in equation (2.19) to get

$$\begin{aligned} \frac{\partial^4 u_2}{\partial x^4} + 2 \frac{\partial^2 u_2}{\partial x^2} + u_2 = & + \left[ -\frac{\partial A_0}{\partial T} + A_0 - 3A_0|A_0|^2 + 4 \frac{\partial^2 A_0}{\partial X^2} \right] \exp(ix) \\ & + \left[ -\frac{\partial \bar{A}_0}{\partial T} + \bar{A}_0 - 3\bar{A}_0|A_0|^2 + 4 \frac{\partial^2 \bar{A}_0}{\partial X^2} \right] \exp(-ix) \\ & - A_0^3 \exp(3ix) - \bar{A}_0^3 \exp(-3ix), \end{aligned} \quad (2.22)$$

where  $\bar{A}_0$  denotes the complex conjugate of  $A_0$ . In order that  $u_2$  is periodic, the secular terms proportional to  $\exp(\pm ix)$  must vanish, requiring that  $A_0$  satisfies the partial differential equation

$$\frac{\partial A_0}{\partial T} = 4 \frac{\partial^2 A_0}{\partial X^2} + A_0 - 3A_0|A_0|^2. \quad (2.23)$$

Since we are interested in periodic solutions, we shall assume  $A_0$  takes the form

$$A_0 \equiv A_p = R \exp(iQX), \quad (2.24)$$

where  $R$  is independent of  $X$ . Equations (2.16), (2.20) and (2.24) now imply that

$$u \approx \sqrt{\epsilon} [R \exp(i(x + QX)) + \bar{R} \exp(-i(x + QX))], \quad (2.25)$$

where  $\bar{R}$  denotes the complex conjugate of  $R$ . Now  $u$  must satisfy the conditions (2.13) at the boundary. The conditions  $u = \frac{\partial^2 u}{\partial x^2} = 0$  at  $x = 0$  imply that

$$\text{Re}(R) = 0, \quad (2.26)$$

and the conditions  $u = \frac{\partial^2 u}{\partial x^2} = 0$  at  $x = L$  imply that

$$\text{Im}(R) \sin(L + Q\epsilon^{1/2}L) = 0. \quad (2.27)$$

A non-trivial solution requires  $\text{Im}(R) \neq 0$  in which case

$$\sin(L + Q\epsilon^{1/2}L) = 0, \quad (2.28)$$

and we have the relationship between  $L$  and  $Q$

$$L(1 + Q\epsilon^{1/2}) = n\pi, \quad \text{for } n = 1, 2, \dots \quad (2.29)$$

Now consider the steady-state solution to equation (2.23). In this case the solution (2.24) satisfying (2.26) has

$$R = \pm \frac{i}{\sqrt{3}} (1 - 4Q^2)^{1/2}, \quad -\frac{1}{2} \leq Q \leq \frac{1}{2}. \quad (2.30)$$

This shows that weakly nonlinear periodic steady-state solutions

$$u \approx \pm 2\sqrt{\frac{\epsilon}{3}}(1 - 4Q^2)^{\frac{1}{2}} \sin \frac{n\pi x}{L}, \quad -\frac{1}{2} \leq Q \leq \frac{1}{2}, \quad (2.31)$$

where  $Q$  and  $L$  are related by (2.29), exist in the regions inside the marginal stability curves, which correspond to the limiting values  $Q = \pm 1/2$ . The results obtained here are thus consistent with the results obtained in the linear analysis, the value of  $q$  here being approximated by  $1 + \sqrt{\epsilon}Q$  near the critical point. In Section 2.4 we shall use the results obtained here to initiate solutions of the fully nonlinear problem.

## 2.4 Numerical Methods for Finding Periodic Solutions

In this section we discuss two different methods which were used to compute periodic solutions for the one-dimensional SH equation.

### 2.4.1 Shooting Method

By converting the boundary value problem into an extended initial value problem we can use the same techniques as in Section 2.2 to solve our problem.

Consider the boundary value problem (2.12)–(2.13). As in Section 2.2, we convert the steady-state version of equation (2.12) to the system of first order ordinary differential equations

$$u_1'(x) = u_2(x), \quad (2.32)$$

$$u_2'(x) = u_3(x), \quad (2.33)$$

$$u_3'(x) = u_4(x), \quad (2.34)$$

$$u_4'(x) = -2u_3(x) - (1 - \epsilon)u_1(x) - (u_1(x))^3. \quad (2.35)$$

The boundary conditions (2.13) become

$$u_1(0) = u_3(0) = 0 \quad \text{and} \quad u_1(L) = u_3(L) = 0, \quad (2.36)$$

where  $L \in \mathbb{R}$ .

Writing the boundary-value problem (2.32)–(2.36) as an initial value problem we get

$$\underline{u}' = \underline{f}(x, \underline{u}), \quad (2.37)$$

subject to the initial condition

$$\underline{u}(\underline{s}, 0) = \underline{s}, \quad (2.38)$$

where  $\underline{u} = [u_1(\underline{s}, x), u_2(\underline{s}, x), u_3(\underline{s}, x), u_4(\underline{s}, x)]^T$ ,  $\underline{s} = [0, \alpha, 0, \beta]^T$  and

$$\underline{f}(x, \underline{u}) = \begin{bmatrix} u_2(\underline{s}, x) \\ u_3(\underline{s}, x) \\ u_4(\underline{s}, x) \\ -2u_3(\underline{s}, x) - (1 - \epsilon)u_1(\underline{s}, x) - (u_1(\underline{s}, x))^3 \end{bmatrix}.$$

The shooting parameters  $\alpha$  and  $\beta$  correspond to the constants  $a$  and  $b$  used in Section 2.2.

We wish to find an  $\underline{s}^* = [0, \alpha^*, 0, \beta^*]^T$  such that  $u_1(\underline{s}, L) = 0$  and  $u_3(\underline{s}, L) = 0$ . First, we define

$$\underline{F}(\alpha, \beta) = \begin{bmatrix} F_1(\alpha, \beta) \\ F_2(\alpha, \beta) \end{bmatrix} = \begin{bmatrix} u_1(\underline{s}, L) \\ u_3(\underline{s}, L) \end{bmatrix}.$$

Newton's method applied to  $\underline{F}(\alpha, \beta) = 0$  is

$$\underline{s}_{k+1} = \underline{s}_k - J^{-1}(\underline{s}_k)\underline{F}(\underline{s}_k),$$

where  $\underline{s}_k = [\alpha^k, \beta^k]^T$  and

$$J(\underline{s}_k) = \begin{bmatrix} \frac{\partial F_1}{\partial \alpha^k}(\underline{s}_k) & \frac{\partial F_1}{\partial \beta^k}(\underline{s}_k) \\ \frac{\partial F_2}{\partial \alpha^k}(\underline{s}_k) & \frac{\partial F_2}{\partial \beta^k}(\underline{s}_k) \end{bmatrix}.$$

We need to find  $\frac{\partial F_1}{\partial \alpha}$ ,  $\frac{\partial F_1}{\partial \beta}$ ,  $\frac{\partial F_2}{\partial \alpha}$  and  $\frac{\partial F_2}{\partial \beta}$ . Differentiating the initial value problem (2.37) with respect to  $\alpha$  we get

$$\frac{\partial \underline{u}'}{\partial \alpha} = \begin{bmatrix} (u_2(\underline{s}, x))_\alpha \\ (u_3(\underline{s}, x))_\alpha \\ (u_4(\underline{s}, x))_\alpha \\ -2(u_3(\underline{s}, x))_\alpha - (1 - \epsilon)(u_1(\underline{s}, x))_\alpha - 3(u_1(\underline{s}, x))^2(u_1(\underline{s}, x))_\alpha \end{bmatrix}. \quad (2.39)$$

Assuming the order of differentiation can be reversed the left hand side of equation (2.39) becomes

$$\frac{\partial \underline{u}'}{\partial \alpha} = \frac{\partial \underline{u}_\alpha}{\partial x} = \begin{bmatrix} (u_1(\underline{s}, x))'_\alpha \\ (u_2(\underline{s}, x))'_\alpha \\ (u_3(\underline{s}, x))'_\alpha \\ (u_4(\underline{s}, x))'_\alpha \end{bmatrix}. \quad (2.40)$$

Let  $u_5 = \frac{\partial u_1}{\partial \alpha}$ ,  $u_6 = \frac{\partial u_2}{\partial \alpha}$ ,  $u_7 = \frac{\partial u_3}{\partial \alpha}$  and  $u_8 = \frac{\partial u_4}{\partial \alpha}$ . Then equation (2.40) becomes

$$\begin{bmatrix} u'_5(\underline{s}, x) \\ u'_6(\underline{s}, x) \\ u'_7(\underline{s}, x) \\ u'_8(\underline{s}, x) \end{bmatrix} = \begin{bmatrix} u_6(\underline{s}, x) \\ u_7(\underline{s}, x) \\ u_8(\underline{s}, x) \\ -2u_7(\underline{s}, x) - (1 - \epsilon)u_5(\underline{s}, x) - 3(u_1(\underline{s}, x))^2 u_5(\underline{s}, x) \end{bmatrix} \quad (2.41)$$

The initial conditions (2.38) imply that

$$u_1(\underline{s}, 0) = 0, \quad u_2(\underline{s}, 0) = \alpha, \quad u_3(\underline{s}, 0) = 0, \quad \text{and} \quad u_4(\underline{s}, 0) = \beta.$$

Differentiating with respect to  $\alpha$  we get

$$\begin{aligned} (u_1(\underline{s}, 0))_\alpha &= 0, \\ (u_2(\underline{s}, 0))_\alpha &= 1, \\ (u_3(\underline{s}, 0))_\alpha &= 0, \\ (u_4(\underline{s}, 0))_\alpha &= 0, \end{aligned} \Rightarrow \begin{cases} u_5(\underline{s}, 0) = 0, \\ u_6(\underline{s}, 0) = 1, \\ u_7(\underline{s}, 0) = 0, \\ u_8(\underline{s}, 0) = 0, \end{cases} \quad (2.42)$$

where  $u_5 = \frac{\partial u_1}{\partial \alpha}$ ,  $u_6 = \frac{\partial u_2}{\partial \alpha}$ ,  $u_7 = \frac{\partial u_3}{\partial \alpha}$  and  $u_8 = \frac{\partial u_4}{\partial \alpha}$ . It can be seen that  $\frac{\partial F_1}{\partial \alpha} = u_5(L)$  and  $\frac{\partial F_2}{\partial \alpha} = u_7(L)$ . Similarly, we differentiate the initial value problem (2.37) with respect to  $\beta$  and use the same argument as above to obtain the initial value problem

$$u'_9(\underline{s}, x) = u_{10}(\underline{s}, x), \quad (2.43)$$

$$u'_{10}(\underline{s}, x) = u_{11}(\underline{s}, x), \quad (2.44)$$

$$u'_{11}(\underline{s}, x) = u_{12}(\underline{s}, x), \quad (2.45)$$

$$u'_{12}(\underline{s}, x) = -2u_{11}(\underline{s}, x) - (1 - \epsilon)u_9(\underline{s}, x) - 3(u_1(\underline{s}, x))^2 u_9(\underline{s}, x), \quad (2.46)$$

subject to

$$\begin{aligned} u_9(\underline{s}, 0) &= 0, \\ u_{10}(\underline{s}, 0) &= 0, \\ u_{11}(\underline{s}, 0) &= 0, \\ u_{12}(\underline{s}, 0) &= 1, \end{aligned}$$

where  $u_9 = \frac{\partial u_1}{\partial \beta}$ ,  $u_{10} = \frac{\partial u_2}{\partial \beta}$ ,  $u_{11} = \frac{\partial u_3}{\partial \beta}$  and  $u_{12} = \frac{\partial u_4}{\partial \beta}$ . It can be seen that  $\frac{\partial F_1}{\partial \beta} = u_9(L)$  and  $\frac{\partial F_2}{\partial \beta} = u_{11}(L)$ .

The original boundary value problem has become the problem to solve the larger initial value problem

$$\begin{aligned} u'_1(\underline{s}, x) &= u_2(\underline{s}, x), \\ u'_2(\underline{s}, x) &= u_3(\underline{s}, x), \\ u'_3(\underline{s}, x) &= u_4(\underline{s}, x), \\ u'_4(\underline{s}, x) &= -2u_3(\underline{s}, x) - (1 - \epsilon)u_1(\underline{s}, x) - (u_1(\underline{s}, x))^3, \\ u'_5(\underline{s}, x) &= u_6(\underline{s}, x), \\ u'_6(\underline{s}, x) &= u_7(\underline{s}, x), \\ u'_7(\underline{s}, x) &= u_8(\underline{s}, x), \\ u'_8(\underline{s}, x) &= -2u_7(\underline{s}, x) - (1 - \epsilon)u_5(\underline{s}, x) - 3(u_1(\underline{s}, x))^2u_5(\underline{s}, x), \\ u'_9(\underline{s}, x) &= u_{10}(\underline{s}, x), \\ u'_{10}(\underline{s}, x) &= u_{11}(\underline{s}, x), \\ u'_{11}(\underline{s}, x) &= u_{12}(\underline{s}, x), \\ u'_{12}(\underline{s}, x) &= -2u_{11}(\underline{s}, x) - (1 - \epsilon)u_9(\underline{s}, x) - 3(u_1(\underline{s}, x))^2u_9(\underline{s}, x), \end{aligned} \tag{2.47}$$

subject to

$$\begin{aligned} u_1(\underline{s}, 0) &= 0, & u_7(\underline{s}, 0) &= 0, \\ u_2(\underline{s}, 0) &= \alpha, & u_8(\underline{s}, 0) &= 0, \\ u_3(\underline{s}, 0) &= 0, & u_9(\underline{s}, 0) &= 0, \\ u_4(\underline{s}, 0) &= \beta, & u_{10}(\underline{s}, 0) &= 0, \\ u_5(\underline{s}, 0) &= 0, & u_{11}(\underline{s}, 0) &= 0, \\ u_6(\underline{s}, 0) &= 1, & u_{12}(\underline{s}, 0) &= 1, \end{aligned} \tag{2.48}$$

and at each step we iterate using

$$\begin{bmatrix} \alpha^{k+1} \\ \beta^{k+1} \end{bmatrix} = \begin{bmatrix} \alpha^k \\ \beta^k \end{bmatrix} - \begin{bmatrix} u_5^k & u_9^k \\ u_{11}^k & u_{11}^k \end{bmatrix}^{-1} \begin{bmatrix} u_1^k \\ u_3^k \end{bmatrix},$$

where  $k$  denotes the iteration step. In this way, starting from an approximate

initial guess  $\alpha^0$  and  $\beta^0$  the scheme is designed to find the values of  $\alpha = u'(0)$  and  $\beta = u'''(0)$  corresponding to a steady-state solution of (2.12) and (2.13). The scheme can be started from small values of  $\epsilon$ , where the weakly nonlinear theory can be used to provide estimates of  $\alpha$  and  $\beta$  for small  $\epsilon$ . Results can then be extended to larger  $\epsilon$  and a range of values of  $L$  by incrementing the values of both  $L$  and  $\epsilon$ .

## 2.4.2 Boundary Value Problem: Finite Difference Method

The shooting method used in Section 2.4.1 often presents problems of numerical instability at large  $L$ . The method we present in this section has better stability characteristics, but generally requires more work to obtain a specified accuracy. This is because in the shooting method each contributing differential equation solution can be made as accurate as we please by use of modern computer routines in which the combined selection of interval size (adaptive stepsize) and order (adaptive order) of the method for a required accuracy are more or less automatic, whereas for the Finite Difference (FD) method described here these parameters (stepsize and order) must be specified from the start. Finite difference methods are generally faster since the relevant equations are solved simultaneously rather than in a step-by-step manner.

Consider the steady-state version of the boundary value problem (2.12)–(2.13). We introduce a finite set of grid points  $x_n = nh$ , for  $n = 1, 2, \dots, N$ , where  $N \in \mathbb{N}$  and  $h = L/(N + 1)$ . Using the finite difference approximations

$$\begin{aligned} u(x_n) &= u_n, \\ h^2 u_{xx}(x_n) &= u_{n+1} - 2u_n + u_{n-1}, \\ h^4 u_{xxxx}(x_n) &= u_{n+2} - 4u_{n+1} + 6u_n - 4u_{n-1} + u_{n-2}, \end{aligned}$$

to approximate  $u$ ,  $u_{xx}$  and  $u_{xxxx}$  respectively, the ordinary differential equation (2.12) becomes

$$\begin{aligned} u_{n+2} + (-4 + 2h^2)u_{n+1} + (6 - 4h^2 + (1 - \epsilon)h^4)u_n + \\ + (-4 + 2h^2)u_{n-1} + u_{n-2} + u_n^3 = 0, \end{aligned} \quad (2.49)$$

at the nodal points  $x_n = nh$ ,  $1 \leq n \leq N$ . The boundary conditions become

$$\begin{aligned} u_0 &= 0, & u_{-1} - 2u_0 + u_1 &= u_{-1} + u_1 = 0, \\ u_{N+1} &= 0, & u_{N+2} - 2u_{N+1} + u_N &= u_{N+2} + u_N = 0. \end{aligned}$$

Substituting for  $u_{-1}$  and  $u_{N+2}$  in the first ( $n = 1$ ) and the last ( $n = N$ ) equations in (2.49), we obtain in matrix form

$$A\mathbf{u} + \mathbf{b} = \mathbf{0}, \quad (2.50)$$

where  $\mathbf{b} = [u_1^3, u_2^3, \dots, u_{N-1}^3, u_N^3]^T$  and  $A$  is an  $N \times N$  matrix defined by

$$A = \begin{bmatrix} a_1 & -4 + 2h^2 & 1 & 0 & \dots & 0 \\ -4 + 2h^2 & a_2 & -4 + 2h^2 & 1 & \ddots & \vdots \\ 1 & -4 + 2h^2 & a_3 & -4 + 2h^2 & \ddots & \vdots \\ \vdots & \ddots & \ddots & \ddots & \ddots & \vdots \\ \vdots & \ddots & \ddots & \ddots & \ddots & \vdots \\ \vdots & \ddots & -4 + 2h^2 & a_{N-2} & -4 + 2h^2 & 1 \\ \vdots & \ddots & 1 & -4 + 2h^2 & a_{N-1} & -4 + 2h^2 \\ 0 & \dots & 0 & 1 & -4 + 2h^2 & a_N \end{bmatrix},$$

with  $a_i$ , for  $i = 1, 2, \dots, N$ , defined by

$$\begin{bmatrix} a_1 \\ a_2 \\ a_3 \\ \vdots \\ a_{N-2} \\ a_{N-1} \\ a_N \end{bmatrix} = \begin{bmatrix} 5 - 4h^2 + (1 - \epsilon)h^4 \\ 6 - 4h^2 + (1 - \epsilon)h^4 \\ 6 - 4h^2 + (1 - \epsilon)h^4 \\ \vdots \\ 6 - 4h^2 + (1 - \epsilon)h^4 \\ 6 - 4h^2 + (1 - \epsilon)h^4 \\ 5 - 4h^2 + (1 - \epsilon)h^4 \end{bmatrix}.$$

The truncation error associated with the system (2.50) can be obtained as

$$\begin{aligned} T_1 &= (59h^6 M_6)/360, \\ T_n &= (h^6 M_6)/6, \quad \text{for } 2 \leq n \leq N - 1, \\ T_N &= (59h^6 M_6)/360, \end{aligned}$$

where  $M_6 = \max_{0 \leq x \leq L} |u^{(6)}(x)|$ . Given a sufficiently close initial guess the non-linear system (2.50) can be efficiently solved using a Newton-Krylov algorithm.

The FD code is used when the shooting method fails. Generally, this is when  $L$  is large.

## 2.5 Numerical Results

We use the ODE solver within Matlab's *ODESUITE* (1996, [46]) to solve the extended initial value problem (2.47)–(2.48).

We can follow the solutions by incrementing<sup>2</sup> in  $L$  or  $\epsilon$ ; and by using the results of the previous *nearby* calculations as our initial Newton iterative guess, denoted by  $\alpha^0$  and  $\beta^0$ , the shooting parameters  $\alpha$  and  $\beta$  can be efficiently calculated within the parameter space  $(L, \epsilon) \in [0, \infty) \times [0, \infty)$ . Fixing  $L = \pi$  and  $\epsilon = 0.1$  we set the algorithm to find solutions for an initial guess of  $(\alpha^0, \beta^0)$  calculated from the results of the weakly nonlinear theory for small  $\epsilon$ . Possible solutions at these values include the trivial solution and a symmetric pair of solutions, i.e.,

$$(\alpha, \beta) \in \{(0, 0), (0.365814, -0.370378), (-0.365814, 0.370378)\}.$$

The plot of the solution with  $(\alpha, \beta) = (0.365814, -0.370378)$  and  $x \in (0, 50)$  together with its phase diagram and its power spectrum is shown in Figure 2.14. From this diagram we can see that if the solution is extended to values of  $x$  beyond the range  $[0, L]$  it eventually diverges from its approximate sine function profile (i.e., the phase plot shows that the solution is moving off the closed loop), as would be expected for a shooting method (due to the linear growth of the error). The variation of  $\alpha$  and  $\beta$  as a function of  $L$  for various values of  $\epsilon$  is shown in Figure 2.15.

Fixing  $L = \pi$  and increasing  $\epsilon$  in steps of 0.1, the results in Figure 2.16 show that the solution has a profile which increases in amplitude as we increase  $\epsilon$ . Increasing  $\epsilon$  further, Figure 2.17, we see that the solution becomes more square in profile.

The behaviour of  $\alpha$  and  $\beta$  as a function of  $L$  at  $\epsilon = 0.65$  indicates a much

---

<sup>2</sup>In our path following-code we used a heuristic method to increment the step-size in  $L$  or  $\epsilon$ . The code monitors the number of Newton iterations and reduces or increases the step-size when the number of iterations increases or decreases respectively. This adaptive code is faster and can also resolve the curvature more finely.

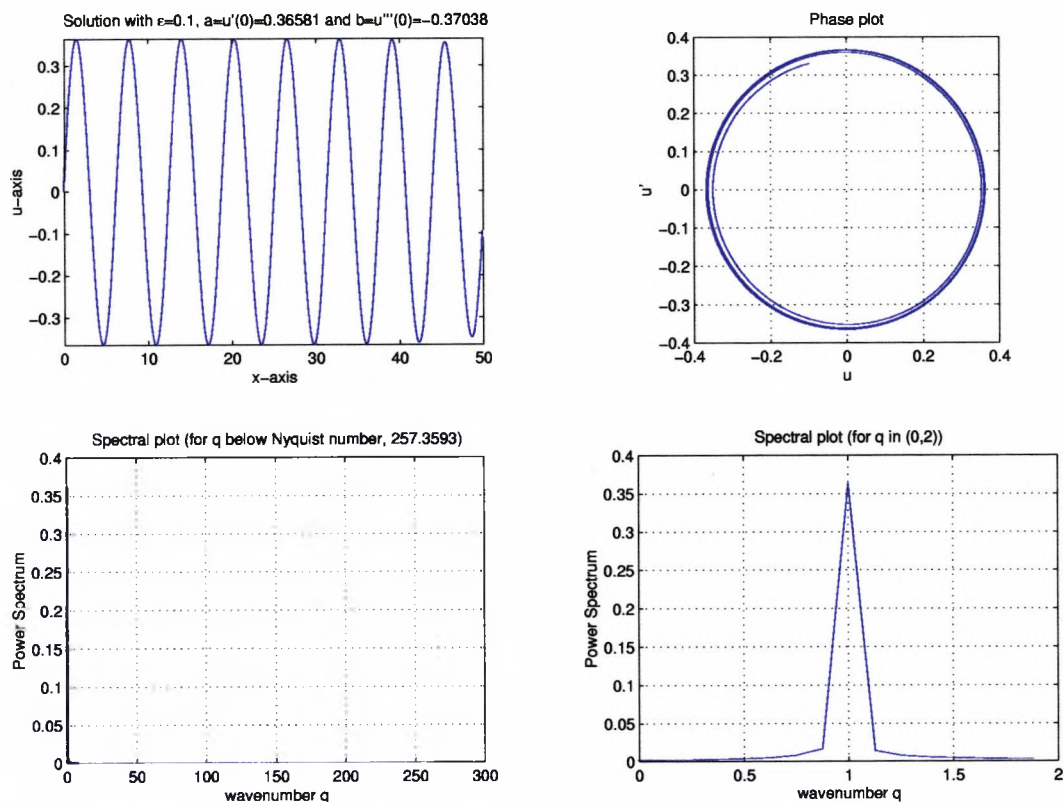


Figure 2.14: A solution at the point  $(L, \epsilon) = (\pi, 0.1)$ . At this parameter point  $(\alpha, \beta) = (0.365814, -0.370378)$ . We have extended the solution by plotting the solution for  $x \in (0, 40)$ .

more complicated bifurcation structure than we had first thought. Fixing  $\epsilon = 0.65$  and increasing  $L$  in steps of 0.1, the results in Figure 2.18 show that the solution changes to a profile with a third of the wavelength. This change can be seen more gradually in Figure 2.19. The change is due to the interaction of different Fourier modes leading to multiple branches at fixed values of  $\epsilon$  and  $L$ . Figures 2.20 and 2.21 show the bifurcation diagram of typical multi-solution structures that exist<sup>3</sup>. The plots are for the regions  $(L, \epsilon) = (L|_{L \in (4.9, 5.2)}, 0.4)$  and  $(L, \epsilon) = (L|_{L \in (7, 7.2)}, 0.65)$  respectively. As we show in Section 2.6 the bifurcation structures in Figures 2.20 and 2.21 are first generated at the points  $(L, \epsilon) = (\sqrt{10}\pi/2, 9/25)$  and  $(L, \epsilon) = (\sqrt{5}\pi, 16/25)$  respectively. With reference

<sup>3</sup>More complicated structures, corresponding to the mixing of higher modes, can exist for sufficiently large  $L$ .

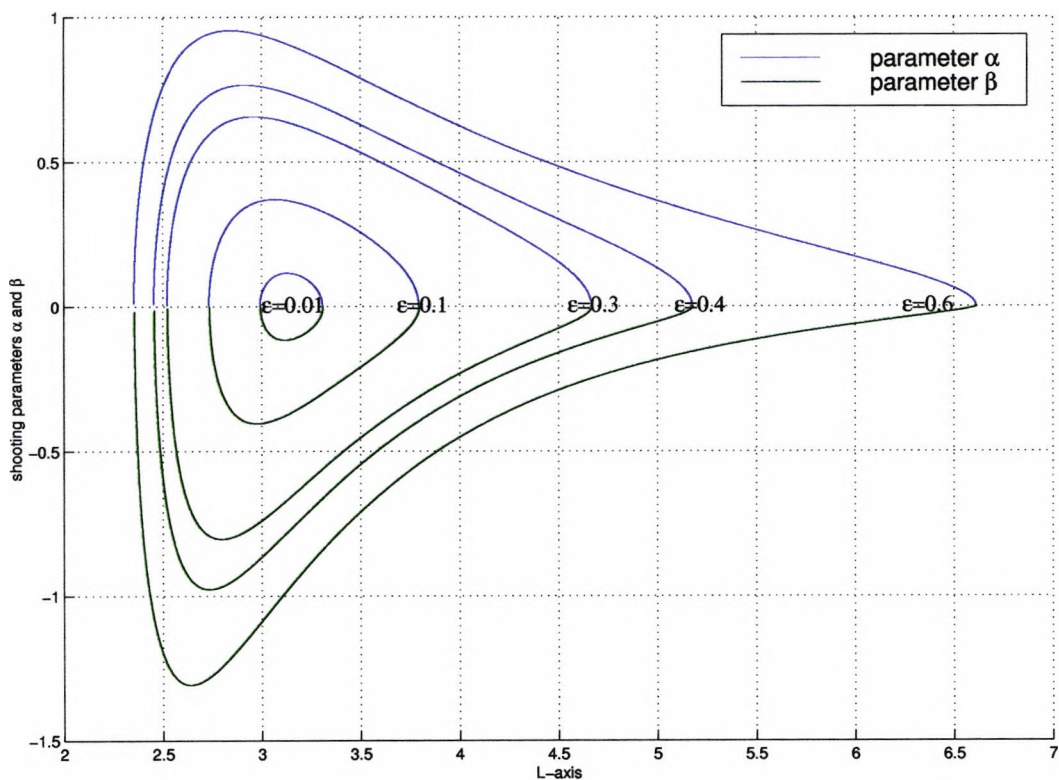


Figure 2.15: Plots of the parameters  $\alpha$  and  $\beta$  as a function of  $L$  for  $\epsilon = 0.01, 0.1, 0.3, 0.4$  and  $0.6$ .

to Figure 2.13, the point  $(L, \epsilon) = (\sqrt{10}\pi/2, 9/25)$  corresponds to the intersection of the first and second curves (we shall call this point the *mixed-1-2* critical point). Similarly, the point  $(L, \epsilon) = (\sqrt{5}\pi, 16/25)$  corresponds to the intersection of the first and third curves (and we shall call this point the *mixed-1-3* critical point). We shall investigate these points in more detail in Section 2.6. Note that there are also symmetric solutions which correspond to both of the parameters  $\alpha$  and  $\beta$  switching signs. These are equivalent to Figure 2.20 or 2.21 flipped upside down.

The profiles of the solutions in Figure 2.20 show three different types of solutions—the *mode 1* solution, the *mode 2* solution and solutions which have a mixture of the first and second modes. Examples of *mixed-1-2-mode* solutions are shown in Figures 2.22–2.24.

The profiles of the solutions in Figure 2.21 show two different types of solutions: the *mode-3* solution and solutions which have a mixture of the first and

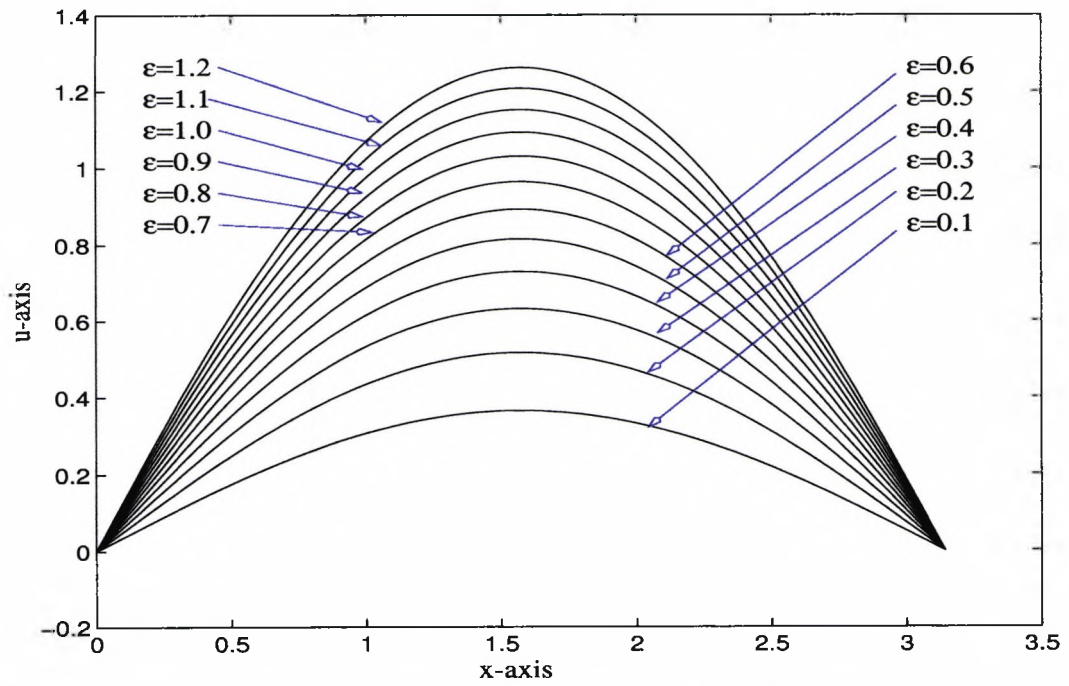


Figure 2.16: Profiles of the solution  $u$  for fixed  $L = \pi$  and increasing  $\epsilon$ .

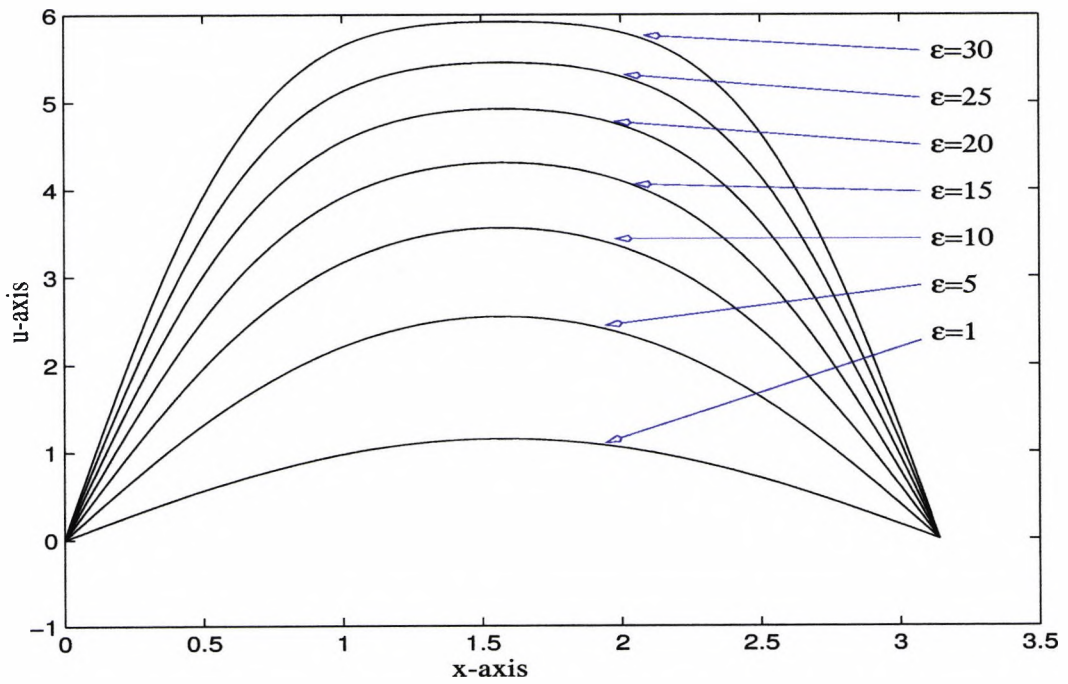


Figure 2.17: Profiles of the solution  $u$  for fixed  $L = \pi$  and higher  $\epsilon$ .

third modes. Our results also indicate that there are no solution branches consisting purely of the first Fourier mode. This will be made clear by the local analysis in Section 2.6. An example of a *mode-3* solution is shown in Figure 2.25; and three examples of mixed mode solutions are shown in Figures 2.26–2.29.

In Section 2.6 we perform a local analysis at the *mode-1-2* and the *mode-1-3* critical points, i.e., at  $(L, \epsilon) = (\sqrt{10}\pi/2, 9/25)$  and  $(L, \epsilon) = (\pi\sqrt{5}, 16/25)$  respectively.

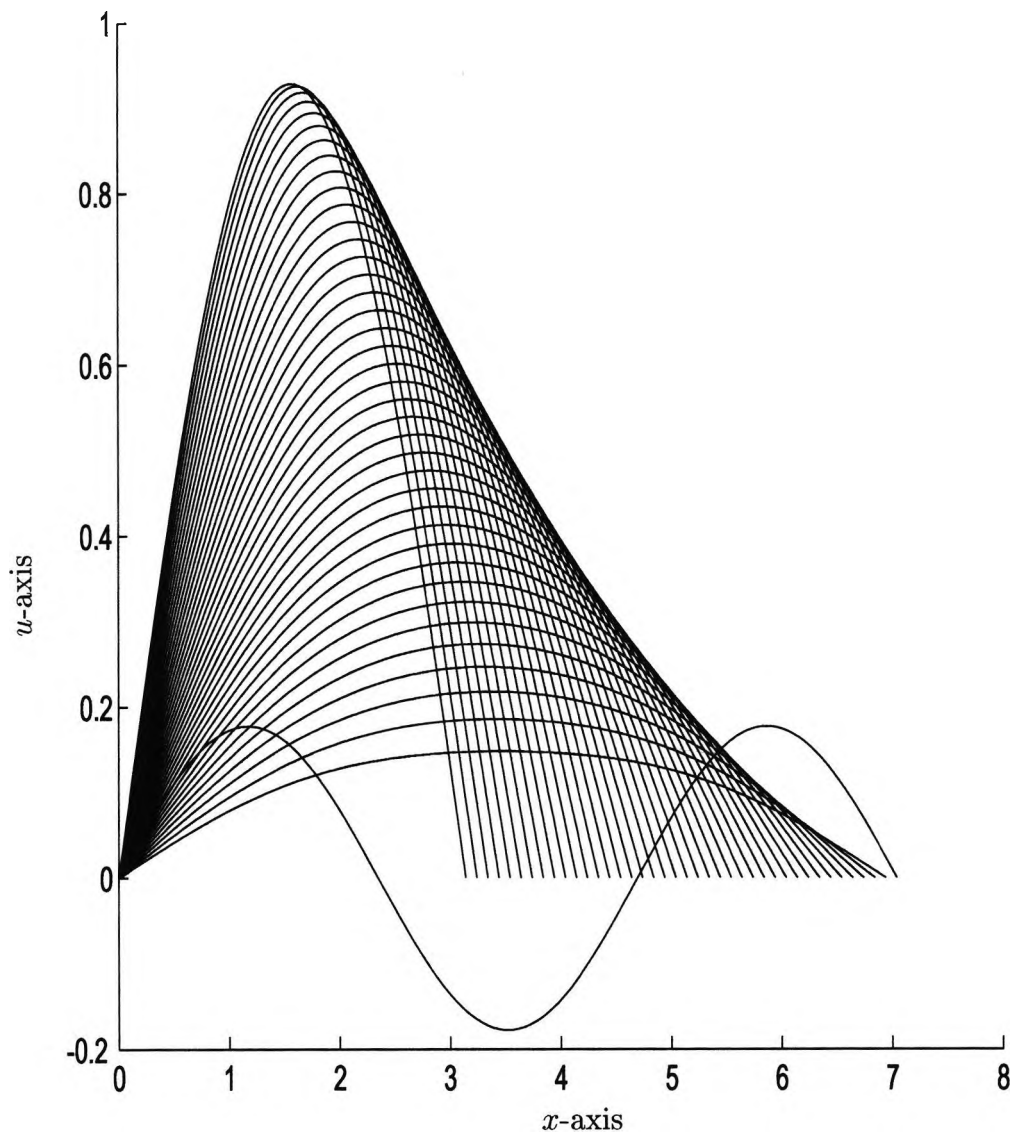


Figure 2.18: Profiles of the solution  $u$  obtained from the numerical scheme for fixed  $\epsilon = 0.65$  and  $L = \pi, \pi+0.1, \pi+0.2, \dots, \pi+3.9$ . A more detailed examination of all possible solutions (displayed in Figure 2.21 below) reveals that the final profile is on the red branch of Figure 2.21, whilst the other profiles are on the green branch.

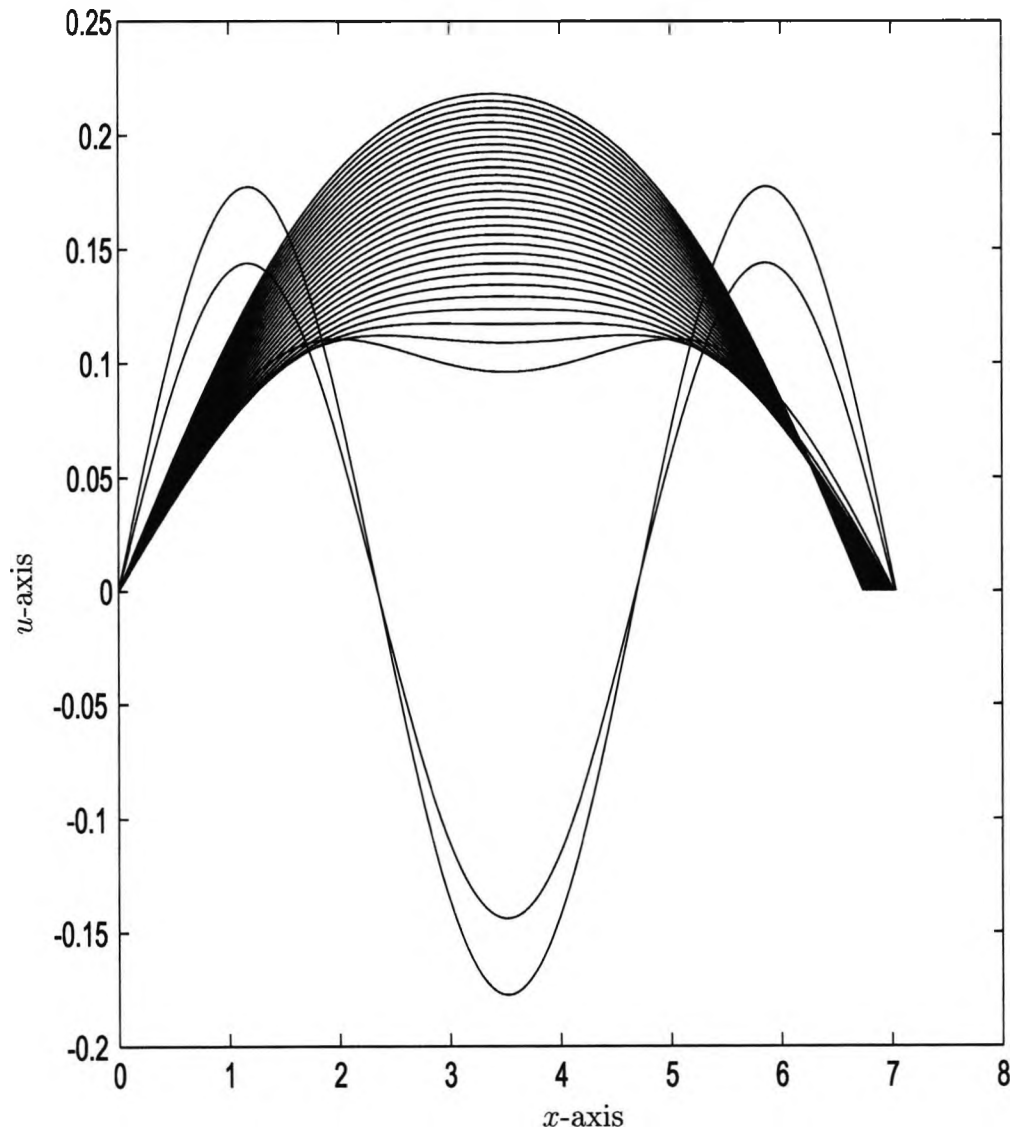


Figure 2.19: Profiles of the solution  $u$  for fixed  $\epsilon = 0.65$  and finer increments of  $L$  near  $\pi + 3.9$ . The final two profiles are on the red branch of Figure 2.21 below, whilst the other profiles are on the green branch.

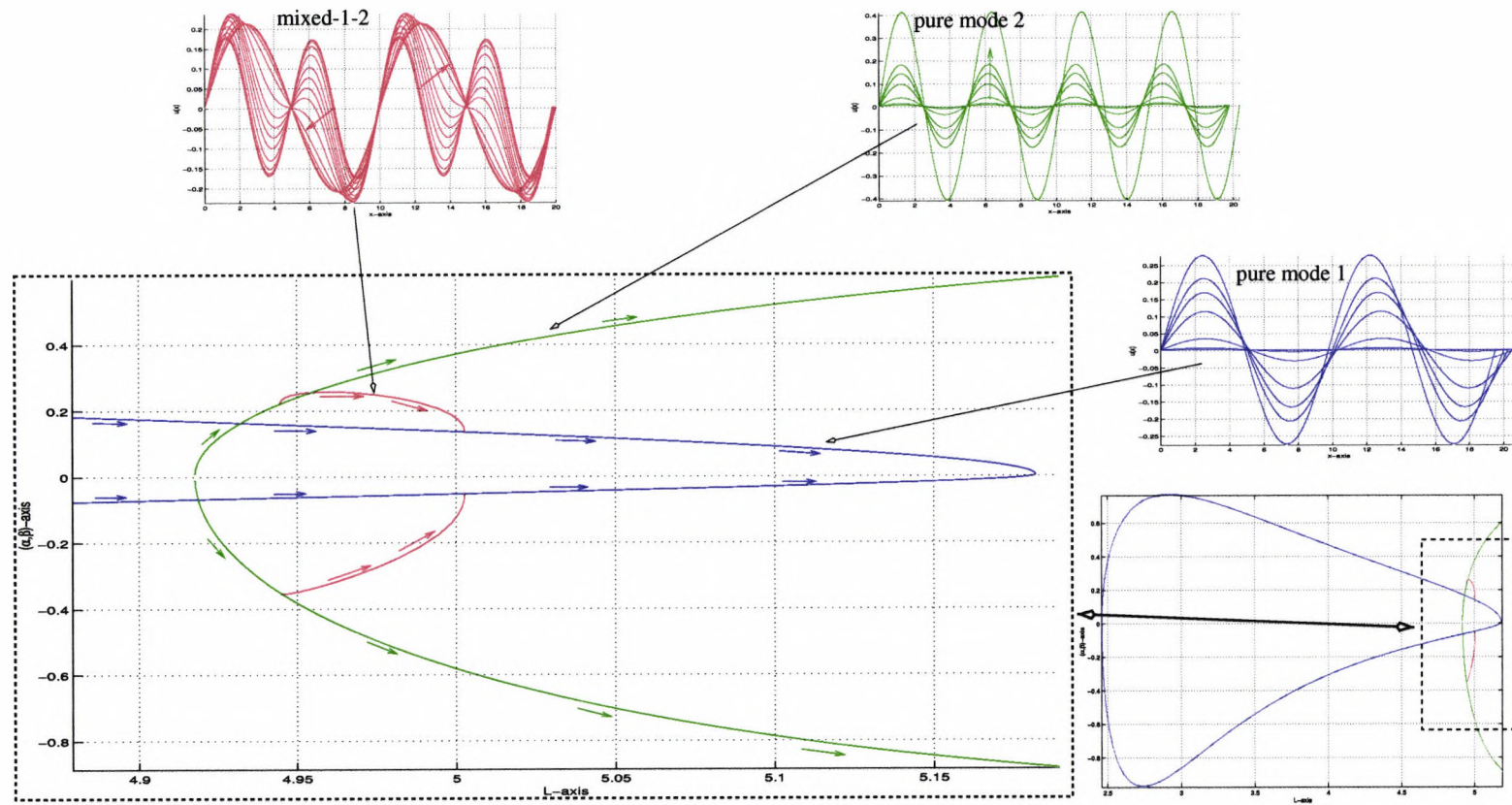


Figure 2.20: Plot showing multiple steady-state solutions in the region  $(L, \epsilon) = (L|_{L \in (4.9, 5.2)}, 0.4)$ . Also shown is the profile of the solution at various points.

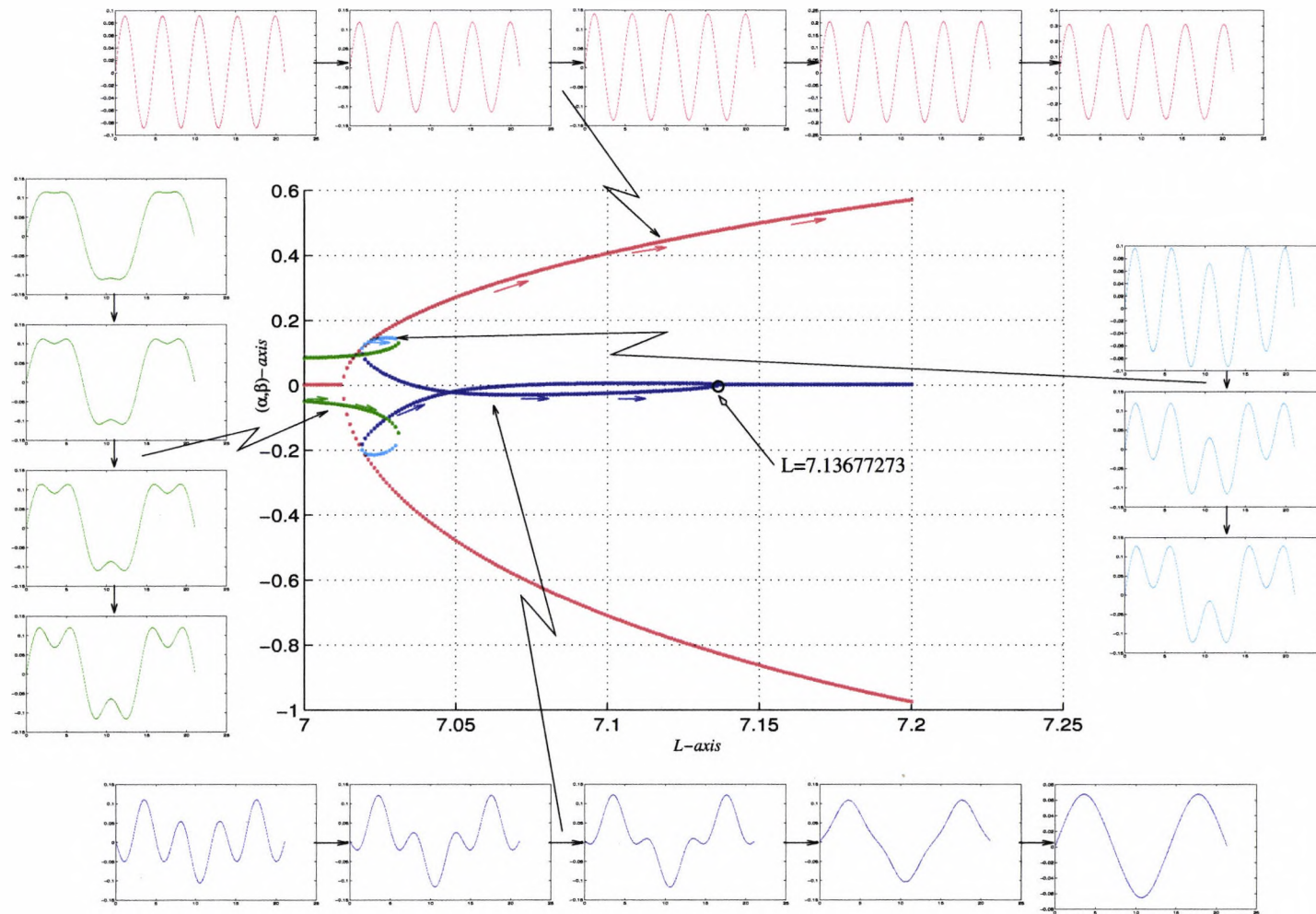


Figure 2.21: Plot showing multiple steady-state solutions in the region  $(L, \epsilon) = (L|_{L \in (7, 7.2)}, 0.65)$ . Also shown is the profile of the solution at various points. Note that the bifurcation point of the dark blue (*mode 1*) solution obtained numerically at  $L = 7.13677273$  is consistent with the value  $L = \pi(1 - \epsilon^{\frac{1}{2}})^{-\frac{1}{2}} = 7.13677275$  predicted by linear theory.

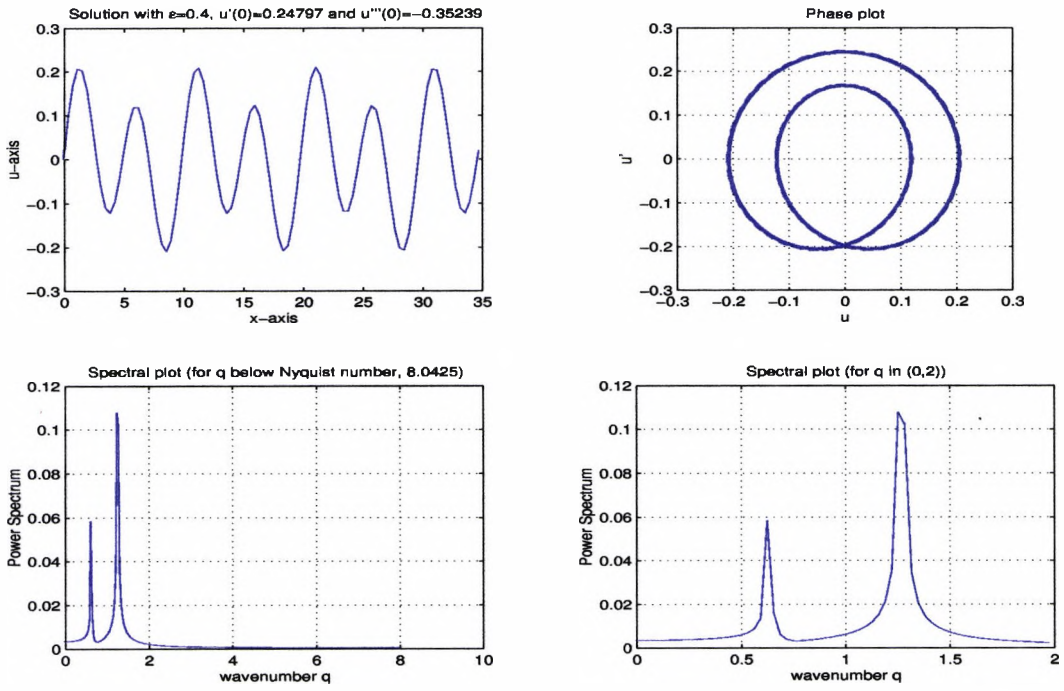


Figure 2.22: An example of a *mixed-1-2-mode* solution at  $L = 4.9495$ ,  $\epsilon = 0.4$ .

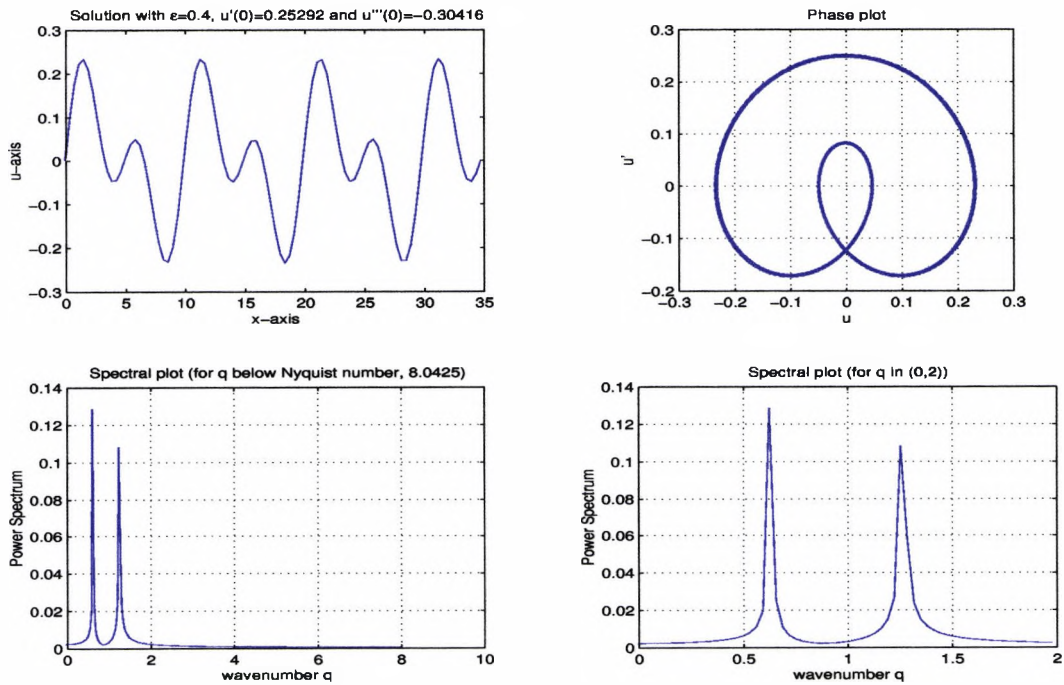


Figure 2.23: An example of a *mixed-1-2-mode* solution at  $L = 4.9673$ ,  $\epsilon = 0.4$ .

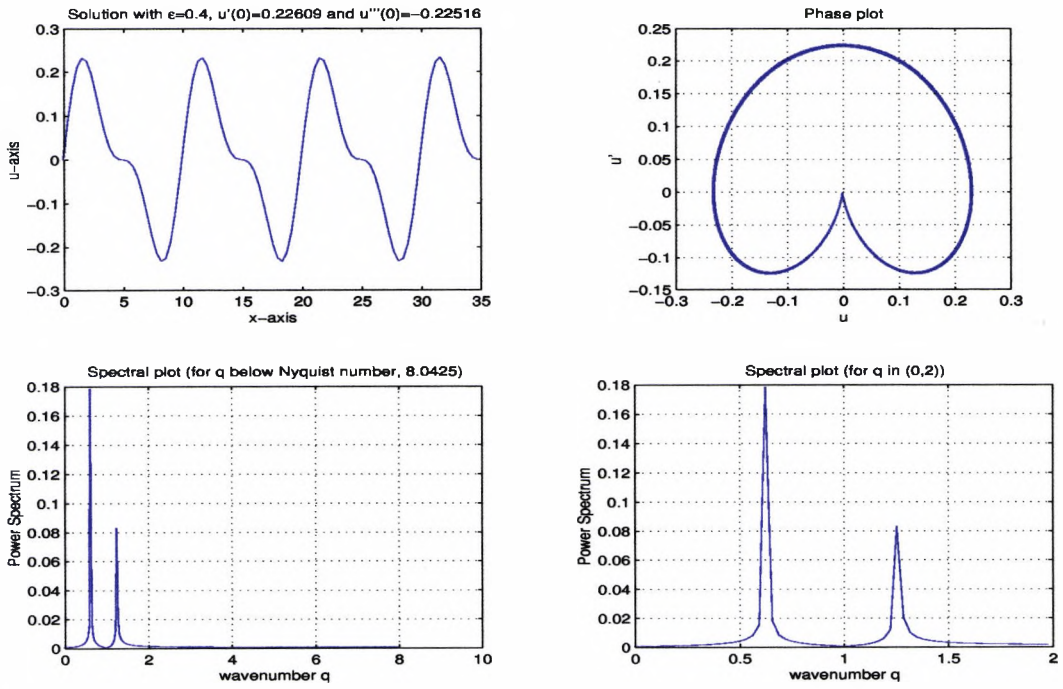


Figure 2.24: An example of a *mixed-1-2-mode* solution at  $L = 4.9867$ ,  $\epsilon = 0.4$ .

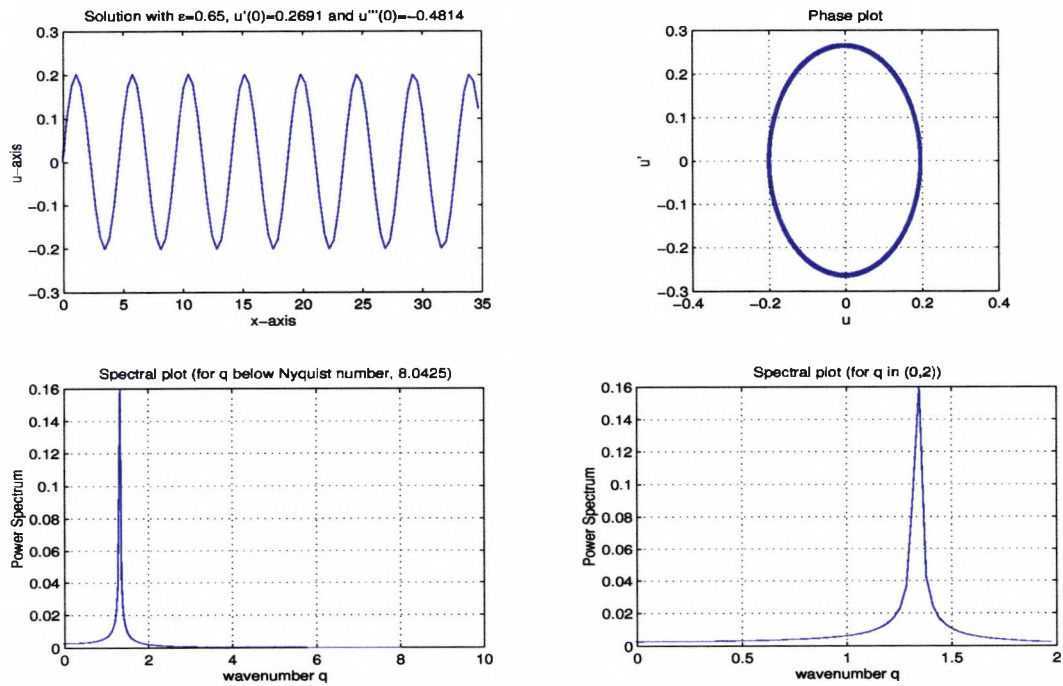


Figure 2.25: An example of a *pure-3-mode* solution at  $L = 7.0248$ ,  $\epsilon = 0.65$ .

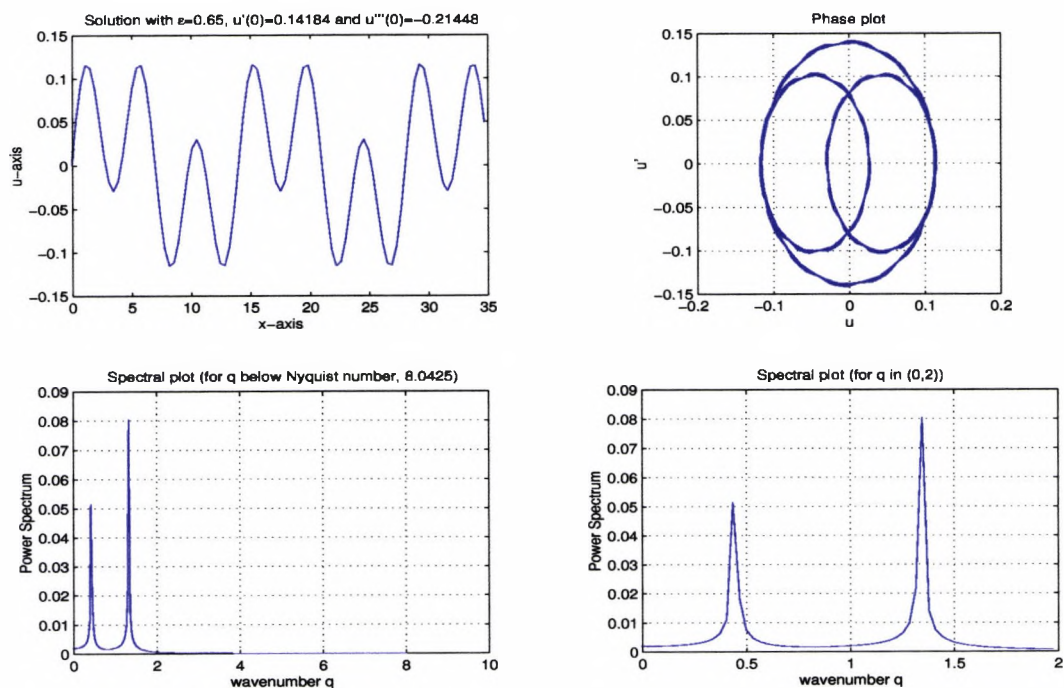


Figure 2.26: An example of a *mixed-1-3-mode* solution at  $L = 7.0248$ ,  $\epsilon = 0.65$ .

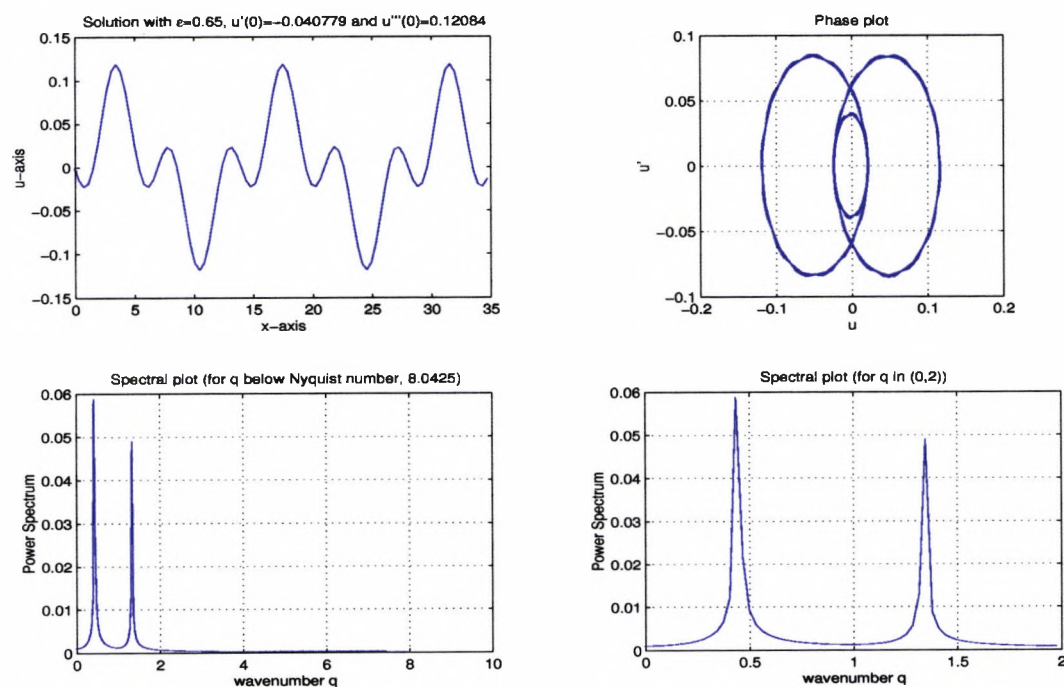


Figure 2.27: An example of a *mixed-1-3-mode* solution at  $L = 7.0248$ ,  $\epsilon = 0.65$ .

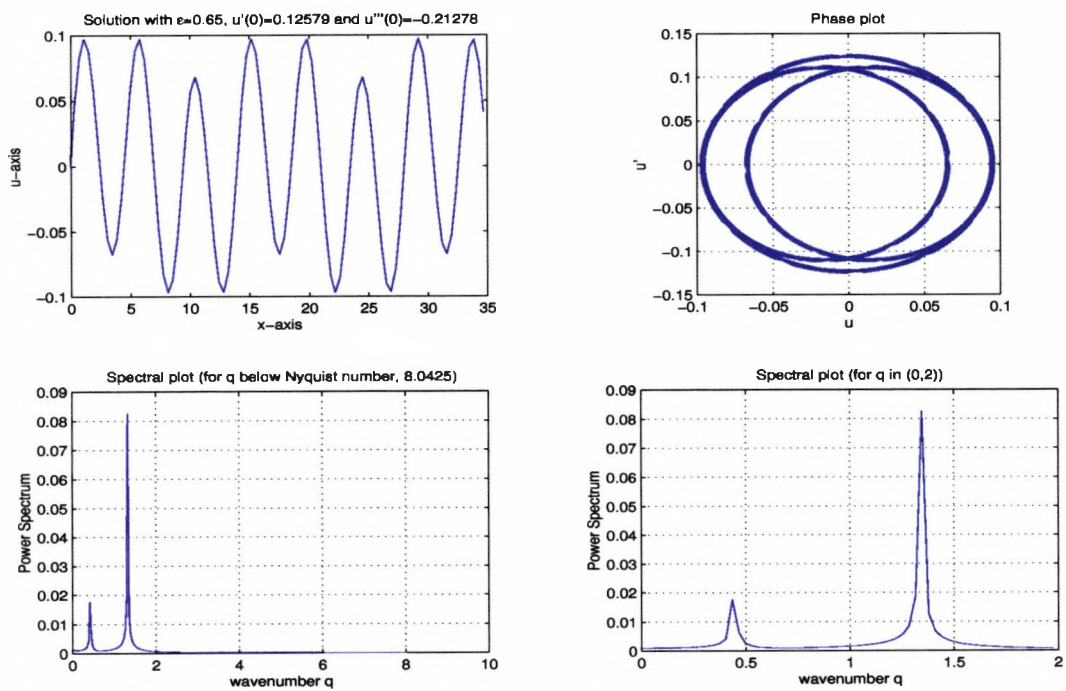


Figure 2.28: An example of a *mixed-1-3-mode* solution at  $L = 7.0203$ ,  $\epsilon = 0.65$ .

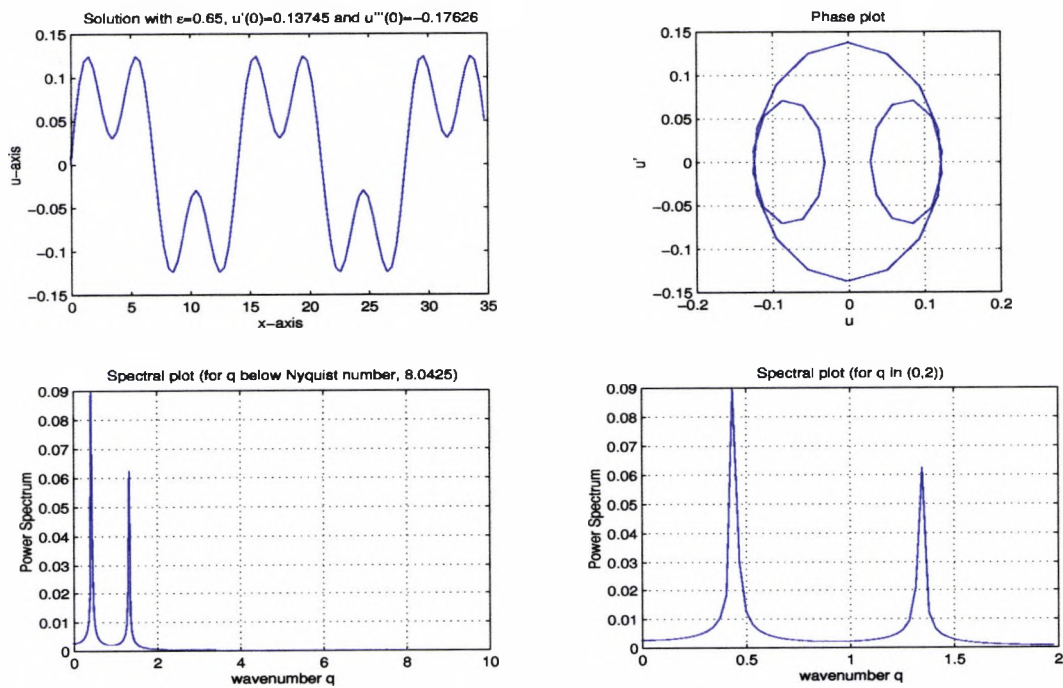


Figure 2.29: Another example of a *mixed-1-3-mode* solution at  $L = 7.0307$ ,  $\epsilon = 0.65$ .

## 2.6 Mode Interactions

In Section 2.5 we have found evidence of the interaction of the first and second Fourier modes (we shall refer to this as the *mode-1-2* interaction); and the first and third Fourier modes (similarly, we shall refer to this as the *mode-1-3* interaction). The numerical results indicate that these interactions produce multiple steady-state solutions. From now on we shall denote by the term ‘*primary* bifurcation’ a bifurcation from the zero state to a non-zero (or primary solution) convective state with increasing  $\epsilon$ ; and by ‘*secondary* bifurcation’ any further bifurcation of the primary convective solution with increasing  $\epsilon$  (we shall denote the solutions that arise at a secondary bifurcation as *secondary* solutions). The marginal curves that we have computed in Section 2.3.1 given by (2.15) (see also Figure 2.13) represent the *primary* bifurcation loci of different individual Fourier modes. In this section we shall derive the loci of *secondary* bifurcations, and in particular, bifurcations to *mixed-1-2* and *mixed-1-3* solutions. The results of Section 2.5 have indicated that the primary solutions first undergo bifurcations to secondary solutions in the neighbourhood of the intersection points of the different marginal curves. The first and second pure mode solutions first undergo bifurcations to *mixed-1-2* solutions near the intersection of the first and second marginal curves, i.e., at the *mixed-1-2* critical point  $(L_c^{(1,2)}, \epsilon_c^{(1,2)}) = (\sqrt{10}\pi/2, 9/25)$ . The first and third pure mode solutions first undergo bifurcations to *mixed-1-3* solutions at the intersection of the first and third marginal curves, i.e., at the *mixed-1-3* critical point  $(L_c^{(1,3)}, \epsilon_c^{(1,3)}) = (\pi\sqrt{5}, 16/25)$ . In this section we shall perform local analyses and derive the bifurcation loci local to the *mixed-1-2* and the *mixed-1-3* critical points. Cox (1996, [10]) has considered similar interactions in Rayleigh-Bénard convection.

First, let us consider the *mixed-1-2* interaction.

### 2.6.1 Mode-1-2 Interaction

Consider the one-dimensional Swift-Hohenberg equation for  $u(x, t)$

$$\frac{\partial u}{\partial t} = \left( \epsilon - \left( \frac{\partial^2}{\partial x^2} + 1 \right)^2 \right) u - u^3, \quad (2.51)$$

with boundary conditions

$$u = \frac{\partial^2 u}{\partial x^2} = 0 \quad \text{at} \quad x = 0, L. \quad (2.52)$$

We seek to calculate the solution structure in the neighbourhood of the *mixed-1-2* critical point, i.e.,  $\epsilon_c^{(1,2)} = 9/25$ . Perturbing about  $\epsilon_c^{(1,2)}$  we substitute  $\epsilon = \epsilon_c^{(1,2)} + \delta\bar{\epsilon}$ , where  $\bar{\epsilon}$  is a small and positive real parameter and  $\delta \in \mathbb{R}$ , into equation (2.51). We have introduced the parameter  $\delta$  to allow consideration of  $\epsilon < \epsilon_c^{(1,2)}$ . Balancing terms in equation (2.51) suggests that  $u(x, t)$  expands in powers of  $\bar{\epsilon}^{1/2}$ , that is

$$u = \bar{\epsilon}^{1/2} u_0 + \bar{\epsilon} u_1 + \bar{\epsilon}^{3/2} u_2 + \dots \quad (2.53)$$

In order to analyse equation (2.51) we shall incorporate modulations on the scales  $X = \bar{\epsilon}x$  and  $T = \bar{\epsilon}t$  so that  $u_i = u_i(x, X, T)$ . After substitution into (2.51), we collect and compare coefficients of powers of  $\bar{\epsilon}$  and we obtain

$$\frac{\partial^4 u_0}{\partial x^4} + 2 \frac{\partial^2 u_0}{\partial x^2} + \frac{16}{25} u_0 = 0, \quad (2.54)$$

$$\frac{\partial^4 u_1}{\partial x^4} + 2 \frac{\partial^2 u_1}{\partial x^2} + \frac{16}{25} u_1 = 0, \quad (2.55)$$

$$\frac{\partial^4 u_2}{\partial x^4} + 2 \frac{\partial^2 u_2}{\partial x^2} + \frac{16}{25} u_2 = - \left[ 4 \frac{\partial^4 u_0}{\partial X \partial x^3} + 4 \frac{\partial^2 u_0}{\partial X \partial x} + \frac{\partial u_0}{\partial T} + u_0^3 - \delta u_0 \right] \quad (2.56)$$

at orders  $\bar{\epsilon}^{1/2}$ ,  $\bar{\epsilon}$  and  $\bar{\epsilon}^{3/2}$  respectively. Solving equation (2.54) we get

$$u_0 = B \exp(i\sqrt{10}x/5) + C \exp(2i\sqrt{10}x/5) + c.c., \quad (2.57)$$

where  $B(X, T)$  and  $C(X, T)$  are complex amplitude functions and *c.c.* denotes the complex conjugate. On substituting for  $u_0(x, X, T)$  into equation (2.56) we obtain

$$\begin{aligned} \frac{\partial^4 u_2}{\partial x^4} + 2 \frac{\partial^2 u_2}{\partial x^2} + \frac{16}{25} u_2 = & - \left[ \frac{\partial B}{\partial T} + 3B|B|^2 + 6B|C|^2 - \delta B \right. \\ & \left. + \frac{12\sqrt{10}}{25} i \frac{\partial B}{\partial X} \right] \exp\left(\frac{ix\sqrt{10}}{5}\right) \\ & - \left[ \frac{\partial C}{\partial T} + 3C|C|^2 + 6C|B|^2 - \delta C \right] \end{aligned}$$

$$\begin{aligned}
& - \frac{24\sqrt{5}}{25} i \frac{\partial C}{\partial X} \Big] \exp\left(\frac{2ix\sqrt{10}}{5}\right) \\
& - (B^3 + 3\bar{B}C^2) \exp\left(\frac{3ix\sqrt{10}}{5}\right) - 3B^2C \exp\left(\frac{4ix\sqrt{10}}{5}\right) \\
& - 3B^2C \exp\left(\frac{4ix\sqrt{10}}{5}\right) - 3BC^2 \exp(ix\sqrt{10}) \\
& - C^3 \exp\left(\frac{6ix\sqrt{10}}{5}\right) + c.c., \tag{2.58}
\end{aligned}$$

where  $\bar{B}$  denotes the complex conjugate of  $B$ . The secular terms arise from the presence of  $\pm \exp(i\sqrt{10}x/5)$  and  $\pm \exp(2i\sqrt{10}x/5)$ . They can be eliminated by setting

$$\frac{\partial B}{\partial T} + 3B|B|^2 + 6B|C|^2 - \delta B + \frac{12\sqrt{10}}{25} i \frac{\partial B}{\partial X} = 0, \tag{2.59}$$

$$\frac{\partial C}{\partial T} + 3C|C|^2 + 6C|B|^2 - \delta C - \frac{24\sqrt{10}}{25} i \frac{\partial C}{\partial X} = 0. \tag{2.60}$$

We are interested in solutions which are periodic in  $x$  and satisfy the boundary conditions (2.52) and so we set

$$B = b(T) \exp(iQX + iD(T)) \quad \text{and} \quad C = c(T) \exp(2iQX + iE(T)), \tag{2.61}$$

where  $b$ ,  $c$ ,  $D$  and  $E$  are real functions of  $T$ ; and  $Q$  is a constant. The boundary conditions  $u = u_{xx} = 0$  at  $x = 0$  then require that  $\cos D = \cos E = 0$  in which case we may take  $D = E = \pi/2$ . The remaining conditions  $u = u_{xx} = 0$  at  $x = L$  are then satisfied provided that

$$\cos\left(\frac{\sqrt{10}}{5}L + Q\tilde{\epsilon}L + \frac{\pi}{2}\right) = \cos\left(\frac{2\sqrt{10}}{5}L + 2Q\tilde{\epsilon}L + \frac{\pi}{2}\right) = 0.$$

This is possible, and requires that

$$\frac{\sqrt{10}}{5}L + Q\tilde{\epsilon}L = n\pi,$$

where  $n$  is an integer. The choice  $n = 1$  ensures that  $Q = 0$  corresponds to the critical point  $L = \sqrt{10}\pi/2$ .

From equations (2.59), (2.60) and (2.61) we get

$$\frac{db}{dT} = (\delta + \bar{q})b - 3b^3 - 6bc^2, \quad (2.62)$$

$$\frac{dc}{dT} = (\delta - 4\bar{q})c - 3c^3 - 6cb^2, \quad (2.63)$$

where  $\bar{q} = 12\sqrt{10}Q/25$ . A more general form of the coupled system (2.62), (2.63) has been studied by Dangelmayr (1986, [17]) and Dangelmayr and Knobloch (1986, [18]) in their examination of steady state mode interactions in the presence of O(2)-symmetry. Define the functions  $f_1$  and  $f_2$  as

$$f_1(b, c) = (\delta + \bar{q})b - 3b^3 - 6bc^2, \quad (2.64)$$

$$f_2(b, c) = (\delta - 4\bar{q})c - 3c^3 - 6cb^2. \quad (2.65)$$

For the steady-state solutions we need to solve the nonlinear system (see, for example, Golubitsky and Schaeffer (1985, [27]))

$$f_1(b, c) = 0, \quad (2.66)$$

$$f_2(b, c) = 0. \quad (2.67)$$

We find that there are four qualitatively different sets of solutions. These are

1. the *trivial* solution set, where  $b = 0$  and  $c = 0$ ,
2. the pure *mode-1* solution set, where  $b = \pm(\sqrt{3\delta + 3\bar{q}})/3$  and  $c = 0$  (solutions exist for  $\delta \geq -\bar{q}$ ),
3. the pure *mode-2* solution set, where  $b = 0$  and  $c = \pm\sqrt{3\delta - 12\bar{q}}/3$  (solutions exist for  $\delta \geq 4\bar{q}$ ),
4. the *mixed-1-2* solution sets, where  $b = \pm\sqrt{\delta - 9\bar{q}}/3$ ,  $c = \pm\sqrt{\delta + 6\bar{q}}/3$  and  $b = \pm\sqrt{\delta - 9\bar{q}}/3$ ,  $c = \mp\sqrt{\delta + 6\bar{q}}/3$  (these solutions exist for  $\delta \geq \max\{-6\bar{q}, 9\bar{q}\}$ ).

Figure 2.30 is a plot of the amplitude,  $\sqrt{b^2 + c^2}$ , against  $\bar{q}$  for the four different sets.

From (2.53), (2.57) and (2.61) these correspond to

$$u \approx \tilde{\epsilon}^{1/2} \left\{ b \sin \left[ \left( \frac{\sqrt{10}}{5} + \frac{25}{12\sqrt{10}} \tilde{q} \right) x \right] + c \sin \left[ 2 \left( \frac{\sqrt{10}}{5} + \frac{25}{12\sqrt{10}} \tilde{q} \right) x \right] \right\}, \quad (2.68)$$

where

$$L \approx \frac{\pi\sqrt{10}}{2} \left( 1 - \frac{25}{24} \tilde{\epsilon} \tilde{q} \right), \quad \epsilon = \frac{9}{25} + \tilde{\epsilon} \delta. \quad (2.69)$$

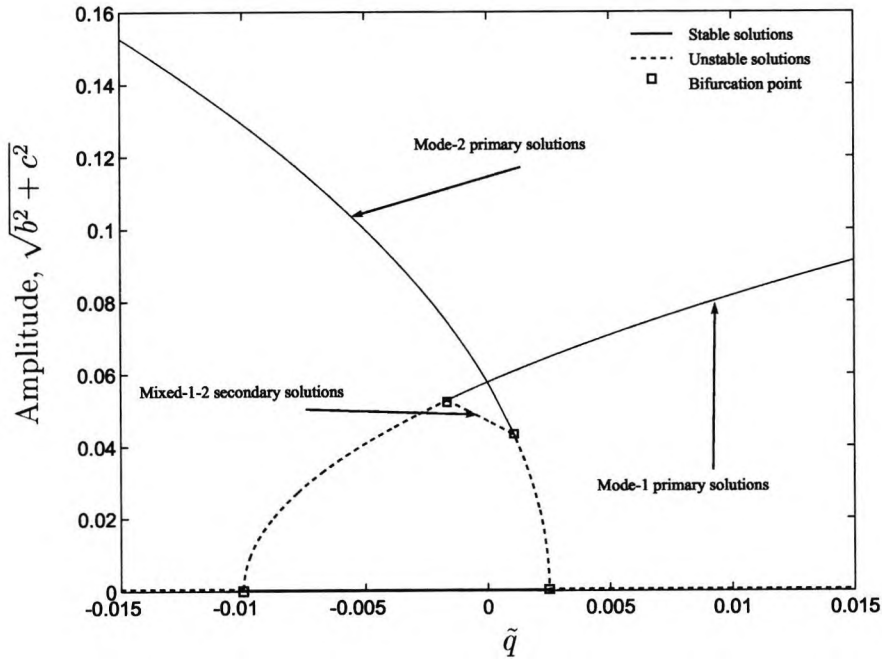


Figure 2.30: An amplitude plot at  $\delta = 0.01$ , showing the bifurcation structure of the mode-1-2 interaction.

## Mode-1-2 Interaction: Stability Analysis

Now, we seek to analyse the stability of the solutions found in Section 2.6.1.

Consider the Jacobian matrix of the nonlinear system (2.64)–(2.65)

$$J = \begin{bmatrix} \frac{\partial f_1}{\partial b} & \frac{\partial f_1}{\partial c} \\ \frac{\partial f_2}{\partial b} & \frac{\partial f_2}{\partial c} \end{bmatrix} = \begin{bmatrix} (\delta + \bar{q}) - 9b^2 - 6c^2 & -12bc \\ -12bc & (\delta - 4\bar{q}) - 9c^2 - 6b^2 \end{bmatrix}.$$

For the *trivial* solution set

$$J|_{(b=0,c=0)} = \begin{bmatrix} \delta + \bar{q} & 0 \\ 0 & \delta - 4\bar{q} \end{bmatrix},$$

and the trivial solution bifurcates to the primary solution along  $\delta = -\bar{q}$  and  $\delta = 4\bar{q}$ . The trivial solution is only stable when  $\min\{-\delta, \delta/4\} \leq \bar{q} \leq \max\{-\delta, \delta/4\}$  (in Figure 2.30 unstable solutions are shown by dashed lines and stable solutions by a solid line). Figure 2.31 shows the bifurcation loci in terms of the parameters  $\epsilon$  and  $q = \pi/L$  using the relations (2.69). Here the results are also compared with the numerical results of Section 2.5.

For the pure *mode-1* primary solutions

$$J|_{(b=\pm(\sqrt{3\delta+3\bar{q}})/3,c=0)} = \begin{bmatrix} -2\delta - 2\bar{q} & 0 \\ 0 & -\delta - 6\bar{q} \end{bmatrix},$$

and the primary solutions bifurcate to the secondary solutions along  $\delta = -6\bar{q}$  for  $\bar{q} < 0$ . The pure *mode-1* primary solution is only stable when  $\bar{q} \geq \max\{-\delta, -\delta/6\}$  and it exists only within the region  $\bar{q} < -\delta$  (see Figures 2.30 and 2.31).

For the pure *mode-2* primary solutions

$$J|_{(b=0,c=\pm\sqrt{3\delta-12\bar{q}}/3)} = \begin{bmatrix} -\delta + 9\bar{q} & 0 \\ 0 & -2\delta + 8\bar{q} \end{bmatrix},$$

and the primary solutions bifurcate to the secondary solutions along  $\delta = 9\bar{q}$  for  $\bar{q} > 0$ . The pure *mode-2* primary solution is only stable when  $\bar{q} \leq \min\{\delta/4, \delta/9\}$  and it exists only in the region  $\bar{q} < \delta/4$  (see Figure 2.30).

For the *mixed-1-2* solutions or secondary solutions

$$J|_{(b=\pm\sqrt{\delta-9\bar{q}}/3,c=\pm\sqrt{\delta+6\bar{q}}/3)} = \begin{bmatrix} -2\delta/3 + 6\bar{q} & -4\sqrt{(\delta-9\bar{q})(\delta+6\bar{q})}/3 \\ -4\sqrt{(\delta-9\bar{q})(\delta+6\bar{q})}/3 & -2\delta/3 - 4\bar{q} \end{bmatrix},$$

and

$$J|_{(b=\pm\sqrt{\delta-9\tilde{q}}/3, c=\mp\sqrt{\delta+6\tilde{q}}/3)} = \begin{bmatrix} -2\delta/3 + 6\tilde{q} & 4\sqrt{(\delta-9\tilde{q})(\delta+6\tilde{q})}/3 \\ 4\sqrt{(\delta-9\tilde{q})(\delta+6\tilde{q})}/3 & -2\delta/3 - 4\tilde{q} \end{bmatrix}.$$

The two Jacobians have the same eigenvalues<sup>4</sup>

$$-\frac{2\delta + 3\tilde{q} \pm \sqrt{16\delta^2 - 48\delta\tilde{q} - 639\tilde{q}^2}}{3},$$

and they vanish when  $\delta = -6\tilde{q}$  and  $\delta = 9\tilde{q}$ . Hence the *mixed-1-2* secondary solutions bifurcate back to the primary solutions along  $\delta = -6\tilde{q}$  for  $\tilde{q} < 0$  and  $\delta = 9\tilde{q}$  for  $\tilde{q} > 0$ . Note that the solution exists only for  $\tilde{q} \leq \min\{-\delta/6, \delta/9\}$  and  $\tilde{q} \geq \max\{-\delta/6, \delta/9\}$  and it is stable when

$$\left( -\frac{2\delta + 3\tilde{q} \pm \sqrt{16\delta^2 - 48\delta\tilde{q} - 639\tilde{q}^2}}{3} \right) \geq 0.$$

This is only true on the lines  $\tilde{q} = -\delta/6$  and  $\tilde{q} = \delta/9$  (see Figures 2.30 and 2.31). Figure 2.31 compares the results from the numerical method with those from the perturbation analysis. The results agree very well for  $(L, \epsilon)$  close to the critical point  $(L_c^{(1,2)}, \epsilon_c^{(1,2)}) = (\sqrt{10}\pi/2, 9/25)$ .

Now, consider the *mode-1-3* interactions.

## 2.6.2 Mode-1-3 Interaction

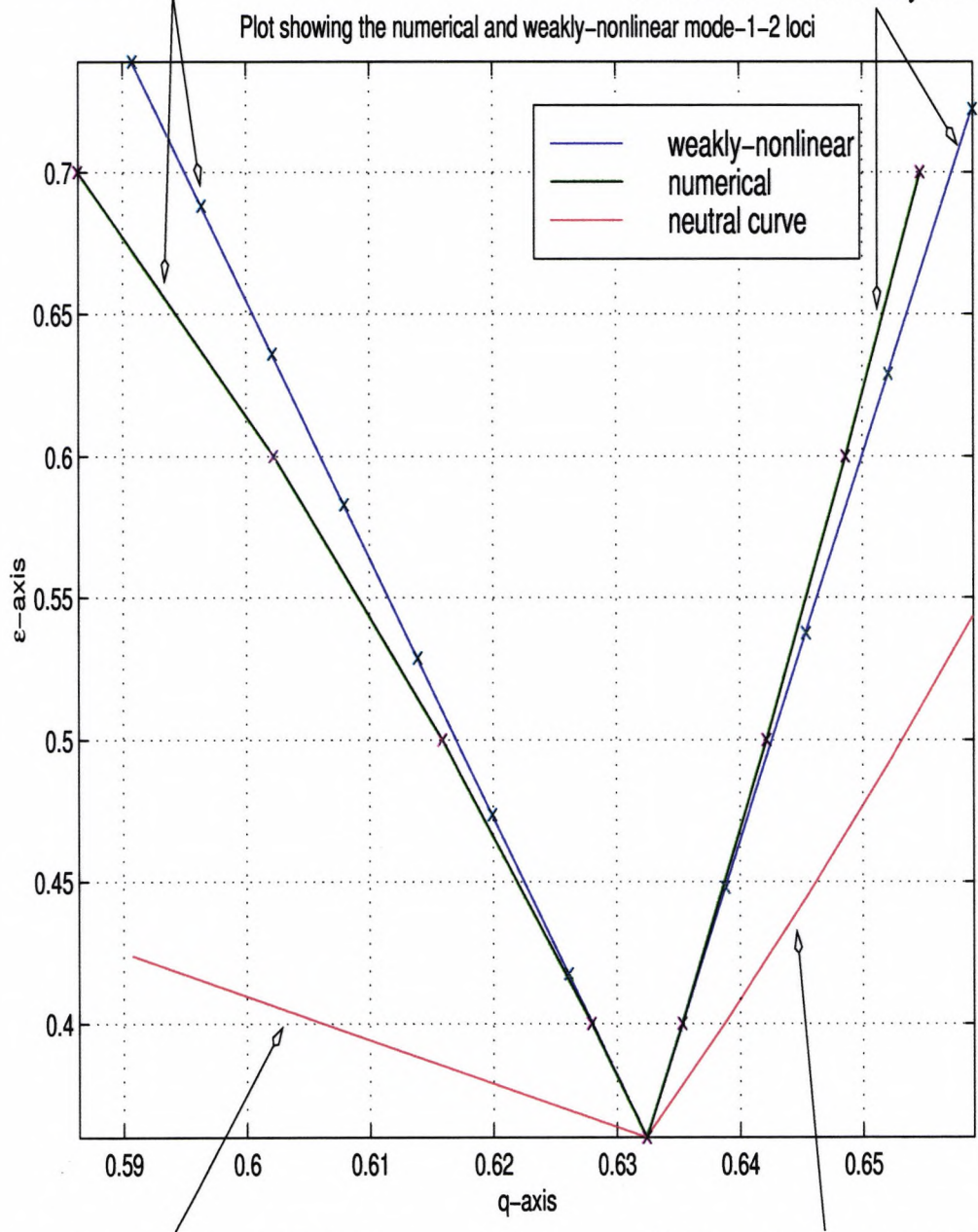
Progressing in a similar way as in Section 2.6.1, we seek to calculate the solution structure in the neighbourhood of the *mixed-1-3* critical point,  $\epsilon_c^{(1,3)} = 16/25$ . As before, perturbing about  $\epsilon_c^{(1,3)}$  we substitute  $\epsilon = \epsilon_c^{(1,3)} + \delta\tilde{\epsilon}$ , where  $\tilde{\epsilon}$  is a small and positive real parameter and  $\delta \in \mathbb{R}$ , into equation (2.51). Assuming  $u(x, t)$  expands in powers of  $\tilde{\epsilon}^{1/2}$ , i.e.

$$u = \tilde{\epsilon}^{1/2}u_0 + \tilde{\epsilon}u_1 + \tilde{\epsilon}^{3/2}u_2 + \dots, \quad (2.70)$$

<sup>4</sup>Notice that the Jacobian is a real and symmetric matrix. Thus all eigenvalues are real.

Bifurcation locus representing the transition from the mode-2 primary to the mixed-1-2 secondary solution.

Bifurcation locus representing the transition from the mode-1 primary to the mixed-1-2 secondary solution.



Bifurcation locus representing the transition from the trivial solution to the mode-2 primary solution.

Bifurcation locus representing the transition from the trivial solution to the mode-1 primary solution.

Figure 2.31: A plot showing the bifurcation set for the mode-1-2 interaction.

and incorporating modulations on the scales  $X = \tilde{\epsilon}x$  and  $T = \tilde{\epsilon}t$  such that  $u_i = u_i(x, X, T)$  we obtain

$$\frac{\partial^4 u_0}{\partial x^4} + 2\frac{\partial^2 u_0}{\partial x^2} + \frac{9}{25}u_0 = 0, \quad (2.71)$$

$$\frac{\partial^4 u_1}{\partial x^4} + 2\frac{\partial^2 u_1}{\partial x^2} + \frac{9}{25}u_1 = 0, \quad (2.72)$$

$$\frac{\partial^4 u_2}{\partial x^4} + 2\frac{\partial^2 u_2}{\partial x^2} + \frac{9}{25}u_2 = - \left[ 4\frac{\partial^4 u_0}{\partial X \partial x^3} + 4\frac{\partial^2 u_0}{\partial X \partial x} + \frac{\partial u_0}{\partial T} + u_0^3 - \delta u_0 \right] \quad (2.73)$$

at orders  $\tilde{\epsilon}^{1/2}$ ,  $\tilde{\epsilon}$  and  $\tilde{\epsilon}^{3/2}$  respectively. Solving equation (2.71) we get

$$u_0 = B \exp(ix/\sqrt{5}) + C \exp(3ix/\sqrt{5}) + c.c., \quad (2.74)$$

where  $B(X, T)$  and  $C(X, T)$  are complex amplitude functions and *c.c.* denotes the complex conjugate. On substituting for  $u_0(x, X, T)$  in equation (2.73) we obtain

$$\begin{aligned} \frac{\partial^4 u_2}{\partial x^4} + 2\frac{\partial^2 u_2}{\partial x^2} + \frac{9}{25}u_2 = & - \left[ \frac{\partial B}{\partial T} + 3B|B|^2 + 6B|C|^2 + 3\bar{B}^2 C \right. \\ & \left. - \delta B + \frac{16\sqrt{5}}{25}i\frac{\partial B}{\partial X} \right] \exp(ix/\sqrt{5}) \\ & - \left[ \frac{\partial C}{\partial T} + 3C|C|^2 + 6C|B|^2 + B^3 \right. \\ & \left. - \delta C - \frac{48\sqrt{5}}{25}i\frac{\partial C}{\partial X} \right] \exp(3ix/\sqrt{5}) \\ & - (3\bar{B}C^2 + 3B^2C) \exp(\sqrt{5}ix) \\ & - 3BC^2 \exp(7ix/\sqrt{5}) - C^3 \exp(9ix/\sqrt{5}) \\ & + c.c., \end{aligned} \quad (2.75)$$

where  $\bar{B}$  denotes the complex conjugate of  $B$ . Here secular terms arise from the presence of  $\pm \exp(ix/\sqrt{5})$  and  $\pm \exp(3ix/\sqrt{5})$  and vanish when

$$\frac{\partial B}{\partial T} + 3B|B|^2 + 6B|C|^2 + 3\bar{B}^2 C - \delta B + \frac{16\sqrt{5}}{25}i\frac{\partial B}{\partial X} = 0, \quad (2.76)$$

$$\frac{\partial C}{\partial T} + 3C|C|^2 + 6C|B|^2 + B^3 - \delta C - \frac{48\sqrt{5}}{25}i\frac{\partial C}{\partial X} = 0. \quad (2.77)$$

We are interested in solutions which are periodic in  $x$  and satisfy the boundary

conditions (2.52) and so we set

$$B = b(T) \exp(i(QX + D(T))) \quad \text{and} \quad C = c(T) \exp(3i(QX + D(T))), \quad (2.78)$$

where  $b$ ,  $c$  and  $D$  are real functions of  $T$  and  $Q$  is a constant. The boundary conditions  $u = u_{xx} = 0$  at  $x = 0$  then require that  $\cos D = \cos 3D = 0$  in which case we may take  $D = \pi/2$ . The remaining conditions  $u = u_{xx} = 0$  at  $x = L$  are satisfied provided that

$$\cos \left( \frac{1}{\sqrt{5}}L + Q\bar{\epsilon}L + \frac{\pi}{2} \right) = \cos \left( \frac{3}{\sqrt{5}}L + 3Q\bar{\epsilon}L + \frac{3\pi}{2} \right) = 0.$$

This is possible, and requires that

$$\frac{1}{\sqrt{5}}L + Q\bar{\epsilon}L = n\pi,$$

where  $n$  is an integer. The choice  $n = 1$  ensures that  $Q = 0$  corresponds to the critical point  $L = \sqrt{5}\pi$ .

From equations (2.76) and (2.77) we get

$$\frac{db}{dT} = (\delta + \bar{q})b - 3b^3 - 6bc^2 - 3b^2c, \quad (2.79)$$

$$\frac{dc}{dT} = (\delta - 9\bar{q})c - 3c^3 - 6cb^2 - b^3, \quad (2.80)$$

where  $\bar{q} = 16\sqrt{5}Q/25$ . Let

$$f_1(b, c) = (\delta + \bar{q})b - 3b^3 - 6bc^2 - 3b^2c, \quad (2.81)$$

$$f_2(b, c) = (\delta - 9\bar{q})c - 3c^3 - 6cb^2 - b^3. \quad (2.82)$$

For the steady-state solutions we need to solve the nonlinear system

$$f_1(b, c) = 0, \quad (2.83)$$

$$f_2(b, c) = 0. \quad (2.84)$$

Here we find that there are three qualitatively different sets of solutions. These are

1. the *trivial* solution set, where  $b = 0$  and  $c = 0$ ,

2. the pure *mode-3* solution set, where  $b = 0$  and  $c = \pm\sqrt{((\delta - 9\tilde{q})/3)}$  (solutions exist for  $\delta > 9\tilde{q}$ ),

3. the *mixed-1-3* solution set, where  $b \neq 0$  and  $c \neq 0$ .

Notice that there are no pure *mode-1* solutions local to this region. This is due to the cubic nonlinearity of the SH equation. We have noticed in Section 2.5 that the *mode-1* solution first bifurcates from the trivial branch (i.e., with respect to the parameter  $L$ ) as a pure Fourier mode solution but the Fourier composition changes with  $L$  to a *mixed-1-3* solution. Also, we have avoided writing down, analytically, the expressions for  $b$  and  $c$  of the *mixed-mode* solutions, because they are quite long expressions. We have found that it is much more efficient to obtain these solutions via numerical methods such as the Newton iteration scheme or the bifurcation analysis package AUTO97 ([24], 1997). We used the Newton iteration scheme to solve for all real and non-zero solutions of  $b$  and  $c$ . The results are presented in Figure 2.32.

From (2.70), (2.74) and (2.78) these correspond to

$$u \approx \tilde{\epsilon}^{1/2} \left\{ b \sin \left[ \left( \frac{1}{\sqrt{5}} + \frac{25}{16\sqrt{5}}\tilde{q} \right) x \right] + c \sin \left[ 3 \left( \frac{1}{\sqrt{5}} + \frac{25}{16\sqrt{5}}\tilde{q} \right) x \right] \right\}, \quad (2.85)$$

where

$$L \approx \pi\sqrt{5} \left( 1 - \frac{25\sqrt{2}}{24}\tilde{\epsilon}\tilde{q} \right), \quad \epsilon = \frac{16}{25} + \tilde{\epsilon}\delta. \quad (2.86)$$

### Mode-1-3 Interaction: Stability Analysis

Now we seek to analyse the stability of the solutions so let us consider the Jacobian matrix of the system (2.81)–(2.82)

$$J = \begin{bmatrix} (\delta + \tilde{q}) - 9b^2 - 6c^2 - 6bc & -12bc - 3b^2 \\ -12bc - 3b^2 & (\delta - 9\tilde{q}) - 9c^2 - 6b^2 \end{bmatrix}. \quad (2.87)$$

For the *trivial* solution

$$J|_{(b=0,c=0)} = \begin{bmatrix} \delta + \tilde{q} & 0 \\ 0 & \delta - 9\tilde{q} \end{bmatrix},$$

and the trivial solution bifurcates to a primary branch along  $\delta = -\tilde{q}$  and  $\delta = 9\tilde{q}$ ; and it is stable for  $\min\{-\delta, \delta/9\} \leq \tilde{q} \leq \max\{-\delta, \delta/9\}$ . Figure 2.32 shows

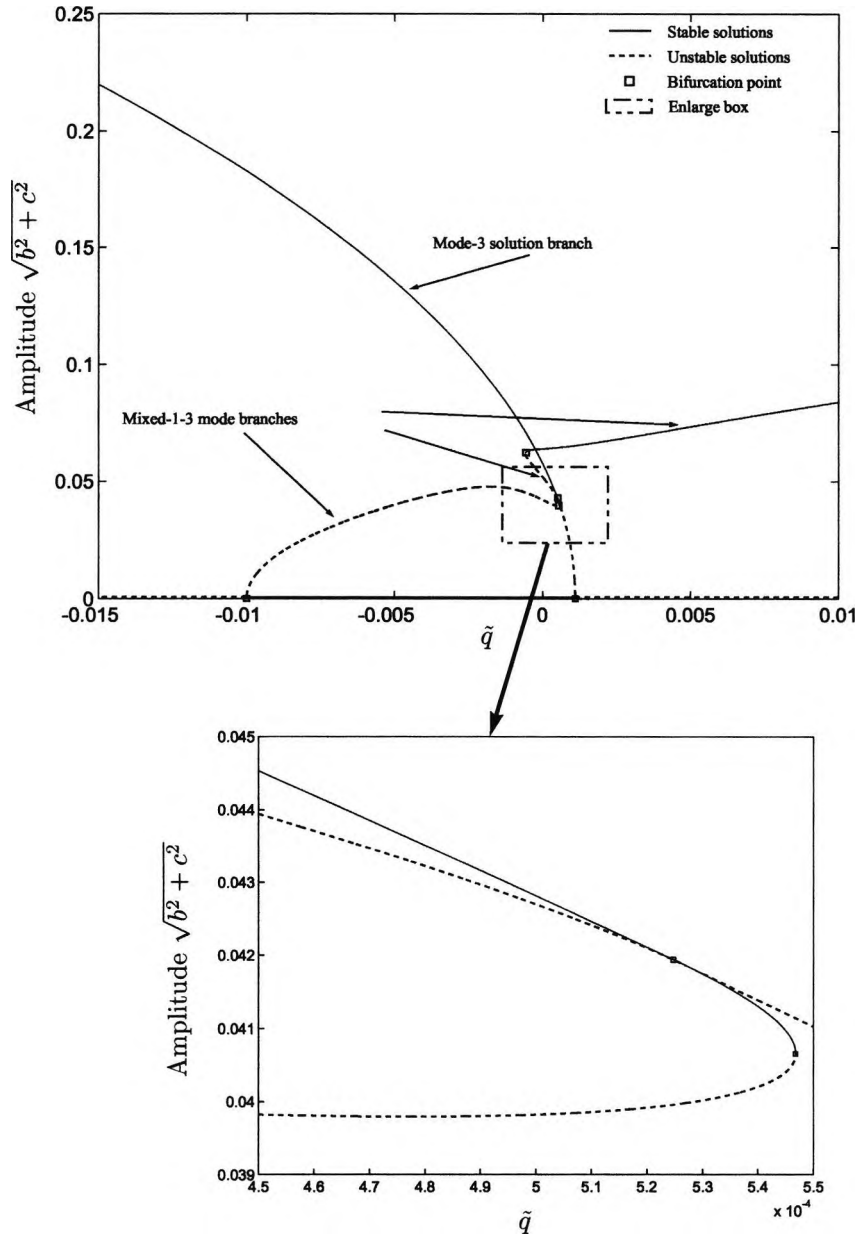


Figure 2.32: An amplitude plot at  $\delta = 0.01$ , showing the bifurcation structure of the mode-1-3 interaction.

the stability regions and Figure 2.33 shows the bifurcation loci in terms of the parameters  $\epsilon$  and  $q = \pi/L$  using the relations (2.86). Here the results are also compared with the numerical results of Section 2.5.

For pure *mode-3* primary solutions

$$J|_{(b=0, c=\pm\sqrt{(\delta-9\tilde{q})/3})} = \begin{bmatrix} -\delta + 19\tilde{q} & 0 \\ 0 & -2\delta + 18\tilde{q} \end{bmatrix},$$

and the primary solutions bifurcate to secondary solutions along  $\delta = 19\tilde{q}$ . The pure *mode-3* primary solution is stable when  $\tilde{q} \leq \min\{\delta/19, 2\delta/18\}$  and it exists only in the region  $\tilde{q} \geq \delta/9$  (see Figures 2.32 and 2.33).

The *mixed-1-3* problem is more complicated than the *mixed-1-2* problem of Section 2.6.1. Here, the analytic solution for  $b \neq 0$  and  $c \neq 0$  is too complex to be considered directly. We shall approach it differently. Consider the determinant of  $J|_{(b \neq 0, c \neq 0)}$ . The solution bifurcates when  $\det J = 0$ , i.e., when

$$[(\delta + \tilde{q}) - 9b^2 - 6c^2 - 6bc] [(\delta - 9\tilde{q}) - 9c^2 - 6b^2] - [12bc + 3b^2]^2 = 0. \quad (2.88)$$

Using equations (2.83) and (2.84) we write  $\delta$  and  $\tilde{q}$  in terms of  $b$  and  $c$

$$\delta = (33cb^2 + 57c^3 + 27bc^2 + b^3)/10c, \quad (2.89)$$

$$\tilde{q} = -(3cb^2 - 3c^3 - 3bc^2 + b^3)/10c. \quad (2.90)$$

Substituting for  $\delta$  and  $\tilde{q}$  in (2.88), and simplifying we get

$$-\frac{6b^5}{c} - 12b^4 - 72cb^3 - 108b^2c^2 + 18c^3b = 0.$$

Define  $\alpha$  such that  $b = \alpha c$  ( $\alpha$  is real since  $b$  and  $c$  are real). Substituting for  $b$  we get

$$\begin{aligned} c^4(-6\alpha^5 - 12\alpha^4 - 72\alpha^3 - 108\alpha^2 + 18\alpha) &= 0, \\ \Rightarrow -6\alpha^4(\alpha^4 + 2\alpha^3 + 12\alpha^2 + 18\alpha - 3) &= 0, \\ \Rightarrow \alpha^4 + 2\alpha^3 + 12\alpha^2 + 18\alpha - 3 &= 0. \end{aligned}$$

Note that we have used the conditions that  $b \neq 0$ ,  $c \neq 0$  and  $\alpha \neq 0$  (note that  $\alpha \neq 0$  since  $b \neq 0$ ). Solving the quartic polynomial in  $\alpha$  we obtain a pair of real roots and a complex conjugate pair. The real solutions are

$$\begin{aligned} \alpha_+ &= -1/2 - c/2 + 1/2\sqrt{(-14c - 392^{(1/3)}c + 14)/c}, \\ \alpha_- &= -1/2 - c/2 - 1/2\sqrt{(-14c - 392^{(1/3)}c + 14)/c}, \end{aligned}$$

where  $c = \sqrt{-7 + 392^{(1/3)}}$ . Numerically,  $\alpha_+ \approx 0.15105$  and  $\alpha_- \approx -1.71550$ .

Substituting  $b = \alpha_{\pm}c$  into equations (2.89) and (2.90) we get

$$\delta = 18.28751\bar{q}, \quad \text{for } \bar{q} > 0, \quad (2.91)$$

$$\delta = -17.33676\bar{q}, \quad \text{for } \bar{q} < 0. \quad (2.92)$$

Equations (2.91) and (2.92) are the loci formed of turning points of the solutions. In Figure 2.32 we can see the two turning points represented by the loci.

To calculate the stability region of the *mixed-1-3* solutions we substitute values of  $b$  and  $c$ , derived from the Newton iteration scheme, into (2.87) and note the points where the eigenvalues change sign. The results can be seen in Figure 2.32.

## 2.7 Summary

In this chapter we have found solutions of the one-dimensional SH equation, with particular emphasis on solutions which are periodic in  $x$  with wavelength  $2L$ .

Summarising what we have found in Chapter 2:

- We have calculated the marginal curves of linear stability to different Fourier modes, i.e.,

$$\epsilon = (q_n^2 - 1)^2 = ((n\pi/L)^2 - 1)^2, \quad \text{for } n = 1, 2, 3, \dots$$

- We have calculated the weakly-nonlinear periodic solutions

$$u \approx 2\sqrt{\frac{\epsilon}{3}}(1 - 4Q^2)^{\frac{1}{2}} \sin \frac{n\pi x}{L}, \quad -\frac{1}{2} \leq Q \leq \frac{1}{2}, \quad \epsilon \rightarrow 0.$$

where  $Q$  is related to  $L$  by (2.29).

- We have calculated numerically nonlinear periodic solutions  $u = u_p$  for different values of  $\epsilon$  and  $L$ .
- We have analysed the interaction of the first and second Fourier modes leading to multiple steady-state periodic forms near  $\epsilon = \frac{9}{25}$  and  $L = \frac{\pi\sqrt{10}}{2}$ .
- We have analysed the interaction of the first and third Fourier modes leading to multiple steady-state periodic forms near  $\epsilon = \frac{16}{25}$  and  $L = \pi\sqrt{5}$ .

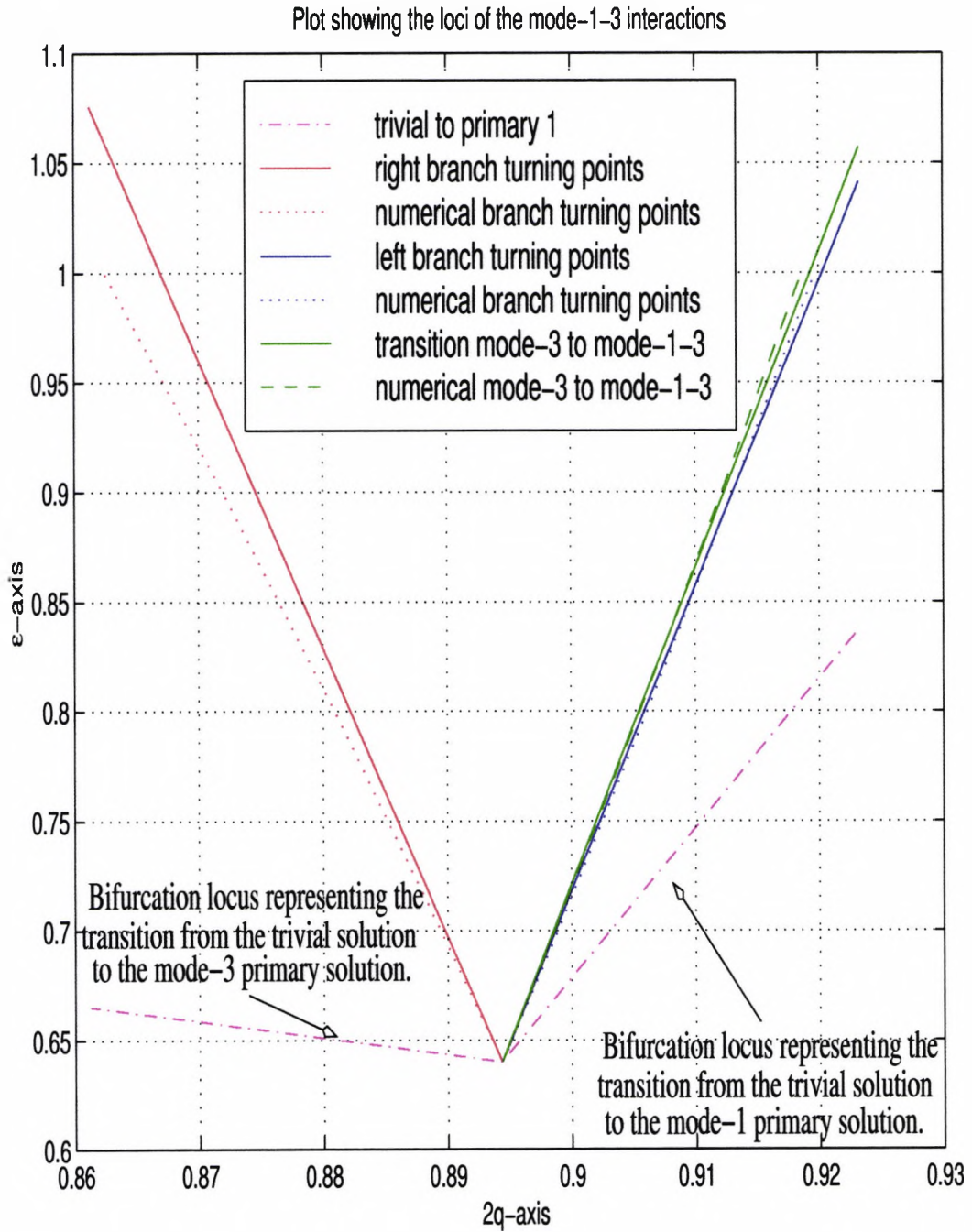


Figure 2.33: A plot showing the bifurcation loci for the mode-1-3 interaction.

# Chapter 3

## Floquet Theory for the One-Dimensional Swift-Hohenberg Equation

### 3.1 Introduction

In this chapter we study the perturbation of periodic solutions at finite  $\epsilon$  to spatial disturbances. In Section 3.2 the perturbed system that is formed suggests the use of Floquet theory. By analysing the *Floquet exponents* we determine the locus that separates the regions where the perturbations are spatially decaying or growing from the regions where the perturbations are oscillatory. The latter constitute what is known as the *Eckhaus instability*. In Section 3.3 we extend the weakly nonlinear analysis of Section 2.3.2 to obtain an approximation to the *Eckhaus instability* boundary<sup>1</sup> for small  $\epsilon$ . In Section 3.4 we compare the weakly nonlinear results with the numerical results for general  $\epsilon$  obtained from the Floquet analysis.

---

<sup>1</sup>We shall refer to it as the *Eckhaus boundary*.

## 3.2 Asymptotic Solution

Consider the steady-state one-dimensional Swift-Hohenberg equation (2.1). We wish to find solutions at finite values of  $\epsilon$  which approach<sup>2</sup> the periodic solution

$$u_p(x) = \sum_{m=1}^{\infty} A_m \sin mqx, \quad (3.1)$$

as  $x \rightarrow \infty$ , where  $q = \frac{\pi}{L}$  is the wavenumber. In practice we can use the numerical form of  $u_p$ , where  $u_p$  is any periodic solution of

$$\left( \frac{d^2}{dx^2} + 1 \right)^2 u_p - \epsilon u_p + u_p^3 = 0, \quad (3.2)$$

subject to the free boundary conditions

$$u_p(0) = \frac{d^2 u_p}{dx^2}(0) = 0 \quad \text{and} \quad u_p(L) = \frac{d^2 u_p}{dx^2}(L) = 0, \quad (3.3)$$

as calculated in Section 2.5. Solutions which tend to the periodic solution,  $u_p$ , as  $x \rightarrow \infty$  may be found by considering a perturbation to  $u_p$  so that  $u$  is written as

$$u(x) = u_p(x) + kU(x) + \dots, \quad (3.4)$$

where the constant  $k \ll 1$ . Substituting (3.4) into equation (2.1) using (3.2) and ignoring nonlinear terms in  $k$  we find that  $U$  satisfies

$$\left( \frac{d^2}{dx^2} + 1 \right)^2 U - \epsilon U + 3u_p^2 U = 0. \quad (3.5)$$

Equation (3.5) is a linear ordinary differential equation with periodic coefficients. Hence Floquet theory (see Ince (1956, [31])) suggests that there is a solution to this equation of the form

$$U(x) = e^{-cx} P(x), \quad (3.6)$$

where  $P(x)$  is periodic and has a period the same as that of  $u_p$ . Note that if  $c$  or  $P$  is complex then the conjugate of  $kU$  is also a solution and can be added in

---

<sup>2</sup>We study solutions which tend to the periodic solution as  $x \rightarrow \infty$  with the view of adding a lateral boundary at  $x = 0$ .

(3.4) to ensure that  $u$  is real. We shall denote the wavelength as  $\lambda = 2L$ . To find the *characteristic exponent*,  $c$ , we assume that the solution  $U(x)$  can be written as

$$U(x) = AU_1(x) + BU_2(x) + CU_3(x) + DU_4(x). \quad (3.7)$$

We shall use the following four different sets of initial conditions to generate the four independent<sup>3</sup> solutions,  $U_1$ ,  $U_2$ ,  $U_3$  and  $U_4$ ,

$$U_1(0) = 1, \quad U_1'(0) = U_1''(0) = U_1'''(0) = 0, \quad (3.8)$$

$$U_2'(0) = 1, \quad U_2(0) = U_2''(0) = U_2'''(0) = 0, \quad (3.9)$$

$$U_3''(0) = 1, \quad U_3(0) = U_3'(0) = U_3'''(0) = 0, \quad (3.10)$$

$$U_4'''(0) = 1, \quad U_4(0) = U_4'(0) = U_4''(0) = 0. \quad (3.11)$$

Substituting equations (3.6) and (3.8)–(3.11) into equations (3.7) we get

$$A = P(0), \quad (3.12)$$

$$B = -cP(0) + P'(0), \quad (3.13)$$

$$C = c^2P(0) - 2cP'(0) + P''(0), \quad (3.14)$$

$$D = -c^3P(0) + 3c^2P'(0) - 3cP''(0) + P'''(0). \quad (3.15)$$

At the boundary  $x = \lambda$  we have

$$AU_1(\lambda) + BU_2(\lambda) + CU_3(\lambda) + DU_4(\lambda) = P(\lambda)e^{-c\lambda}, \quad (3.16)$$

$$AU_1'(\lambda) + BU_2'(\lambda) + CU_3'(\lambda) + DU_4'(\lambda) = (-cP(\lambda) + P'(\lambda))e^{-c\lambda}, \quad (3.17)$$

$$AU_1''(\lambda) + BU_2''(\lambda) + CU_3''(\lambda) + DU_4''(\lambda) = (c^2P(\lambda) - 2cP'(\lambda) + P''(\lambda))e^{-c\lambda}, \quad (3.18)$$

$$AU_1'''(\lambda) + BU_2'''(\lambda) + CU_3'''(\lambda) + DU_4'''(\lambda) = (-c^3P(\lambda) + 3c^2P'(\lambda) - 3cP''(\lambda) + P'''(\lambda))e^{-c\lambda}. \quad (3.19)$$

Using equations (3.12)–(3.15) and the periodicity conditions, i.e.  $P(0) = P(\lambda)$ ,  $P'(0) = P'(\lambda)$ ,  $P''(0) = P''(\lambda)$  and  $P'''(0) = P'''(\lambda)$ , equations (3.16)–(3.19)

<sup>3</sup>The independent set of solutions is a basis for the solution space of equation (3.5); and so (3.7) is a general solution.

become

$$AU_1(\lambda) + BU_2(\lambda) + CU_3(\lambda) + DU_4(\lambda) = Ae^{-c\lambda}, \quad (3.20)$$

$$AU_1'(\lambda) + BU_2'(\lambda) + CU_3'(\lambda) + DU_4'(\lambda) = Be^{-c\lambda}, \quad (3.21)$$

$$AU_1''(\lambda) + BU_2''(\lambda) + CU_3''(\lambda) + DU_4''(\lambda) = Ce^{-c\lambda}, \quad (3.22)$$

$$AU_1'''(\lambda) + BU_2'''(\lambda) + CU_3'''(\lambda) + DU_4'''(\lambda) = De^{-c\lambda}. \quad (3.23)$$

Writing (3.20)–(3.23) in matrix form we obtain the condition for a non-trivial solution as

$$\det \mathbf{W} = 0, \quad (3.24)$$

where  $\mathbf{W}$ , also known as the *Wronskian* matrix, is defined by

$$\mathbf{W}(c) = \begin{bmatrix} U_1(\lambda) - e^{-c\lambda} & U_2(\lambda) & U_3(\lambda) & U_4(\lambda) \\ U_1'(\lambda) & U_2'(\lambda) - e^{-c\lambda} & U_3'(\lambda) & U_4'(\lambda) \\ U_1''(\lambda) & U_2''(\lambda) & U_3''(\lambda) - e^{-c\lambda} & U_4''(\lambda) \\ U_1'''(\lambda) & U_2'''(\lambda) & U_3'''(\lambda) & U_4'''(\lambda) - e^{-c\lambda} \end{bmatrix}. \quad (3.25)$$

Equation (3.24) is a complex determinantal equation for  $c$ . By solving the ordinary differential equation (3.5) with the four sets of initial values (3.8)–(3.11) we can obtain values for  $U_1(\lambda)$ ,  $U_2(\lambda)$ ,  $U_3(\lambda)$ ,  $U_4(\lambda)$  and their derivatives respectively, i.e., all terms required to find  $c$ , the *Floquet exponent*. The calculations were done numerically using a method similar to that of Section 2.2. We also use the numerical values of  $u_p(x)$  from Section 2.4.1. The *Floquet multipliers*,  $e^{-c\lambda}$ , are then obtained from the eigenvalues of the *Wronskian* matrix, equation (3.25). Once we have values for  $c$  we can derive the corresponding  $P(x)$  from equations (3.6)–(3.7) and the eigenvector<sup>4</sup>  $(A, B, C, D)$  corresponding to  $e^{-c\lambda}$ .

Note that  $U = u_p'$  is a solution of equation (3.5). We use this solution, for which  $c = 0$ , as a check on our numerical algorithm.

The Eckhaus boundary is the boundary separating solutions  $U(x)$  that are spatially decaying or growing from solutions  $U(x)$  that are oscillatory. We shall find that this occurs when  $c = 0$  (or when  $e^{-c\lambda} = 1$ ).

First let us extend the results of Section 2.3.2 and calculate the weakly non-linear approximation of the Eckhaus boundary.

<sup>4</sup>To avoid ambiguity the eigenvector,  $(A, B, C, D)$ , is chosen such that  $\sqrt{A^2 + B^2 + C^2 + D^2} = 1$ .

### 3.3 Weakly Nonlinear Analysis

Consider the steady-state amplitude equation (2.23) of Section 2.3.2, that is

$$4 \frac{\partial^2 A_0}{\partial X^2} + A_0 - 3A_0|A_0|^2 = 0. \quad (3.26)$$

We study perturbations to the spatially periodic solutions for  $A_0$  found in Section 2.3.2, which can be written in the form

$$A_p = \sqrt{\frac{1}{3}(1 - 4Q^2)} e^{i(QX+C)}, \quad (3.27)$$

where the value of  $C$  corresponding to (2.30), (2.31) is  $\pi/2$ . Introducing a perturbation  $kB$ ,  $A_0$  is written as

$$A_0(X) = A_p(X) + kB(X) + \dots, \quad (3.28)$$

where the constant  $k$  is small and real. Substituting (3.28) into (3.26) and neglecting nonlinear terms in  $k$  we find that  $B$  satisfies

$$4 \frac{d^2 B}{dX^2} + B - 6B|A_p|^2 - 3A_p^2 \bar{B} = 0. \quad (3.29)$$

Writing

$$B = \beta e^{i(QX+C)+KX}, \quad (3.30)$$

where  $K$  is real and  $\beta$  is complex, equation (3.29) becomes

$$(4K^2 - 1 + 4Q^2 + 8iQK)\beta + (-1 + 4Q^2)\bar{\beta} = 0, \quad (3.31)$$

where  $\bar{\beta}$  is the conjugate of  $\beta$ . Writing  $\beta = \beta_r + i\beta_i$  equation (3.31) becomes

$$(2K^2 - 1 + 4Q^2)\beta_r - 4QK\beta_i + i(2K^2\beta_i + 4QK\beta_r) = 0. \quad (3.32)$$

Comparing real and imaginary parts and writing this in matrix form we get

$$M\bar{\beta} = 0, \quad (3.33)$$

where

$$M = \begin{bmatrix} 2K^2 - 1 + 4Q^2 & -4QK \\ 4QK & 2K^2 \end{bmatrix} \quad (3.34)$$

and  $\tilde{\beta} = [\beta_r, \beta_i]^T$ . This is an eigenvalue problem for  $K$ , so for non-trivial solutions we equate the determinant of the matrix  $M$  to zero, i.e.,

$$K^2(2K^2 + 12Q^2 - 1) = 0. \quad (3.35)$$

Solving equation (3.35) we get

$$K^2 = 0, \quad (3.36)$$

or

$$K^2 = \frac{1}{2}(1 - 12Q^2), \quad (3.37)$$

and in the second case  $K$  is real when

$$-\frac{1}{2\sqrt{3}} < Q < \frac{1}{2\sqrt{3}}. \quad (3.38)$$

The parameter  $K$  is related to  $c$  from Section 3.2 and this shows that when  $-\frac{1}{2\sqrt{3}} < Q < \frac{1}{2\sqrt{3}}$  there are always two zero Floquet exponents and two that are real<sup>5</sup>. Thus in this region, perturbations exist which are spatially decaying or growing. Figure 3.1 shows this region in the  $\epsilon, q$  plane, the overall wavenumber  $q$  being related to  $Q$  by the formula  $q = 1 + \sqrt{\epsilon}Q$  from the analysis of Section 2.3.2. The results of this weakly nonlinear theory can be related to the general form (3.4) with  $U$  given by (3.6) by noting from (3.33) that  $\beta_i = -2QK^{-1}\beta_r$  so that in (3.30)

$$B = \beta_r(1 - 2QK^{-1}i)e^{KX+i(QX+C)}. \quad (3.39)$$

Then since  $u$  and  $A_0$  are related by (2.16) and (2.20), and setting  $C = \pi/2$ , we have

$$u_p \sim \frac{2\epsilon^{\frac{1}{2}}}{\sqrt{3}}(1 - 4Q^2)^{\frac{1}{2}} \sin \left[ x \left( 1 + \epsilon^{\frac{1}{2}}Q \right) \right], \quad \epsilon \rightarrow 0, \quad (3.40)$$

and, for the perturbation which decays as  $x \rightarrow \infty$ ,

$$U = e^{-cx}P(x) \quad (3.41)$$

---

<sup>5</sup>Notice that the two real exponents have opposite sign. This indicates that there is one growing and one decaying solution.

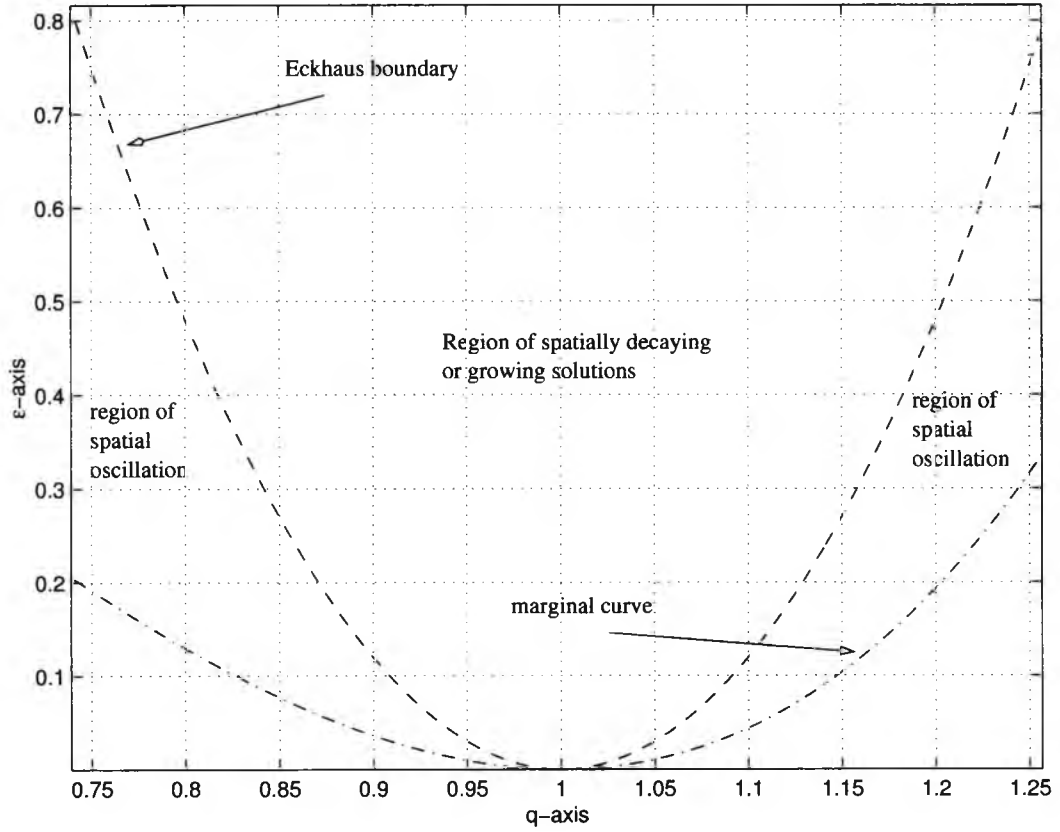


Figure 3.1: Plot displaying regions of spatially decaying/growing and spatially oscillatory solutions for  $\epsilon \ll 1$ . The Eckhaus boundary separates the two regions.

where the Floquet exponent

$$c \sim \frac{\epsilon^{\frac{1}{2}}}{\sqrt{2}} (1 - 12Q^2)^{\frac{1}{2}}, \quad \epsilon \rightarrow 0, \quad (3.42)$$

and the periodic eigenfunction

$$P(x) \sim \beta_r \epsilon^{\frac{1}{2}} \left\{ \sin \left[ x \left( 1 + \epsilon^{\frac{1}{2}} Q \right) \right] + 2\sqrt{2} Q (1 - 12Q^2)^{-\frac{1}{2}} \cos \left[ x \left( 1 + \epsilon^{\frac{1}{2}} Q \right) \right] \right\}, \quad (3.43)$$

as  $\epsilon \rightarrow 0$ .

For perturbations associated with  $K = 0$ , we clearly have  $c = 0$  in (3.41) and since, from (3.34), it follows that  $\beta_r = 0$ , the periodic eigenfunction is given by

$$P(x) \sim -\beta_i \epsilon^{\frac{1}{2}} \cos \left[ x \left( 1 + \epsilon^{\frac{1}{2}} Q \right) \right], \quad \epsilon \rightarrow 0. \quad (3.44)$$

Comparing with (3.40), we see that (to within an arbitrary multiplicative constant) this is equivalent to the solution  $U = u'_p$  mentioned earlier.

Now we search for solutions for  $B$  that are spatially oscillatory by writing

$$B = e^{i(QX+C)} (\beta e^{iKX} + \gamma e^{-iKX}), \quad (3.45)$$

where  $K$  is real and  $\beta$  and  $\gamma$  are complex. A more general form can be assumed in which the term  $e^{iKX}$  is replaced by  $e^{-i\bar{K}X}$  with  $K$  allowed to be complex, but it emerges that fully complex solutions for  $K$  do not occur. Equation (3.29) becomes

$$\begin{aligned} & [(4Q^2 - 8QK - 4K^2 - 1)b + (-1 + 4Q^2)\bar{\gamma}] e^{iKX} + \\ & + [(-1 + 4Q^2)\bar{\beta} + (4Q^2 + 8QK - 4K^2 - 1)\gamma] e^{-iKX} = 0. \end{aligned} \quad (3.46)$$

Comparing the coefficients of  $e^{iKX}$  and  $e^{-iKX}$  and taking the conjugate in the second case gives

$$(4Q^2 - 8QK - 4K^2 - 1)\beta + (-1 + 4Q^2)\bar{\gamma} = 0, \quad (3.47)$$

$$(4Q^2 + 8QK - 4K^2 - 1)\bar{\gamma} + (-1 + 4Q^2)\beta = 0, \quad (3.48)$$

or, in matrix form

$$M\bar{\beta} = 0, \quad (3.49)$$

where

$$M = \begin{bmatrix} 4Q^2 - 8QK - 4K^2 - 1 & -1 + 4Q^2 \\ -1 + 4Q^2 & 4Q^2 + 8QK - 4K^2 - 1 \end{bmatrix}, \quad (3.50)$$

and  $\bar{\beta} = [\beta, \bar{\gamma}]^T$ . Equation (3.49) is an eigenvalue problem for  $K$ , so for non-trivial solutions we equate the determinant of the matrix  $M$  to zero and get the condition

$$K^2(2K^2 - 12Q^2 + 1) = 0. \quad (3.51)$$

Solving equation (3.51) we get

$$K^2 = 0, \quad (3.52)$$

or

$$K^2 = \frac{1}{2}(12Q^2 - 1), \quad (3.53)$$

and in the second case  $K$  is real when

$$Q < -\frac{1}{2\sqrt{3}} \quad \text{or} \quad Q > \frac{1}{2\sqrt{3}}. \quad (3.54)$$

This indicates that when  $Q < -\frac{1}{2\sqrt{3}}$  or  $Q > \frac{1}{2\sqrt{3}}$  (see Figure 3.1) there are two zero Floquet exponents and two that are purely imaginary. Equivalently, there exist two Floquet multipliers that are unity and two that are complex and within this region we see that perturbations are spatially oscillatory. The weakly nonlinear form of the Eckhaus boundary for the one-dimensional SH equation has been found previously by Kramer and Hohenberg (1984, [34]).

The weakly nonlinear results plotted in Figure 3.1 show the region of spatially decaying or growing solutions and the region of spatially oscillatory solutions. The results also show that there are always two Floquet multipliers that are unity, which correspond to the solution  $U = u'_p$ ,  $c = 0$  mentioned in Section 3.2.

Now let us consider the numerical results for general  $\epsilon$ .

### 3.4 Numerical Results

We used the ODEsolver within Matlab's *ODESUITE* by Shampine and Reichelt (1996, [46]) to solve the ordinary differential equation (3.5) with the four sets of initial values (3.8)–(3.11).

As in Section 2.5 wherever we can find the periodic solution<sup>6</sup>,  $u_p$ , in our parameter space,  $(\lambda, \epsilon)$ , we can also calculate the *Floquet multipliers*,  $e^{-c\lambda}$ , for each point  $(\lambda, \epsilon)$ . Note that there are four Floquet multipliers for each  $(\lambda, \epsilon)$ . Figures 3.2–3.5 show the results for  $\epsilon \in \{0.01, 0.1, 0.4, 0.6\}$ .

Consider Figure 3.2. This is the result for a fixed  $\epsilon = 0.01$ . The top plot is the plot of the *shooting*-parameters  $\alpha$  and  $\beta$  of  $u_p$  as given in Section 2.5. It shows that non-trivial solutions exist for  $5.991 < \lambda < 6.623$ . The bottom plot is the plot of the real and imaginary parts (blue and green lines respectively) of all four Floquet multipliers within the marginal stability curve. Two Floquet multipliers are always equal to one (this solution exists for all  $(\lambda, \epsilon)$  and is equivalent to the solution  $U = u'_p$  mentioned in Section 3.2). For the other two Floquet multipliers we found regions where they are real and regions where they are complex (Eckhaus instability). At the *join*, where  $e^{-c\lambda} = 1$  and  $c = 0$ , is the Eckhaus boundary. This

<sup>6</sup>Note that  $u_p$  is non-unique at some points within the parameter space.

shows that the periodic solutions (represented by the top plot of Figure 3.2) are unstable to the Eckhaus instability except where  $6.11 < \lambda < 6.47$ . Figures 3.3–3.5 are plots at higher values of  $\epsilon$ .

Figure 3.6 shows the plots of the Floquet exponent  $c$  corresponding to Figures 3.2–3.5. Here we see two Floquet exponents that are always zero; and the other two exponents separate into regions where both are real (with equal and opposite values) and regions where both are purely imaginary, with equal and opposite values and  $|e^{-c\lambda}| = 1$  (Eckhaus instability). At the *join* is the Eckhaus boundary.

Figure 3.7 shows the plot of the eigenfunctions  $P_1(x)$ ,  $P_2(x)$ ,  $P_3(x)$  and  $P_4(x)$  at  $(\lambda, \epsilon) = (2\pi, 0.1)$ , corresponding to the four Floquet exponents  $c$  given by  $c_1 = -0.21956$ ,  $c_2 = 0.21956$ ,  $c_3 = 0$  and  $c_4 = 0$  respectively.

The Eckhaus instability develops between the marginal stability curve and the *Eckhaus boundary* which for small  $\epsilon$  is given in Section 3.3 as

$$\epsilon = 12 \left( \frac{2\pi}{\lambda} - 1 \right)^2. \quad (3.55)$$

The numerical method described here was used to trace the Eckhaus boundary ( $c = 0$ ) for general values of  $\epsilon$ . A comparison of the numerical results and the weakly nonlinear result is shown in Figure 3.8; this shows that the weakly nonlinear theory is remarkably accurate even up to  $\epsilon = 1$ . The Eckhaus boundary for the one-dimensional SH equation and general values of  $\epsilon$  found here is consistent with earlier results reported by Kramer and Hohenberg (1984, [34])<sup>7</sup>.

Inspecting Figure 3.5 and the lower-right plot in Figure 3.6 near  $\lambda = 10.3$  we can see that for  $\epsilon = 0.6$  there is a gap (the blue bubble at  $\lambda = 10.3$ ) in the *Eckhaus instability* region. This region lies in the neighbourhood of the mode-1-2 interaction (which we have considered in Section 2.6.1). This gap seems to emanate from the *mixed-1-2* critical point. We shall leave the investigation of this phenomenon as a proposal for further investigation.

## 3.5 Summary

Summarising what we have found in Chapter 3:

<sup>7</sup>Kramer and Hohenberg (1984, [34]) gave no details of the numerical method that they used.

- We have considered perturbations to periodic solutions of wavelength  $2L$  of the one-dimensional SH equation.
- The weakly-nonlinear results show analytically that there are regions where there are spatially decaying or growing solutions and regions of spatially oscillatory solutions (Eckhaus instabilities).
- For small  $\epsilon$  the weakly-nonlinear locus of the Eckhaus boundary is given by

$$\epsilon = 12 \left( \frac{2\pi}{\lambda} - 1 \right)^2,$$

where  $\lambda = 2L$ .

- We have computed the numerical results for the Eckhaus boundary at arbitrary  $\epsilon$ .
- The numerical results and the weakly-nonlinear theory of the Eckhaus boundary show good agreement even up to  $\epsilon = 1$ .
- We have determined the form of steady nonlinear solutions of the one-dimensional SH equation which approach the periodic form  $u_p(x)$  as  $x \rightarrow \infty$ . Such solutions exist within the Eckhaus boundary and at other isolated locations within the neutral curve.

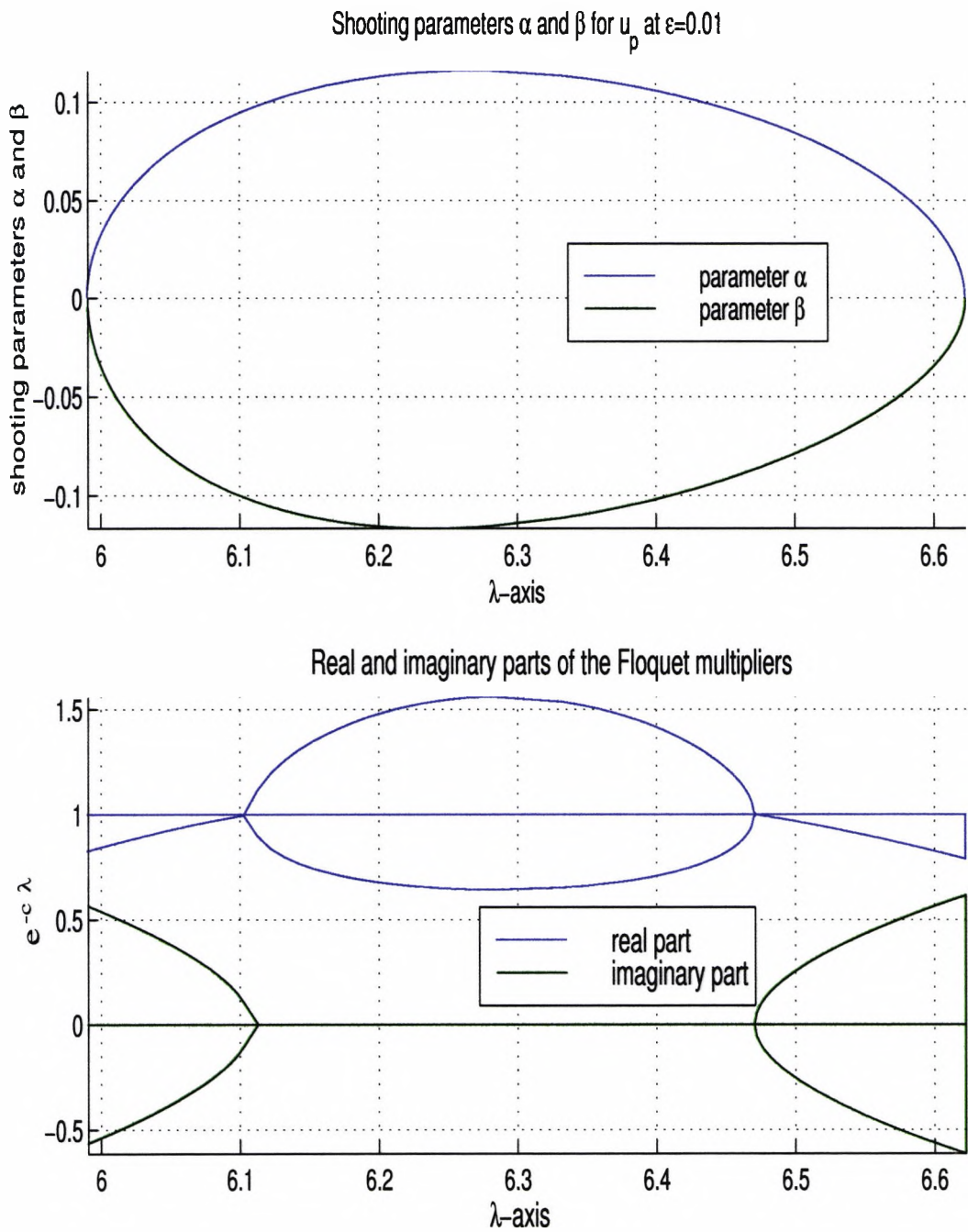


Figure 3.2: Plot of the real and imaginary part of the *Floquet multipliers* for fixed  $\epsilon = 0.01$  and for  $\lambda$  such that  $(\lambda, \epsilon)$  lies above the neutral curve.

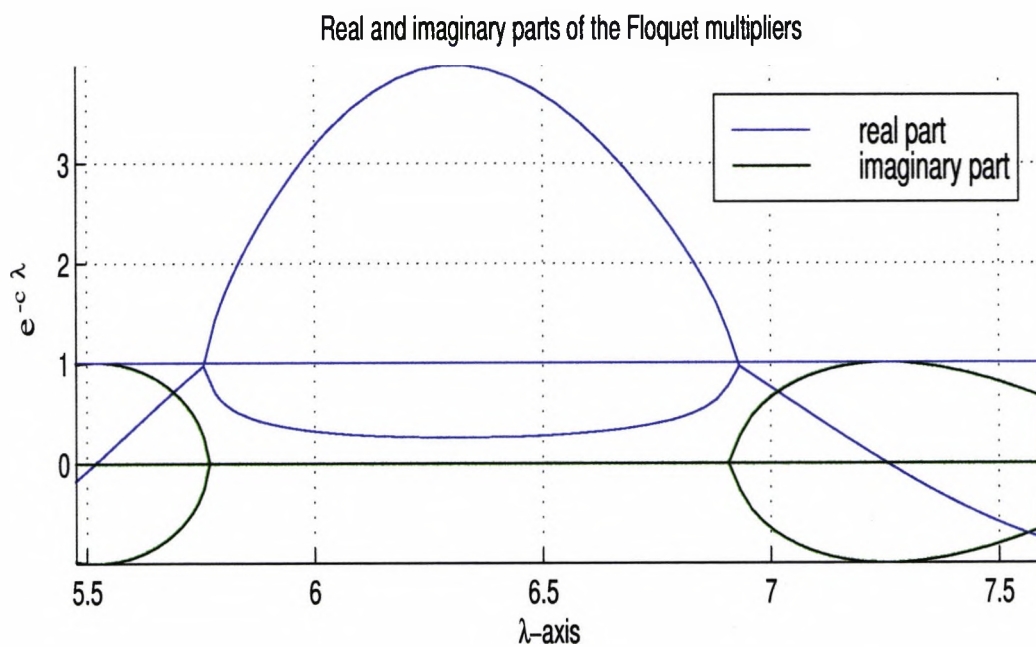
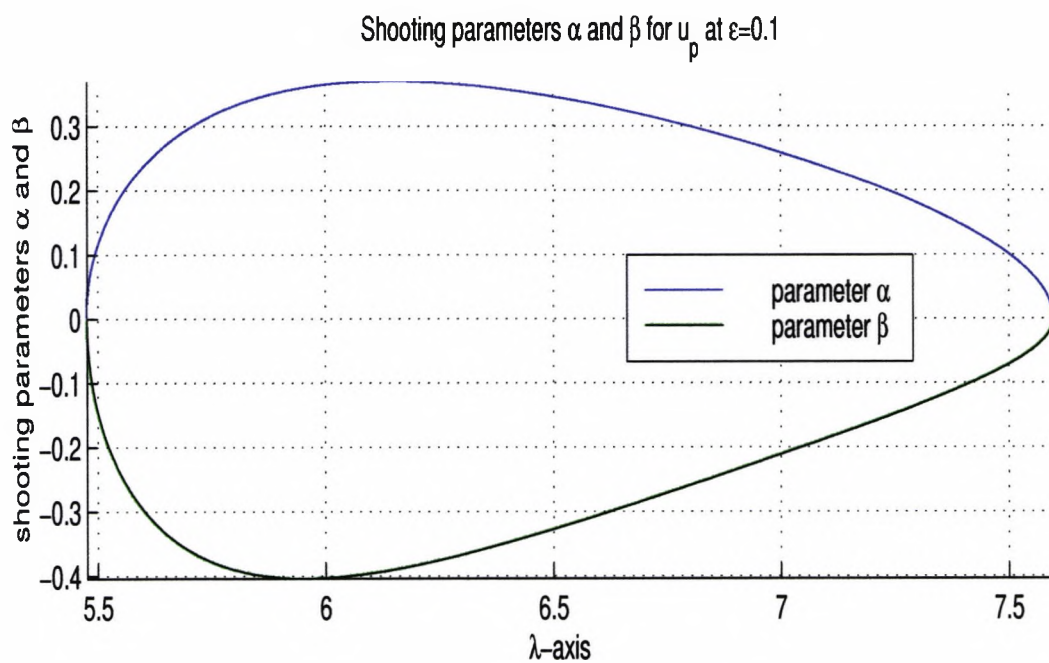


Figure 3.3: Plot of the real and imaginary part of the *Floquet multipliers* for fixed  $\epsilon = 0.1$  and for  $\lambda$  such that  $(\lambda, \epsilon)$  lies above the neutral curve.

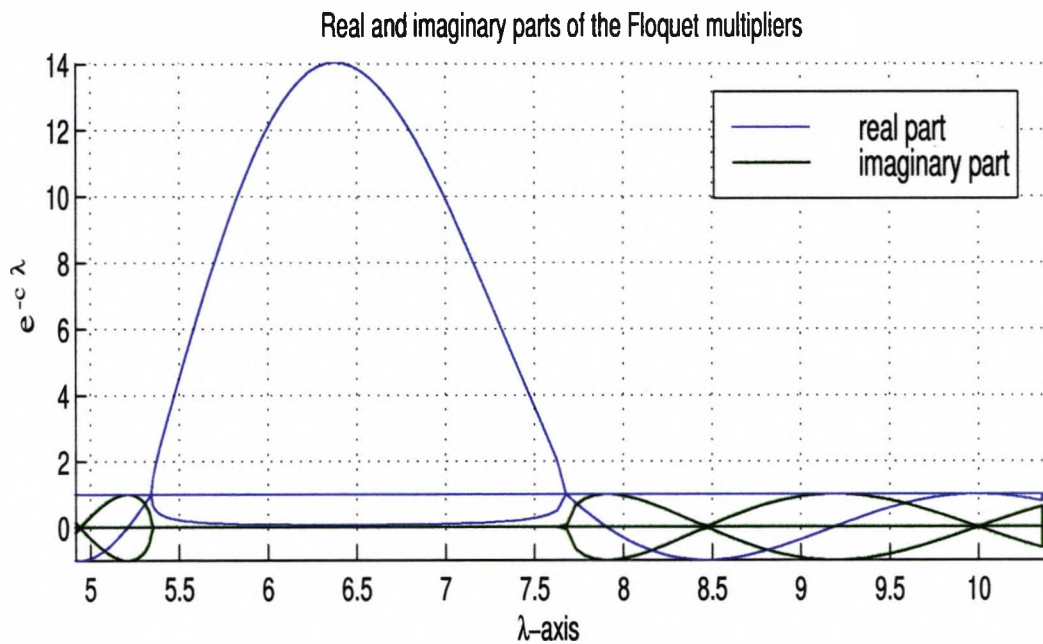
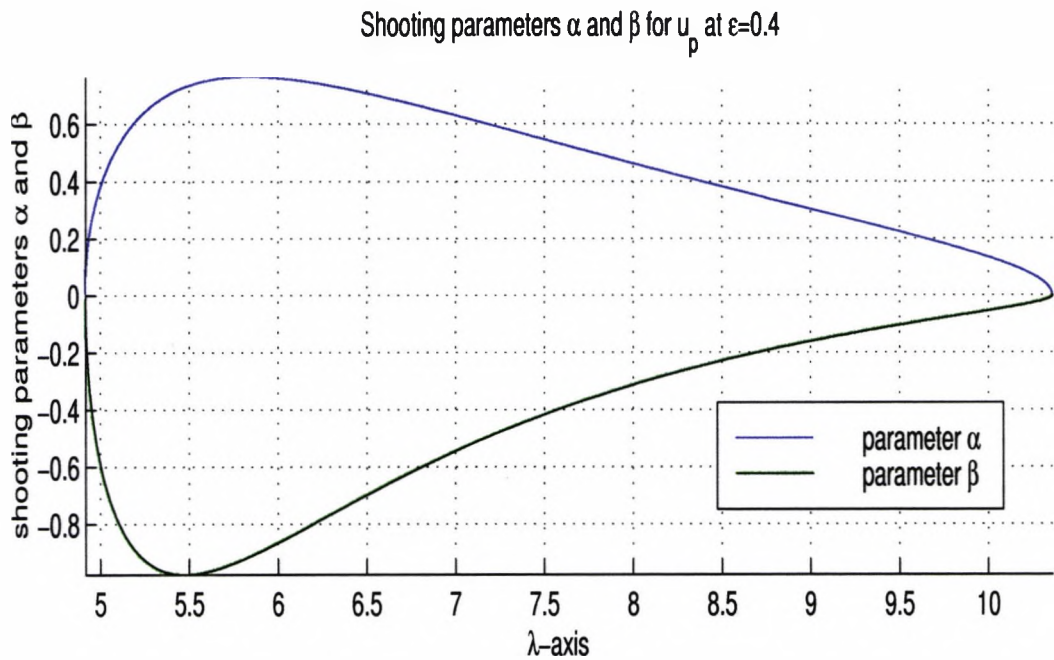


Figure 3.4: Plot of the real and imaginary part of the *Floquet multipliers* for fixed  $\epsilon = 0.4$  and for  $\lambda$  such that  $(\lambda, \epsilon)$  lies above the neutral curve.

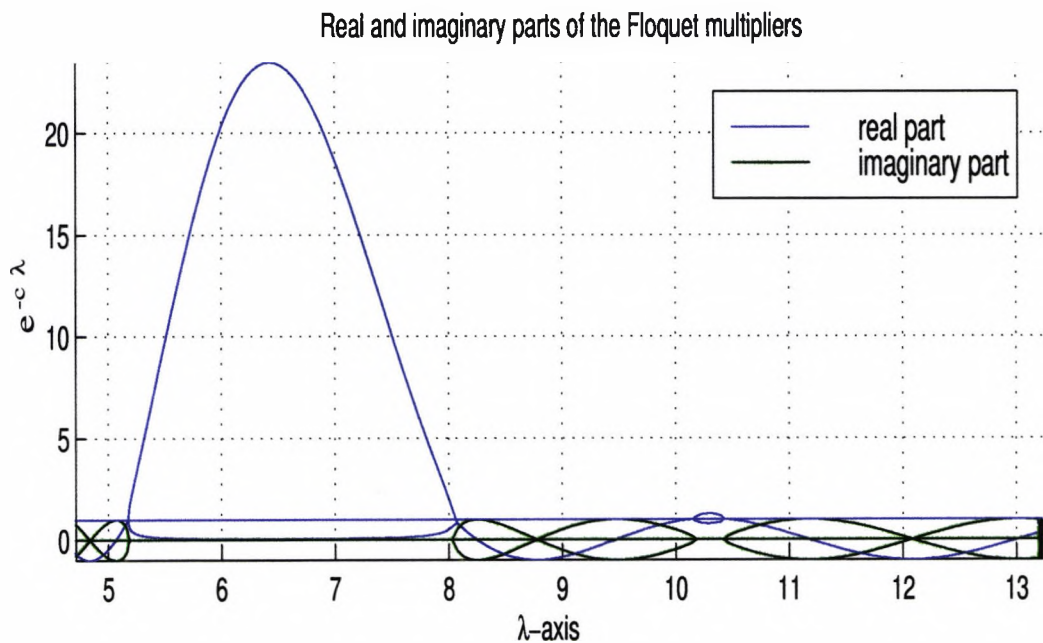
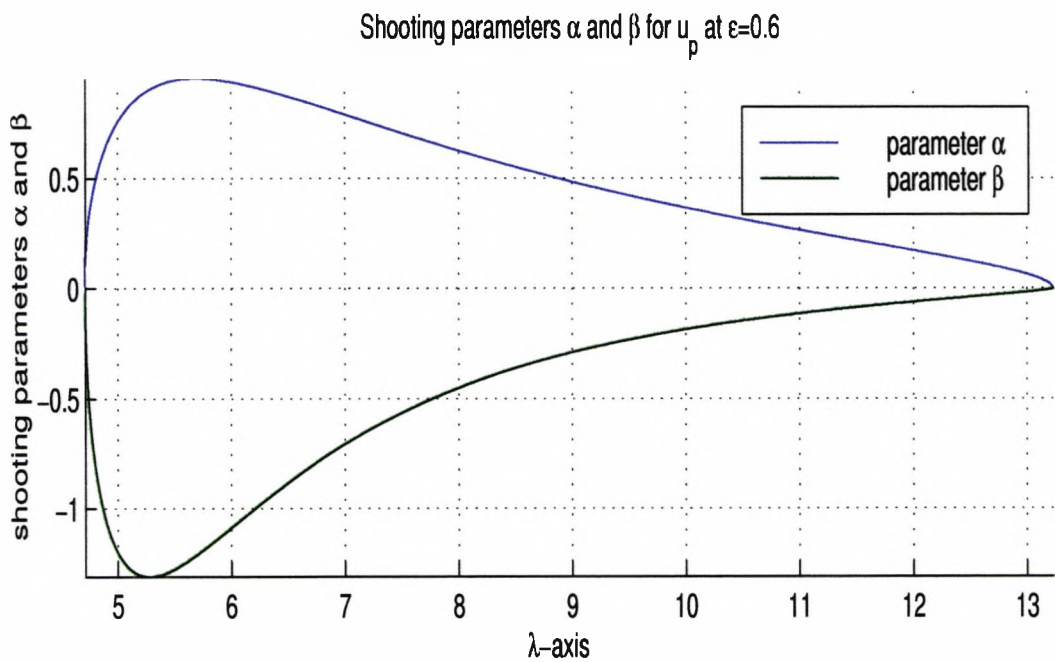


Figure 3.5: Plot of the real and imaginary part of the *Floquet multipliers* for fixed  $\epsilon = 0.6$  and for  $\lambda$  such that  $(\lambda, \epsilon)$  lies above the neutral curve.

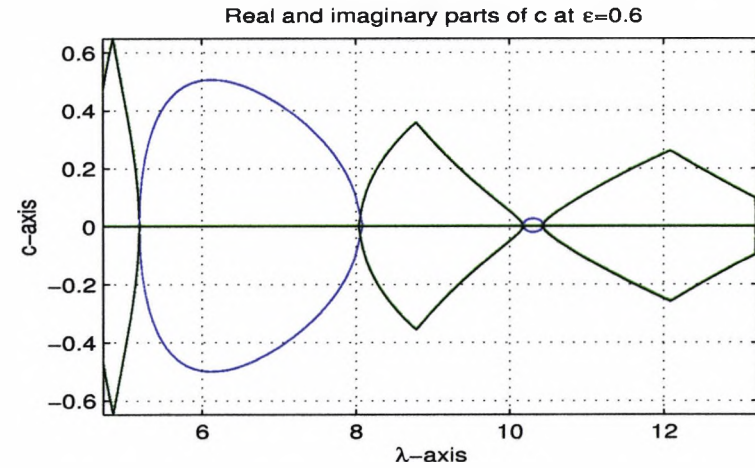
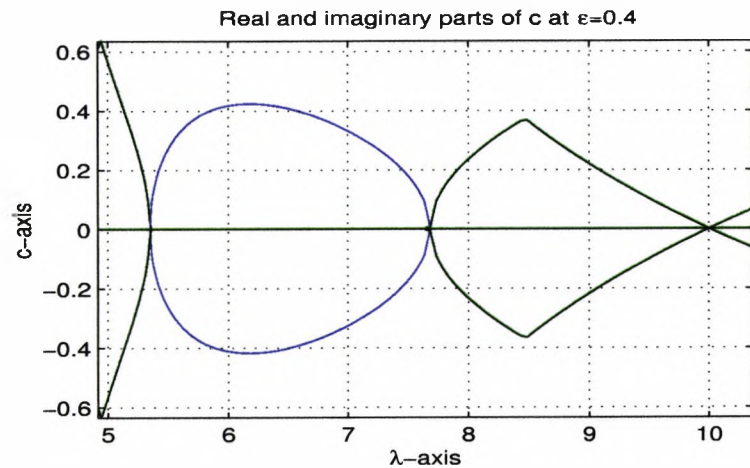
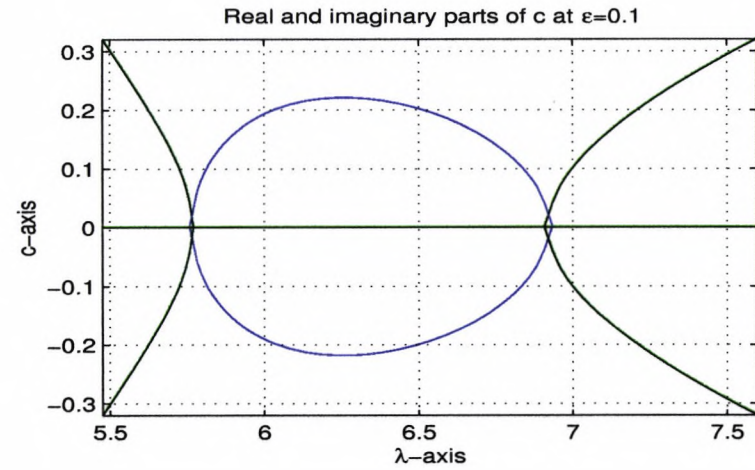
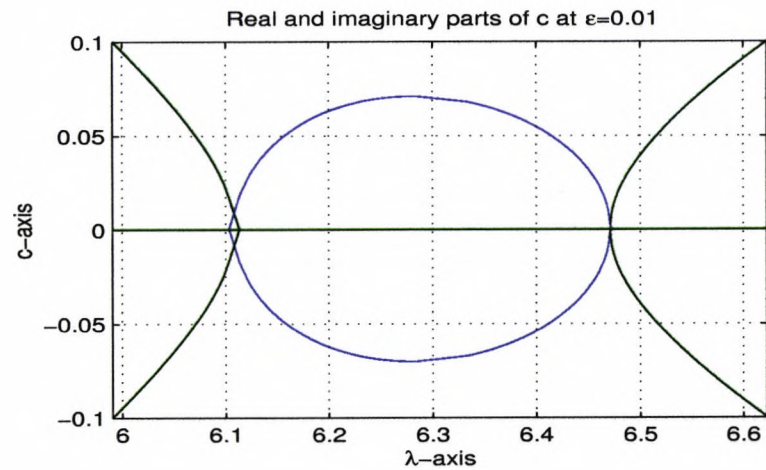


Figure 3.6: Plot of the real and imaginary part of the *Floquet exponent*,  $c$  for  $\epsilon \in \{0.01, 0.1, 0.4, 0.6\}$  and for  $\lambda$  such that  $(\lambda, \epsilon)$  lies above the neutral curve. The blue and green lines represent the real and imaginary parts respectively.

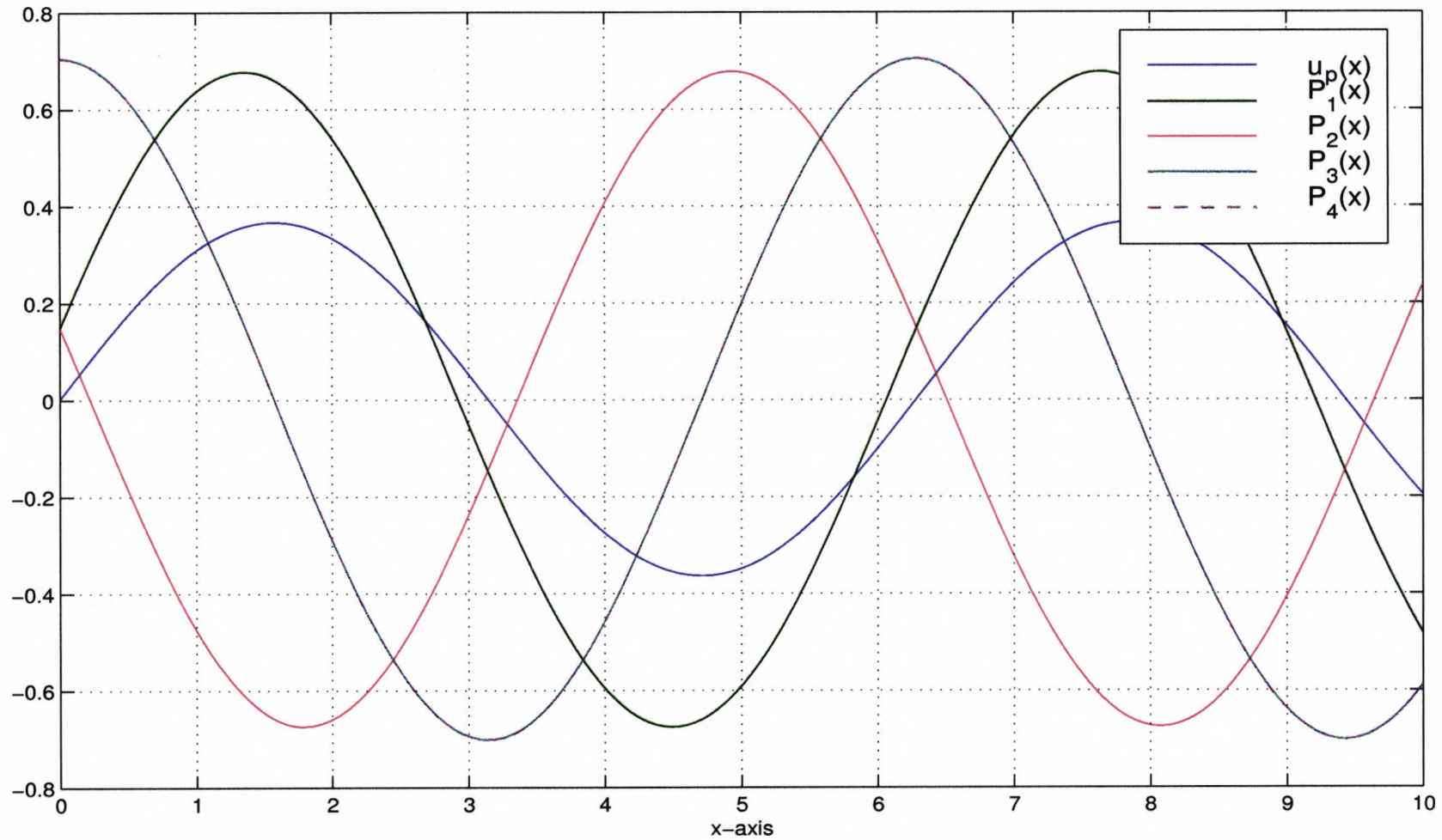


Figure 3.7: Plot of the functions  $u_p(x)$ ,  $P_1(x)$ ,  $P_2(x)$ ,  $P_3(x)$  and  $P_4(x)$  at the parameter point  $(\lambda, \epsilon) = (2\pi, 0.1)$  where  $P_1$ ,  $P_2$ ,  $P_3$  and  $P_4$  correspond to the  $c$  values  $c_1 = -0.21956$ ,  $c_2 = 0.21956$ ,  $c_3 = 0$  and  $c_4 = 0$  respectively.

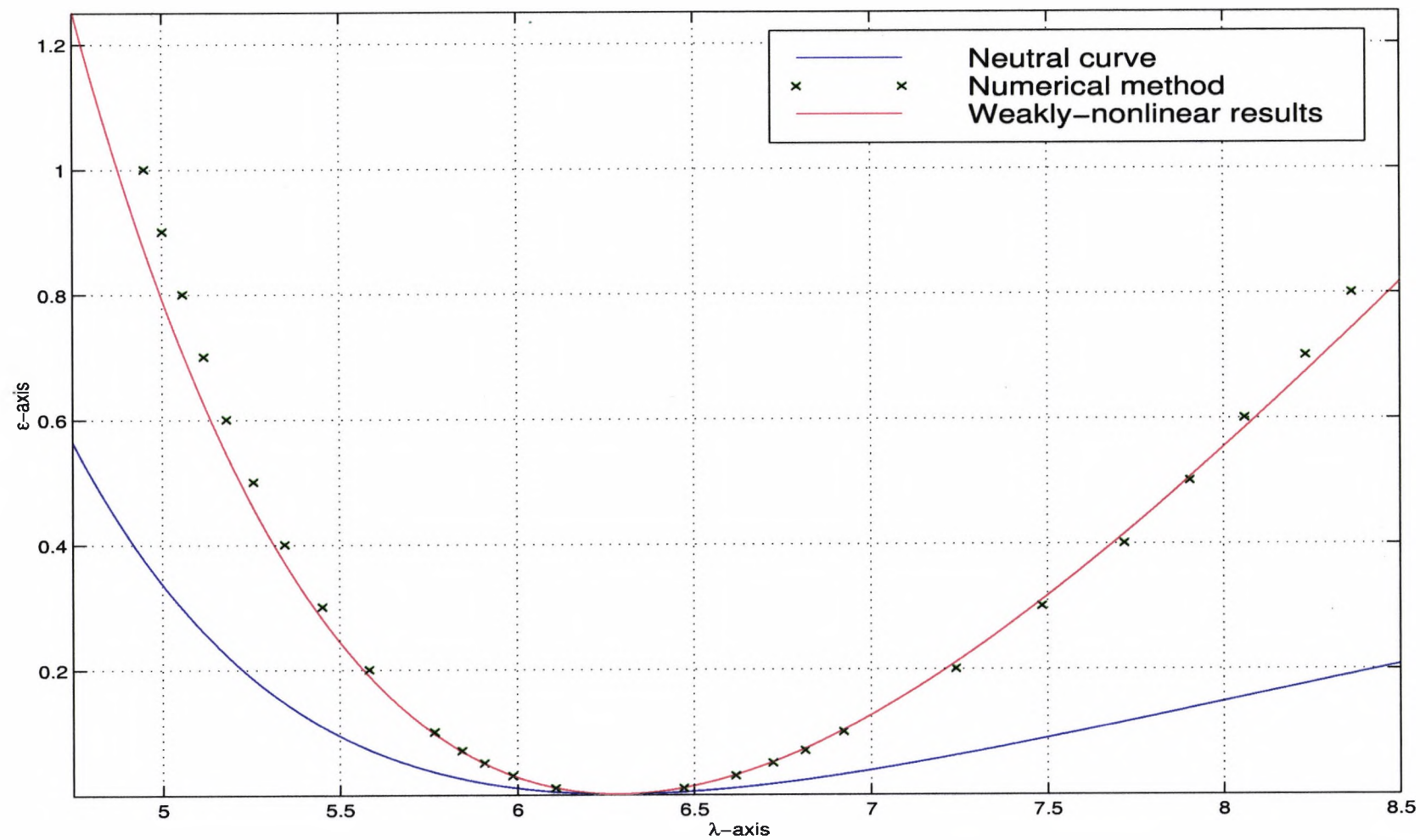


Figure 3.8: Plot comparing the numerical results from the *Floquet* method and the weakly-nonlinear approximation of the Eckhaus boundary.

## Chapter 4

# Steady Solutions of the One-Dimensional Swift-Hohenberg Equation in a Semi-infinite Domain

### 4.1 Introduction

In this chapter we consider solutions in a semi-infinite domain  $x \geq 0$  with no-slip boundary conditions applied at a lateral wall at  $x = 0$ . Thus the problem is to solve

$$u'''' + 2u'' + (1 - \epsilon)u + u^3 = 0, \quad (4.1)$$

subject to

$$u = u' = 0, \quad \text{at } x = 0, \quad (4.2)$$

and

$$u \rightarrow u_p(x + \phi), \quad \text{as } x \rightarrow \infty. \quad (4.3)$$

Here it is assumed that the solution approaches a periodic form at large distances from the wall, with the phase shift  $\phi$  to be determined as part of the solution. We expect the periodic form (4.3) to be achieved through an exponential decay of the form

$$u \sim u_p(x + \phi) + ke^{-cx}P(x + \phi), \quad x \rightarrow \infty, \quad (4.4)$$

where  $c$  and  $P(x)$  are the Floquet exponent and eigenfunction determined in Chapter 3; the coefficient  $k$ , like  $\phi$ , is to be found as part of the solution. In Section 4.2 we consider the solution of this problem for small  $\epsilon$ . By extending the weakly-nonlinear analysis of Section 2.3.2 to higher orders of approximation and by matching solutions in inner and outer regions we find that the wall imposes a restriction on the choice of the wavenumber  $q = \pi/L$ . We shall call this restriction, first discussed by Cross *et al* (1983, [15]), the  $q$ -restriction. In Sections 4.3 and 4.4 we use the Floquet analysis of Section 3.2 and obtain two different methods for calculating the  $q$ -restriction at general  $\epsilon$ . The first method (Section 4.3) is an approximate asymptotic method based on the use of (4.4) for all  $x \geq 0$ . This is easy to implement but is found to have poor accuracy. The second method (Section 4.4) solves the fully-nonlinear SH equation (4.1) and is therefore accurate but involves more effort to implement. We compare the weakly nonlinear result with the results from the second numerical method and obtain good agreement even for values of  $\epsilon$  up to  $\epsilon = 1$ . Previously Kramer and Hohenberg (1984, [34]) have used a purely numerical method to obtain the wavenumber restriction at two values of  $\epsilon$ . However, our method has the advantage of ensuring an accurate representation of the solution as  $x \rightarrow \infty$ , by making use of the Floquet form and allowing analytical insight into the existence and non-uniqueness of solutions. In addition, we obtain results over a range of values of  $\epsilon$  up to  $\epsilon = 1$  and make a detailed comparison with the weakly nonlinear theory.

## 4.2 Weakly Nonlinear Analysis

We proceed as in Section 2.3.2 with an (outer) expansion in the region where  $X = \epsilon^{1/2}x = O(1)$  but here we need to consider higher orders of approximation. We also need to introduce an inner region near the wall where  $x = O(1)$  (see Figure 4.1).

Assuming that in the outer region  $u(x)$  develops with the form,

$$u = \epsilon^{1/2}u_0 + \epsilon u_1 + \epsilon^{3/2}u_2 + \epsilon^2u_3 + \dots, \quad (4.5)$$

we let the solution contain a modulation on the scale  $X = \sqrt{\epsilon}x$  so that  $u_i = u_i(x, X)$ . Substituting into (2.12) and collecting and comparing coefficients of

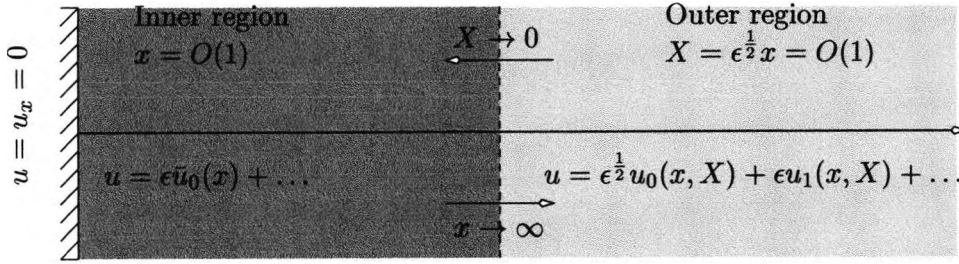


Figure 4.1: Diagram illustrating the inner and outer approximation regions and the matching that is required. The inner solution is formulated in equation (4.45) below.

powers of  $\epsilon$  we obtain

$$\frac{\partial^4 u_0}{\partial x^4} + 2\frac{\partial^2 u_0}{\partial x^2} + u_0 = 0, \quad (4.6)$$

$$\frac{\partial^4 u_1}{\partial x^4} + 2\frac{\partial^2 u_1}{\partial x^2} + u_1 = -4 \left[ \frac{\partial^4 u_0}{\partial x^3 \partial X} + \frac{\partial^2 u_0}{\partial x \partial X} \right], \quad (4.7)$$

$$\begin{aligned} \frac{\partial^4 u_2}{\partial x^4} + 2\frac{\partial^2 u_2}{\partial x^2} + u_2 = & - \left[ 4\frac{\partial^4 u_1}{\partial X \partial x^3} + 4\frac{\partial^2 u_1}{\partial X \partial x} + 6\frac{\partial^4 u_0}{\partial X^2 \partial x^2} \right. \\ & \left. + 2\frac{\partial^2 u_0}{\partial X^2} + u_0^3 - u_0 \right], \end{aligned} \quad (4.8)$$

$$\begin{aligned} \frac{\partial^4 u_3}{\partial x^4} + 2\frac{\partial^2 u_3}{\partial x^2} + u_3 = & - \left[ 4\frac{\partial^4 u_2}{\partial X \partial x^3} + 4\frac{\partial^2 u_2}{\partial X \partial x} \right. \\ & + 4\frac{\partial^4 u_0}{\partial X^3 \partial x} + 6\frac{\partial^4 u_1}{\partial X^2 \partial x^2} + 2\frac{\partial^2 u_1}{\partial X^2} \\ & \left. + 3u_0^2 u_1 - u_1 \right], \end{aligned} \quad (4.9)$$

at orders  $\epsilon^{1/2}$ ,  $\epsilon$ ,  $\epsilon^{3/2}$  and  $\epsilon^2$  respectively. Solving equation (4.6), the relevant periodic form is

$$u_0(x, X) = A_0(X) \exp(ix) + \text{c.c.}, \quad (4.10)$$

where  $A_0$  is a complex amplitude function and c.c. denotes the complex conjugate. Substituting for  $u_0(x, X)$ , equation (4.7) becomes

$$\frac{\partial^4 u_1}{\partial x^4} + 2\frac{\partial^2 u_1}{\partial x^2} + u_1 = 0, \quad (4.11)$$

and the relevant periodic form is

$$u_1(x, X) = A_1(X) \exp(ix) + \text{c.c.}, \quad (4.12)$$

where  $A_1$  is another complex amplitude function. We substitute for  $u_0(x, X)$  and  $u_1(x, X)$  in equation (4.8) to get

$$\begin{aligned} \frac{\partial^4 u_2}{\partial x^4} + 2\frac{\partial^2 u_2}{\partial x^2} + u_2 &= \left[ A_0 - 3A_0|A_0|^2 + 4\frac{d^2 A_0}{dX^2} \right] \exp(ix) \\ &+ \left[ \bar{A}_0 - 3\bar{A}_0|A_0|^2 + 4\frac{d^2 \bar{A}_0}{dX^2} \right] \exp(-ix) \\ &- A_0^3 \exp(3ix) - \bar{A}_0^3 \exp(-3ix), \end{aligned} \quad (4.13)$$

where  $\bar{A}$  denotes the complex conjugate of  $A$ . In order for  $u_2$  to remain finite for  $X = O(1)$  the secular terms proportional to  $\exp(\pm ix)$  must vanish, requiring  $A_0$  to satisfy the *first order* condition

$$4\frac{d^2 A_0}{dX^2} + A_0 - 3A_0|A_0|^2 = 0. \quad (4.14)$$

Equation (4.13) becomes

$$\frac{\partial^4 u_2}{\partial x^4} + 2\frac{\partial^2 u_2}{\partial x^2} + u_2 = -A_0^3 \exp(3ix) - \bar{A}_0^3 \exp(-3ix), \quad (4.15)$$

and the relevant solution is

$$u_2(x, X) = -\frac{1}{64}A_0^3 \exp(3ix) + A_2(X) \exp(ix) + \text{c.c.}, \quad (4.16)$$

where  $A_2$  is a further complex amplitude function. Substituting equations (4.10), (4.12) and (4.16) into (4.9) we get

$$\begin{aligned} \frac{\partial^4 u_3}{\partial x^4} + 2\frac{\partial^2 u_3}{\partial x^2} + u_3 &= - \left[ 4i\frac{d^3 A_0}{dX^3} + 6A_1|A_0|^2 - 4\frac{d^2 A_1}{dX^2} + \right. \\ &\quad \left. + 3A_0^2 \bar{A}_1 - A_1 \right] e^{ix} + \\ &\quad - \left[ 3A_1 A_0^2 + \frac{9}{2}iA_0^2 \frac{dA_0}{dX} \right] e^{3ix} + \text{c.c.} \end{aligned} \quad (4.17)$$

In order for  $u_3$  to remain finite for  $X = O(1)$  the secular terms proportional to  $\exp(\pm ix)$  must vanish, requiring  $A_1$  to satisfy the *second order* condition

$$4i\frac{d^3 A_0}{dX^3} + 6A_1|A_0|^2 - 4\frac{d^2 A_1}{dX^2} + 3A_0^2 \bar{A}_1 - A_1 = 0, \quad (4.18)$$

Consider the *first order* condition (4.14). Writing  $A_0(X) = r(X)e^{i\theta(X)}$  and comparing real and imaginary parts we get the equations

$$4r'' + r - 3r^3 - 4r(\theta')^2 = 0, \quad (4.19)$$

$$2r'\theta' + r\theta'' = 0, \quad (4.20)$$

from the real and imaginary parts respectively. Integrating (4.20) with respect to  $X$  we get

$$r^2\theta' = K_0, \quad (4.21)$$

where  $K_0$  is an arbitrary constant. Assuming that the condition  $u = 0$  at  $x = 0$  can be applied to the leading order solution at  $X = 0$  (alternative strategies lead to inconsistencies) it follows that

$$0 = A_0(0) = r(0)e^{i\theta(0)}, \quad (4.22)$$

which implies that

$$r(0) = 0, \quad (4.23)$$

and so

$$K_0 = 0. \quad (4.24)$$

Then

$$r^2\theta' = 0. \quad (4.25)$$

We are interested in solutions for  $u$  that are non-trivial, bounded and periodic as  $X \rightarrow \infty$  in the *outer region*, so we require that  $r$  be non-zero. This implies that  $\theta' = 0$ , so that  $\theta$  is a constant, independent of  $X$ .

Since  $\theta' = 0$ , (4.19) becomes

$$4r'' + r - 3r^3 = 0. \quad (4.26)$$

For a stable solution it is expected that  $r$  remains positive for  $X > 0$  in which case

$$r \rightarrow \frac{1}{\sqrt{3}} \quad \text{as} \quad X \rightarrow \infty. \quad (4.27)$$

Letting  $s = r'$ , then  $r'' = s' = s \frac{ds}{dr}$ . Equation (4.26) becomes

$$4s \frac{ds}{dr} + r - 3r^3 = 0, \quad (4.28)$$

and integrating we get

$$4 \int s ds = \int (3r^3 - r) dr. \quad (4.29)$$

Thus

$$8(r')^2 = 3r^4 - 2r^2 + K, \quad (4.30)$$

where  $K$  is a constant. Using (4.27) and the condition  $r' \rightarrow 0$  as  $X \rightarrow \infty$  we get  $K = 1/3$  and equation (4.30) becomes

$$8(r')^2 = 3r^4 - 2r^2 + \frac{1}{3}. \quad (4.31)$$

Solving for  $r$  we get

$$r = \frac{1}{\sqrt{3}} \tanh \left[ \frac{X}{2\sqrt{2}} + K' \right], \quad (4.32)$$

where  $K'$  is an arbitrary constant. Using the condition  $r(0) = 0$  we get

$$r = \frac{1}{\sqrt{3}} \tanh \frac{X}{2\sqrt{2}}, \quad (4.33)$$

and thus

$$A_0 = e^{i\theta} \frac{1}{\sqrt{3}} \tanh \frac{X}{2\sqrt{2}}. \quad (4.34)$$

The solution for  $r$  is shown in Figure 4.2.

Consider the *second order* condition (4.18), which is an inhomogeneous equation for  $A_1$

$$4 \frac{d^2 A_1}{dX^2} + A_1 - 6A_1 |A_0|^2 - 3A_0^2 \bar{A}_1 = 4i \frac{d^3 A_0}{dX^3}. \quad (4.35)$$

Writing  $A_1 = e^{i\theta} (A_r + iA_i)$  and comparing real and imaginary parts we get

$$4A_r'' + A_r - 3A_r \tanh^2 \frac{X}{2\sqrt{2}} = 0, \quad (4.36)$$

$$4A_i'' + A_i - A_i \tanh^2 \frac{X}{2\sqrt{2}} = \frac{1}{2\sqrt{6}} \operatorname{sech}^2 \frac{X}{2\sqrt{2}} \left( 3 \tanh^2 \frac{X}{2\sqrt{2}} - 1 \right), \quad (4.37)$$

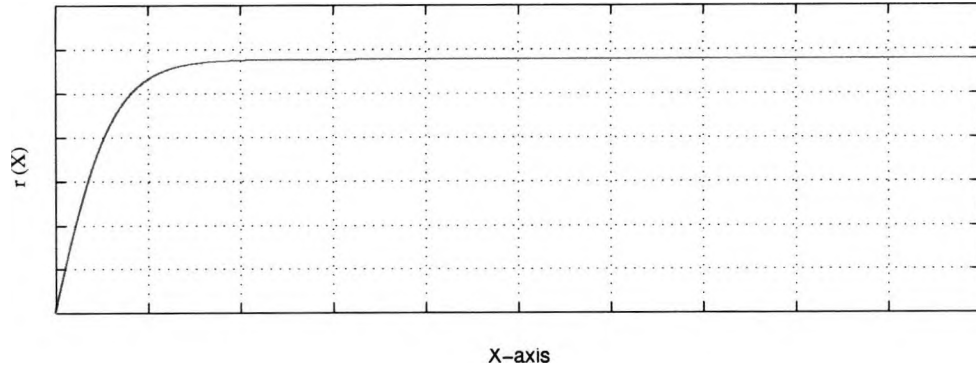


Figure 4.2: The solution for  $r$ .

from the real and imaginary parts respectively. The bounded solution of (4.36) is  $A_r = k_r \operatorname{sech}^2\left(\frac{X}{2\sqrt{2}}\right)$  where  $k_r$  is an arbitrary real constant. The other possible solution is exponentially large as  $X \rightarrow \infty$  and so we can ignore it. The general solution for  $A_i$  is

$$A_i(X) = \frac{1}{4\sqrt{6}} - \frac{3}{4\sqrt{6}} \tanh^2 \frac{X}{2\sqrt{2}} + k_i \tanh \frac{X}{2\sqrt{2}} + l \left( X \tanh \frac{X}{2\sqrt{2}} - 2\sqrt{2} \right), \quad (4.38)$$

where  $k_i$  and  $l$  are arbitrary real constants. This solution was checked using the symbolic mathematics package *MapleVR5* ([51], 1998). Then

$$A_1(X) = e^{i\theta} \left\{ k_r \operatorname{sech}^2 \frac{X}{2\sqrt{2}} + i \left[ \frac{1}{4\sqrt{6}} - \frac{3}{4\sqrt{6}} \tanh^2 \frac{X}{2\sqrt{2}} + k_i \tanh \frac{X}{2\sqrt{2}} + l \left( X \tanh \frac{X}{2\sqrt{2}} - 2\sqrt{2} \right) \right] \right\}. \quad (4.39)$$

As  $X \rightarrow \infty$ , the solution (4.5) develops into a periodic solution of uniform amplitude

$$u \sim \frac{\epsilon^{\frac{1}{2}}}{\sqrt{3}} e^{iqx+i\theta} + \text{c.c.} \quad (4.40)$$

For an infinite layer it was shown that solutions of more general amplitude

$$\frac{\epsilon^{\frac{1}{2}}}{\sqrt{3}} (1 - 4Q^2)^{\frac{1}{2}}, \quad (4.41)$$

exist for  $|Q| < 1/2$  with  $q = 1 + \epsilon^{1/2}Q$  but the relevant solutions here correspond to small values of  $Q$ , of order  $\epsilon^{1/2}$ . Indeed, since from (4.34) and (4.39) as  $X \rightarrow \infty$

$$u \sim \frac{\epsilon^{1/2}}{\sqrt{3}} e^{ix+i\theta} \left(1 + i\epsilon^{1/2}lX\sqrt{3}\right) + \text{c.c.}, \quad (4.42)$$

$$= \frac{\epsilon^{1/2}}{\sqrt{3}} e^{ix+i\theta} (1 + i\epsilon l x \sqrt{3}) + \text{c.c.}, \quad (4.43)$$

it is seen that matching with (4.40) requires that, correct to order  $\epsilon$ , the wavenumber  $q$  must be given by

$$q = 1 + \epsilon l \sqrt{3}. \quad (4.44)$$

A formal derivation of the solution (4.40) and (4.44) obtained by assuming a two-scale expansion with length scales  $x \sim 1$  and  $x \sim \epsilon^{-1}$  is given by Cross *et al* ([15], 1983) in their Appendix E. It is seen that the parameter  $l$  is equivalent to an order  $\epsilon$  correction to the critical wavenumber in the solution at large distances from the wall. An alternative procedure (Proctor (2000, [42])) is to incorporate the correction (4.44) to the wavenumber directly in the outer expansion (4.5) (and the inner expansion (4.45) below), in which case an outer expansion can be formulated which remains uniformly valid as  $X \rightarrow \infty$ .

Consider the solution in the *inner region* (see Figure 4.1). The outer solution, (4.5), breaks down on the scale  $x = O(1)$  where locally the solution has the form

$$u = \epsilon \bar{u}_0(x) + \dots, \quad \text{as } \epsilon \rightarrow 0. \quad (4.45)$$

Substitution into (4.45) shows that  $\bar{u}_0$  satisfies the equation

$$\frac{d^4 \bar{u}_0}{dx^4} + 2 \frac{d^2 \bar{u}_0}{dx^2} + \bar{u}_0 = 0. \quad (4.46)$$

The general solution is

$$\bar{u}_0 = (\varphi + \sigma x) e^{ix} + (\bar{\varphi} + \bar{\sigma} x) e^{-ix}, \quad (4.47)$$

where  $\varphi$  and  $\sigma$  are complex constants. We would like to match this solution as  $x \rightarrow \infty$  with the solution from the *outer region* as  $X \rightarrow 0$  (see Figure 4.1) where

$$u = \epsilon^{1/2} (A_0 e^{ix} + \bar{A}_0 e^{-ix}) + \epsilon (A_1 e^{ix} + \bar{A}_1 e^{-ix}) + \dots, \quad \epsilon \rightarrow 0. \quad (4.48)$$

Writing

$$A_0 \simeq A_0(0) + X A_0'(0) + \dots$$

and

$$A_1 \simeq A_1(0) + X A_1'(0) + \dots,$$

as  $X \rightarrow 0$  and comparing with equation (4.47) we get

$$0 = A_0(0), \quad \sigma = A_0'(0), \quad \varphi = A_1(0). \quad (4.49)$$

The first of these conditions has already been used in obtaining the outer solution. The other two give

$$\sigma = \frac{1}{2\sqrt{6}} e^{i\theta}, \quad (4.50)$$

$$\varphi = e^{i\theta} \left( k_r - \left[ 2\sqrt{2}l - \frac{1}{4\sqrt{6}} \right] i \right). \quad (4.51)$$

Consider the conditions at the no-slip wall. Applying these wall conditions to the solution (4.47) we get

$$u = 0 \quad \text{at} \quad x = 0 \Rightarrow \varphi + \bar{\varphi} = 0, \quad (4.52)$$

$$u_x = 0 \quad \text{at} \quad x = 0 \Rightarrow i\varphi + \sigma - i\bar{\varphi} + \bar{\sigma} = 0. \quad (4.53)$$

Writing

$$\varphi = \varphi_r + i\varphi_i \quad (4.54)$$

and

$$\sigma = \sigma_r + i\sigma_i \quad (4.55)$$

then the equation (4.52) implies  $\varphi_r = 0$ , equation (4.53) implies  $\sigma_r = \varphi_i$  and from equation (4.50),  $\sigma_r = \frac{1}{2\sqrt{6}} \cos \theta$  and  $\sigma_i = \frac{1}{2\sqrt{6}} \sin \theta$ . Thus equation (4.51) gives

$$\varphi_r = 0 = k_r \cos \theta - \left( \frac{1}{4\sqrt{6}} - 2\sqrt{2}l \right) \sin \theta, \quad (4.56)$$

$$\varphi_i = \frac{1}{2\sqrt{6}} \cos \theta = k_r \sin \theta + \left( \frac{1}{4\sqrt{6}} - 2\sqrt{2}l \right) \cos \theta. \quad (4.57)$$

Solving for  $l$  and  $k_r$  we get

$$l = -\frac{1}{16\sqrt{3}} \cos 2\theta, \quad (4.58)$$

$$k_r = \frac{1}{4\sqrt{6}} \sin 2\theta, \quad (4.59)$$

respectively. Thus this gives a range of solutions with  $|l| \leq \frac{1}{16\sqrt{3}}$ , i.e., the wavenumber restriction

$$1 - \frac{1}{16}\epsilon \leq q \leq 1 + \frac{1}{16}\epsilon. \quad (4.60)$$

Figure 4.3 shows this  $q$ -restriction as the region between the two red lines.

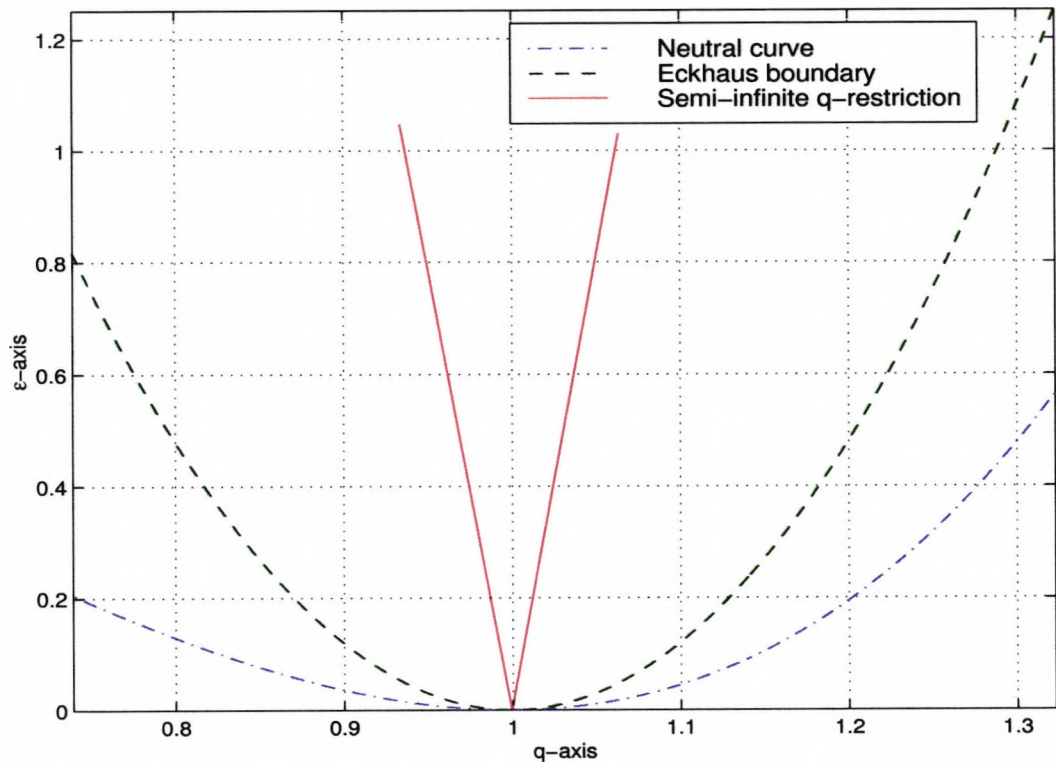


Figure 4.3: Plots of the wavenumber restriction, equation (4.60), together with the neutral curve and the Eckhaus boundary.

For a given wavenumber and its corresponding value of  $l$  there are two possible values of  $\theta$ , say

$$\theta = \theta_0, \quad (4.61)$$

$$\theta = \pi - \theta_0. \quad (4.62)$$

The solutions for  $k_r$  corresponding to (4.61) and (4.62) are

$$k_r = \frac{1}{4\sqrt{6}} \sin 2\theta_0, \quad (4.63)$$

$$k_r = -\frac{1}{4\sqrt{6}} \sin 2\theta_0, \quad (4.64)$$

respectively. These two solutions coalesce when  $\theta_0$  reaches  $\frac{\pi}{2}$  and  $l = \frac{1}{16\sqrt{3}}$ , and when  $\theta_0$  reaches 0 and  $l = -\frac{1}{16\sqrt{3}}$  at the other extreme (see Figure 4.4). In both limits  $k_r$  approaches zero. Next we identify the main features of the two solutions in order to facilitate a comparison with the numerical results for general  $\epsilon$  to be obtained in Section 4.4 below.

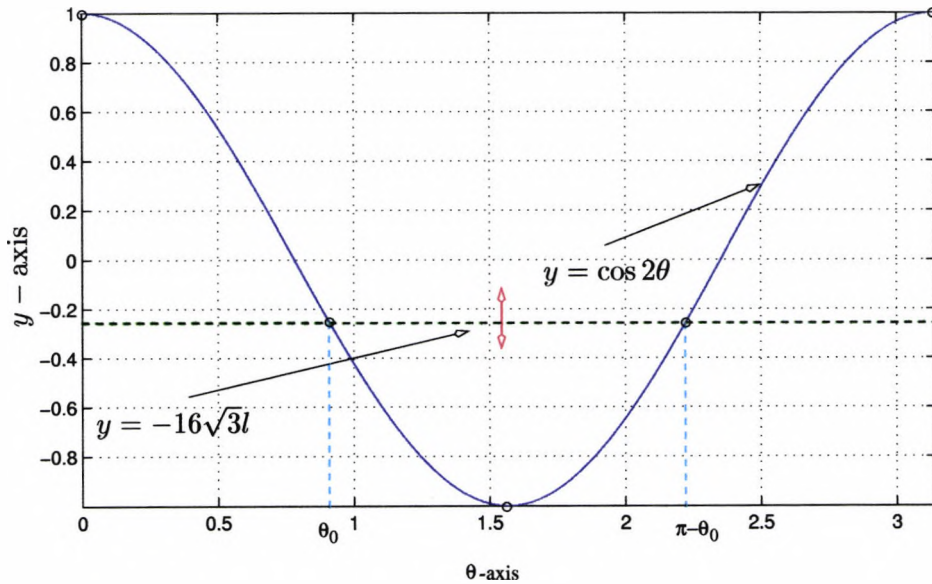


Figure 4.4: The figure shows the two possible values of  $\theta$  as the intersections of the blue and green lines. The red arrow indicates the possible positions that the green line can take.

First consider the inner solution and its derivatives

$$u(x) = \epsilon \{ (\varphi + \sigma x) e^{ix} + (\bar{\varphi} + \bar{\sigma} x) e^{-ix} \} + \dots, \quad (4.65)$$

$$u'(x) = \epsilon \{ [i(\varphi + \sigma x) + \sigma] e^{ix} + [-i(\bar{\varphi} + \bar{\sigma} x) + \bar{\sigma}] e^{-ix} \} + \dots, \quad (4.66)$$

$$u''(x) = \epsilon \{ [-(\varphi + \sigma x) + 2i\sigma] e^{ix} + [-(\bar{\varphi} + \bar{\sigma} x) - 2i\bar{\sigma}] e^{-ix} \} + \dots, \quad (4.67)$$

$$u'''(x) = \epsilon \{ [-i(\varphi + \sigma x) - 3\sigma] e^{ix} + [i(\bar{\varphi} + \bar{\sigma} x) - 3\bar{\sigma}] e^{-ix} \} + \dots. \quad (4.68)$$

At  $x = 0$  the wall conditions require that  $u = u' = 0$  but the second and third derivatives of  $u$  are non-zero. At  $x = 0$  we have

$$u'' = \epsilon \{-\varphi + 2i\sigma + (-\bar{\varphi} - 2i\bar{\sigma})\} + \dots, \quad (4.69)$$

and since  $\varphi + \bar{\varphi} = 0$  we have

$$u'' = -4\epsilon\sigma_i + \dots = -\frac{2}{\sqrt{6}}\epsilon \sin \theta + \dots, \quad \text{when } x = 0. \quad (4.70)$$

Similarly, at  $x = 0$  we have

$$u''' = \epsilon \{-i\varphi - 3\sigma + i\bar{\varphi} - 3\bar{\sigma}\} + \dots, \quad (4.71)$$

and since  $-i\varphi - \sigma + i\bar{\varphi} - \bar{\sigma} = 0$  we have

$$u''' = -4\epsilon\sigma_r + \dots = -\frac{2}{\sqrt{6}}\epsilon \cos \theta + \dots, \quad \text{when } x = 0. \quad (4.72)$$

Second, consider the behaviour as  $X \rightarrow \infty$  implied by the outer solution (4.48). Taking into account the decay of the tanh solution as  $X \rightarrow \infty$  and writing the solution in terms of the variable  $x$ , this gives

$$u \sim \frac{2\epsilon^{\frac{1}{2}}}{\sqrt{3}} \sin \left\{ \left(1 + \epsilon\sqrt{3}l\right) x + \theta + \frac{\pi}{2} + O(\epsilon^{\frac{1}{2}}) \right\} \left(1 - 2 \left[1 - \frac{\epsilon^{\frac{1}{2}}}{2\sqrt{2}} \sin 2\theta\right] e^{-\frac{\epsilon^{\frac{1}{2}}x}{\sqrt{2}}}\right), \quad (4.73)$$

as  $x \rightarrow \infty$ , and comparing with (4.4) we see that we may assume that the Floquet exponent and eigenfunction have the forms

$$c \sim \frac{\epsilon^{\frac{1}{2}}}{\sqrt{2}}, \quad P(x) \sim \left(\frac{3}{8\epsilon}\right)^{\frac{1}{2}} u_p(x), \quad \epsilon \rightarrow 0, \quad (4.74)$$

and that the phase shift  $\phi$  is given by

$$\phi \sim \theta + \frac{\pi}{2}, \quad \epsilon \rightarrow 0, \quad (4.75)$$

and the coefficient  $k$  is given by

$$k \sim -\frac{4\sqrt{2}}{\sqrt{3}}\epsilon^{\frac{1}{2}} \left(1 - \frac{\epsilon^{\frac{1}{2}}}{2\sqrt{2}} \sin 2\theta\right), \quad \epsilon \rightarrow 0. \quad (4.76)$$

Here, the normalisation of  $P(x)$  in (4.74) is chosen to be consistent with that defined in Section 3.2. For the two solution branches (4.61) and (4.62), the two values of  $k$  coalesce at  $-2$  when  $\theta_0 = 0$  ( $l = -\frac{1}{16\sqrt{3}}$ ) and when  $\theta_0 = \frac{\pi}{2}$  ( $l = \frac{1}{16\sqrt{3}}$ ). The phase shifts of the two solutions are  $\phi = \theta_0 + \frac{\pi}{2}$  and  $\phi = \frac{3\pi}{2} - \theta_0$  so that these differ by  $\pi$  at  $\theta_0 = 0$  and are equal at  $\theta_0 = \frac{\pi}{2}$ .

### 4.3 Approximate Theory for General $\epsilon$

In this section we consider an approximate method of incorporating the lateral wall by assuming the asymptotic form (4.4) is valid for all  $x \geq 0$ . In other words, we assume that the solution for  $u(x)$  is given by

$$u(x) = u_p(x + \phi) + kP(x + \phi)e^{-cx}, \quad (4.77)$$

for all  $x \geq 0$  where  $c$  and  $P$  are the Floquet exponent and eigenfunction. We now apply the wall conditions to this solution. At  $x = 0$  we have  $u(0) = 0$  which implies

$$u_p(\phi) + kP(\phi) = 0. \quad (4.78)$$

Also we have  $u'(0) = 0$  which implies that

$$u'_p(\phi) + k[P'(\phi) - cP(\phi)] = 0. \quad (4.79)$$

Eliminating the parameter  $k$  we get

$$F(\phi) \equiv u'_p(\phi)P(\phi) - u_p(\phi)[P'(\phi) - cP(\phi)] = 0. \quad (4.80)$$

Thus we look for the roots  $\phi$  of  $F$  and then use (4.78) to fix the corresponding values of  $k$ . Since  $u_p$ ,  $c$  and  $P$  are functions of  $\epsilon$  and  $\lambda$  ( $= 2L$ ), the existence of roots is dependent on the values of  $\epsilon$  and  $\lambda$ . Figure 4.5 shows the range of values of  $\lambda$  for which zeros of  $F$  exist when  $\epsilon = 0.1$ . Corresponding results for  $\epsilon = 0.5$  and  $\epsilon = 1.0$  are shown in Figures 4.6 and 4.7 respectively. The results are summarised in Figure 4.8 and are seen to be skewed to the left in the  $\epsilon, \lambda$  plane relative to the weakly nonlinear theory.

An alternative method was also used to compute the above solutions. Setting

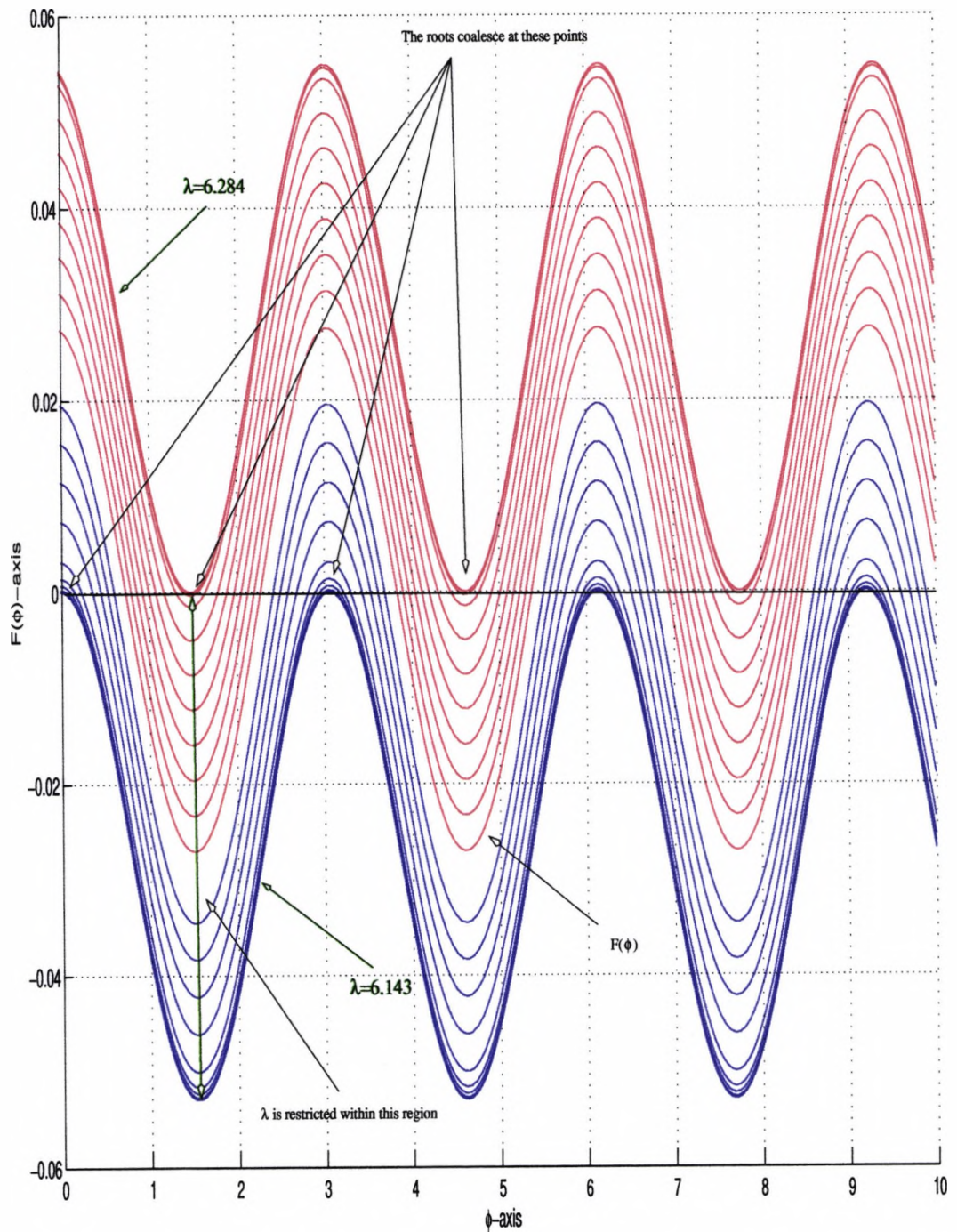


Figure 4.5: The red and blue lines are plots of  $F(\phi)$  for a fixed  $\epsilon = 0.1$  and different values of  $\lambda$ . Their positions in the  $(\lambda, \epsilon)$  space are represented respectively by the red and blue crosses in Figure 4.8.

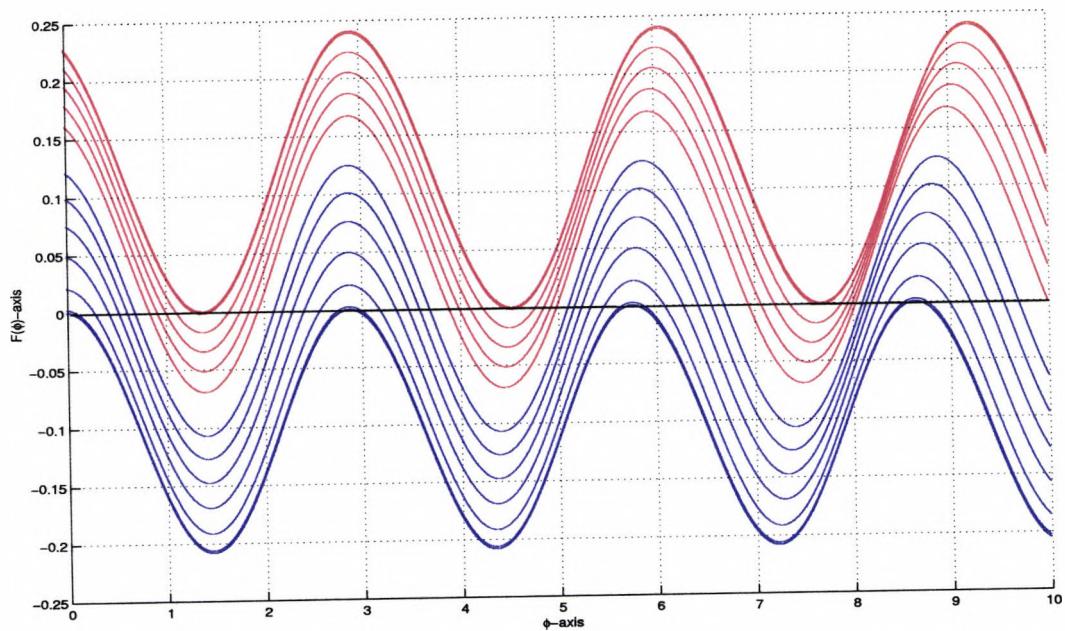


Figure 4.6: The red and blue lines are plots of  $F(\phi)$  for a fixed  $\epsilon = 0.5$  and different values of  $\lambda$ . Their positions in the  $(\lambda, \epsilon)$  space are represented respectively by the red and blue crosses in Figure 4.8.

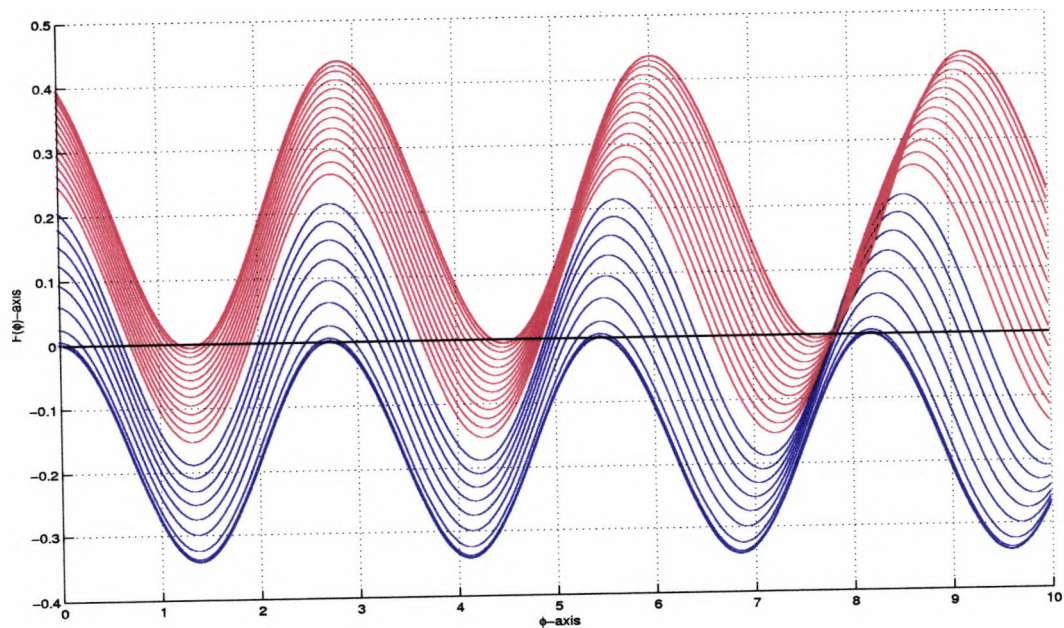


Figure 4.7: The red and blue lines are plots of  $F(\phi)$  for a fixed  $\epsilon = 1$  and different values of  $\lambda$ . Their positions in the  $(\lambda, \epsilon)$  space are represented respectively by the red and blue crosses in Figure 4.8.

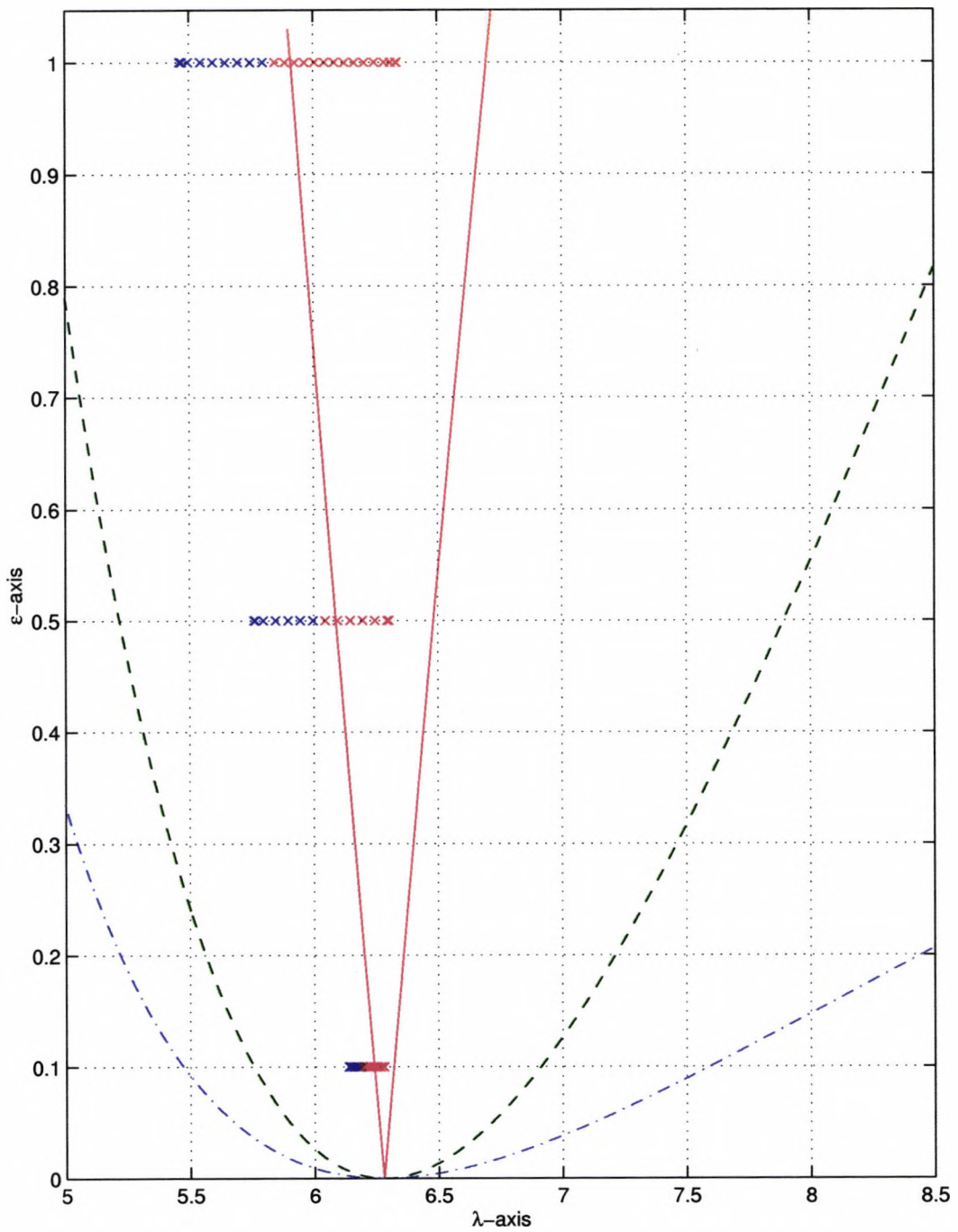


Figure 4.8: The blue and green curves are the marginal curve and the Eckhaus boundary respectively. The red lines represent the weakly-nonlinear result for the wavenumber restriction (from Section 4.2). The red and blue crosses are the solutions determined by the zeros of  $F$  in Figures 4.5–4.7.

$k = \bar{k}e^{-c\phi}$  in (4.77), then we have

$$u(x) = u_p(x + \phi) + \bar{k}P(x + \phi)e^{-c(x+\phi)}. \quad (4.81)$$

Using the substitution  $\bar{x} = x + \phi$  equation (4.81) becomes

$$u(x) = u_p(\bar{x}) + \bar{k}P(\bar{x})e^{-c\bar{x}}, \quad (4.82)$$

We are interested in solutions that have the periodic form  $u_p$  when  $\bar{x}$  is sufficiently large but as we approach the boundary of the semi-infinite domain we would like the solution to satisfy the no-slip boundary conditions. We shall assume that the no-slip boundary conditions are satisfied at some free boundary,  $\bar{x} = \bar{x}^*$  where  $\bar{x}^*$  is large and negative. Presumably this can be done for a suitable choice of  $\bar{k}$  which we shall denote as  $\bar{k}^*$ . We would like to calculate values of  $\bar{x}^*$  and  $\bar{k}^*$  in the parameter space  $(\lambda, \epsilon)$  such that if we define

$$\bar{u}(\bar{x}; \bar{k}) = u_p(\bar{x}) + \bar{k}P(\bar{x})e^{-c\bar{x}}, \quad (4.83)$$

then  $\bar{u}(\bar{x}^*; \bar{k}^*) = \bar{u}'(\bar{x}^*; \bar{k}^*) = 0$ . We used an iterative method to solve the free boundary problem. The method proceeds as follows.

Given an initial guess for  $\bar{k}$  which we shall denote as  $\bar{k}_0$  we define the point  $\bar{x}_0$  such that  $\bar{u}'(\bar{x}_0; \bar{k}_0) = 0$  at the  $m$ 'th maximum<sup>1</sup> measured from the point  $\bar{x} = 0$  (see Figure 4.9). We can iterate for  $\bar{k}_1$  by using

$$\bar{k}_n = -\frac{u_p(\bar{x}_{n-1})}{P(\bar{x}_{n-1})e^{-c\bar{x}_{n-1}}} \quad (4.84)$$

where  $n = 1$ . We repeat the process by choosing  $\bar{x}_1$  such that  $\bar{u}'(\bar{x}_1; \bar{k}_1) = 0$  at the  $m$ 'th maximum and iterate for  $\bar{k}_2$  using equation (4.84). We continue until the no-slip boundary condition at the free boundary is reached. We denote the final iterands as  $\bar{k}^*$  and  $\bar{x}^*$ . Once  $\bar{x}^*$  is known the phase shift  $\phi$  can be calculated from the relation  $\phi = \bar{x}^*$  and then  $k = \bar{k}^*e^{-c\phi}$ .

Figures 4.10–4.12 show the results of all possible solutions at the parameter values  $\epsilon = 0.1, 0.5, 1$ . The results agree with those of the previous method using  $F(\phi)$ . Both  $k$  and  $\phi \pmod{\lambda}$  are shown as a function of  $\lambda$ . At any given  $\epsilon$  the

<sup>1</sup>We need to choose  $m$  sufficiently large so that  $\bar{u}(\bar{x}; \bar{k})$  is sufficiently close to the periodic form  $u_p$  for  $\bar{x} = 0$ . Refer to Figure 4.9 where we have chosen  $m = 5$  and  $\bar{k}_0 = 0$

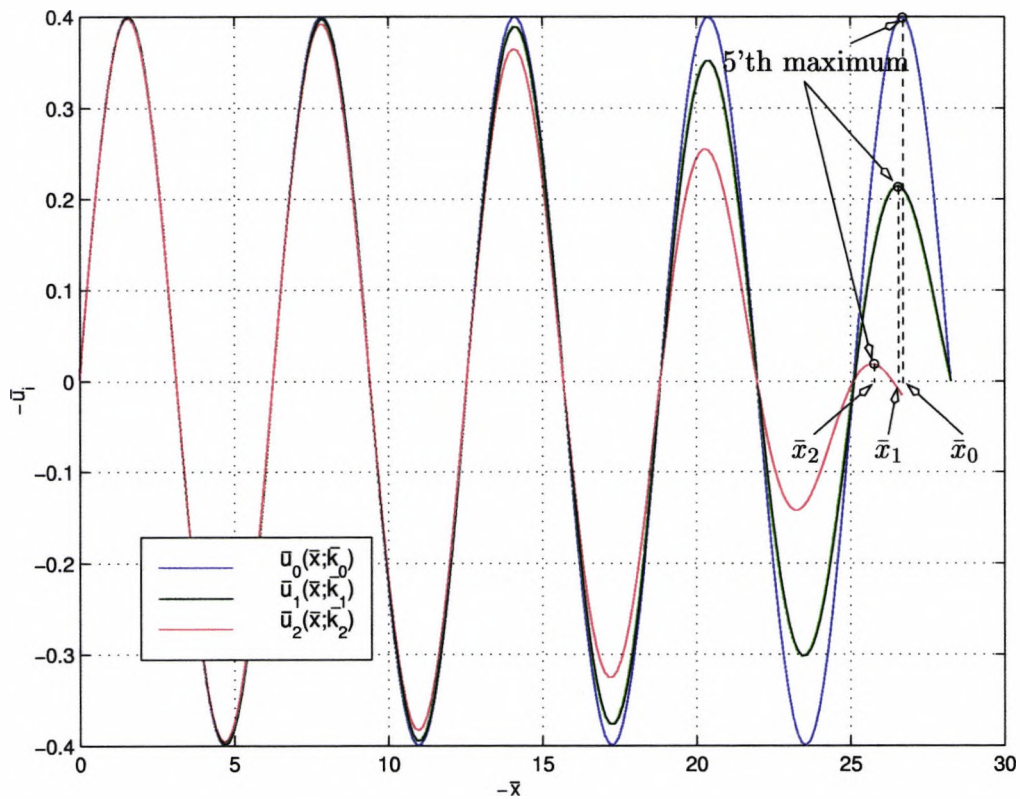


Figure 4.9: An example of an iterative scheme used for the evaluation of  $\bar{x}^*$  and  $\bar{k}^*$ , where  $m = 5$  and  $\bar{k}_0 = 0$ .

solutions are restricted to a specific range of  $\lambda$ , for example Figure 4.10 shows that the solutions are restricted to the range  $6.14 < \lambda < 6.28$ . Outside this range the solution is complex. The solutions appear as pairs which coalesce as the parameter  $\lambda$  reaches its limiting values. This is illustrated in Figures 4.10–4.12 by the upper-left plots showing the red and blue crosses merging<sup>2</sup>. The two lower diagrams show the profile of the solution, i.e.,  $u(x)$ . If we super-imposed the two lower diagrams we would see the two profiles coalesce at  $\lambda = 6.28$ . At  $\lambda = 6.14$  the lower-left profile is the negation of the lower-right profile.

Figure 4.13 shows the results of the restriction limit obtained from the iterative method for a larger set of values of  $\epsilon$  up to  $\epsilon = 1$ . The red lines are the weakly nonlinear results obtained from Section 4.2. The approximate method does not give good agreement with the weakly nonlinear theory, even at low values of  $\epsilon$ .

<sup>2</sup>The solutions from the iteration scheme can jump interchangeably between the two branches of solutions (the upper and lower curves of the top-left plots) when we are near the restriction limits. This is due to the inaccurate initial solution guess for our iterative scheme.

The derivation of (4.77) assumes the second term on the right-hand side is small compared to the first, so that the approximation is expected to be good only if the solution is close to its periodic form,  $u_p$ . By applying the no-slip boundary condition we diverge from this assumption and hence lose accuracy. We shall look at an accurate method that uses the fully nonlinear equation in the next section.

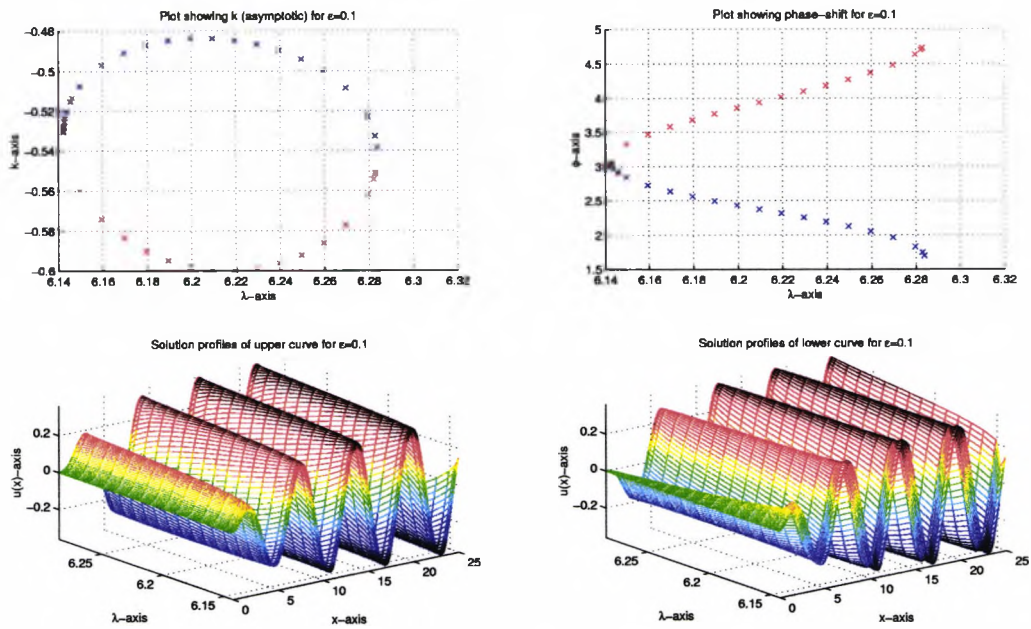


Figure 4.10: Results of the approximate method at  $\epsilon = 0.1$ .

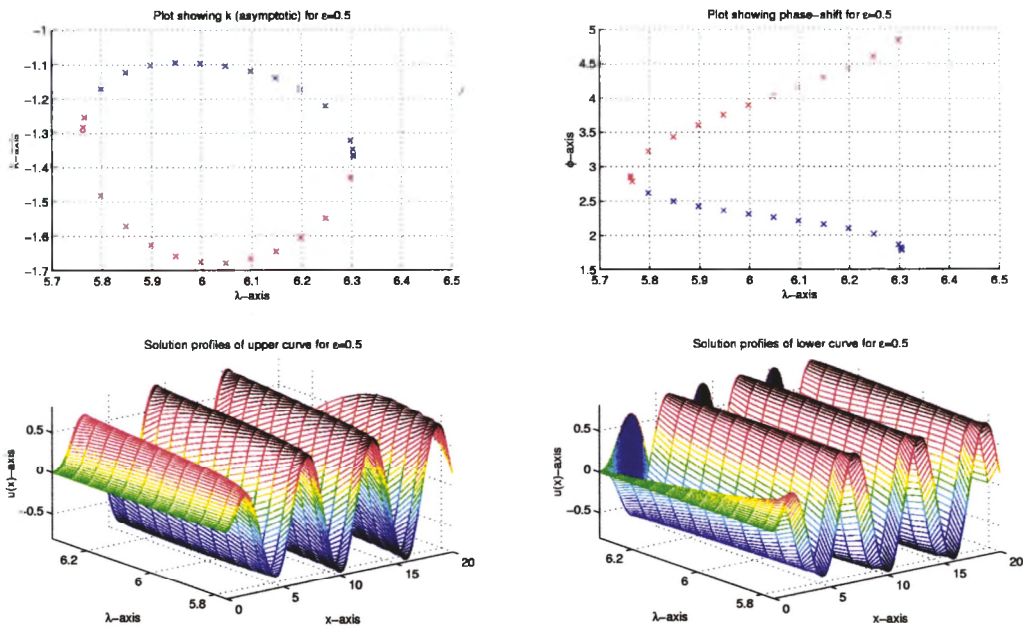


Figure 4.11: Results of the approximate method at  $\epsilon = 0.5$ .

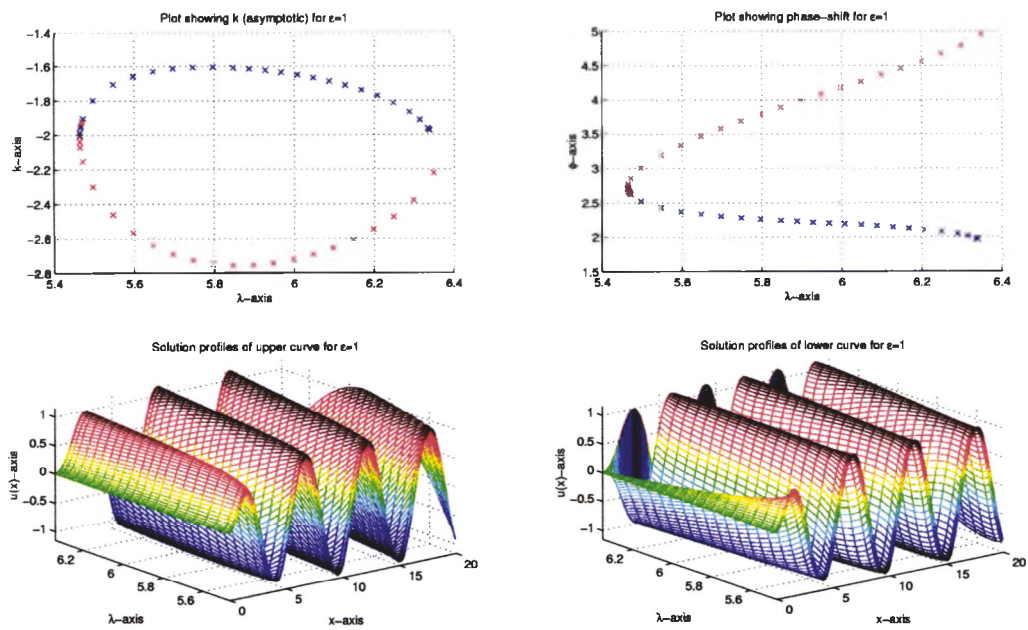


Figure 4.12: Results of the approximate method at  $\epsilon = 1$ .

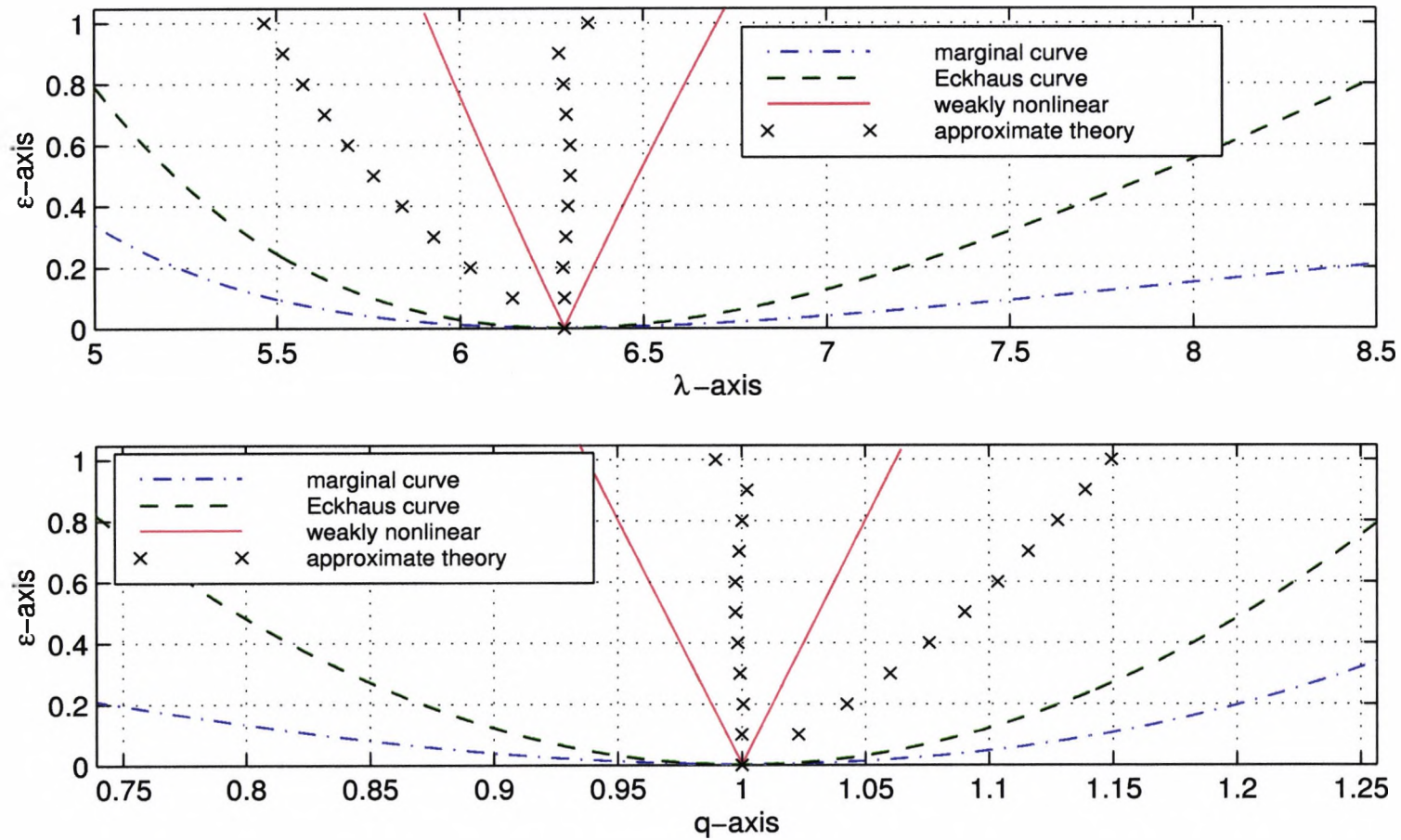


Figure 4.13: Plot comparing the approximate theory for the wavenumber restriction (crosses) with the weakly-nonlinear results (red line). The top graph shows the wavelength,  $\lambda$ , and the lower graph shows the wavenumber,  $q$ .

## 4.4 Nonlinear Theory for General $\epsilon$

We proceed as in the second method of Section 4.3 but instead of using the asymptotic form for all  $\bar{x}$  we solve the fully nonlinear SH equation for  $\bar{u}(\bar{x}) = u(x)$  where  $\bar{x} = x + \phi$ , namely,

$$\bar{u}'''' + 2\bar{u}'' + (1 - \epsilon)\bar{u} + \bar{u}^3 = 0. \quad (4.85)$$

We need to calculate values of  $\bar{x}^*$  and  $\bar{k}^*$  in the parameter space  $(\lambda, \epsilon)$  such that  $\bar{u}$  and its derivatives are given by the asymptotic formula

$$\bar{u} \sim u_p(\bar{x}) + \bar{k}P(\bar{x})e^{-c\bar{x}}, \quad (4.86)$$

at a suitably chosen value of  $\bar{x}$  (in practice this was taken as  $\bar{x} = 0$ ) and  $\bar{u}(\bar{x}^*) = \bar{u}'(\bar{x}^*) = 0$ . We use an iterative method to solve the free boundary problem. The method we used proceeds as follows.

Given an initial guess for  $\bar{k}$  which we shall denote as  $\bar{k}_0$  we first calculate the initial values  $\bar{u}(0)$ ,  $\bar{u}'(0)$ ,  $\bar{u}''(0)$  and  $\bar{u}'''(0)$  from (4.86). We use these initial values together with equation (4.85) to calculate  $\bar{u}(\bar{x})$ , defining the point  $\bar{x}_0$  such that  $\bar{u}'(\bar{x}_0) = 0$  at the  $m$ 'th maximum<sup>3</sup> (*cf.* Figure 4.9). We then repeat the calculation for a neighbouring value of  $\bar{k}$  and use a Newton iteration to define the next approximation  $\bar{k}_1$ . We then repeat the whole process, defining  $\bar{x}_1$  such that  $\bar{u}'(\bar{x}_1) = 0$  at the  $m$ 'th maximum, and so on, until the second no-slip boundary condition ( $\bar{u} = 0$ ) is satisfied at the free boundary. We denote the final iterands as  $\bar{k}^*$  and  $\bar{x}^*$ . Once  $\bar{x}^*$  is known, the phase shift  $\phi$  can be calculated from the relation  $\phi = \bar{x}^*$  and then  $k = \bar{k}^*e^{-c\phi}$ .

Figures 4.14–4.16 show the results of all possible solutions at the parameter values  $\epsilon = 0.1, 0.5, 1$ . Both  $k$  and  $\phi \pmod{\lambda}$  are shown as functions of  $\lambda$ . We can see in Figure 4.14 that the two solution branches (the lines of red and blue crosses) coalesce at  $\lambda = 6.245$  and  $\lambda = 6.325$  and are restricted to only a specific range of  $\lambda$ . Outside this range the solution becomes complex. The two lower diagrams from Figure 4.14 show the profile of the solution for  $6.245 < \lambda < 6.325$ . If we super-imposed the two lower diagrams we would see the two profiles coalesce at  $\lambda = 6.245$ . At  $\lambda = 6.325$  the lower-left profile is the negation of the lower-right

<sup>3</sup>We choose  $m$  sufficiently large so that  $u(\bar{x})$  is sufficiently close to the periodic form  $u_p$  for  $\bar{x} = 0$ . Checks were made with different values of  $m$  to test the validity of the results.

profile.

The weakly-nonlinear results are seen to agree really well with the nonlinear results for small values of  $\epsilon$ . The variation of  $k$  and  $\phi$  is consistent with the weakly nonlinear predictions (4.76) and (4.75) and the variation of  $u''(0)$  and  $u'''(0)$  (see Figures 4.17–4.19) is consistent with (4.70) and (4.72) as  $\epsilon \rightarrow 0$ . Figure 4.20 shows the results of the  $q$ -restriction for the range of values of  $\epsilon$  up to  $\epsilon = 1$ . The black crosses are the  $q$ -restriction limits for  $\epsilon \leq 1$  and the red lines are the weakly-nonlinear theory. As  $\epsilon$  increases, the allowed waveband is somewhat larger than that predicted by the weakly nonlinear theory.

## 4.5 Summary

Summarising what we have found in Chapter 4:

- We have determined solutions of the one-dimensional SH equation in a semi-infinite domain  $x \geq 0$  which approach a periodic form with wavenumber  $q = \pi/L$  as  $x \rightarrow \infty$  and satisfy the no-slip boundary conditions at  $x = 0$ .
- Solutions are restricted to a band of wavenumber  $q$  within the Eckhaus boundary which for small  $\epsilon$  is given by

$$1 - \frac{1}{16}\epsilon \leq q \leq 1 + \frac{1}{16}\epsilon,$$

and for larger  $\epsilon$  has been determined numerically.

- We have shown that within this band there are two solutions which coalesce at the limits of the restriction.
- We have found profiles of the solutions and determined how rapidly the periodic form is attained as  $x \rightarrow \infty$ . This length scale  $x$  is associated with the inverse of the Floquet exponent,  $c^{-1}$ , and is long ( $\sim \sqrt{2}\epsilon^{-\frac{1}{2}}$ ) as  $\epsilon \rightarrow 0$  but relatively short (just a few roll widths) for  $\epsilon \gtrsim 0.5$ .

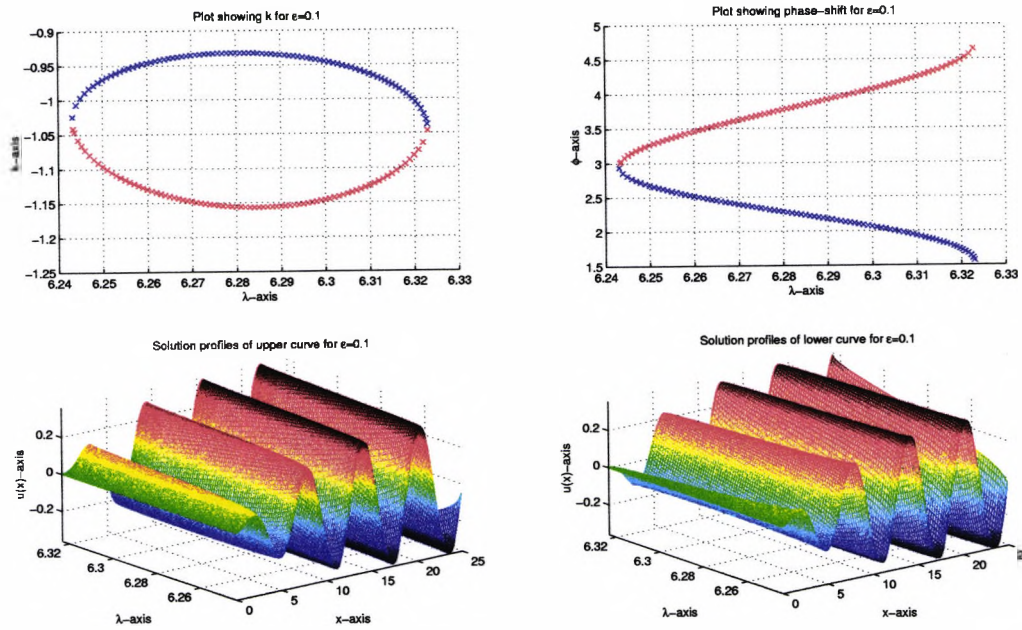


Figure 4.14: Results of the nonlinear method at  $\epsilon = 0.1$ .

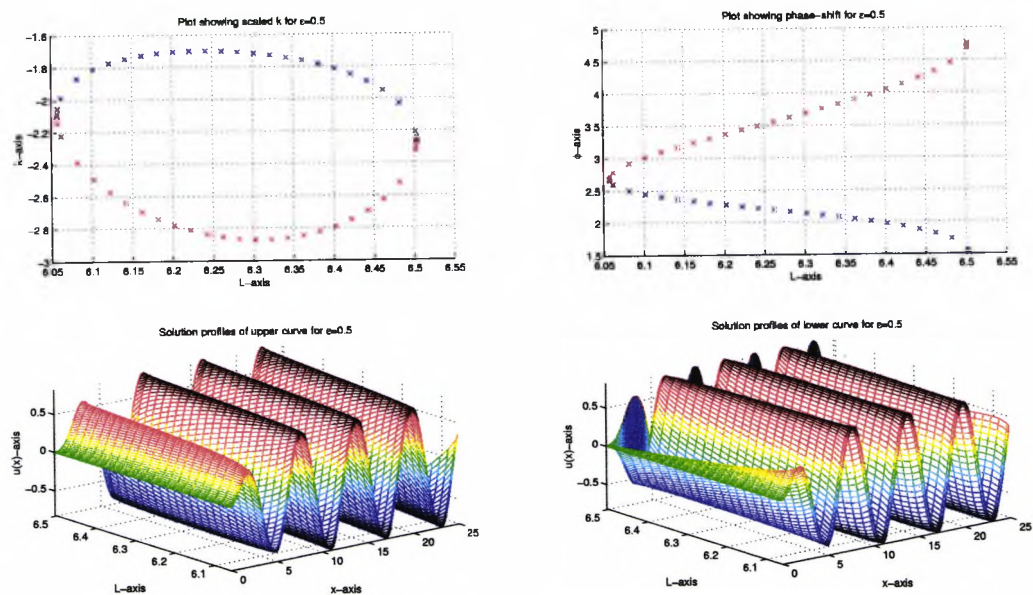


Figure 4.15: Results of the nonlinear method at  $\epsilon = 0.5$ .

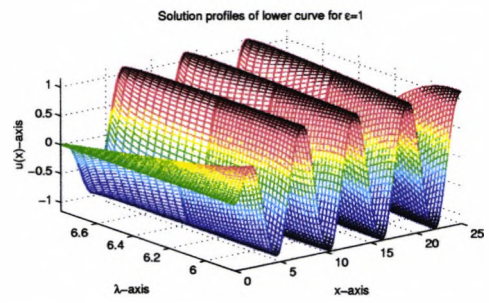
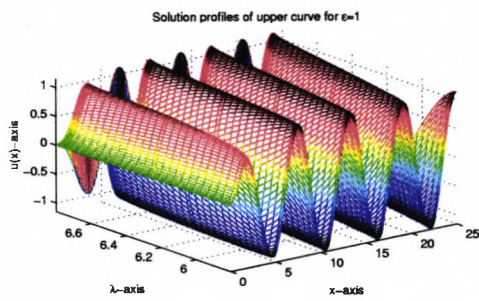
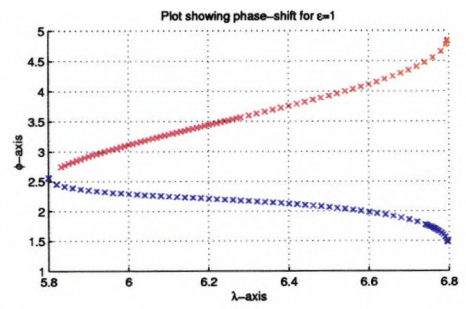
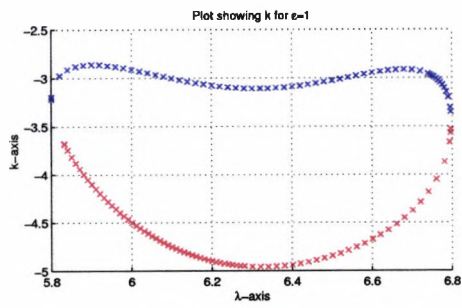


Figure 4.16: Results of the nonlinear method at  $\epsilon = 1$ .

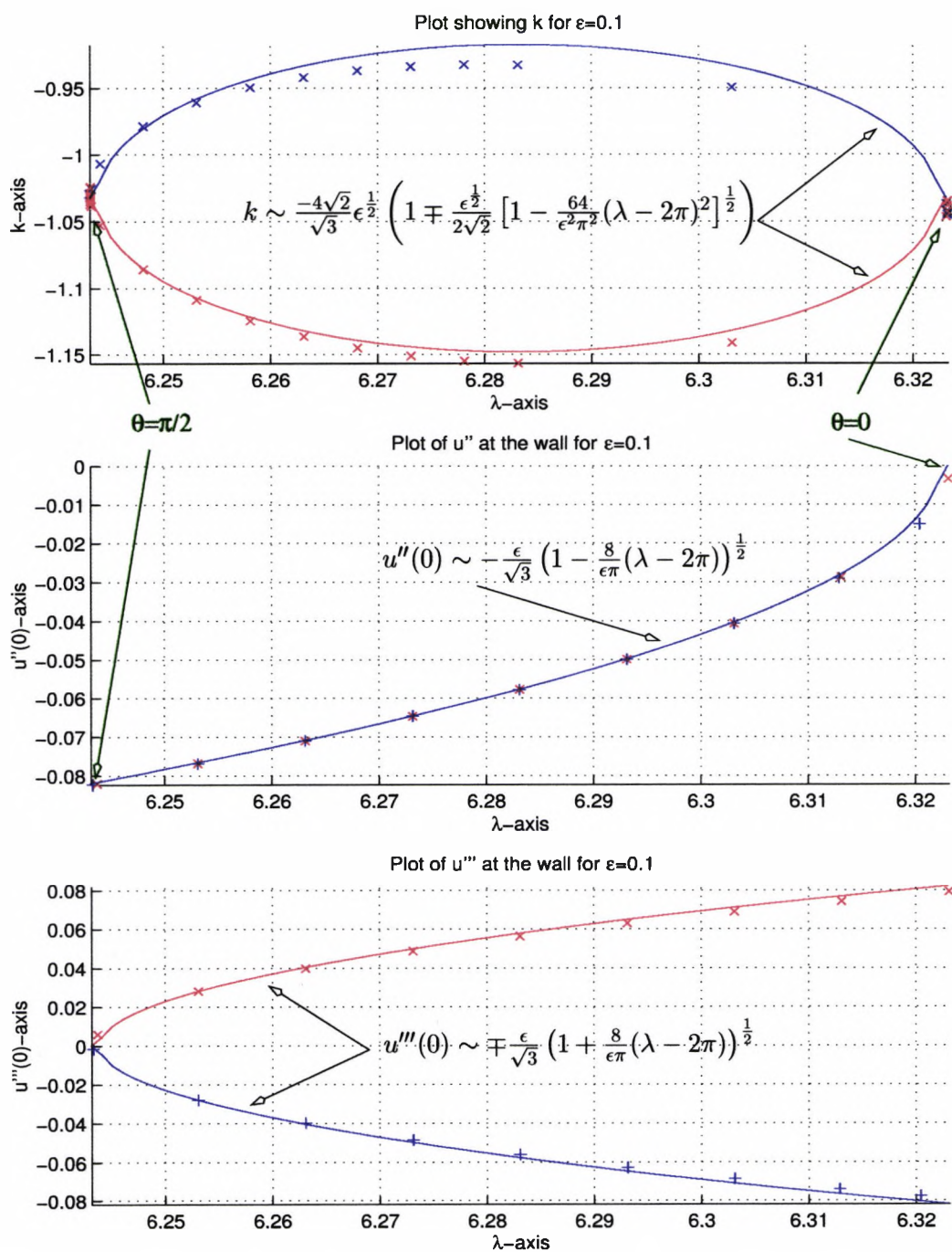


Figure 4.17: Plots comparing the results of the nonlinear method (crosses) and the weakly nonlinear approximation (lines) of  $k$ ,  $u''(0)$  and  $u'''(0)$  at  $\epsilon = 0.1$ . Notice that we have used  $\lambda = 2\pi/q$ , (4.44) and (4.58) to get an expression in  $\lambda$ .

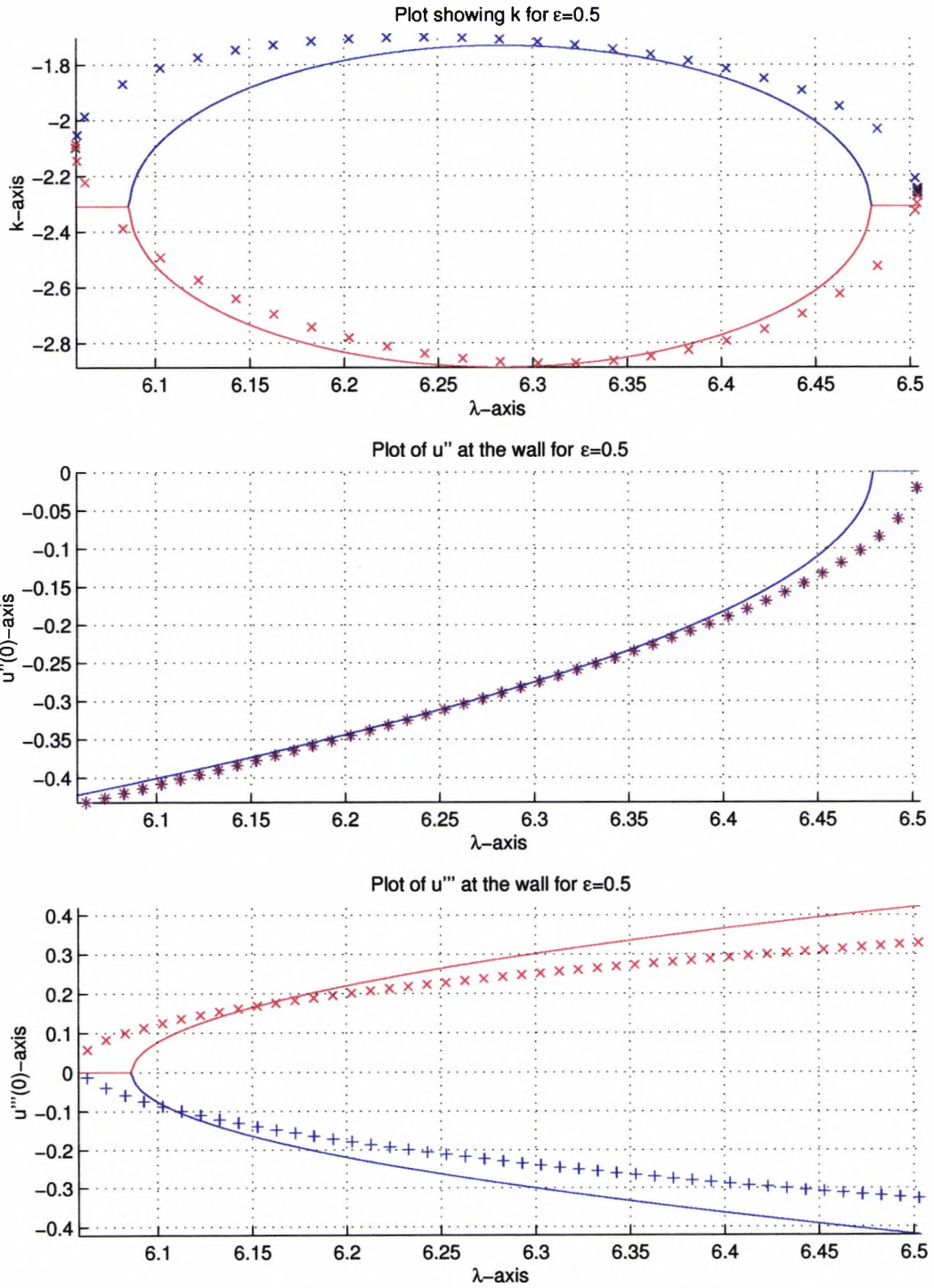


Figure 4.18: Plots comparing the results of the nonlinear method (crosses) and the weakly nonlinear approximation (lines) of  $k$ ,  $u''(0)$  and  $u'''(0)$  at  $\epsilon = 0.5$ .

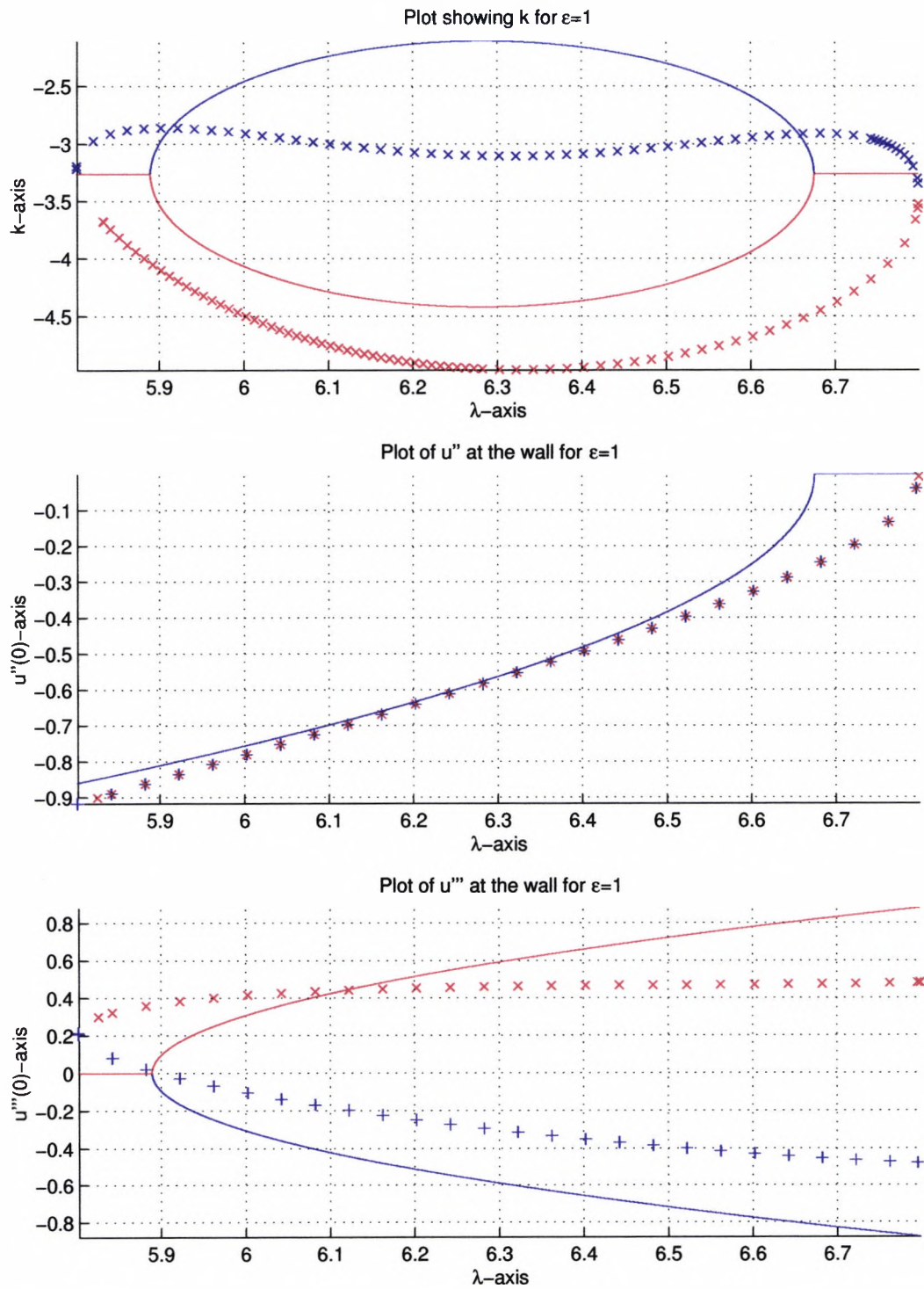


Figure 4.19: Plots comparing the results of the nonlinear method (crosses) and the weakly nonlinear approximation (lines) of  $k$ ,  $u''(0)$  and  $u'''(0)$  at  $\epsilon = 1$ .

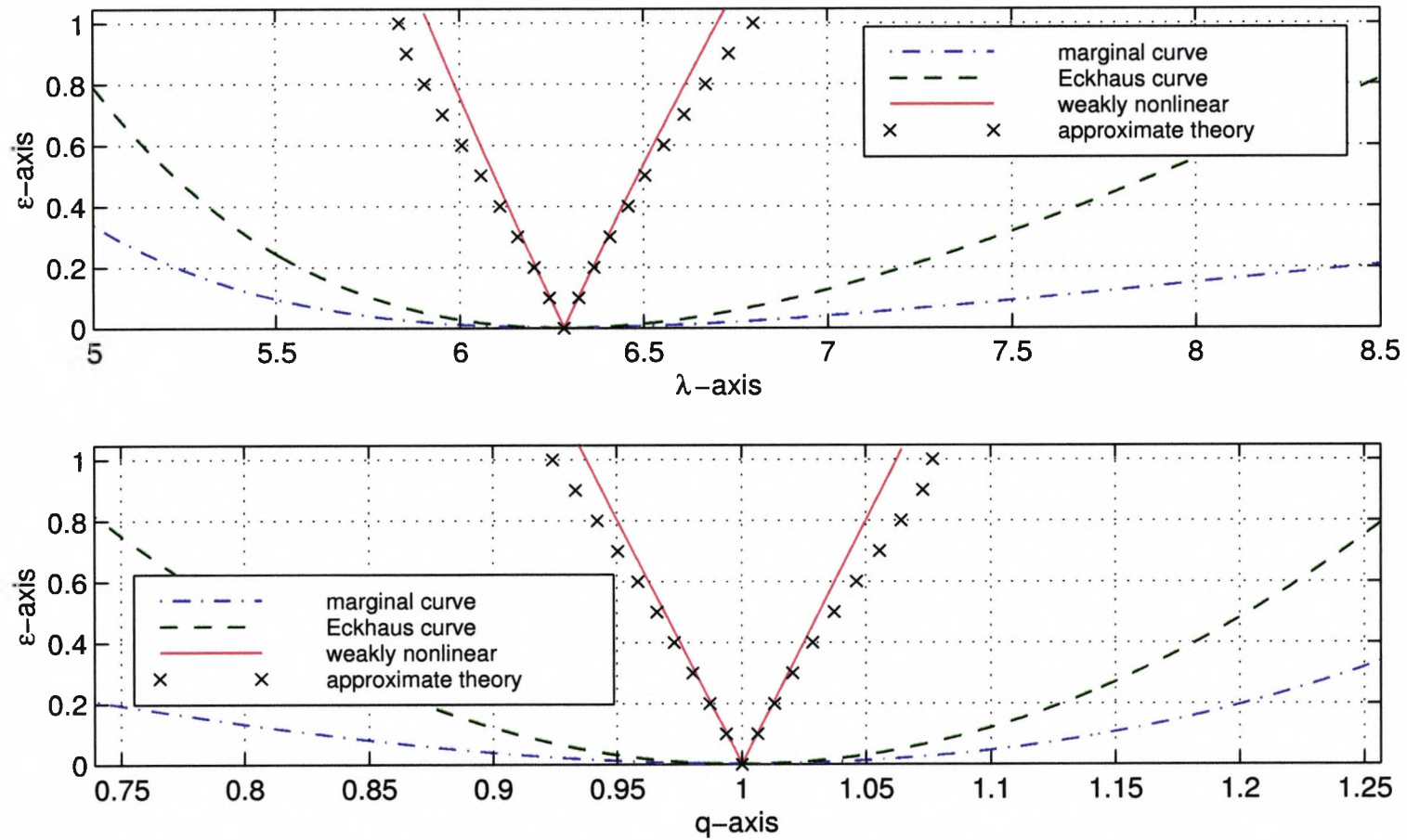


Figure 4.20: Plot comparing the nonlinear results for the wavenumber restriction (crosses) with the weakly-nonlinear result (red line). The top graph shows the wavelength,  $\lambda = 2L$ , and the lower graph shows the wavenumber,  $q$ .

# Chapter 5

## Solutions of the Two Dimensional Swift-Hohenberg Equation

### 5.1 Introduction

In this chapter we investigate the two dimensional Swift-Hohenberg equation. The equivalent physical system is the Rayleigh-Bénard problem in a channel with no-slip boundary conditions applied at the channel wall (Figure 5.1). We shall consider the two dimensional steady-state Swift-Hohenberg equation

$$(\nabla^2 + 1)^2 u - \epsilon u + u^3 = 0, \quad (5.1)$$

subject to the boundary conditions

$$u = \frac{\partial u}{\partial y} = 0, \quad \text{at } y = 0, L_y, \quad (5.2)$$

where  $u = u(x, y)$  and  $\nabla^2 = \frac{\partial^2}{\partial x^2} + \frac{\partial^2}{\partial y^2}$ . In Section 5.2 we investigate the linearised version of (5.1) and look for the existence of solutions periodic along the channel, which therefore take the form  $u(x, y) = e^{iqx}\bar{U}(y)$  (i.e., linear stability analysis of the trivial solution,  $u = 0$ ). Then in Section 5.3 we compute fully nonlinear solutions that are periodic along the channel. These are found using a Fourier decomposition in  $x$  and a finite difference representation in the  $y$  direction.

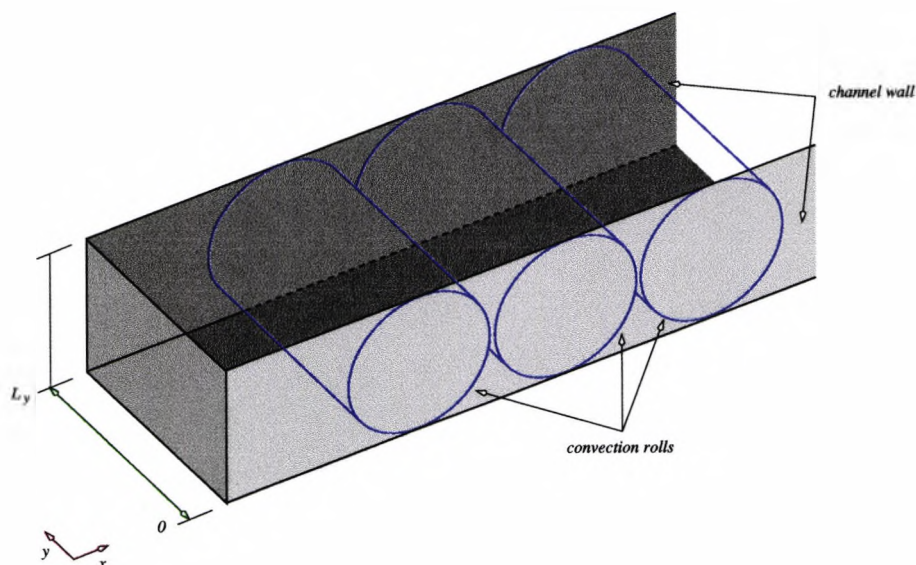


Figure 5.1: Diagram illustrating the geometry of the equivalent Rayleigh-Bénard problem.

## 5.2 Linear Analysis

Any infinitesimal perturbation from the trivial state is governed by the linearised form of the Swift-Hohenberg equation

$$(\nabla^2 + 1)^2 u - \epsilon u = 0, \quad (5.3)$$

where  $u = u(x, y)$  and  $\nabla^2 = \frac{\partial^2}{\partial x^2} + \frac{\partial^2}{\partial y^2}$ . This must be solved subject to the no-slip boundary conditions (5.2) at the channel wall (see Figure 5.1), i.e.,

$$u = \frac{\partial u}{\partial y} = 0, \quad \text{at } y = 0, L_y. \quad (5.4)$$

A complex solution for  $u$ , the real part of which will give the actual solution, is assumed to take the form

$$u(x, y) = e^{iqx} \bar{U}(y), \quad (5.5)$$

where  $q$  is the wavenumber in the  $x$ -direction. Substituting for  $u$  in (5.3) we get

$$\left( \frac{d^2}{dy^2} - q^2 + 1 \right)^2 \bar{U} - \epsilon \bar{U} = 0, \quad (5.6)$$

and from (5.4)

$$\bar{U} = \bar{U}' = 0, \quad \text{at } y = 0, L_y. \quad (5.7)$$

We simplify this system by reducing the number of parameters from three ( $L_y$ ,  $q$  and  $\epsilon$ ) to two ( $K$  and  $\bar{\epsilon}$ ) by the following transformations

$$y = L_y Y, \quad (5.8)$$

$$q^2 = 1 + \frac{K}{L_y^2}, \quad (5.9)$$

$$\bar{U}(y) = U(Y), \quad (5.10)$$

$$\epsilon = \frac{\bar{\epsilon}}{L_y^4}. \quad (5.11)$$

Then the system (5.3), (5.4) becomes

$$\left( \frac{d^2}{dY^2} - K \right)^2 U - \bar{\epsilon}U = 0, \quad (5.12)$$

$$U = U' = 0, \quad \text{at } Y = 0, 1, \quad (5.13)$$

and depends only on the modified wavenumber  $K$  and  $\bar{\epsilon}$ . Solving equation (5.12) we get

$$U(Y) = Ae^{\alpha Y} + Be^{\beta Y} + Ce^{-\alpha Y} + De^{-\beta Y}, \quad (5.14)$$

where

$$\alpha = \left( K + \bar{\epsilon}^{\frac{1}{2}} \right)^{\frac{1}{2}}, \quad (5.15)$$

$$\beta = \left( K - \bar{\epsilon}^{\frac{1}{2}} \right)^{\frac{1}{2}}, \quad (5.16)$$

and  $A$ ,  $B$ ,  $C$  and  $D$  are arbitrary constants. Using the no-slip conditions of equation (5.13), we obtain the condition for the existence of non-trivial solutions

$$\det(M) = 0 \quad (5.17)$$

where

$$M = \begin{bmatrix} 1 & 1 & 1 & 1 \\ \beta & \alpha & -\beta & -\alpha \\ e^{\beta} & e^{\alpha} & e^{-\beta} & e^{-\alpha} \\ \beta e^{\beta} & \alpha e^{\alpha} & -\beta e^{-\beta} & -\alpha e^{-\alpha} \end{bmatrix}. \quad (5.18)$$

Expanding (5.17) we obtain the equation that determines the existence of linearised solutions as

$$(-\alpha^2 - \beta^2 + 2\alpha\beta) \cosh(\alpha + \beta) + (\alpha^2 + \beta^2 + 2\alpha\beta) \cosh(\alpha - \beta) - 4\alpha\beta = 0. \quad (5.19)$$

Simplifying we get

$$-(\alpha^2 + \beta^2) \sinh \alpha \sinh \beta + 2\beta\alpha \cosh \alpha \cosh \beta - 2\beta\alpha = 0. \quad (5.20)$$

If we consider the nature of  $\alpha$  and  $\beta$  for different values of  $K$  and  $\bar{\epsilon}$ , there are four possible regions of the  $(K, \bar{\epsilon})$ -plane which are as follows.

1. When  $K = -\bar{\epsilon}^{\frac{1}{2}}$  we have  $\alpha = 0$ , i.e., an apparent solution but in fact the eigenfunction  $U$  is zero, except at certain discrete points.
2. When  $-\bar{\epsilon}^{\frac{1}{2}} < K < \bar{\epsilon}^{\frac{1}{2}}$ ,  $\alpha$  is real and  $\beta$  is imaginary, so we have two exponential and two oscillatory functions in (5.14).
3. When  $K < -\bar{\epsilon}^{\frac{1}{2}}$ ,  $\alpha$  and  $\beta$  are imaginary, so we have four oscillatory functions in (5.14).
4. When  $K > \bar{\epsilon}^{\frac{1}{2}}$ ,  $\alpha$  and  $\beta$  are real, so we have four exponential functions in (5.14).

As mentioned above, one solution of (5.20) is  $K = -\bar{\epsilon}^{\frac{1}{2}}$  which we shall refer to as the *1D-neutral-curve* locus since it is equivalent to the marginal curve for the one-dimensional case found in Section 2.3.1. However, in the present problem it only corresponds to a non-zero eigenfunction where it intersects other branches of solutions of (5.20). These other branches were found by using a numerical iterative scheme based on the Newton-Krylov method to trace the roots of (5.20). The first two solution branches are shown in Figure 5.2. The eigenfunctions associated with these two branches are even and odd about  $Y = \frac{1}{2}$  and so we shall refer to these as the *even-solution* and *odd-solution* respectively. The *even-solution* has the lowest  $\bar{\epsilon}$  and *inter-weaves* with the *odd-solution* as  $K$  decreases. The critical point corresponding to a solution with the lowest value of  $\bar{\epsilon}$  is at

$$K = K_c = -12.69043, \quad \bar{\epsilon} = \bar{\epsilon}_c = 343.7456. \quad (5.21)$$

Notice that in practice the minimum occurs at finite wavelengths only for sufficiently wide channels ( $L_y > 3.562$ ) with

$$q_c = \left(1 - \frac{12.69043}{L_y^2}\right)^{\frac{1}{2}}, \quad \epsilon_c = \frac{343.7456}{L_y^4}. \quad (5.22)$$

Figure 5.3 shows the solution branches scaled back to the  $(q, \epsilon)$ -plane for the case  $L_y = 2\pi$ . Figures 5.4 and 5.5 show the eigenfunction  $U(Y)$  to the right of the first intersection between the *even-solution* and *odd-solution* branches respectively. As we trace the curves left of the first intersection point the  $U(Y)$ -profile changes. For the even solution two further rolls start to develop at the channel wall which then grow and move inwards as we move further left of the first intersection (see Figure 5.6). More rolls develop in a similar way at further intersection points.

There are further solution loci above the calculated loci and they appear at much larger values of  $\bar{\epsilon}$  which are outside our region of interest (see Figure 5.7).

### 5.2.1 Even and Odd Solutions

We consider here briefly the decomposition of the solution into even and odd eigenfunctions. Writing equation (5.14) in symmetric form we get

$$U(Y) = \bar{A} \cosh \alpha \left(Y - \frac{1}{2}\right) + \bar{B} \sinh \alpha \left(Y - \frac{1}{2}\right) + \bar{C} \cosh \beta \left(Y - \frac{1}{2}\right) + \bar{D} \sinh \beta \left(Y - \frac{1}{2}\right), \quad (5.23)$$

where  $\bar{A}$ ,  $\bar{B}$ ,  $\bar{C}$  and  $\bar{D}$  are arbitrary constants.

Consider first the *even* form of (5.23) which we shall denote as  $U_e$ . Setting  $\bar{B} = \bar{D} = 0$  we have non-trivial solutions in the two cases:

$$U_e(Y) = \begin{cases} \bar{A} \cosh \alpha \left(Y - \frac{1}{2}\right) + \bar{C} \cos \bar{\beta} \left(Y - \frac{1}{2}\right), & \text{for } -\bar{\epsilon}^{\frac{1}{2}} < K < \bar{\epsilon}^{\frac{1}{2}}, \\ \bar{A} \cos \bar{\alpha} \left(Y - \frac{1}{2}\right) + \bar{C} \cos \bar{\beta} \left(Y - \frac{1}{2}\right), & \text{for } K < -\bar{\epsilon}^{\frac{1}{2}}, \end{cases} \quad (5.24)$$

where  $\alpha$  and  $\beta$  given by (5.15), (5.16) and  $\bar{\alpha} = \sqrt{-K - \bar{\epsilon}^{\frac{1}{2}}}$  and  $\bar{\beta} = \sqrt{-K + \bar{\epsilon}^{\frac{1}{2}}}$  are all real. Applying the no-slip conditions at  $Y = 1$ , i.e.,

$$U_e(1) = U_e'(1) = 0, \quad (5.25)$$

we get the condition for existence of solutions as

$$\det(M_e) = 0, \quad (5.26)$$

where  $M_e$  is real and is given by

$$M_e = \begin{cases} \begin{bmatrix} \cosh \frac{\alpha}{2} & \cos \frac{\bar{\beta}}{2} \\ \alpha \sinh \frac{\alpha}{2} & -\bar{\beta} \sin \frac{\bar{\beta}}{2} \end{bmatrix}, & \text{for } -\bar{\epsilon}^{\frac{1}{2}} < K < \bar{\epsilon}^{\frac{1}{2}}, \\ \begin{bmatrix} \cos \frac{\bar{\alpha}}{2} & \cos \frac{\bar{\beta}}{2} \\ -\bar{\alpha} \sin \frac{\bar{\alpha}}{2} & -\bar{\beta} \sin \frac{\bar{\beta}}{2} \end{bmatrix}, & \text{for } K < -\bar{\epsilon}^{\frac{1}{2}}. \end{cases} \quad (5.27)$$

Expanding (5.26) we obtain the equations for the existence of even solutions as

$$\left. \begin{aligned} -\bar{\beta} \cosh \frac{\alpha}{2} \sin \frac{\bar{\beta}}{2} - \alpha \sinh \frac{\alpha}{2} \cos \frac{\bar{\beta}}{2} &= 0, & \text{for } -\bar{\epsilon}^{\frac{1}{2}} < K < \bar{\epsilon}^{\frac{1}{2}}, \\ -\bar{\beta} \cos \frac{\bar{\alpha}}{2} \sin \frac{\bar{\beta}}{2} + \bar{\alpha} \sin \frac{\bar{\alpha}}{2} \cos \frac{\bar{\beta}}{2} &= 0, & \text{for } K < -\bar{\epsilon}^{\frac{1}{2}}. \end{aligned} \right\} \quad (5.28)$$

Note that the critical eigenfunction associated with (5.21) corresponds to a solution with the first of the two forms given in (5.24).

Similarly we can consider the *odd* form of (5.23) which we shall denote as  $U_o$ . Setting  $\bar{A} = \bar{C} = 0$  we again have non-trivial solutions in the two cases:

$$U_o(Y) = \begin{cases} \bar{B} \sinh \alpha (Y - \frac{1}{2}) + \bar{D} \sin \bar{\beta} (Y - \frac{1}{2}), & \text{for } -\bar{\epsilon}^{\frac{1}{2}} < K < \bar{\epsilon}^{\frac{1}{2}}, \\ \bar{B} \sin \bar{\alpha} (Y - \frac{1}{2}) + \bar{D} \sin \bar{\beta} (Y - \frac{1}{2}), & \text{for } K < -\bar{\epsilon}^{\frac{1}{2}}. \end{cases} \quad (5.29)$$

The equations for the existence of odd solutions are

$$\left. \begin{aligned} \bar{\beta} \sinh \frac{\alpha}{2} \cos \frac{\bar{\beta}}{2} - \alpha \cosh \frac{\alpha}{2} \sin \frac{\bar{\beta}}{2} &= 0, & \text{for } -\bar{\epsilon}^{\frac{1}{2}} < K < \bar{\epsilon}^{\frac{1}{2}}, \\ \bar{\beta} \sin \frac{\bar{\alpha}}{2} \cos \frac{\bar{\beta}}{2} - \bar{\alpha} \cos \frac{\bar{\alpha}}{2} \sin \frac{\bar{\beta}}{2} &= 0, & \text{for } K < -\bar{\epsilon}^{\frac{1}{2}}. \end{aligned} \right\} \quad (5.30)$$

Equations (5.30) and (5.28) are equivalent to (5.20). By inspection of equation (5.28) it is seen that intersections of the even branches with the *1D-neutral-curve* are at  $(K, \bar{\epsilon}) = (-2n^2\pi^2, 4n^4\pi^4)$  where  $n = 1, 2, \dots$  and

$$U(Y) = (-1)^n \bar{C} (\cos [2n\pi Y] - 1).$$

Similarly, intersections of the odd branches with the *1D-neutral-curve* occur at the roots of  $\tan \frac{\bar{\beta}}{2} = \frac{\bar{\beta}}{2}$ . Four of these intersections are shown in Figure 5.7.

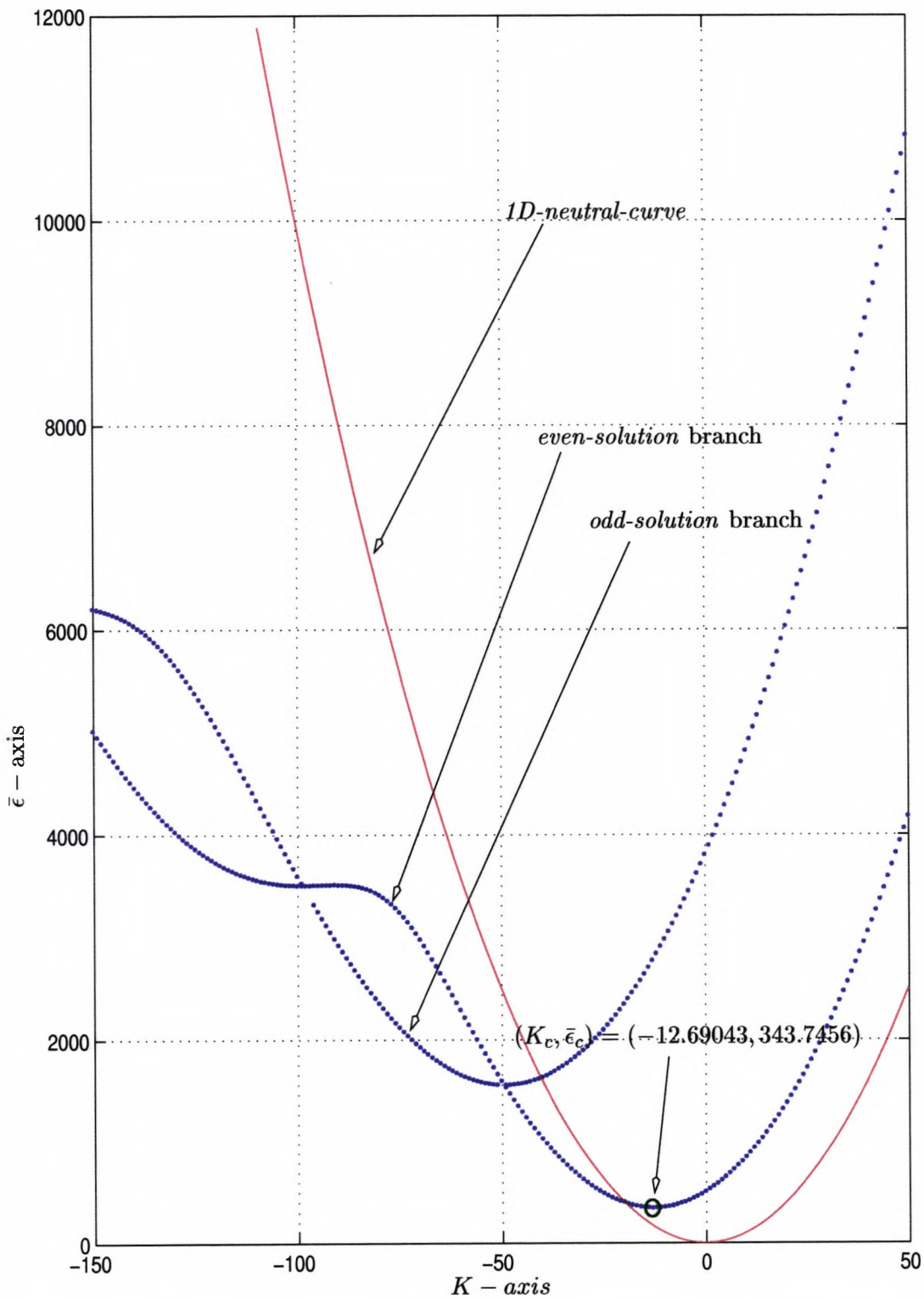


Figure 5.2: The lowest even and odd solution branches. The critical point,  $(K_c, \bar{\epsilon}_c)$ , is also shown, along with the locus of the 1D-neutral-curve (red curve).

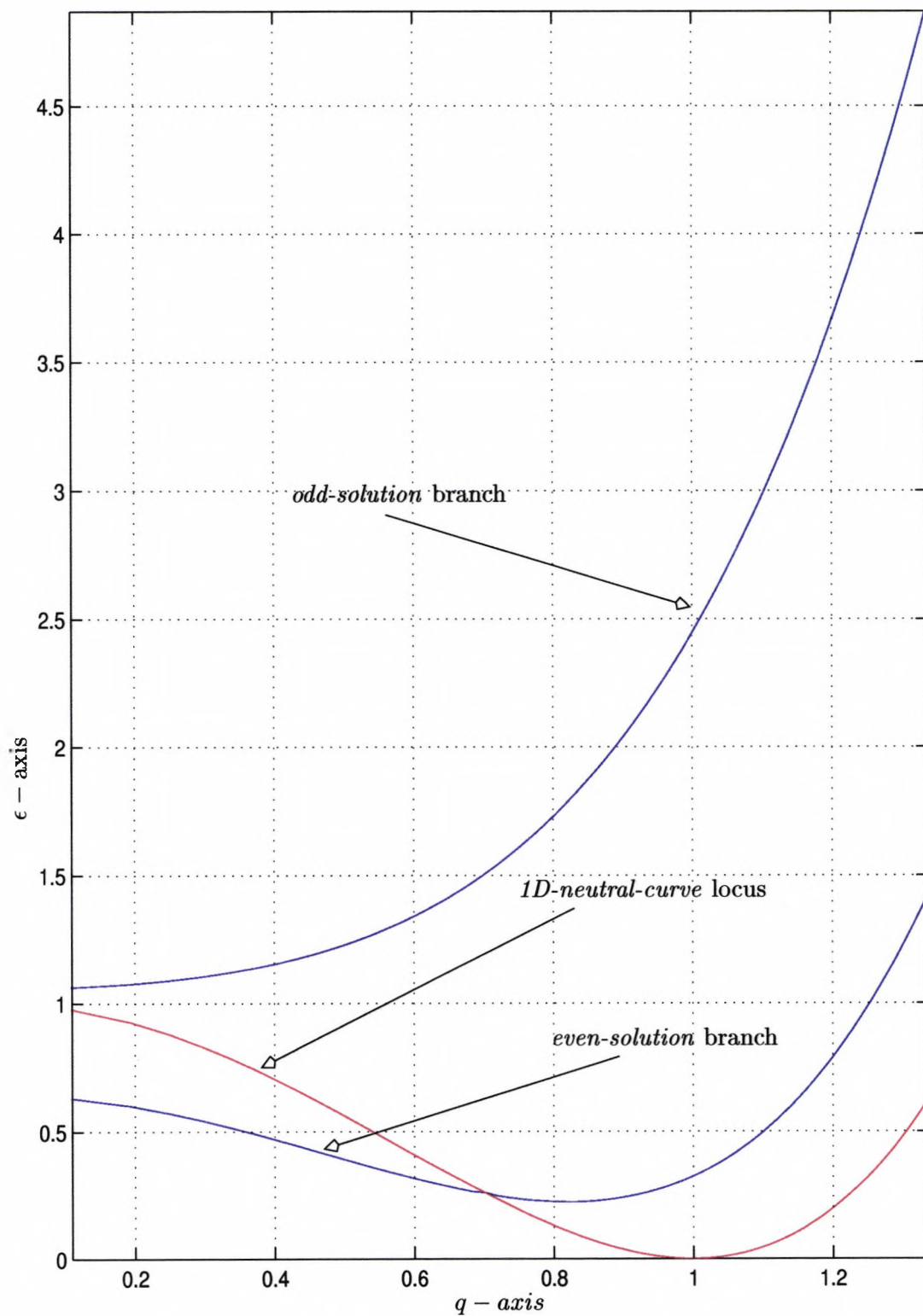


Figure 5.3: The two lowest solution branches scaled back to the  $(q, \epsilon)$ -parameter space for the case  $L_y = 2\pi$ . The critical point corresponds to  $(q_c, \epsilon_c) = (0.82374, 0.22056)$  in this case, and the  $1D$ -neutral-curve is also shown (red curve).

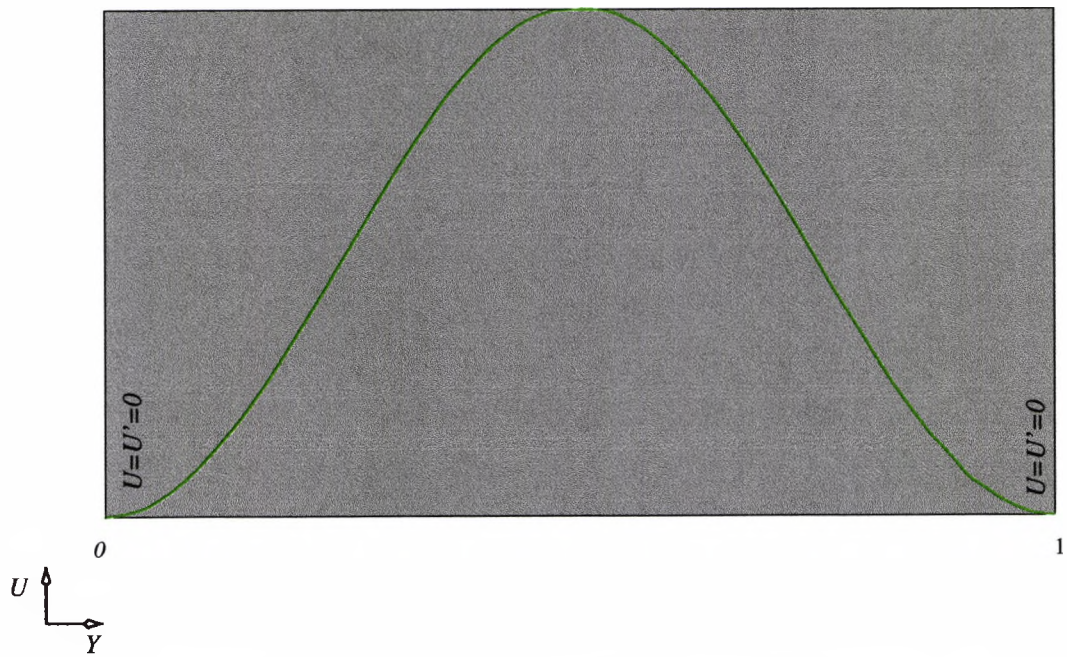


Figure 5.4: Profile of  $U(Y)$  in the lower region of the *even-solution* branch.

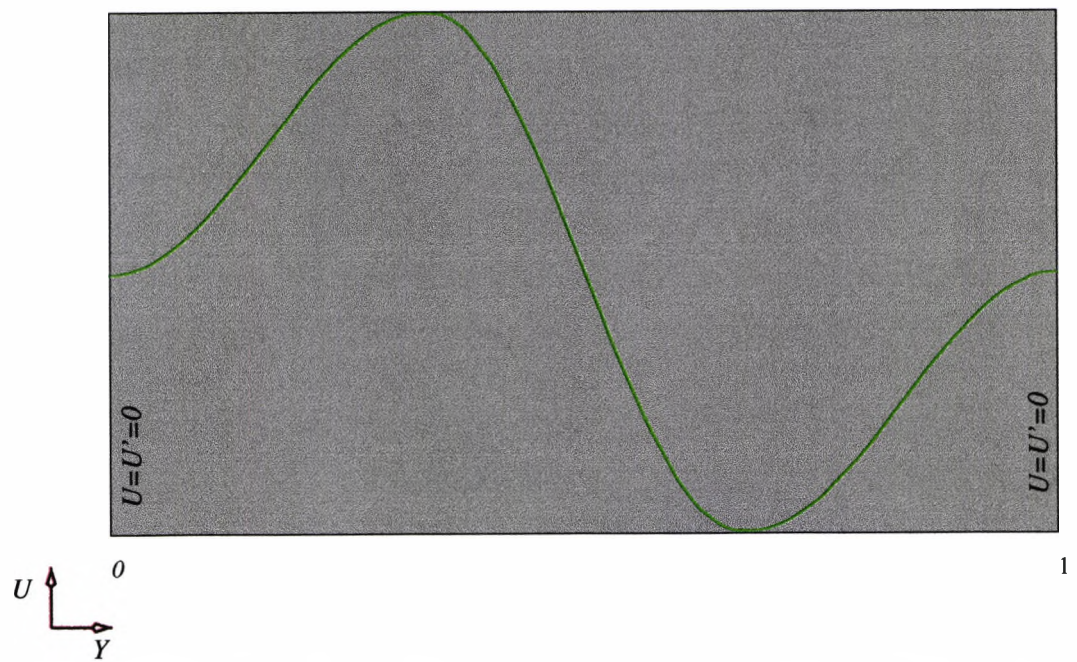


Figure 5.5: Profile of  $U(Y)$  in the lower region of the *odd-solution* branch.

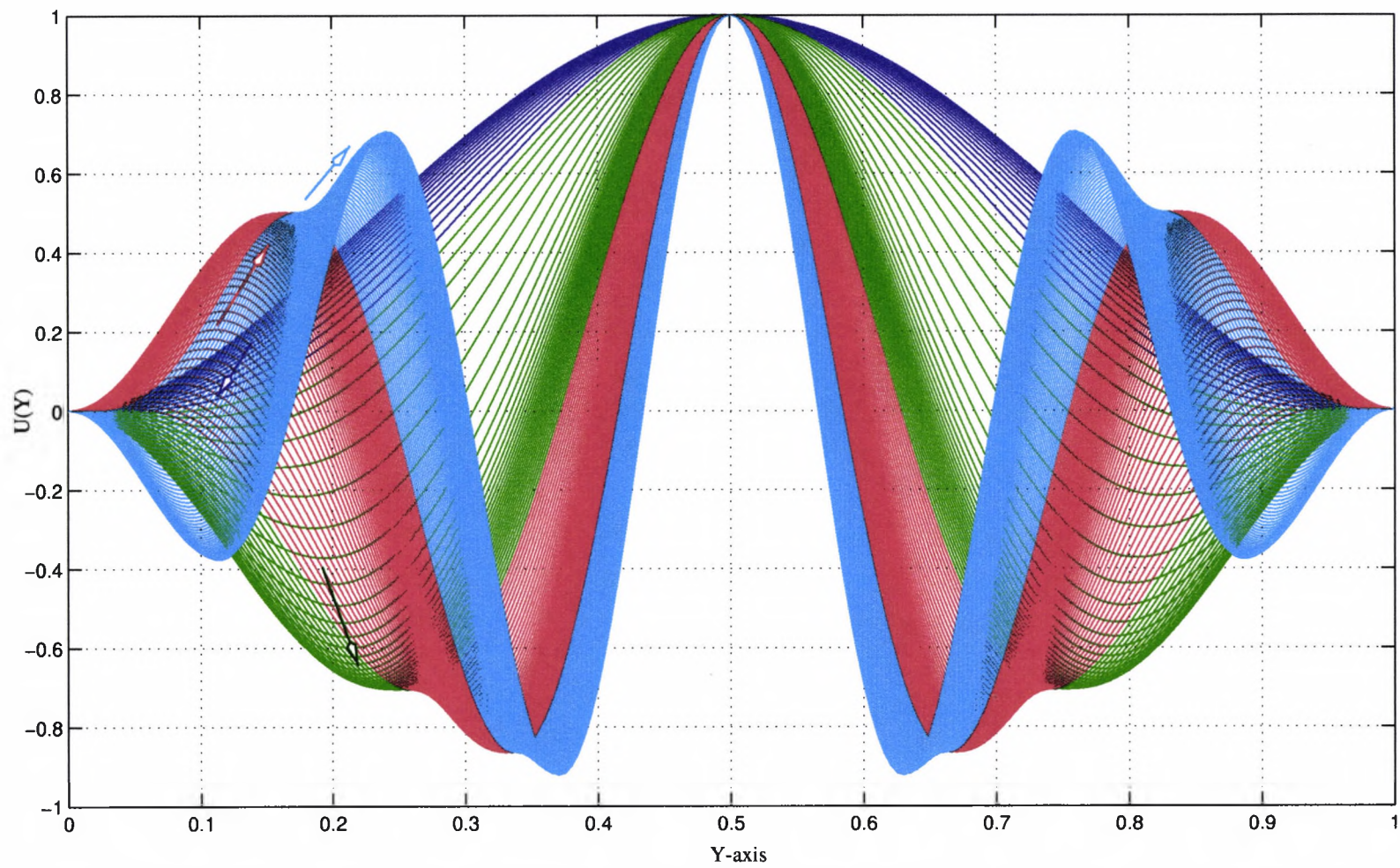


Figure 5.6: Profile of  $U(Y)$  showing rolls developing at the channel wall which then grow in amplitude and move inwards as we decrease  $K$ .

### 5.3 Two Dimensional Periodic Solutions

Now consider the fully nonlinear Swift-Hohenberg equation

$$(\nabla^2 + 1)^2 u - \epsilon u = -u^3, \quad (5.31)$$

where  $u = u(x, y)$  and  $\nabla^2 = \frac{\partial^2}{\partial x^2} + \frac{\partial^2}{\partial y^2}$ . We consider no-slip boundary conditions at the channel wall (see Figure 5.8) and periodic conditions in the  $x$  direction, that is

$$u = u_y = 0, \quad \text{at } y = 0, L_y, \quad (5.32)$$

$$u = u_{xx} = 0, \quad \text{at } x = 0, L. \quad (5.33)$$

We search for solutions that have the form

$$u_p(x, y) = \sum_{j=1}^N a_j(y) \sin jqx, \quad (5.34)$$

where  $q = \pi/L$  is the wavenumber in the  $x$  direction. The value of  $N$  is infinite in general, but in practice solutions can be found by truncating the infinite series. Note that (5.34) excludes the possibility of rolls with axes parallel to the  $x$ -axis, equivalently to  $q = 0$ , but the linear theory indicates that in general these are not significant until relatively high values of  $\epsilon$  which for a given value of  $L_y$  can be determined by setting  $K = -L_y^2$  in Figure 5.2.

In the one-dimensional problem we used a shooting method to determine periodic solutions, but a similar method proves difficult to implement in the two-dimensional case; for example, a Galerkin representation in the variable  $y$  results in individual modes at the higher end of the spectrum which, if the nonlinearity is weak, have rapid exponential growth in the  $x$  direction, leading to numerical instability in the coupled set of equations. Instead we consider a finite difference method. Substituting (5.34) into (5.31) we get

$$\sum_{j=1}^N \left[ \frac{d^4 a_j}{dy^4} + 2(1 - j^2 q^2) \frac{d^2 a_j}{dy^2} + (j^4 q^4 - 2j^2 q^2 + 1 - \epsilon) a_j \right] \sin jqx = - \left[ \sum_{j=1}^N a_j \sin jqx \right]^3, \quad (5.35)$$

subject to the boundary conditions

$$a_j(0) = a'_j(0) = a_j(L_y) = a'_j(L_y) = 0, \quad \text{for } j = 1, \dots, N. \quad (5.36)$$

When the truncation level is taken as  $N = 1$  we have the ordinary differential equation

$$\begin{aligned} & \left[ \frac{d^4 a_1}{dy^4} + (2 - 2q^2) \frac{d^2 a_1}{dy^2} + (q^4 - 2q^2 + 1 - \epsilon) a_1 \right] \sin qx \\ & = - (a_1 \sin qx)^3 = - \frac{a_1^3}{4} (3 \sin qx - \sin 3qx). \end{aligned} \quad (5.37)$$

Comparing coefficients of  $\sin qx$  we get

$$\mathcal{L}_1 a_1 = -b_1 \quad (5.38)$$

where

$$\mathcal{L}_1 = \frac{d^4}{dy^4} + 2(1 - q^2) \frac{d^2}{dy^2} + (q^4 - 2q^2 + 1 - \epsilon),$$

and

$$b_1 = \frac{3a_1^3}{4}.$$

To solve equation (5.38) we use finite difference approximations. First we introduce a finite set of grid points  $y_r = rh$ , for  $r = 0, 1, \dots, M$ , where  $M \in \mathbb{N}$  and  $h = L_y/M$ . We can write (5.38) as

$$\begin{bmatrix} \frac{da_{1,0}}{dy} \\ \left( \frac{d^4}{dy^4} + 2(1 - q^2) \frac{d^2}{dy^2} + (q^4 - 2q^2 + 1 - \epsilon) \right) a_{1,0} \\ \left( \frac{d^4}{dy^4} + 2(1 - q^2) \frac{d^2}{dy^2} + (q^4 - 2q^2 + 1 - \epsilon) \right) a_{1,1} \\ \left( \frac{d^4}{dy^4} + 2(1 - q^2) \frac{d^2}{dy^2} + (q^4 - 2q^2 + 1 - \epsilon) \right) a_{1,2} \\ \dots \dots \dots \\ \left( \frac{d^4}{dy^4} + 2(1 - q^2) \frac{d^2}{dy^2} + (q^4 - 2q^2 + 1 - \epsilon) \right) a_{1,M-2} \\ \left( \frac{d^4}{dy^4} + 2(1 - q^2) \frac{d^2}{dy^2} + (q^4 - 2q^2 + 1 - \epsilon) \right) a_{1,M-1} \\ \left( \frac{d^4}{dy^4} + 2(1 - q^2) \frac{d^2}{dy^2} + (q^4 - 2q^2 + 1 - \epsilon) \right) a_{1,M} \\ \frac{da_{1,M}}{dy} \end{bmatrix} = -\frac{3}{4} \begin{bmatrix} 0 \\ 0 \\ a_{1,1}^3 \\ a_{1,2}^3 \\ \dots \\ a_{1,M-2}^3 \\ a_{1,M-1}^3 \\ 0 \\ 0 \end{bmatrix}, \quad (5.39)$$



where

$$\underline{a}_1 = [a_{1,-2}, a_{1,-1}, a_{1,1}, a_{1,2}, \dots, a_{1,M-2}, a_{1,M-1}, a_{1,M+1}, a_{1,M+2}]^T$$

and

$$\underline{b} = \frac{3}{4}[0, 0, a_{1,1}^3, a_{1,2}^3, \dots, a_{1,M-1}^3, a_{1,M+1}^3, 0, 0]^T.$$

Given a sufficiently close initial guess the nonlinear system (5.43) can be efficiently solved using the numerical Newton-Krylov iterative scheme.

When  $N > 1$  the problem (5.35) and (5.36) becomes a coupled system of ordinary differential equations. For example, when  $N = 2$  we have

$$\mathcal{L} \mathbf{a} = -\mathbf{b} \quad (5.44)$$

where

$$\mathcal{L} = \begin{bmatrix} \mathcal{L}_1 & 0 \\ 0 & \mathcal{L}_2 \end{bmatrix}, \quad (5.45)$$

$$\mathcal{L}_1 = \frac{d^4}{dy^4} + 2(1 - q^2) \frac{d^2}{dy^2} + (q^4 - 2q^2 + 1 - \epsilon), \quad (5.46)$$

$$\mathcal{L}_2 = \frac{d^4}{dy^4} + 2(1 - 4q^2) \frac{d^2}{dy^2} + (16q^4 - 8q^2 + 1 - \epsilon), \quad (5.47)$$

$$\mathbf{a} = [a_1, a_2]^T, \quad (5.48)$$

and

$$\mathbf{b} = \begin{bmatrix} \frac{3a_1^3}{4} + \frac{3a_1 a_2^2}{2} \\ \frac{3a_2^3}{4} + \frac{3a_2 a_1^2}{2} \end{bmatrix}. \quad (5.49)$$

We can use the same finite difference approach as for the case with  $N = 1$ , with appropriate adjustments to cater for the additional terms involved at the higher truncation levels, where the symbolic algebra package *Maple VR5* ([51], 1998) was used to good effect.

We found that it is most efficient to solve the problem for small  $N$  first and then use the solutions as initial guesses for problems with higher values of  $N$ . The problem was solved for  $N = 1, 2, \dots, 9$  and for  $N = 9$  the results are shown in Figures 5.9–5.13.

Figure 5.9 shows the profiles of  $a_j(y)$ ,  $j = 1, 2, \dots, 9$ , for a channel of width  $L_y = 2\pi$ , wavenumber  $q = 1$  and the discretisation parameter  $M = 50$ . Notice

that the figures show that as  $\epsilon$  decreases and as we move in our parameter space  $(q, \epsilon)$  toward the 2D-linear stability boundary from above (see Figure 5.12) the profiles of  $a_j(y)$ ,  $j = 1, 2, \dots, 9$  become zero. Also note that  $a_j(y)$ ,  $j = 2, 4, 6, 8$  in Figure 5.9 are considered to be zero since their numerical values are insignificantly small. It is readily established that the cubic nonlinearity in (5.35) only generates sine functions whose arguments are odd multiples of  $qx$ .

Figure 5.10 shows contour plots of  $a_j(y)$ ,  $j = 1, 3, \dots, 9$  as a function of wavenumber for a channel width  $L_y = 2\pi$  and  $\epsilon = 0.5$ . As expected,  $a_j(y)$ ,  $j = 1, 3, \dots, 9$  (and thus  $u(x, y)$ ) are non-zero above the neutral curve and zero below. The neutral curve is the boundary that separates the two regions. We can see a clearer plot of  $a_1(y)$  in Figure 5.11 which shows the profile decreasing to zero outside the relevant band of values of  $q$ . By varying the wavenumber  $q$  at different values of  $\epsilon$  until the profiles of  $a_j(y)$ ,  $j = 1, 3, \dots, 9$  are zero we can trace the 2D neutral curve. The results for  $\epsilon = 0.4, 0.5, 0.6$  are shown in Figure 5.12 by the red crosses and are in good agreement with the results of the linear stability theory.

Notice also that there are spikes in the plot of the maximum values of  $a_j(y)$ ,  $j = 3, 7, 9$  in Figure 5.10. This may be an indication of mode interactions and the possibility that there is a more complex bifurcation structure in this region. We shall not investigate this here but hope to investigate this region in further studies.

Figure 5.13 shows the solution  $u(x, y) = \sum_{j=1}^9 a_j(y) \sin jqx$  as a function of  $x$  and  $y$  for a channel of width  $L_y = 2\pi$ , wavenumber  $q = 1$  and  $\epsilon = 0.5$ . This is a typical solution that is periodic along the  $x$ -axis. We shall use this periodic property in Chapter 6 where we undertake a Floquet analysis of the two dimensional periodic solutions.

## 5.4 Summary

Summarising what we have found in Chapter 5:

- We have found the neutral curve for the two-dimensional SH equation in a channel with no-slip sidewalls of arbitrary width  $L_y$ . The critical value of  $\epsilon$  and the critical wavenumber  $q$  are given by (5.22) provided  $L_y \geq 3.562$ . For narrow channels, the linear theory predicts that disturbances will set in with infinite wavelength ( $q = 0$ ) but the corresponding value of  $\epsilon$  is greater

than  $\epsilon = 2.134$ , so that the results in such cases are expected to be of limited physical significance.

- The critical disturbance corresponds to a solution which is even in  $y$  about the centre of the channel. For sufficiently wide channels and at lower wavenumbers the odd and even modes are alternately the most dangerous mode of disturbance.
- We have obtained numerical approximations to nonlinear periodic solutions of the form

$$u_p(x, y) = \sum_{j=1}^{\infty} a_j(y) \sin jqx.$$

and have verified that these are consistent with the linear stability results for a channel of width  $L_y = 2\pi$ .

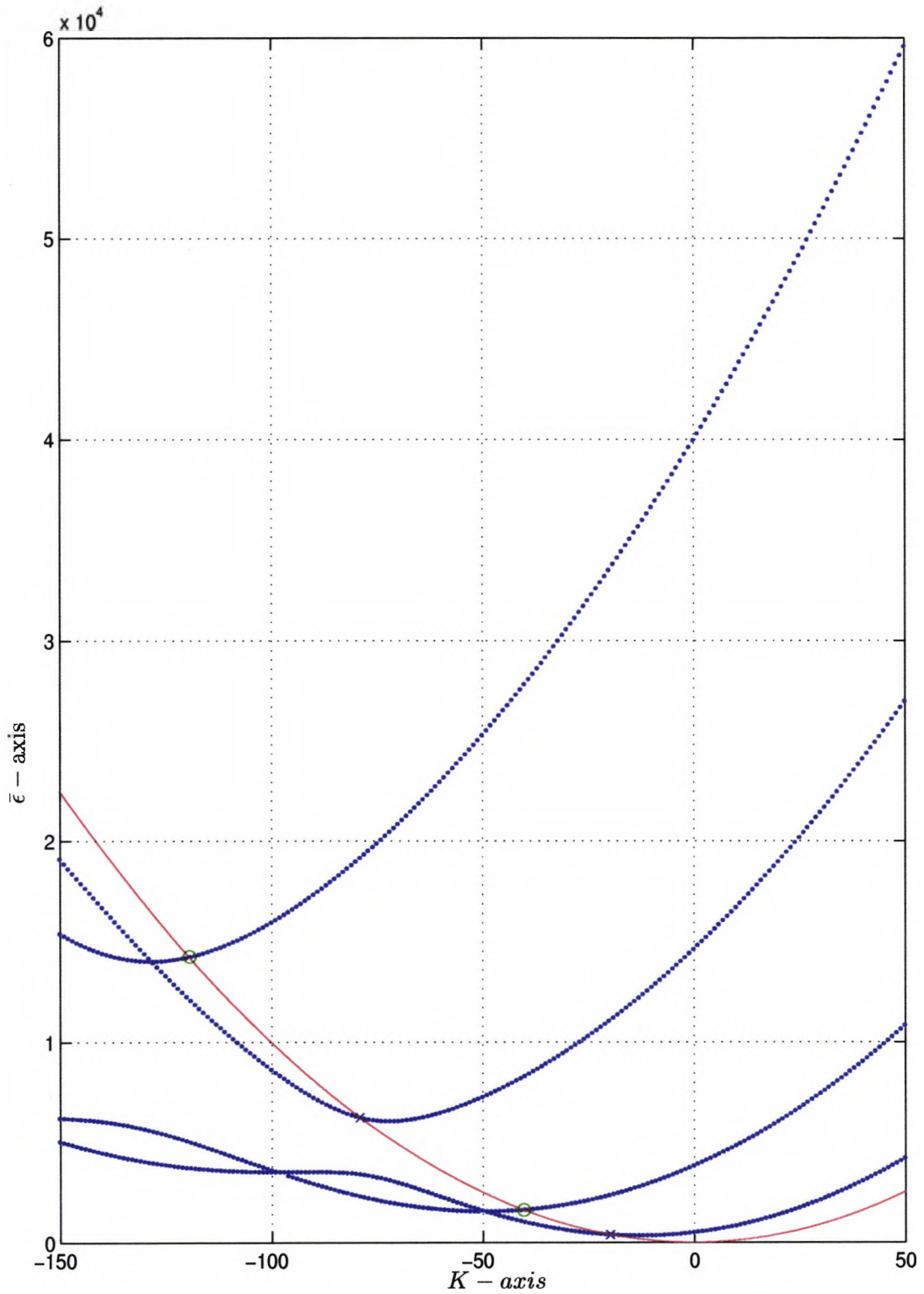


Figure 5.7: The first four even and odd solution branches. The crosses and circles show the intersection of the even and odd branches with the  $1D$ -neutral-curve.

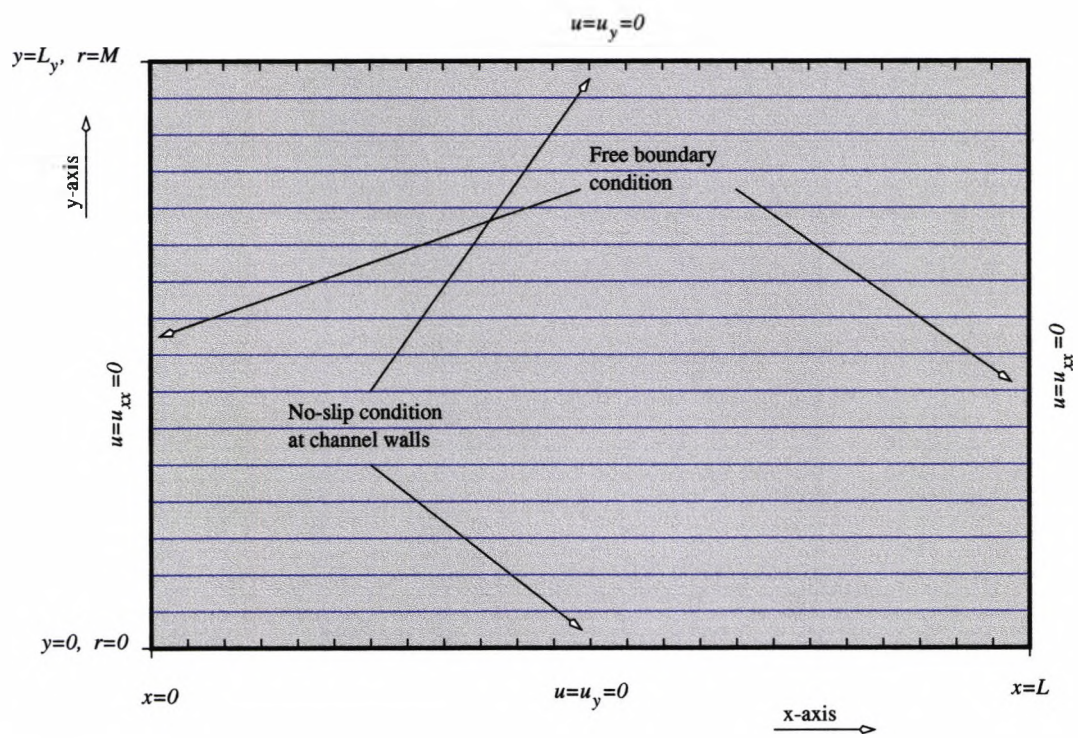


Figure 5.8: The geometry and boundary conditions of the two-dimensional problem.

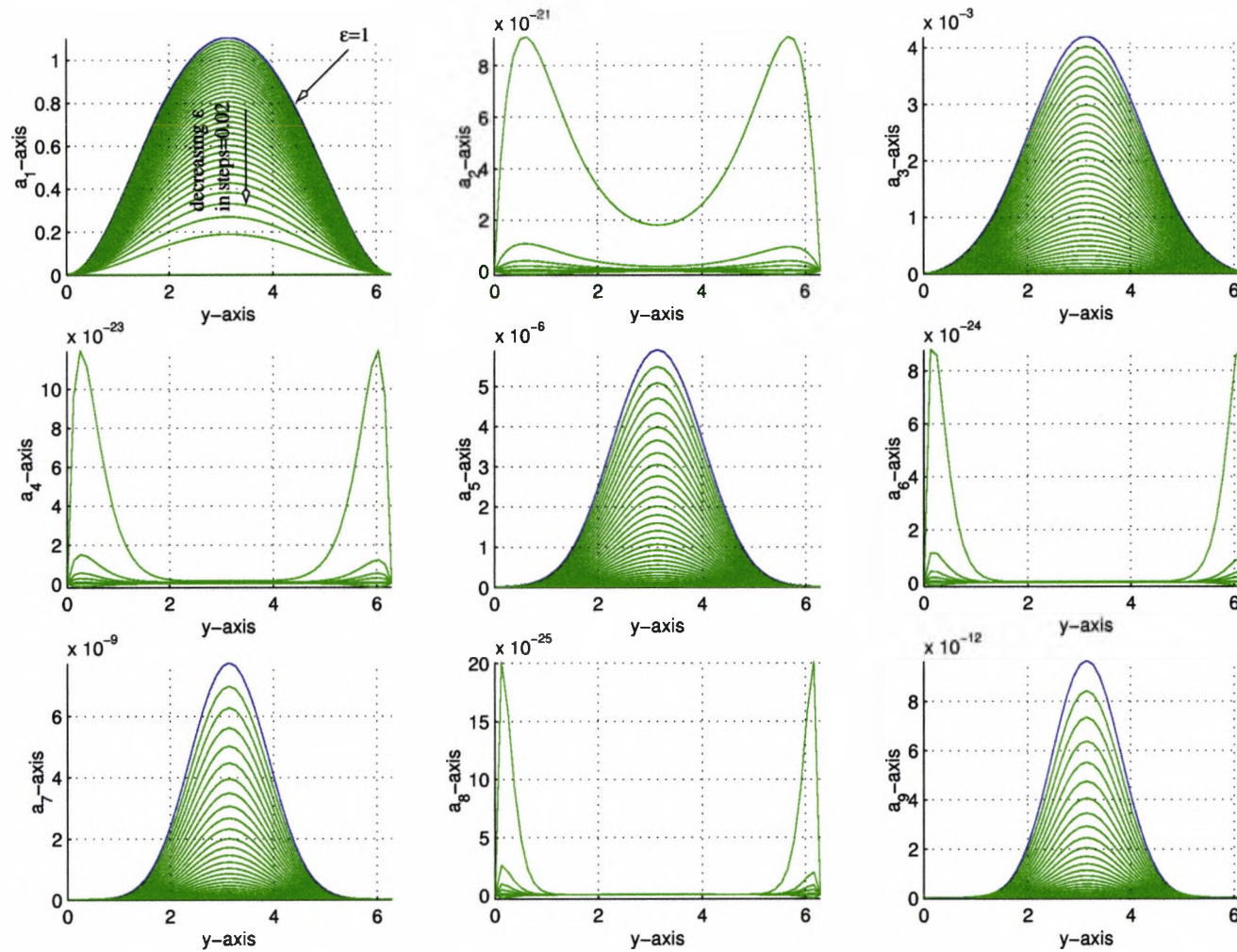


Figure 5.9: Profiles of  $a_j(y)$  for  $j = 1, 2, \dots, 9$  with  $\epsilon = 1$  (blue profile) and decreasing in steps of 0.02 (green profiles). The solution is for a channel of width  $L_y = 2\pi$ , wavenumber  $q = 1$  and discretisation parameter  $M = 50$ .

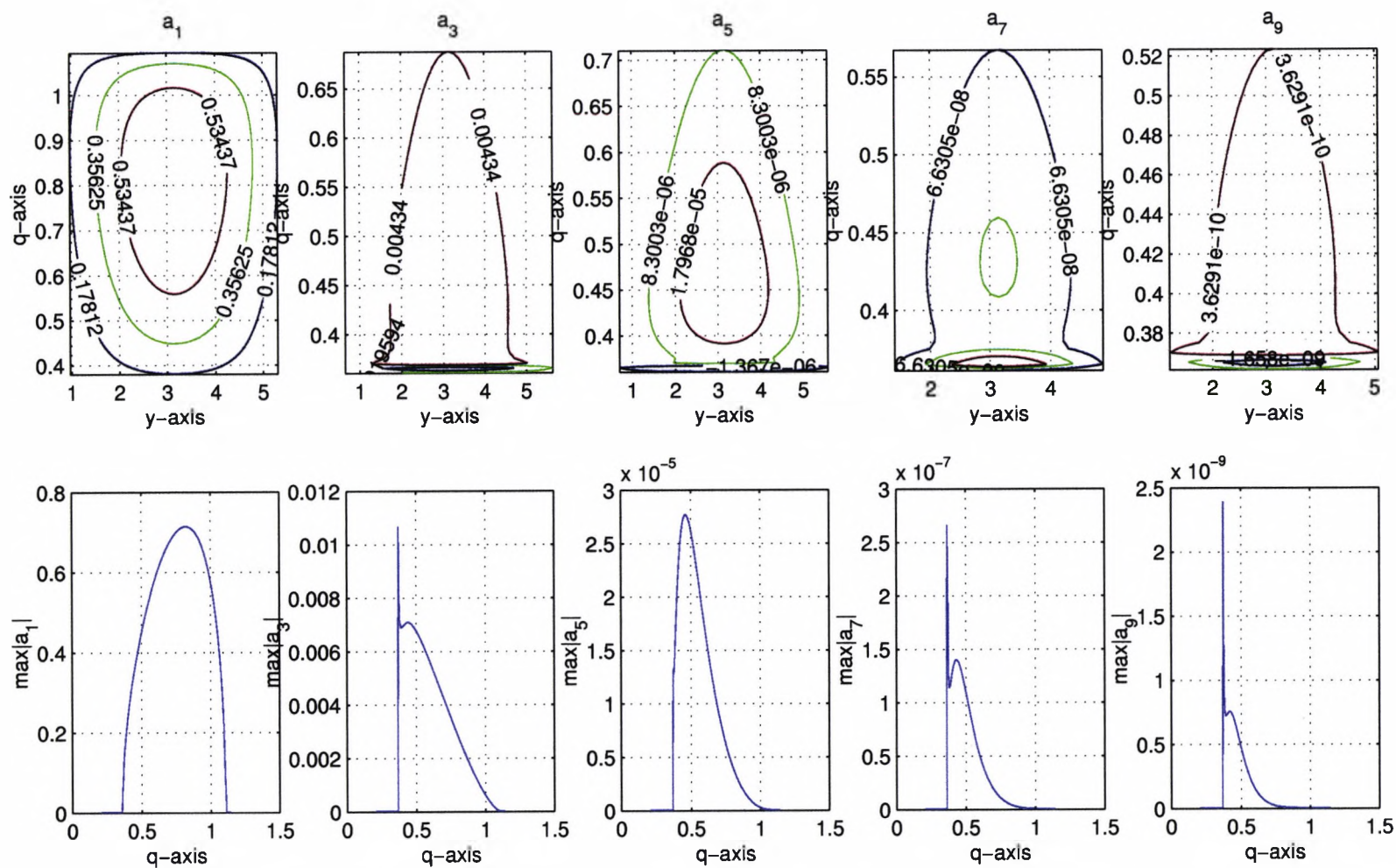


Figure 5.10: The top row shows the contour plots of  $a_j(y)$ ,  $j = 1, 3, \dots, 9$  for  $L_y = 2\pi$ ,  $\epsilon = 0.5$  and discretisation parameter  $M = 50$ . The bottom row shows plots of the maximum values of  $a_j(y)$ ,  $j = 1, 3, \dots, 9$  with the same parameters.

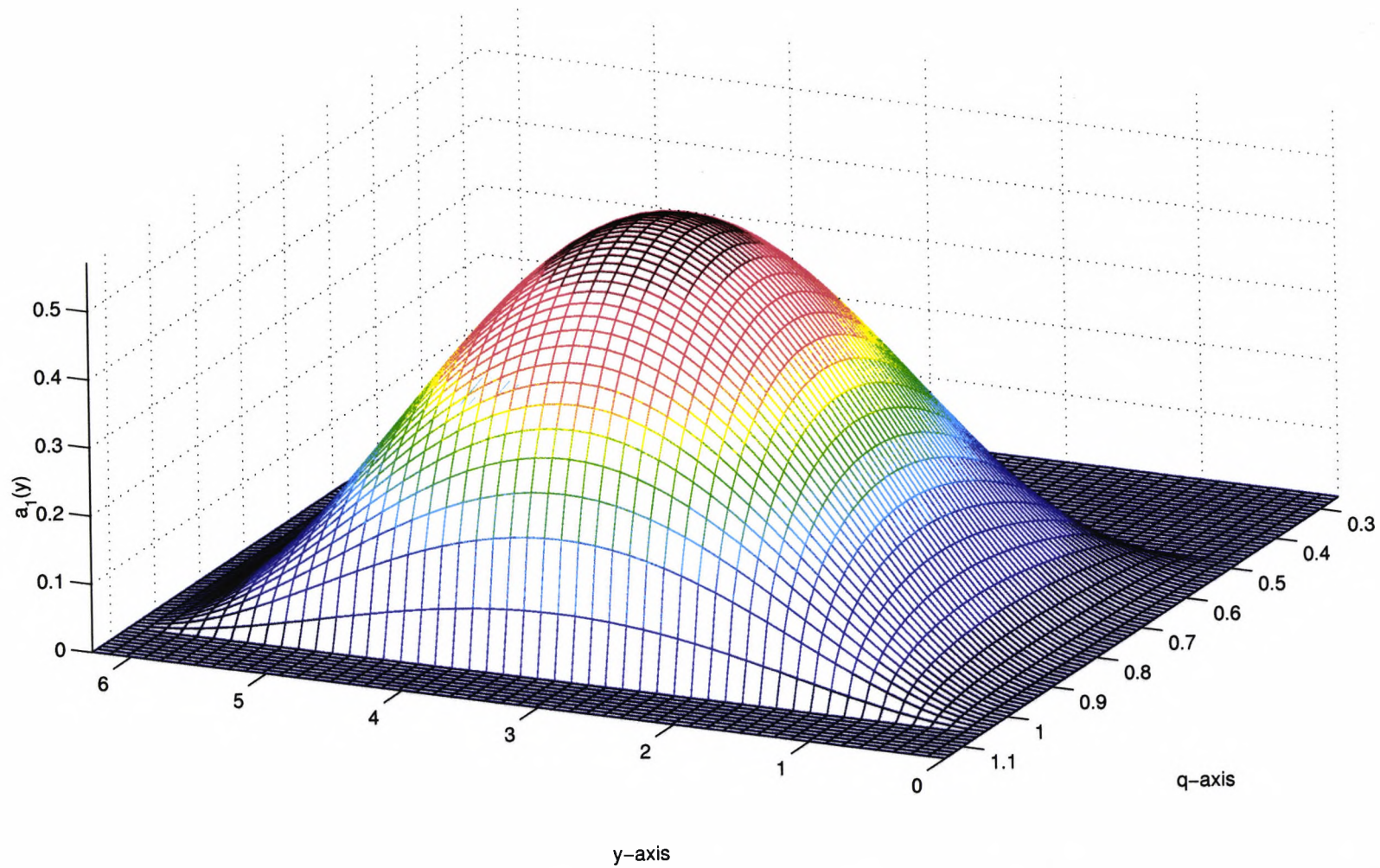


Figure 5.11: Profiles of  $a_1(y)$  for different wavenumbers  $q$  with  $L_y = 2\pi$ ,  $\epsilon = 0.5$  and the discretisation parameter  $M = 50$ .

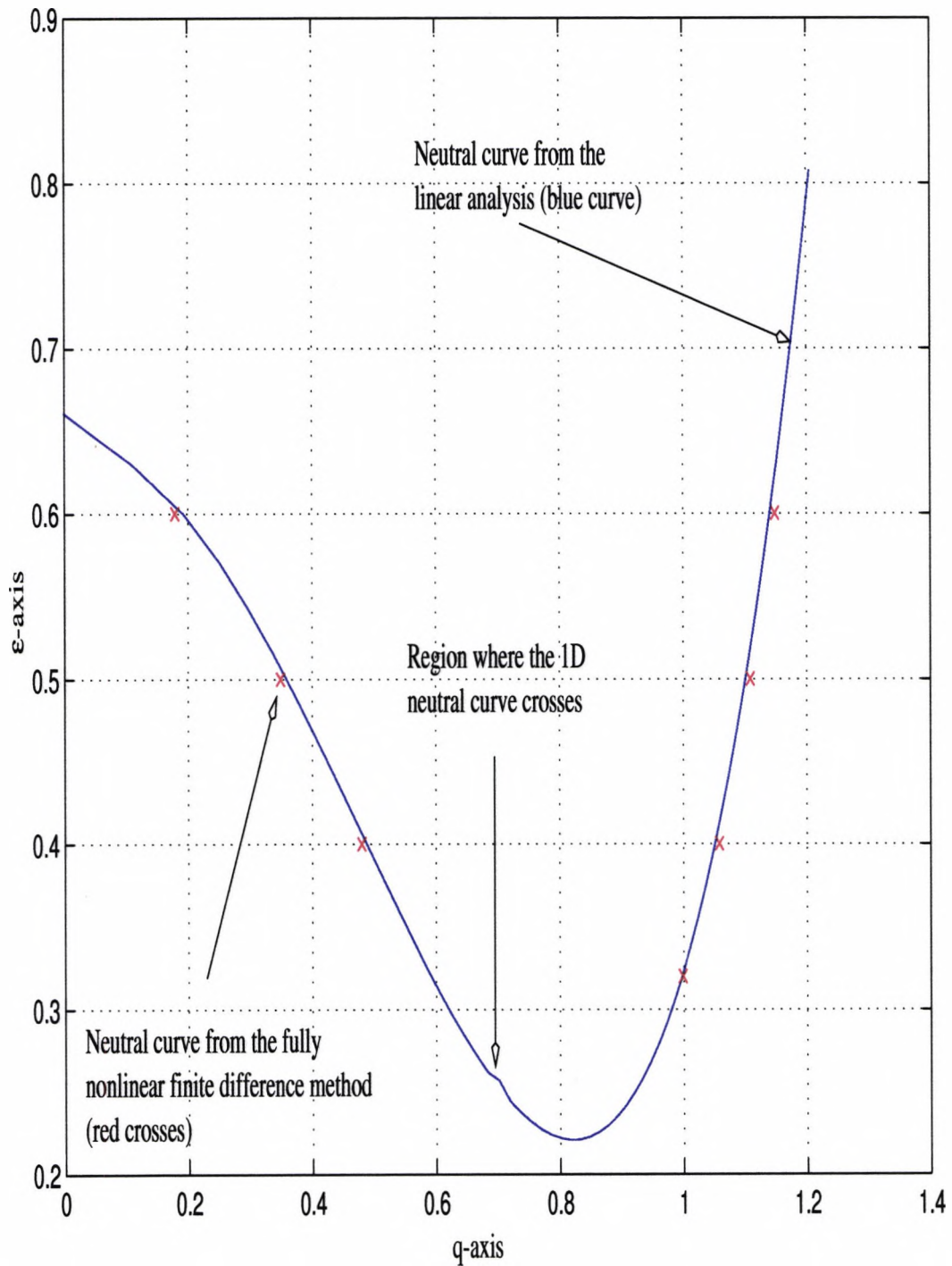


Figure 5.12: Plot comparing the 2D neutral curve derived in Section 5.2 with the neutral curve derived from the fully nonlinear finite difference method. The results are for a fixed channel width  $L_y = 2\pi$ . The small kink should be ignored, being an artifact introduced by the numerical procedure used to solve equation (5.20) which has a non-meaningful solution  $\alpha = 0$ , equivalent to the one-dimensional neutral curve.

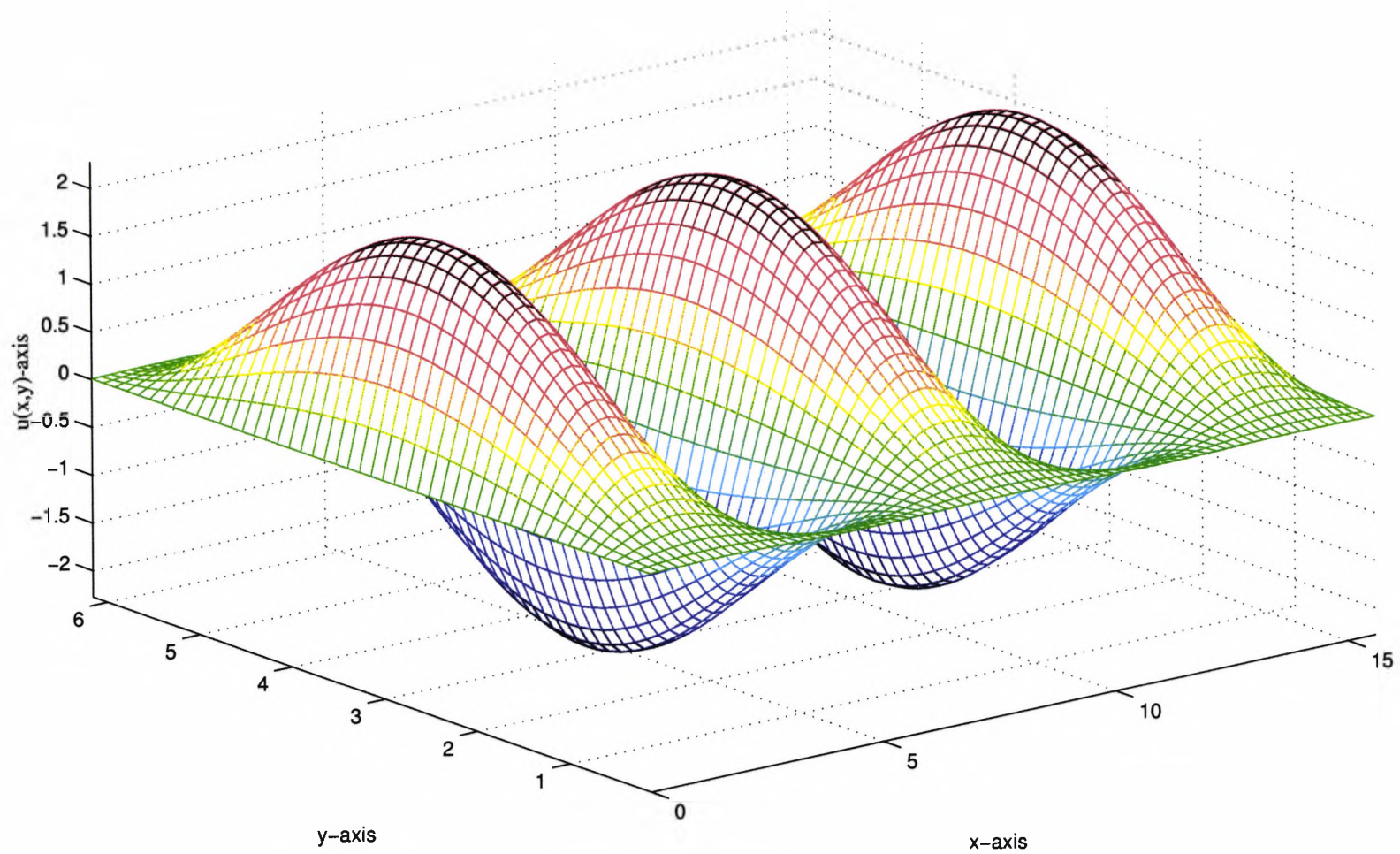


Figure 5.13: The solution  $u(x, y) = \sum_{j=1}^9 a_j(y) \sin jqx$  for a channel width  $L_y = 2\pi$ , wavenumber  $q = 1$  and  $\epsilon = 0.5$ .

## Chapter 6

# Floquet Theory for the Two Dimensional Swift-Hohenberg Equation

### 6.1 Introduction

In this chapter we investigate more general solutions of the steady two dimensional Swift-Hohenberg equation for a channel of width  $L_y$ . We proceed by introducing a perturbation to the 2D periodic solution determined in Chapter 5 and classifying regions where the perturbation is spatially decaying or growing and regions where the perturbation is spatially oscillatory. The boundary separating the two regions is the Eckhaus stability boundary. One aim, as in the one dimensional theory of Chapter 3, is to determine the asymptotic form of the solution which will apply in the channel at large distances  $x$  from a lateral wall at  $x = 0$ .

### 6.2 Floquet-Fourier Method

We proceed as in Section 3.2 and search for solutions which approach the two dimensional periodic solution

$$u_p(x, y) = \sum_{j=1}^N a_j(y) \sin jqx, \quad (6.1)$$

as  $x \rightarrow \infty$ . Notice that we have already calculated the coefficients  $a_j(y)$  which appear in this formula for  $u_p(x, y)$  in Section 5.3. Now consider a perturbation to  $u_p$  so that  $u$  is written as

$$u(x, y) = u_p(x, y) + kU(x, y) + \dots, \quad (6.2)$$

where the constant  $k$  is small. Substituting into (5.1) and (5.2), expanding and taking terms of order  $k$  we get the equation

$$\frac{\partial^4 U}{\partial x^4} + \frac{\partial^4 U}{\partial y^4} + 2 \left( \frac{\partial^2 U}{\partial x^2} + \frac{\partial^4 U}{\partial x^2 \partial y^2} + \frac{\partial^2 U}{\partial y^2} \right) + (1 - \epsilon)U = -3u_p^2 U, \quad (6.3)$$

for  $U$  to be solved subject to the boundary conditions

$$U = U_y = 0 \quad \text{at} \quad y = 0, L_y. \quad (6.4)$$

Equation (6.3) is a linear partial differential equation with periodic coefficients. We again found that if we use a shooting method (via the Method of Lines) to solve (6.3), (6.4) this leads to numerical instability. Instead, the solution for  $U$  is expressed in the Floquet form

$$U(x, y) = e^{-\mathcal{C}x} \sum_{n=0}^{\widehat{N}} (b_n(y) \cos nqx + c_n(y) \sin nqx), \quad (6.5)$$

where  $\mathcal{C}$  is the characteristic exponent and the periodic part of the solution is expressed as a Fourier series in  $x$  whose coefficients  $b_n(y)$  ( $n = 0, 1, 2, \dots, \widehat{N}$ ) and  $c_n(y)$  ( $n = 1, 2, \dots, \widehat{N}$ ), are bounded functions of  $y$ . Note that if  $\mathcal{C}$  is complex then the conjugate of  $kU$  can be added in (6.2) to obtain the real solution for  $u$ . The value of  $\widehat{N}$  is infinite in general but in practice approximate solutions can be found by truncating the infinite series in both (6.1) and (6.5).

For example, when  $\widehat{N} = 1$  and  $N = 1$  equation (6.3) gives

$$\begin{aligned} & \frac{d^4 b_0}{dy^4} + 2(\mathcal{C}^2 + 1) \frac{d^2 b_0}{dy^2} + (\mathcal{C}^4 + 2\mathcal{C}^2 + 1 - \epsilon)b_0 + \\ & + \left[ \frac{d^4 b_1}{dy^4} + 2(\mathcal{C}^2 - q^2 + 1) \frac{d^2 b_1}{dy^2} - 4q\mathcal{C} \frac{d^2 c_1}{dy^2} + \right. \\ & + (\mathcal{C}^4 + 2(1 - 3q^2)\mathcal{C}^2 + q^4 - 2q^2 + 1 - \epsilon)b_1 + \\ & \left. + 4q\mathcal{C}(-\mathcal{C}^2 + q^2 - 1)c_1 \right] \cos qx + \end{aligned}$$

$$\begin{aligned}
& + \left[ \frac{d^4 c_1}{dy^4} + 2(\mathcal{C}^2 - q^2 + 1) \frac{d^2 c_1}{dy^2} + 4q\mathcal{C} \frac{d^2 c_1}{dy^2} + \right. \\
& + (\mathcal{C}^4 + 2(1 - 3q^2)\mathcal{C}^2 + q^4 - 2q^2 + 1 - \epsilon)c_1 + \\
& \quad \left. + 4q\mathcal{C}(\mathcal{C}^2 - q^2 + 1)b_1 \right] \sin qx = -3a_1^2 \sin^2 qx (b_0 + b_1 \cos qx + \\
& \quad + c_1 \sin qx).
\end{aligned} \tag{6.6}$$

Using the orthogonality property of sines and cosines we get the system of ordinary differential equations

$$\frac{d^4 b_0}{dy^4} + 2(\mathcal{C}^2 + 1) \frac{d^2 b_0}{dy^2} + (\mathcal{C}^4 + 2\mathcal{C}^2 + 1 - \epsilon)b_0 = -\frac{3}{2}a_1^2 b_0, \tag{6.7}$$

$$\begin{aligned}
& \frac{d^4 b_1}{dy^4} + 2(\mathcal{C}^2 - q^2 + 1) \frac{d^2 b_1}{dy^2} - 4q\mathcal{C} \frac{d^2 c_1}{dy^2} + \\
& + (\mathcal{C}^4 + 2(1 - 3q^2)\mathcal{C}^2 + q^4 - 2q^2 + 1 - \epsilon)b_1 + \\
& \quad + 4q\mathcal{C}(-\mathcal{C}^2 + q^2 - 1)c_1 = -\frac{3}{4}a_1^2 b_1,
\end{aligned} \tag{6.8}$$

$$\begin{aligned}
& \frac{d^4 c_1}{dy^4} + 2(\mathcal{C}^2 - q^2 + 1) \frac{d^2 c_1}{dy^2} + 4q\mathcal{C} \frac{d^2 c_1}{dy^2} + \\
& + (\mathcal{C}^4 + 2(1 - 3q^2)\mathcal{C}^2 + q^4 - 2q^2 + 1 - \epsilon)c_1 + \\
& \quad + 4q\mathcal{C}(\mathcal{C}^2 - q^2 + 1)b_1 = -\frac{9}{4}a_1^2 c_1,
\end{aligned} \tag{6.9}$$

for the coefficients  $b_0$ ,  $b_1$  and  $c_1$ . Notice that the equation for  $b_0$  is disjoint from that for  $b_1$  and  $c_1$ . Moving the right-hand sides of equations (6.7)–(6.9) to the left gives the system

$$\mathcal{M}\bar{\alpha} = 0, \tag{6.10}$$

where

$$\mathcal{M} = \begin{bmatrix} \mathcal{L}_{0,0,b} & 0 & 0 \\ 0 & \mathcal{L}_{1,1,b} & \mathcal{L}_{1,2,c} \\ 0 & \mathcal{L}_{2,1,b} & \mathcal{L}_{2,2,c} \end{bmatrix}, \tag{6.11}$$

$$\mathcal{L}_{0,0,b} = \frac{d^4}{dy^4} + 2(\mathcal{C}^2 + 1) \frac{d^2}{dy^2} + \mathcal{C}^4 + 2\mathcal{C}^2 + 1 - \epsilon + \frac{3}{2}a_1^2, \tag{6.12}$$

$$\begin{aligned}
\mathcal{L}_{1,1,b} = & \frac{d^4}{dy^4} + 2(\mathcal{C}^2 - q^2 + 1) \frac{d^2}{dy^2} + \\
& + \mathcal{C}^4 + 2(1 - 3q^2)\mathcal{C}^2 + q^4 - 2q^2 + 1 - \epsilon + \frac{3}{4}a_1^2,
\end{aligned} \tag{6.13}$$

$$\mathcal{L}_{1,2,c} = -4qC \left[ \frac{d^2}{dy^2} + (C^2 - q^2 + 1) \right], \quad (6.14)$$

$$\mathcal{L}_{2,1,b} = 4qC \left[ \frac{d^2}{dy^2} + (C^2 - q^2 + 1) \right], \quad (6.15)$$

$$\begin{aligned} \mathcal{L}_{2,2,c} = & \frac{d^4}{dy^4} + 2(C^2 - q^2 + 1) \frac{d^2}{dy^2} + \\ & + C^4 + 2(1 - 3q^2)C^2 + q^4 - 2q^2 + 1 - \epsilon + \frac{9}{4}a_1^2, \end{aligned} \quad (6.16)$$

and  $\bar{\alpha} = [b_0, b_1, c_1]^T$ . The boundary conditions are

$$b_0(0) = b_0(L_y) = \frac{db_0}{dy}(0) = \frac{db_0}{dy}(L_y) = 0, \quad (6.17)$$

$$b_1(0) = b_1(L_y) = \frac{db_1}{dy}(0) = \frac{db_1}{dy}(L_y) = 0, \quad (6.18)$$

$$c_1(0) = c_1(L_y) = \frac{dc_1}{dy}(0) = \frac{dc_1}{dy}(L_y) = 0. \quad (6.19)$$

We use the same finite difference scheme from Section 5.3 to discretise the differential operator  $\mathcal{M}$  in equation (6.10), subject to the boundary conditions (6.17)–(6.19). From now on we shall denote the finite difference approximation of the operator  $\mathcal{M}$  as  $\mathcal{M}^{fd}$ . The formulae (6.10)–(6.19) can be expanded to incorporate higher truncation levels  $N$  and  $\hat{N}$  in a straightforward but lengthy manner. The discretised system forms an eigenvalue problem and for solutions  $\mathcal{M}^{fd}$  must have a zero determinant or equivalently,  $\mathcal{M}^{fd}$  has a zero eigenvalue<sup>1</sup>. This is possible within our parameter space defined by  $L_y$ ,  $q$ ,  $\epsilon$  and  $C$ .

Notice that if we differentiate equation (5.1) with respect to  $x$  we see that  $U = \frac{\partial u_p}{\partial x}$  is a solution of (6.3) which satisfies the boundary conditions (6.4). We can use this solution, for which  $C = 0$  for all  $(L_y, q, \epsilon)$ , as a check on our numerical algorithm. Notice that  $a_i$ , for  $i = 1, 2, \dots, 9$ , was calculated in Section 5.3 and that  $a_i = 0$  for even  $i$ . Therefore we expect either solutions with  $b_0; b_2, c_2; b_4, c_4, \dots$  non-zero or solutions with  $b_1, c_1; b_3, c_3; \dots$  non-zero. Freedom in the choice of the imaginary part of  $C$  suggests we can restrict attention to the latter case.

<sup>1</sup>The product of the eigenvalues of  $\mathcal{M}^{fd}$  is equal to the determinant of  $\mathcal{M}^{fd}$  so the zeros of  $\det \mathcal{M}^{fd}$  are equivalent to the zeros of eigenvalues.

### 6.3 Numerical Results

Here we concentrate on the case when  $\widehat{N} = 1$  and  $N = 1$ , and it follows from (6.10)–(6.19) that the eigenfunctions  $b_1$ ,  $c_1$  and the characteristic exponent  $\mathcal{C}$  are solutions of the sub-problem

$$\mathcal{M}_1 \bar{\alpha}_1 = 0, \quad (6.20)$$

where

$$\mathcal{M}_1(\mathcal{C}) = \begin{bmatrix} \mathcal{L}_{1,1,b} & \mathcal{L}_{1,2,c} \\ \mathcal{L}_{2,1,b} & \mathcal{L}_{2,2,c} \end{bmatrix}, \quad (6.21)$$

$\mathcal{L}_{1,1,b}$ ,  $\mathcal{L}_{1,2,b}$ ,  $\mathcal{L}_{2,1,b}$  and  $\mathcal{L}_{2,2,b}$  are defined in equations (6.13)–(6.16) and  $\bar{\alpha}_1 = [b_1, c_1]^T$ . The relevant boundary conditions are

$$b_1(0) = b_1(L_y) = \frac{db_1}{dy}(0) = \frac{db_1}{dy}(L_y) = 0, \quad (6.22)$$

$$c_1(0) = c_1(L_y) = \frac{dc_1}{dy}(0) = \frac{dc_1}{dy}(L_y) = 0. \quad (6.23)$$

We proceed as in Section 5.3 and introduce a finite set of grid points  $y_r = rh$ , for  $r = 0, 1, \dots, M$ , where  $M \in \mathbb{N}$  and  $h = L_y/M$ . Then using the central difference formulae (5.40)–(5.42) we discretise the linear operators  $\mathcal{L}_{1,1,b}$ ,  $\mathcal{L}_{1,2,b}$ ,  $\mathcal{L}_{2,1,b}$  and  $\mathcal{L}_{2,2,b}$  which we shall denote as  $\mathcal{L}_{1,1,b}^{fd}$ ,  $\mathcal{L}_{1,2,b}^{fd}$ ,  $\mathcal{L}_{2,1,b}^{fd}$  and  $\mathcal{L}_{2,2,b}^{fd}$  respectively. The problem (6.20)–(6.23) becomes the eigenvalue problem

$$\mathcal{M}_1^{fd} \bar{\alpha}_1 = 0, \quad (6.24)$$

where

$$\mathcal{M}_1^{fd}(\mathcal{C}) = \begin{bmatrix} \mathcal{L}_{1,1,b}^{fd} & \mathcal{L}_{1,2,c}^{fd} \\ \mathcal{L}_{2,1,b}^{fd} & \mathcal{L}_{2,2,c}^{fd} \end{bmatrix} \quad (6.25)$$

and

$$\bar{\alpha}_1 = [b_{1,-2}, b_{1,-1}, b_{1,1}, b_{1,2}, \dots, b_{1,m-2}, b_{1,m-1}, b_{1,m+1}, b_{1,m+2}, \\ c_{1,-2}, c_{1,-1}, c_{1,1}, c_{1,2}, \dots, c_{1,m-2}, c_{1,m-1}, c_{1,m+1}, c_{1,m+2}]^T. \quad (6.26)$$

Normally, the function  $\det \mathcal{M}_1^{fd}(\mathcal{C}; L_y, q, \epsilon)$  is a very large complex function so to avoid truncation errors we search for zeros of the eigenvalue with the minimum modulus, i.e.,  $\min |(\text{eig } \mathcal{M}_1^{fd})|$ , instead. The value of  $M$  was taken as  $M = 16$  for most computations.

Initially, the parameter values were fixed at  $(L_y, q, \epsilon) = (2\pi, 0.82374, 0.5)$  and  $\mathcal{C}$  varied within the complex plane to find the zeros of  $\min |(\text{eig } \mathcal{M}_1^{fd})|$ . Figure 6.1 shows the shading and contour plots of the function

$$\min \left| \text{eig } \mathcal{M}_1^{fd}(\mathcal{C}; 2\pi, 0.82374, 0.5) \right|$$

for  $-5 < \text{Re}(\mathcal{C}) < 5$  and  $-5 < \text{Im}(\mathcal{C}) < 5$ . The plots show the regions where the zeros of  $\min |(\text{eig } \mathcal{M}_1^{fd})|$  are located; a Newton iterative scheme was used to home in on the precise location of the zeros. Notice that the three roots of smallest absolute value lie on the real axis, located at  $\mathcal{C} \approx -0.4$ ,  $0.4$ , and  $\mathcal{C} = 0$ . We shall denote them as  $\mathcal{C}_-$ ,  $\mathcal{C}_+$  and  $\mathcal{C}_0$  respectively. The root  $\mathcal{C} = 0$  represents the solution  $\frac{\partial u_p}{\partial x}$  which was mentioned in Section 6.2 and occurs for all  $(L_y, q, \epsilon)$ . Figure 6.1 also shows that there appear to be two sets of roots in the first quadrant of the complex  $\mathcal{C}$ -plane (the sets are represented by the magenta coloured lines; and individual roots by the red crosses). These roots occur in conjugate pairs and also pairs that are symmetric about the imaginary axis. Although we expect there to be an infinite number of roots associated with a complete set of eigenfunctions in  $y$ , the distribution shown in Figure 6.1 is likely to be significantly affected by the severe truncation as the value of  $|\mathcal{C}|$  increases. In addition, the various roots are only guaranteed to represent distinct solutions if the value of  $\text{Re}(\mathcal{C})$  is distinct, because any multiple of  $q$  in the imaginary component can also be incorporated in the periodic part of the Floquet form. The highest set of roots in Figure 6.1 *approximates* to a reflection of the lowest set about the line  $\mathcal{C} = iq$ , suggesting that the lowest and highest sets are equivalent, and leaving one significant set of roots in the first quadrant. This argument suggests that the root  $\mathcal{C}_+$  defines the dominant term in the spatial decay of the solution (6.5) as  $x \rightarrow \infty$  and its behaviour is therefore of greatest interest.

Figure 6.2 summarises the main results at a particular point in parameter space, showing the geometry of the channel, the coefficient  $a_1$  of the periodic solution  $u_p$  and the eigenfunctions  $b_1$  and  $c_1$  at the parameter values  $(L_y, q, \epsilon) = (2\pi, 0.82374, 0.4)$ , corresponding to the characteristic exponent  $\mathcal{C}_+ = 0.3533$ . Figure 6.3 shows a shading plot of the functions  $u_p(x, y) = a_1(y) \sin qx$  and  $[b_1(y) \cos qx + c_1(y) \sin qx]$  at the same parameter values.

From now on we concentrate our investigation on the three values of  $\mathcal{C}$  of smallest absolute value. By fixing  $(L_y, \epsilon) = (2\pi, 0.45)$  and evaluating  $\min |(\text{eig } \mathcal{M}_1^{fd})|$  for a range of values of  $q$  about the critical wavenumber,  $q_c = 0.82374$ , we

can follow the transition that  $\mathcal{C}_\pm$  makes. Figure 6.4 shows the contour plots of  $\min |(\text{eig } \mathcal{M}_1^{fd})|$  for  $q \in \{0.5, 0.6, 0.7, 0.8, 0.82374, 0.85, 0.9, 1\}$ . From these plots we see that if we increase or decrease the value of  $q$  from its critical value we pass a boundary where the values of  $\mathcal{C}_\pm$  reach zero and thereafter become purely imaginary. Equations (6.2) and (6.5) indicate that these purely imaginary values of  $\mathcal{C}_\pm$  represent spatially oscillatory solutions (Eckhaus instability). We can see the transition more clearly in Figure 6.5. This shows the continuous plot of  $|\mathcal{C}_+|$  for  $\epsilon = \{0.3, 0.35, 0.4, 0.45\}$ . Consider the curve with  $\epsilon = 0.3$ . The red arrows indicate the region where  $\mathcal{C}_+$  is real and the green arrows indicate the region where  $\mathcal{C}_+$  is purely imaginary. At the join,  $\mathcal{C}_+ = 0$ , is the Eckhaus boundary for a channel of width  $L_y = 2\pi$ .

Fixing  $L_y = 2\pi$  and inspecting the values of  $(q, \epsilon)$  at which  $\mathcal{C}_+ = 0$  we can plot the entire Eckhaus curve for a channel of width  $L_y = 2\pi$ . The plot is shown in Figure 6.6. Notice that the lower part of the Eckhaus curve is missing. We found that it is difficult to resolve the values of  $\mathcal{C}_+$  in this region since it is relatively small and also close to the root at the origin (i.e.,  $\mathcal{C}_0$ ). The red crosses on the plot indicate the points in parameter space at which the plots of Figure 6.4 are evaluated and the red pluses indicate the points at which further plots in Figure 6.7 are evaluated. Figure 6.7 shows the contour plot of  $\min |(\text{eig } \mathcal{M}_1^{fd})|$  for the values  $(L_y, q) = (2\pi, 0.82374)$  and  $\epsilon \in \{0.25, 0.35, 0.45, 0.5, 0.55, 0.75\}$ . The plot shows how the roots  $\mathcal{C}_\pm$  approach the origin as the value of  $\epsilon$  approaches the critical value  $\epsilon_c = 0.22056$ . This creates the difficulty in resolving the zeros corresponding to  $\mathcal{C}_\pm$  for  $\epsilon$  near  $\epsilon_c$ .

Figures 6.8–6.14 show the profiles of  $a_1$ ,  $b_1$  and  $c_1$  with  $\mathcal{C} = \mathcal{C}_+$  as  $q$  varies between the critical wavenumber  $q_c = 0.82374$  and  $q = 0.96874$  for  $\epsilon = 0.4$ . The plots in Figures 6.9–6.14 also include *mesh* plots of  $b_1 \cos qx + c_1 \sin qx$  and  $e^{Cx}[b_1 \cos qx + c_1 \sin qx]$ .

Note that we have taken the truncation levels at the lowest values  $\widehat{N} = N = 1$ . At these truncation levels the even modes in  $x$  are not represented, but we do not expect that this would affect our results since the even and odd modes in  $x$  do not couple (due to the cubic nonlinearity). We expect the accuracy to increase as we increase  $\widehat{N}$  and  $N$  but observe that in the nonlinear periodic form,  $a_1$  is significantly larger than  $a_3, a_5, \dots$  for the range of  $\epsilon$  under consideration. By increasing  $\widehat{N}$  and  $N$  we would also be able to consider solutions which involve mode interactions.

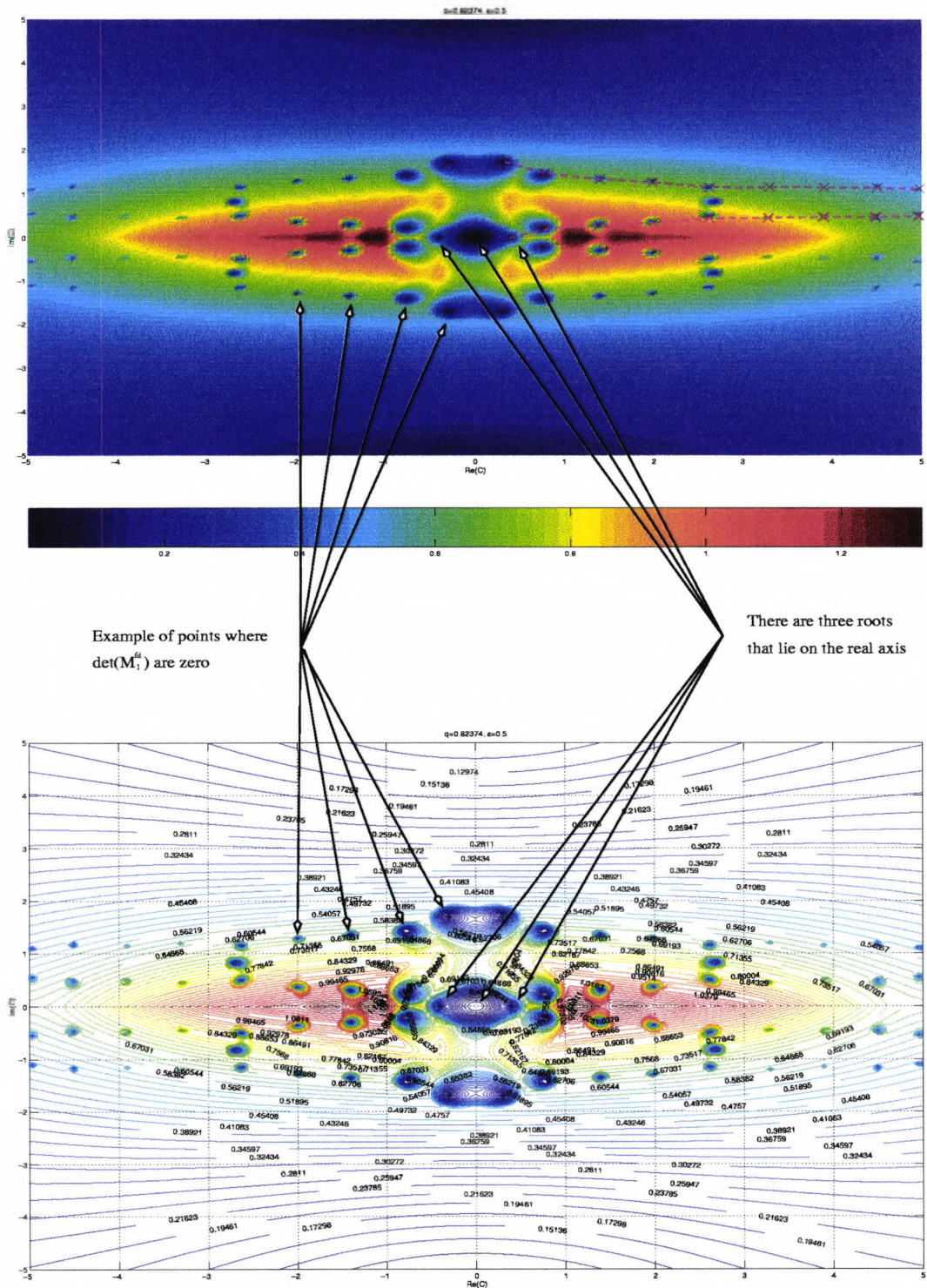


Figure 6.1: The two plots show the zeros of  $\min |(eig \mathcal{M}_1^{fd})|$ . The upper and the lower plots are of the identical region and differ by representing values of  $\min |(eig \mathcal{M}_1^{fd})|$  as shades and contours respectively. The zeros (examples are indicated by the arrows) correspond to different eigenvalues becoming zero. Notice that there are three zero-eigenvalues on the real axis.

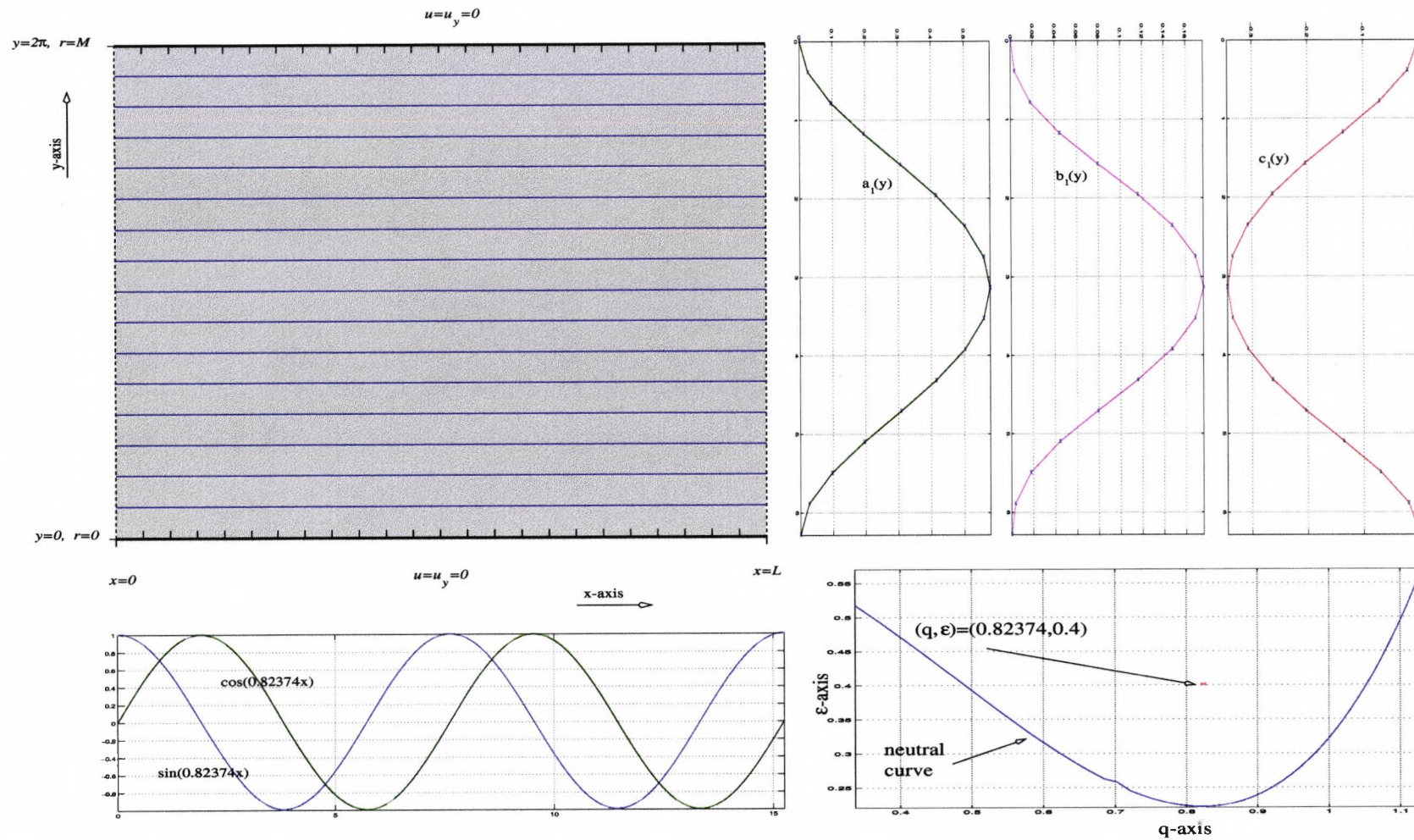


Figure 6.2: Diagram illustrating the geometry of the 2D problem and showing the coefficient  $a_1$  of the periodic solution  $u_p$  and the eigenfunctions  $b_1$  and  $c_1$  at  $(L_y, q, \epsilon) = (2\pi, 0.82374, 0.4)$  corresponding to the characteristic exponent  $\mathcal{C}_+ = 0.3533$ .

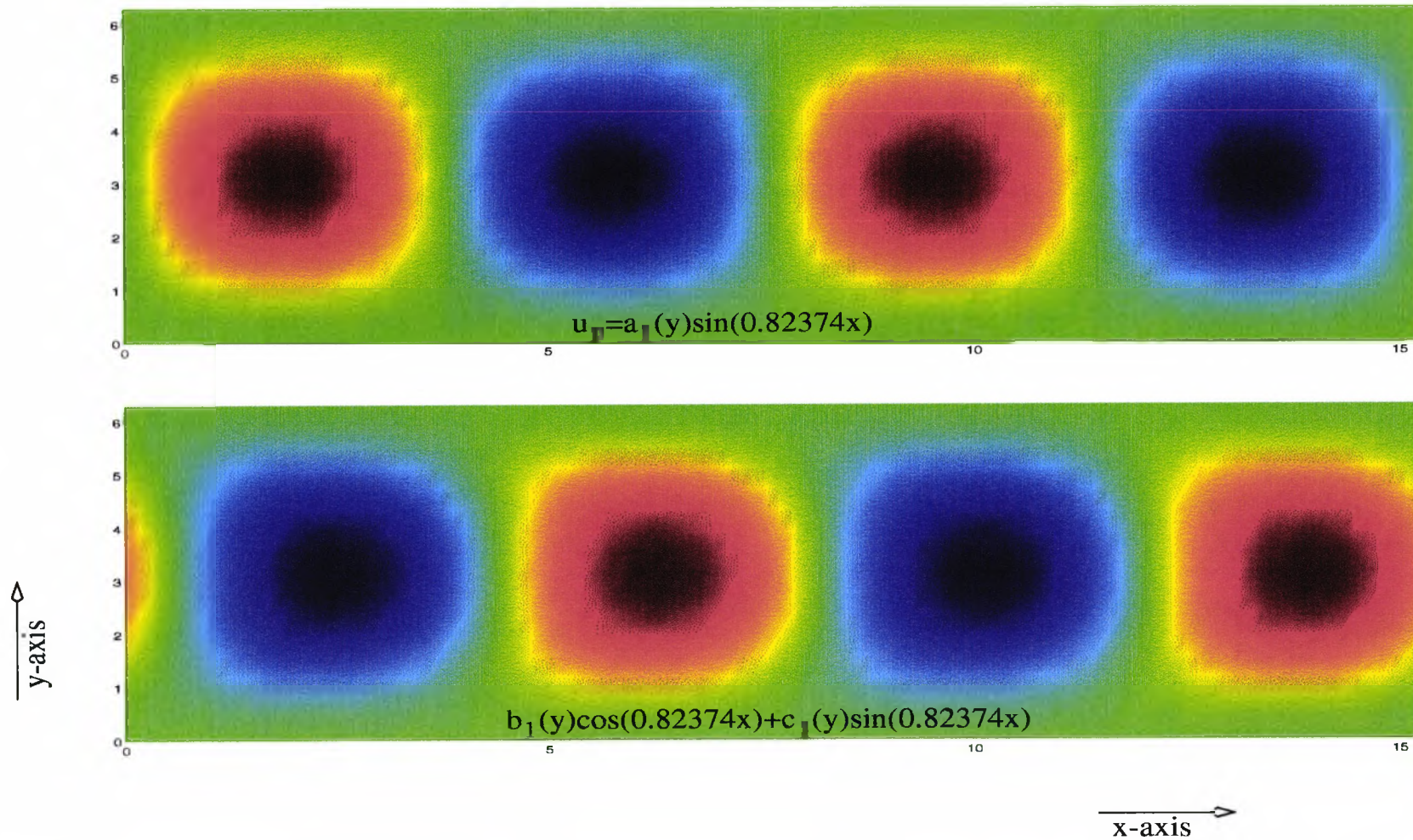


Figure 6.3: Shading plot of the functions  $u_p(y) = a_1(y) \sin qx$  and  $[b_1(y) \cos qx + c_1(y) \sin qx]$  at the parameter values  $(L_y, q, \epsilon) = (2\pi, 0.82374, 0.4)$  and  $C_+ = 0.3533$ .

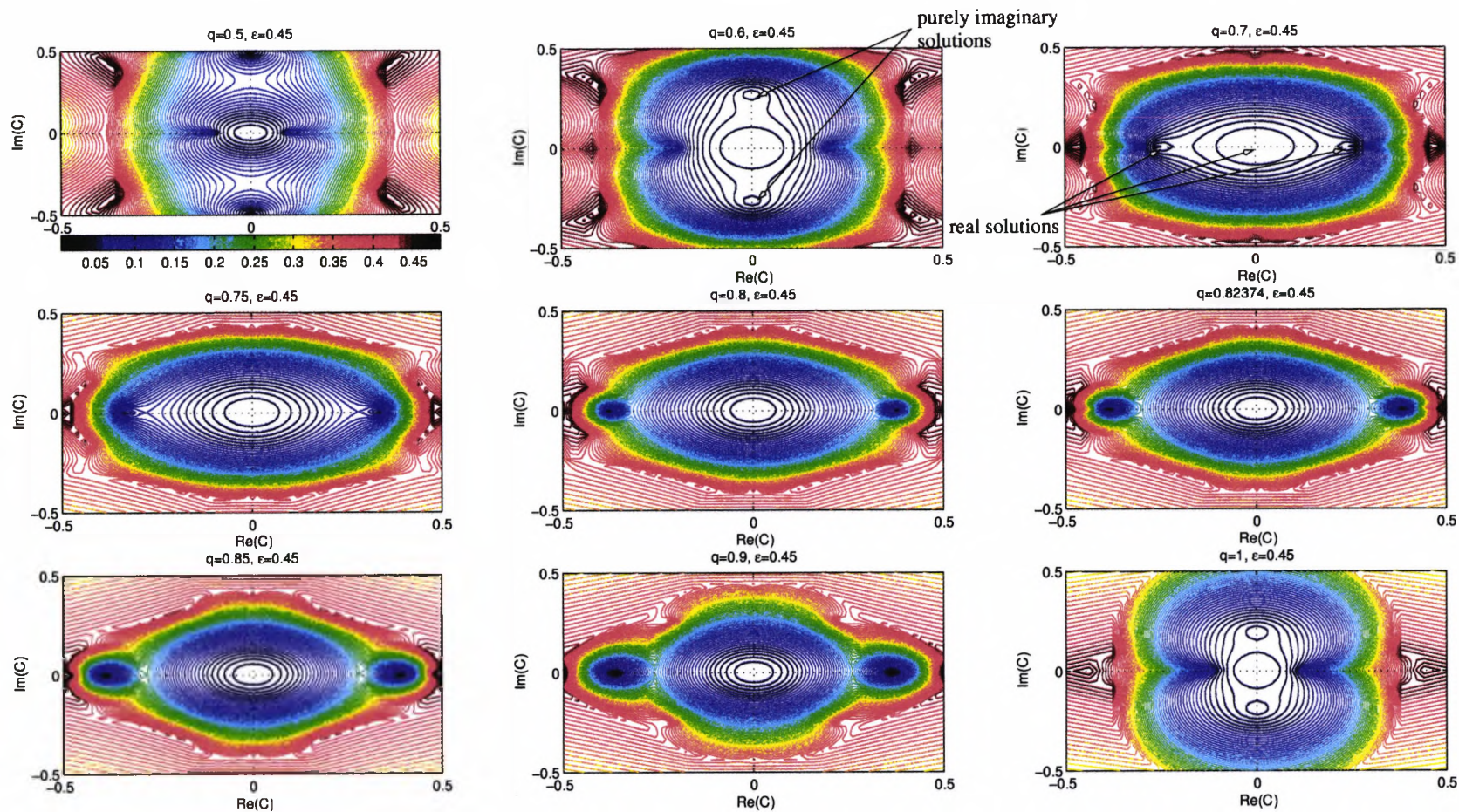


Figure 6.4: Contour plots of  $\min |(\text{eig } \mathcal{M}_1^{fd})|$  for the fixed parameter values  $(L_y, \epsilon) = (2\pi, 0.45)$  and  $q \in \{0.5, 0.6, 0.7, 0.8, 0.82374, 0.85, 0.9, 1\}$ .

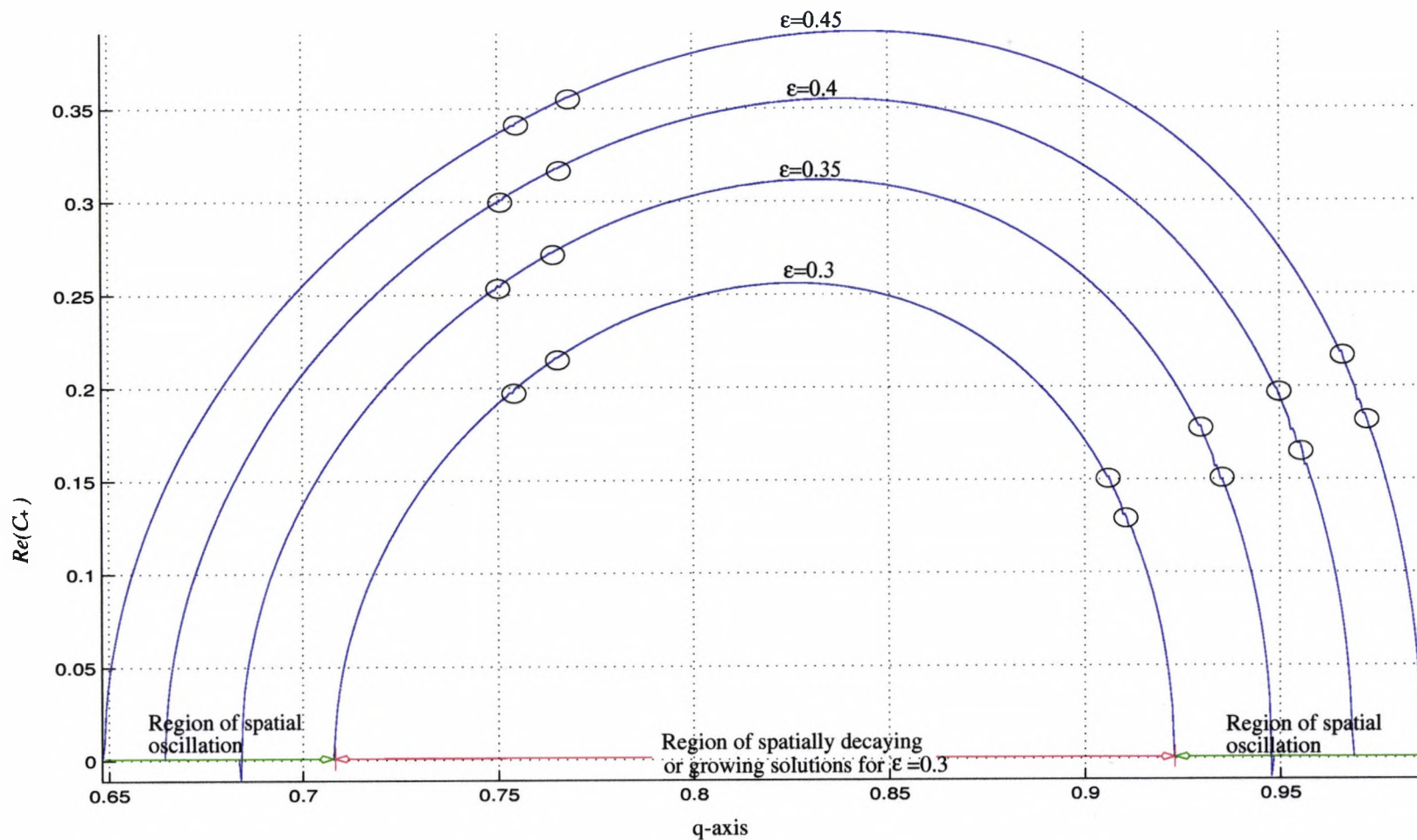


Figure 6.5: Plots of  $|\mathcal{C}|$  for parameter values  $L_y = 2\pi$  and  $\epsilon \in \{0.5, 0.6, 0.7, 0.8\}$ . The circles marking a kink on the curves indicate that the numerical algorithm may be converging to another nearby solution branch. The investigation of such solution branches is left for future work.

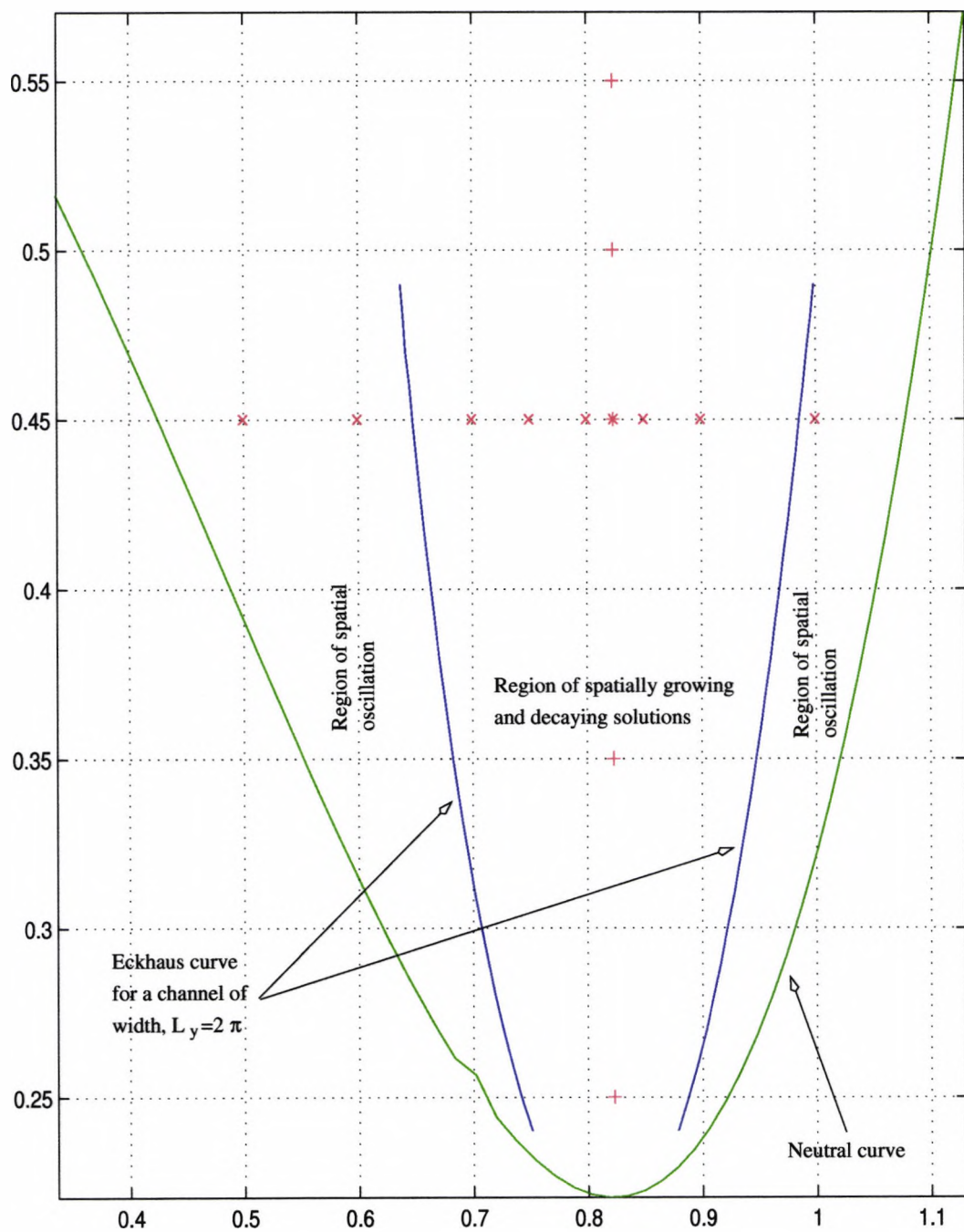


Figure 6.6: Plots showing the neutral curve (green curve) and the Eckhaus boundary (blue curves) for a channel of width  $L_y = 2\pi$ . The red crosses indicate points at which the plots in Figure 6.4 are evaluated and the red pluses indicate points at which the plots in Figure 6.7 are evaluated.

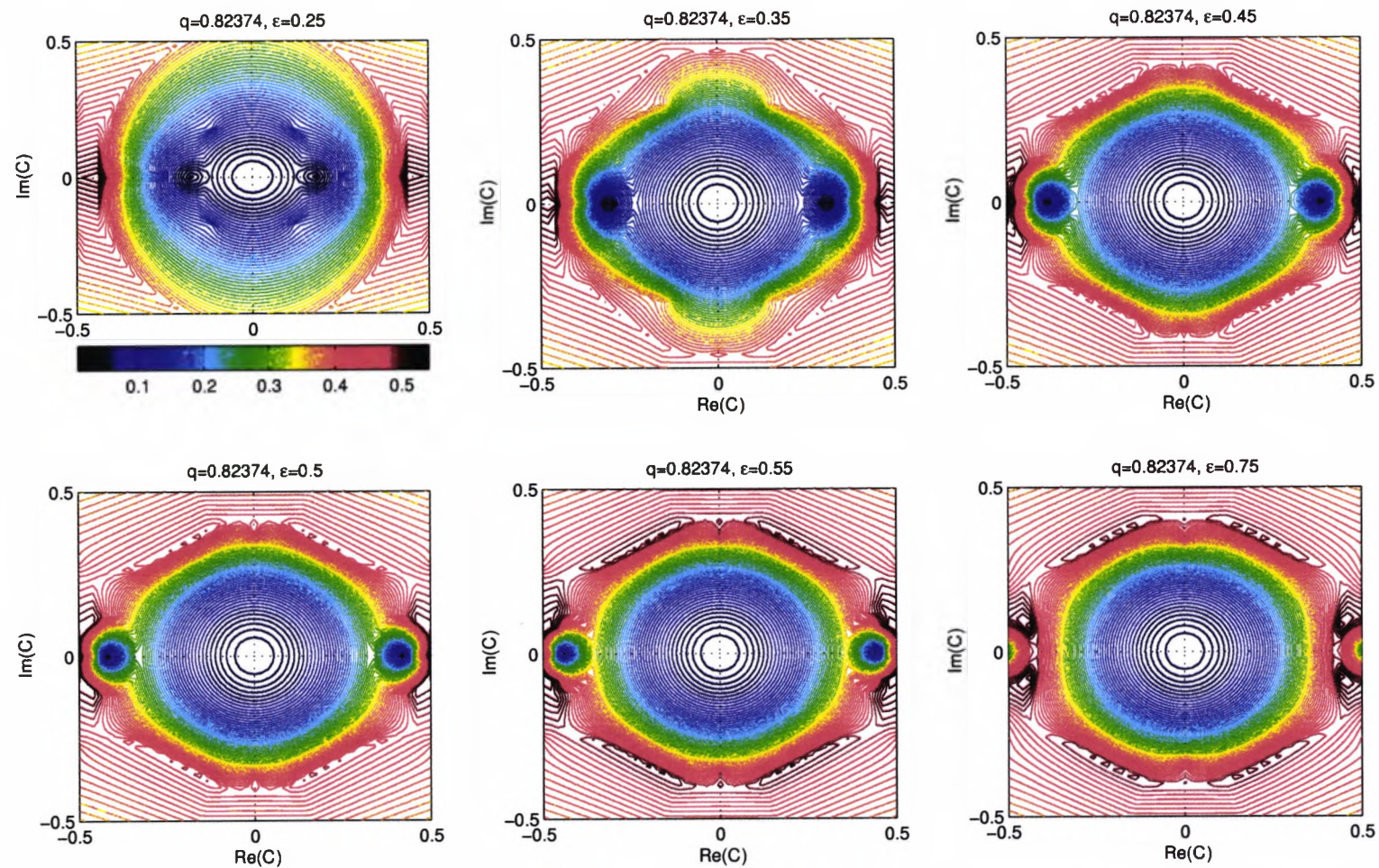


Figure 6.7: Contour plot of  $\min|\text{eig } \mathcal{M}_1^{fd}|$  for the fixed parameter values  $(L_y, q) = (2\pi, 0.82374)$  and  $\epsilon \in \{0.25, 0.35, 0.45, 0.5, 0.55, 0.75\}$ .

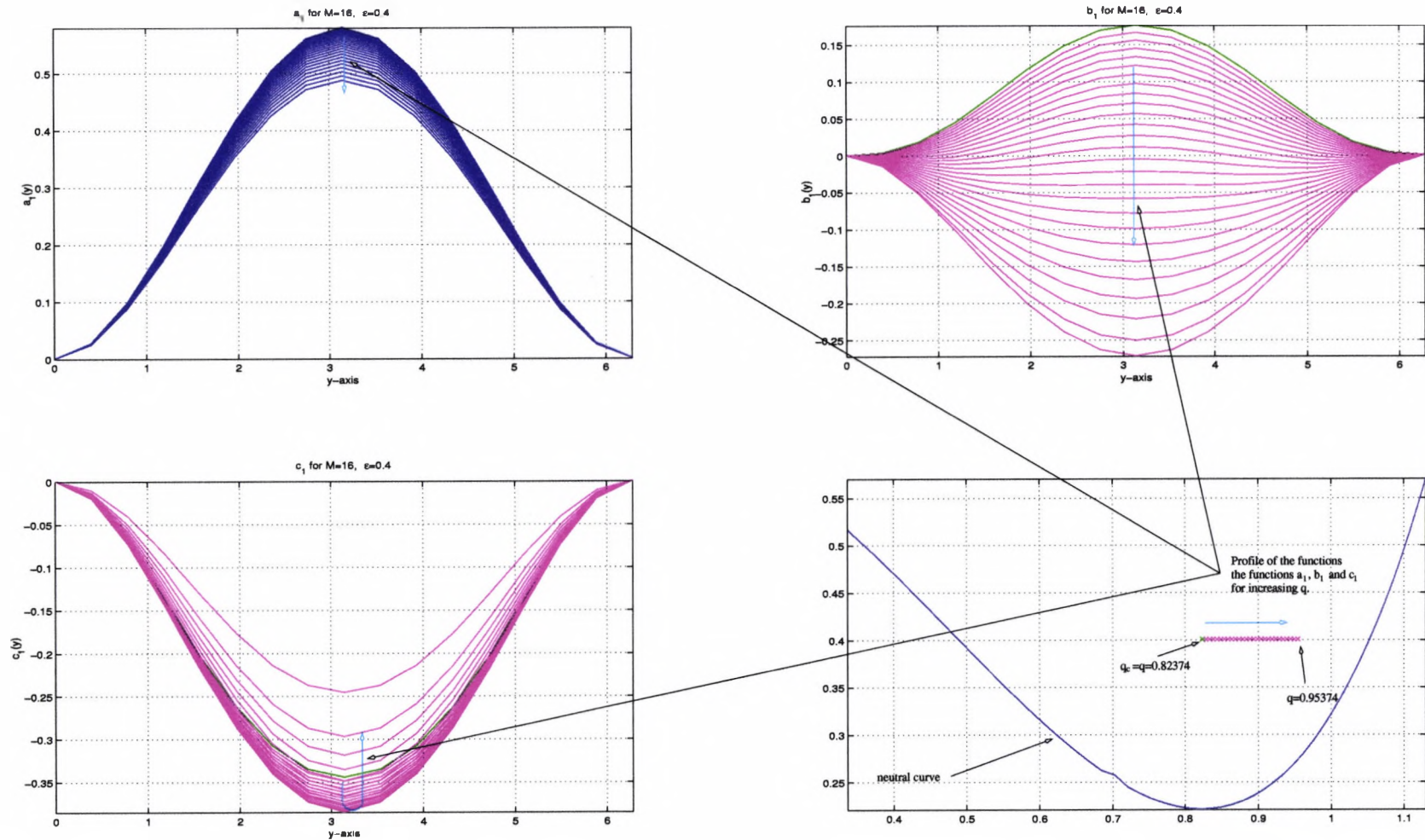


Figure 6.8: Plots showing the profiles of  $a_1$ ,  $b_1$  and  $c_1$  at fixed  $(L_y, \epsilon) = (2\pi, 0.4)$  and  $q_c = 0.82374 \leq q \leq 0.95374$ . The green profiles represent the profiles at  $q_c = 0.82374$ . The cyan arrow points in the direction of increasing values of  $q$ .

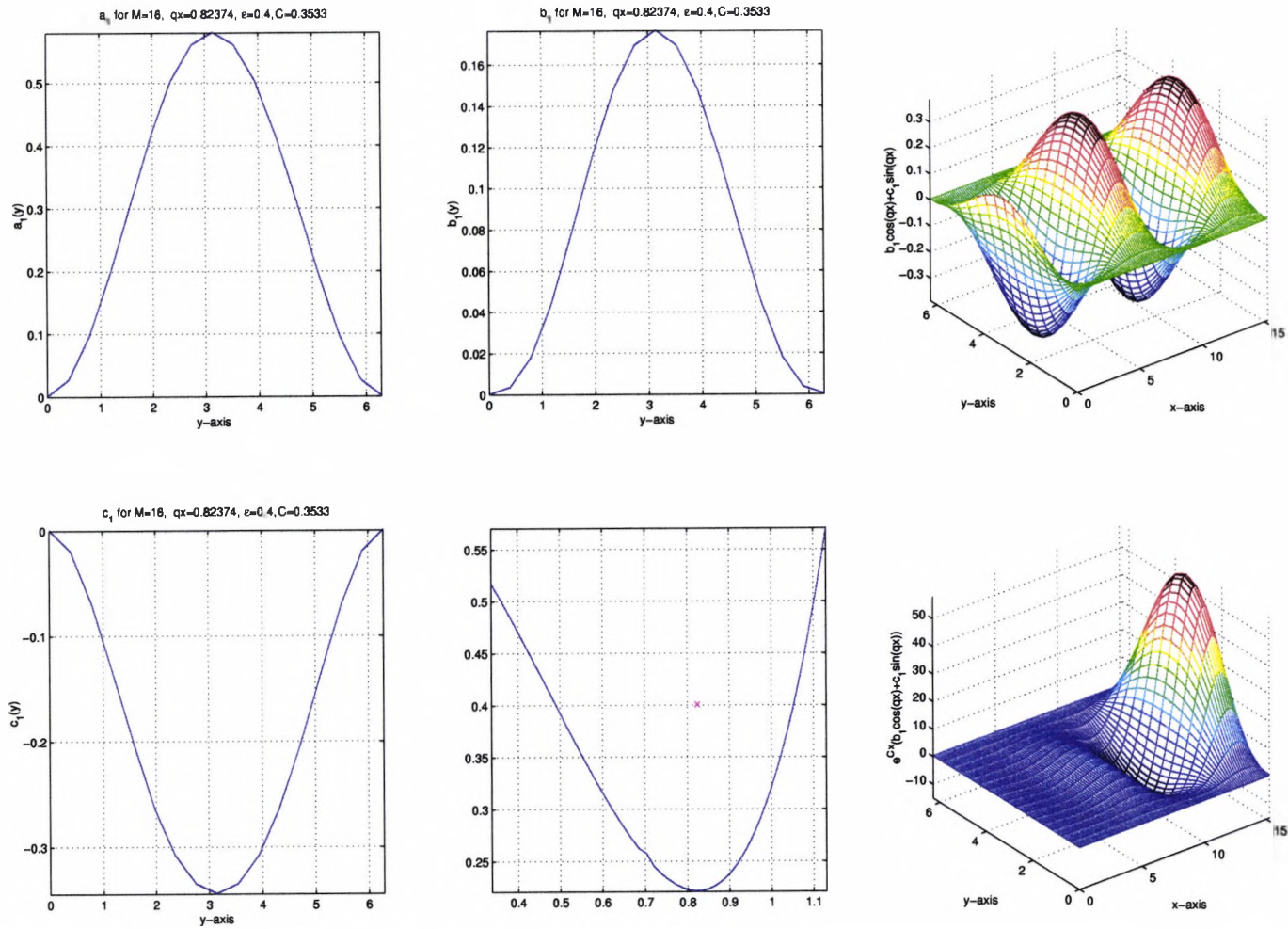


Figure 6.9: Plots of the profiles of  $a_1$ ,  $b_1$  and  $c_1$ ; and the functions  $b_1 \cos qx + c_1 \sin qx$  and  $e^{Cx} [b_1 \cos qx + c_1 \sin qx]$  at  $q = 0.82374$

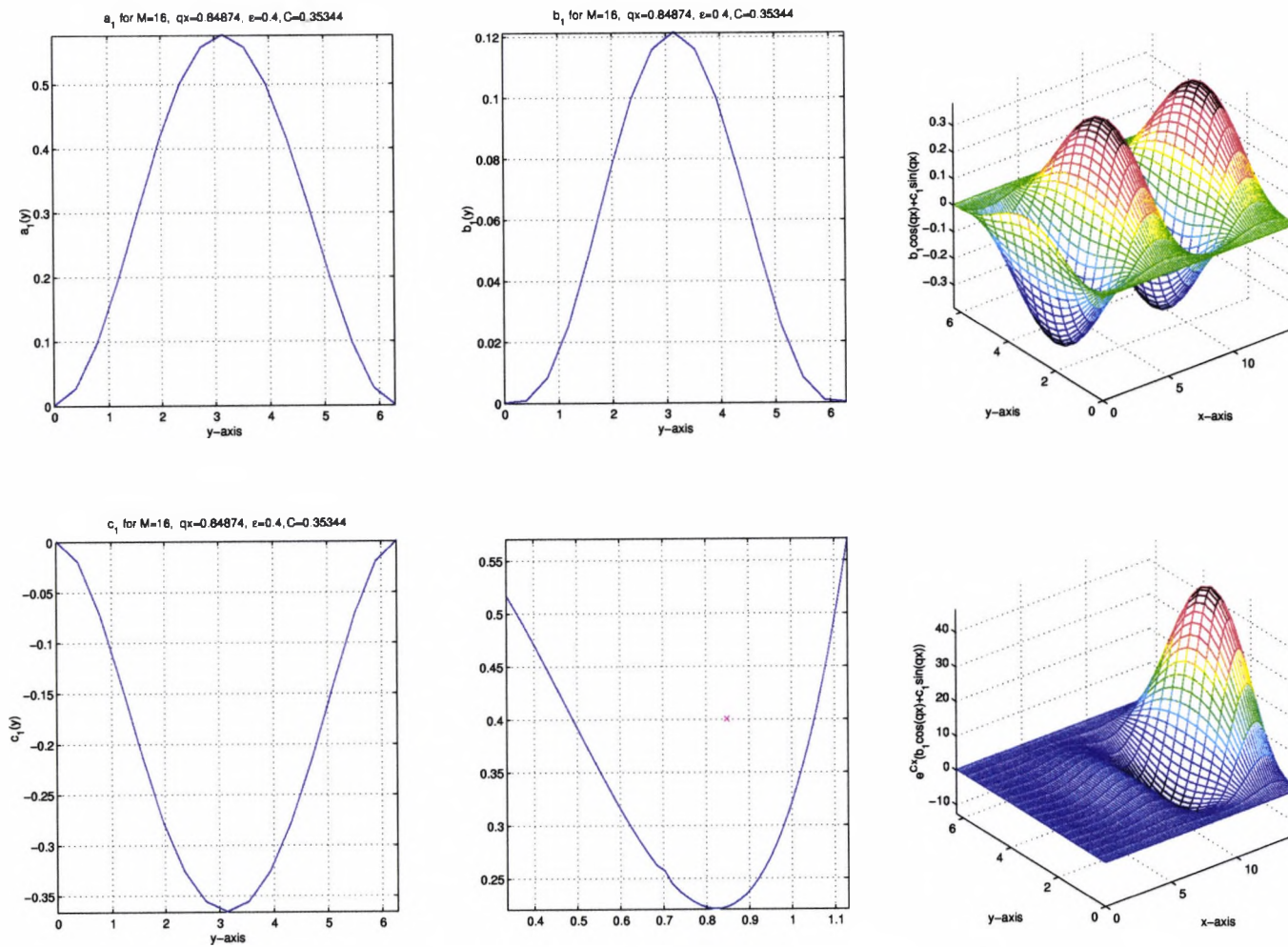


Figure 6.10: Plots of the profiles of  $a_1$ ,  $b_1$  and  $c_1$ ; and the functions  $b_1 \cos qx + c_1 \sin qx$  and  $e^{Cx} [b_1 \cos qx + c_1 \sin qx]$  at  $q = 0.84874$

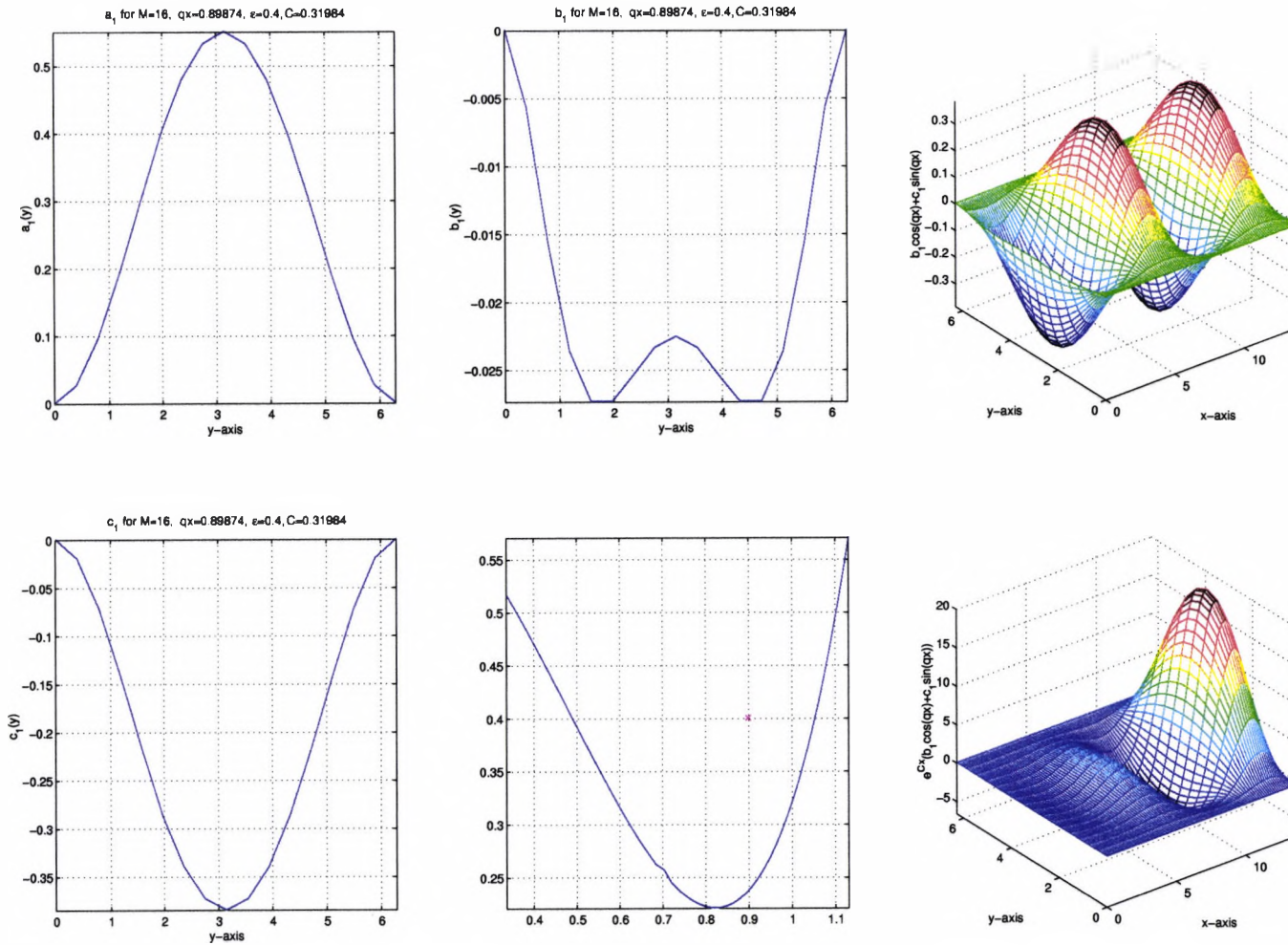


Figure 6.11: Plots of the profiles of  $a_1$ ,  $b_1$  and  $c_1$ ; and the functions  $b_1 \cos qx + c_1 \sin qx$  and  $e^{Cx} [b_1 \cos qx + c_1 \sin qx]$  at  $q = 0.89874$

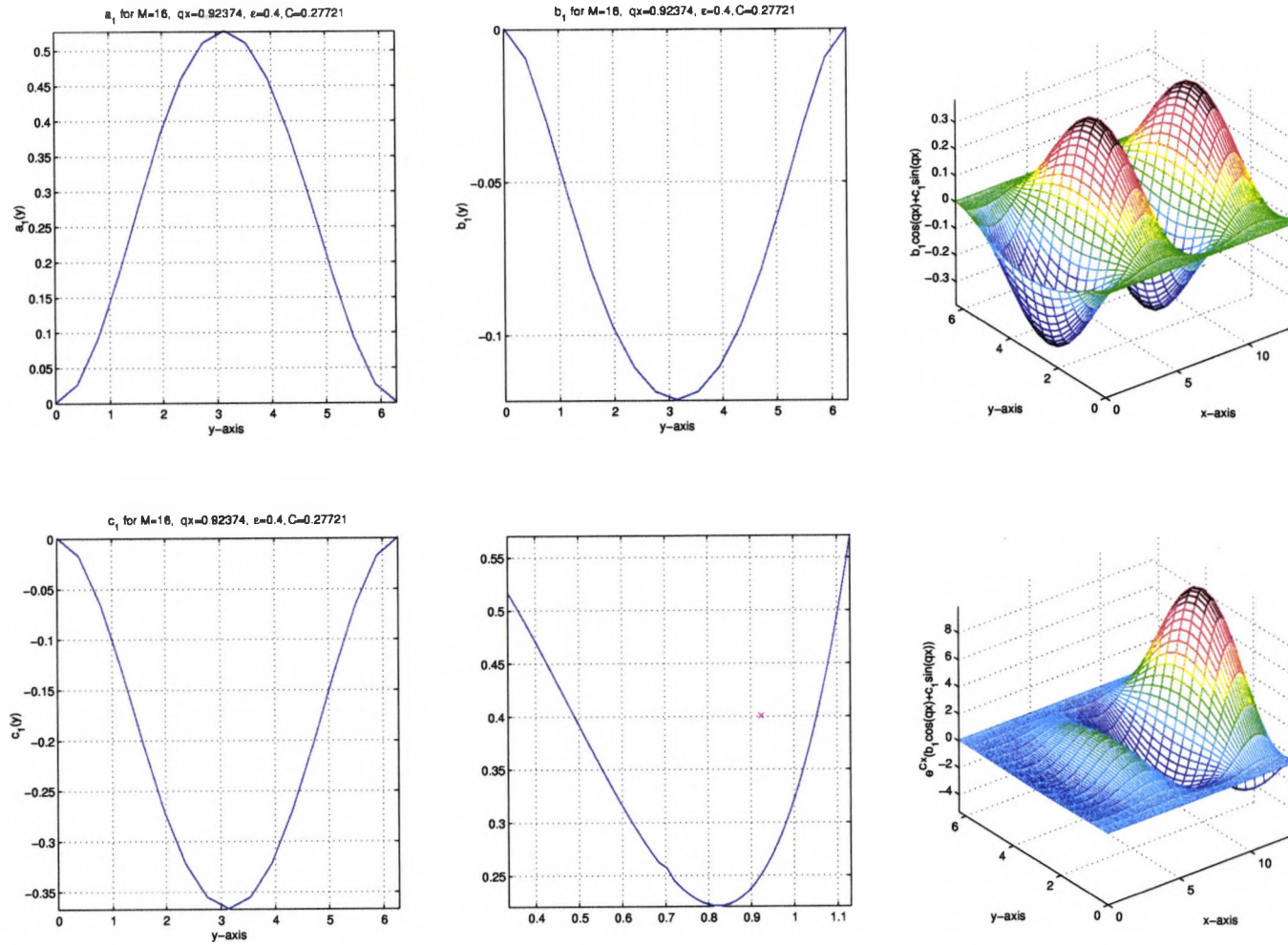


Figure 6.12: Plots of the profiles of  $a_1$ ,  $b_1$  and  $c_1$ ; and the functions  $b_1 \cos qx + c_1 \sin qx$  and  $e^{Cx}[b_1 \cos qx + c_1 \sin qx]$  at  $q = 0.92374$

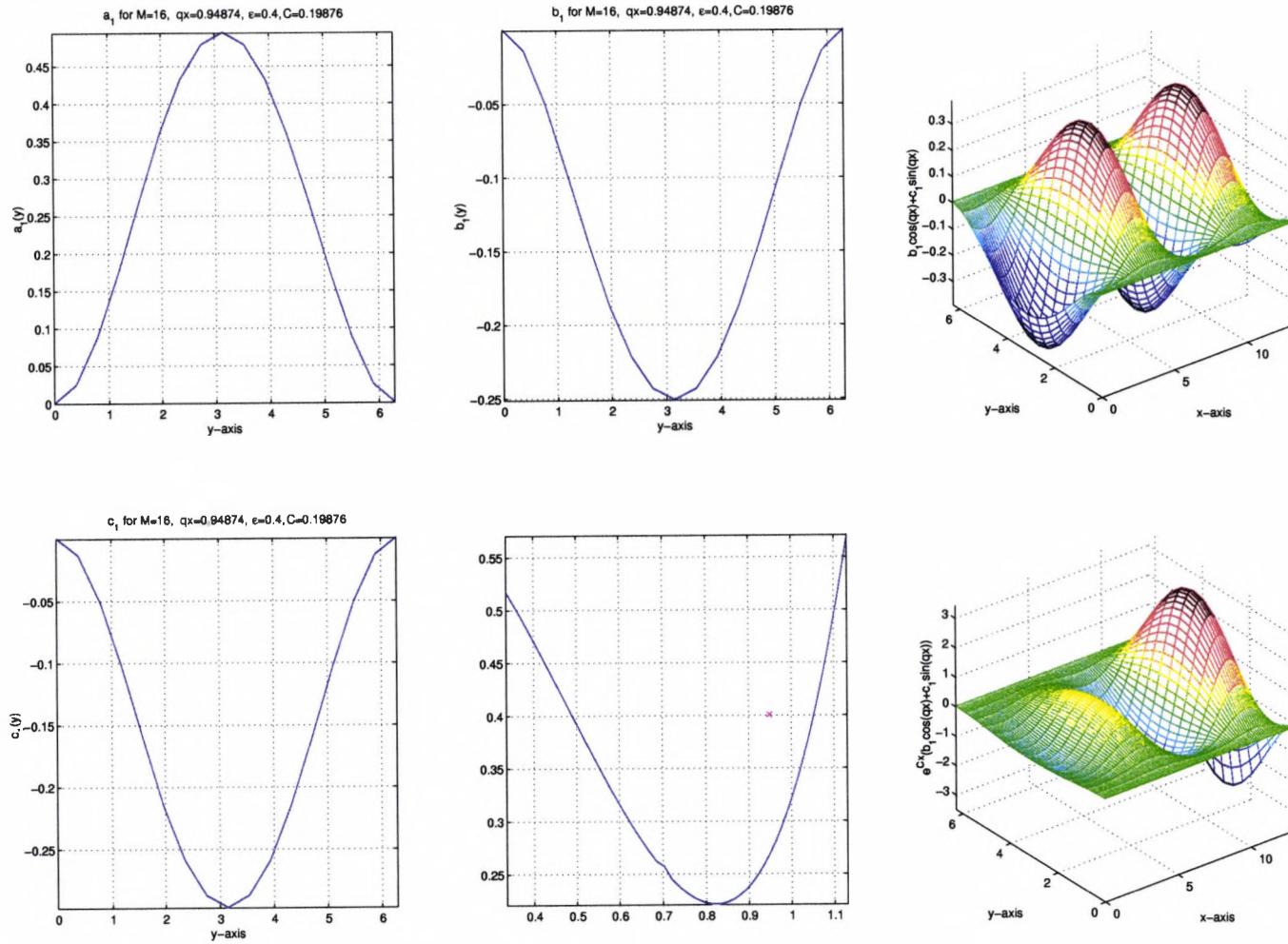


Figure 6.13: Plots of the profiles of  $a_1$ ,  $b_1$  and  $c_1$ ; and the functions  $b_1 \cos qx + c_1 \sin qx$  and  $e^{Cx}[b_1 \cos qx + c_1 \sin qx]$  at  $q = 0.94874$

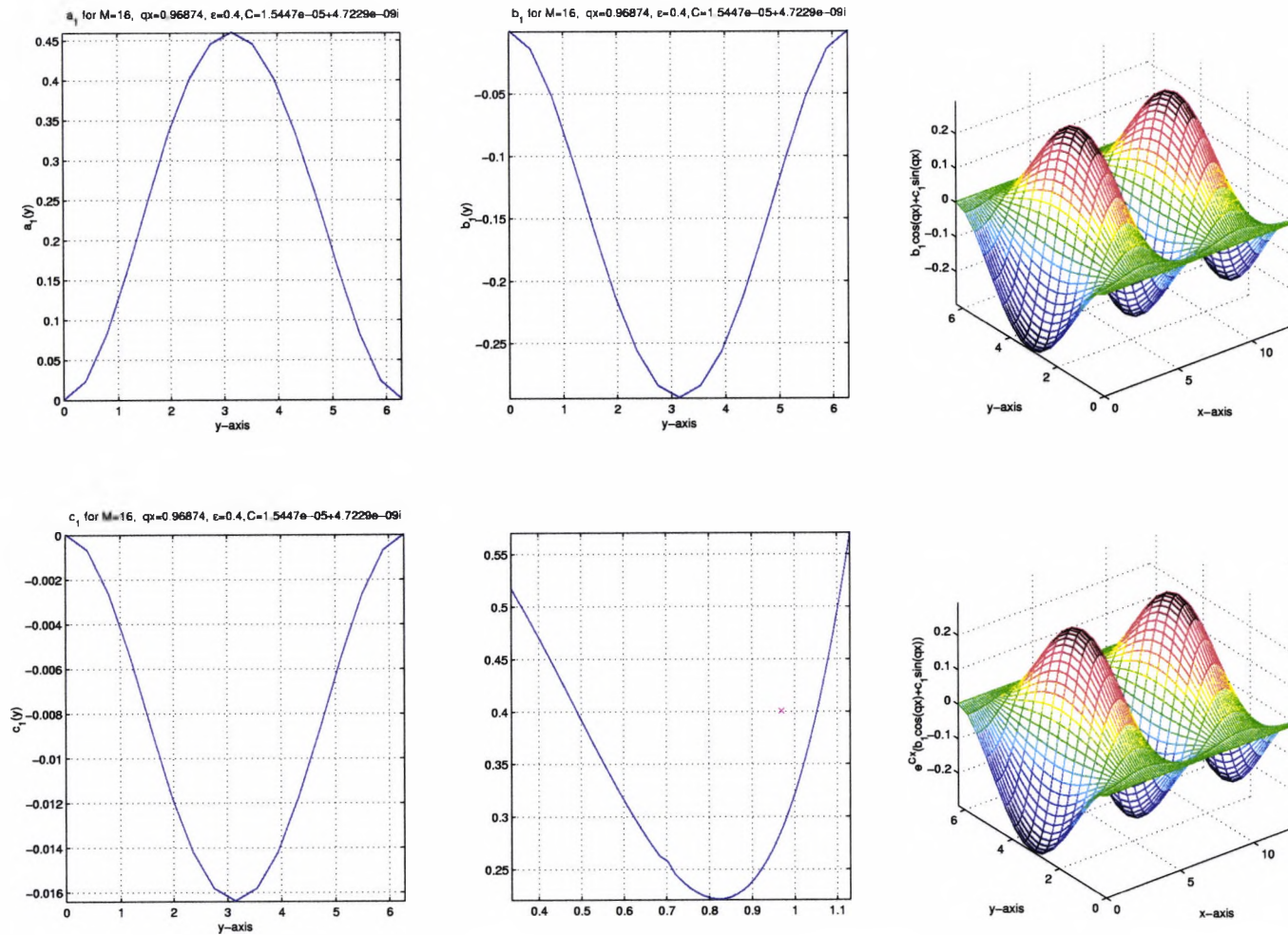


Figure 6.14: Plots of the profiles of  $a_1$ ,  $b_1$  and  $c_1$ ; and the functions  $b_1 \cos qx + c_1 \sin qx$  and  $e^{Cx} [b_1 \cos qx + c_1 \sin qx]$  at  $q = 0.96874$

## 6.4 Summary

Summarising what we have found in Chapter 6:

- We have considered perturbations to two-dimensional periodic solutions of the SH equation in a channel with no-slip sidewalls. We have found regions where there are spatially decaying or growing solutions and regions of spatially oscillatory solutions (Eckhaus instabilities).
- We have calculated numerically the two dimensional Eckhaus boundary for a channel with width  $L_y = 2\pi$ .
- We have found solutions in the first quadrant of the complex  $\mathcal{C}$ -plane (see Figure 6.1) which, within the Eckhaus boundary, provide solutions which decay as  $x \rightarrow \infty$ . Outside the Eckhaus boundary, one of these solutions becomes spatially oscillatory.
- Our solutions in this chapter are limited to the severest Fourier truncation of both the periodic form  $u_p$  and the Floquet perturbation. However, we have seen in Chapter 5 that the periodic form  $u_p$  is dominated by the first Fourier mode and it may be that the same is true of the Floquet perturbation for the roots  $\mathcal{C}$  of smallest absolute value. This remains to be investigated in detail.

## Chapter 7

# Solutions of the Two-Dimensional Swift-Hohenberg Equation in a Semi-infinite Channel

### 7.1 Introduction

In this chapter we consider solutions in a semi-infinite channel  $x \geq 0$  of width  $L_y = 2\pi$  with no-slip boundary conditions applied at a lateral wall at  $x = 0$ . Thus the problem is to solve

$$(\nabla^2 + 1)^2 u - \epsilon u + u^3 = 0, \quad (7.1)$$

subject to the boundary conditions

$$u = \frac{\partial u}{\partial y} = 0, \quad \text{at } y = 0, L_y, \quad (7.2)$$

$$u = \frac{\partial u}{\partial x} = 0, \quad \text{at } x = 0, \quad (7.3)$$

and

$$u \rightarrow u_p(x + \phi, y), \quad \text{as } x \rightarrow \infty, \quad (7.4)$$

where  $u = u(x, y)$  and  $\nabla^2 = \frac{\partial^2}{\partial x^2} + \frac{\partial^2}{\partial y^2}$ . As in Chapter 4 we assume that the solution approaches a periodic form at large distances from the wall, with the phase shift  $\phi$  to be determined as part of the solution. We expect the periodic

form (7.4) to be achieved through an exponential decay of the form

$$u(x, y) \sim u_p(x + \phi, y) + ke^{-Cx}P(x + \phi, y) + \dots, \quad x \rightarrow \infty, \quad (7.5)$$

where  $C = C_+$  and  $u_p(x, y)$  and  $P(x, y)$  can be approximated by their Fourier representations

$$u_p(x, y) = \sum_{j=1}^N a_j(y) \sin jqx, \quad P(x, y) = \sum_{n=0}^{\hat{N}} (b_n(y) \cos nqx + c_n(y) \sin nqx). \quad (7.6)$$

The coefficient  $k$ , like  $\phi$ , is to be found as part of the solution. In Sections 7.2 we use the periodic solutions,  $u_p$ , found in Chapter 6 and derive an approximate method for calculating the two-dimensional  $q$ -restriction at general  $\epsilon$ . The method is similar to the approximate asymptotic method used for the one-dimensional problem in Section 4.3 and is based on the use of (7.5) for all  $x \geq 0$ . It is relatively easy to implement but is likely to have poor accuracy. We obtain results over a range of values of  $\epsilon$  up to  $\epsilon = 0.5$ .

## 7.2 Approximate Theory for General $\epsilon$

The solution (7.5) is used as an approximate solution for all  $x \geq 0$  with  $C = C_+$  and  $u_p(x, y)$  and  $P(x, y)$  approximated by their one-mode Fourier truncations

$$u_p(x, y) = a_1(y) \sin qx, \quad P(x, y) = b_1(y) \cos qx + c_1(y) \sin qx. \quad (7.7)$$

A proper approximate treatment would also require the infinite number of other spatially decaying modes to be incorporated in (7.5), allowing the wall conditions

$$u = u_x = 0, \quad \text{at } x = 0, \quad (7.8)$$

to be satisfied for all values of  $y$ . However, noting from Figure 6.8 that the shapes of the profiles  $a_1$ ,  $b_1$  and  $c_1$  are very similar, we can make a further approximation and apply the conditions (7.8) at the central point  $y = \frac{L_y}{2}$  only. Elimination of  $k$  then leads to the requirement that the phase shift  $\phi$  is determined by solutions of the equation

$$B_1 \sin 2q\phi - C_1 \cos 2q\phi = -2qC^{-1}B_1 - C_1, \quad (7.9)$$

where  $B_1 = b_1(\frac{L_y}{2})$  and  $C_1 = c_1(\frac{L_y}{2})$ . The left-hand side is an oscillatory function of  $\phi$  with amplitude  $(B_1^2 + C_1^2)^{\frac{1}{2}}$  so that solutions exist only if

$$|2q\mathcal{C}^{-1}B_1 + C_1| < (B_1^2 + C_1^2)^{\frac{1}{2}}. \quad (7.10)$$

As an example, consider the detailed results for  $\epsilon = 0.4$  shown in Figure 6.8, along with the variation of  $\mathcal{C}$  shown in Figure 6.5. It is evident that the left-hand side of (7.10) becomes large at the Eckhaus boundary ( $q \approx 0.67$  and  $q \approx 0.97$ ) where  $\mathcal{C} \rightarrow 0$  and is zero near the position where  $q \approx 0.87$  (with  $B_1 \approx 0.07$ ,  $C_1 \approx -0.37$  and  $\mathcal{C} \approx 0.34$ ). Solutions of (7.9) for  $\epsilon = 0.4$  are thus confined to a narrow band of wavenumbers centred around  $q = 0.87$  and, in fact, roughly within the band shown in Figure 6.8.

Figure 7.1 shows the wavenumber restriction for values of  $\epsilon$  between  $0.25 \leq \epsilon \leq 0.5$  calculated from (7.10). Notice that the restriction region is skewed to the right. This skewness is also a property of the equivalent approximate method for the one-dimensional case (see Figure 4.13).

### 7.3 Summary

Summarising what we have found in Chapter 7:

- We have provided an approximate theory for solutions of the two-dimensional SH equation in a semi-infinite channel  $x \geq 0$  of width  $L_y = 2\pi$  which approach a periodic form with wavenumber  $q = \pi/L$  as  $x \rightarrow \infty$  and satisfy the no-slip boundary conditions at the channel walls and at the lateral wall at  $x = 0$ .
- We have found that solutions are restricted to a band of wavenumber  $q$  within the Eckhaus boundary. As in the one-dimensional case, we might anticipate that the skewness of this band (*cf.* Figure 7.1 and Figure 4.13) which is due to the approximate use of (7.5) for all  $x \geq 0$  and may not be a feature of the actual solution. However, we can expect that in the presence of a lateral wall at  $x = 0$ , the present theory will lead to the identification of a restricted band of two-dimensional solutions, the precise nature of which remains to be determined.

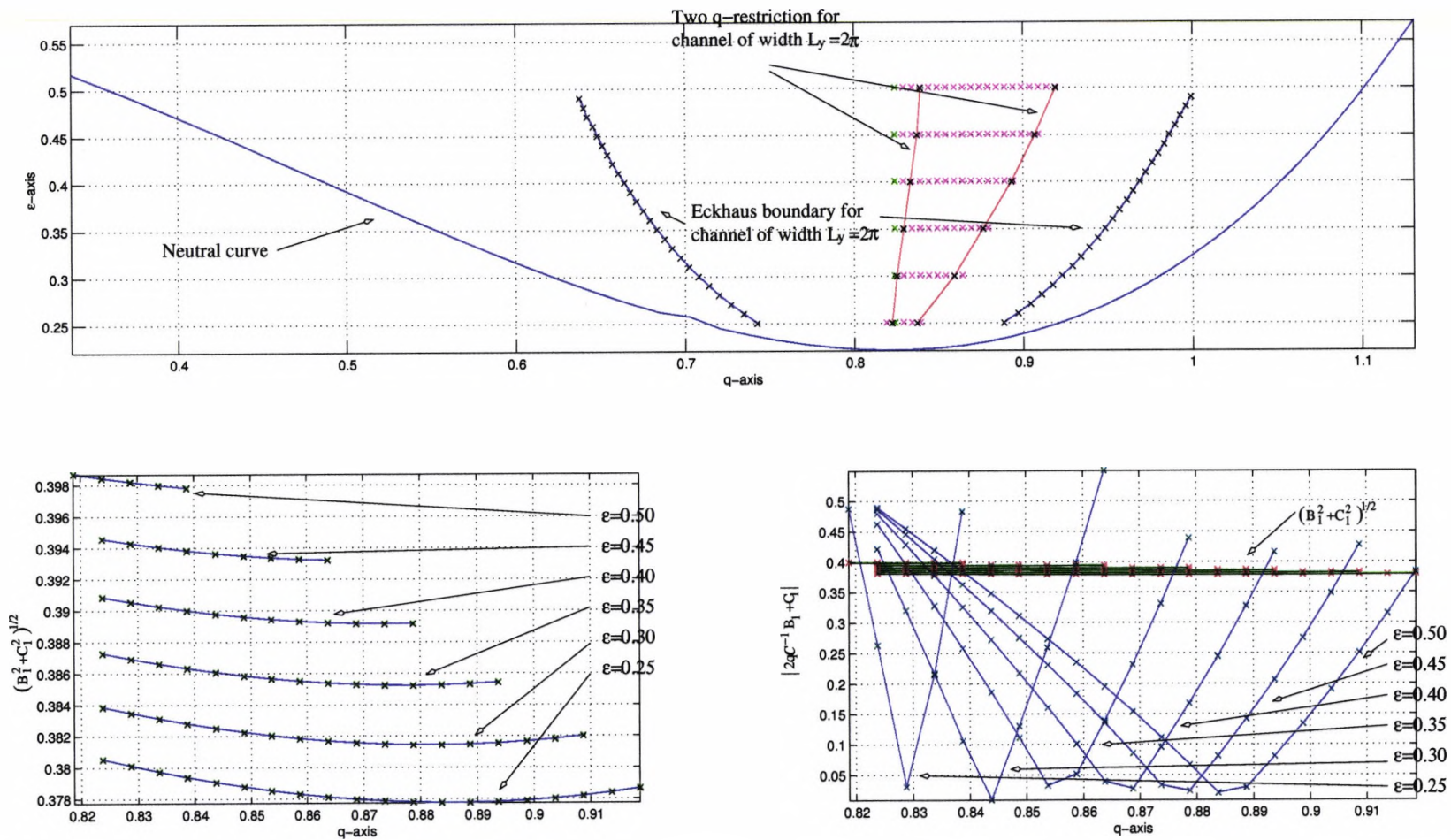


Figure 7.1: The top plot shows the neutral curve, the Eckhaus boundary and the wavenumber restriction (red lines) for the channel of width  $L_y = 2\pi$ . The lower plot shows the functions  $(B_1^2 + C_1^2)^{1/2}$  and  $|2qC^{-1}B_1 + C_1|$  for values of  $\epsilon = 0.25, 0.3, 0.35, 0.4, 0.45$  and  $0.5$ .

# Chapter 8

## Discussion

### 8.1 Conclusions

The Swift-Hohenberg equation is a relaxational model equation which we have used for the study of pattern selection in Rayleigh-Bénard convection. The equation can capture much of the observed physical behaviour and has become a general tool for investigating certain features of other pattern forming systems, see Cross and Hohenberg (1993, [16]). Although it is a relaxational model equation our aim has been to develop methods for a fully nonlinear system which can then be applied to the nonlinear Boussinesq equations.

In this thesis we started by giving a linear stability analysis of the trivial solution to the different Fourier modes for the one dimensional case and used this as a basis for finding one-dimensional nonlinear periodic solutions. We showed the existence of nonlinear mode interaction solutions and studied their bifurcation structure and stability.

We used Floquet theory to analyse, in a spatial sense, the departure of the nonlinear solutions from their periodic form. We found regions consisting of spatially growing or decaying solutions and regions of spatially oscillatory solutions, and located the Eckhaus boundary which separates these regions, in agreement with previous results for the one-dimensional case.

We used the Floquet analysis to find nonlinear solutions to the SH equation in the presence of a lateral boundary (the semi-infinite problem), finding the wavenumber restriction, at arbitrary  $\epsilon$ , for the one-dimensional case.

We also obtained linear stability results for the two dimensional case, in a form that explicitly determines the dependence of the solution on the channel

width  $L_y$  and used this as a basis for finding two-dimensional nonlinear periodic solutions. As  $L_y \rightarrow \infty$ , the two dimensional linear stability results approach those of the one dimensional case. We did not investigate mode interactions for the two dimensional case but propose this as a topic for further investigation.

We used Floquet theory to analyse, in a spatial sense, the departure of the nonlinear solutions from their periodic form, giving specific results for a channel of width  $L_y = 2\pi$ . The corresponding results for a channel of arbitrary width  $L_y$  can also be calculated in a straightforward manner.

We also used an approximate method based on the Floquet analysis to find solutions for the channel in the presence of a lateral boundary at  $x = 0$ , and to find the wavenumber restriction at arbitrary  $\epsilon$ . Further work is needed to determine its precise form.

## 8.2 Further Work

Due to time constraints, there are a number of aspects which we have not explored. We would like to propose the following for further study:

- To extend the two-dimensional Floquet analysis of Chapter 6 to higher levels of truncation to check the accuracy of results.
- To complete the determination of the wavenumber restriction for the two-dimensional problem, enabling results to be compared with numerical solutions of the SH equation in large boxes (e.g., Greenside and Coughran (1984, [29])).
- To undertake a weakly-nonlinear analysis of periodic solutions, the Eckhaus boundary and the wavenumber restriction for the two dimensional problem, in particular to resolve the lower parts of the Eckhaus boundary in Figure 6.6.
- To undertake a stability analysis of the two branches of solutions within the restricted wavenumber region, both for the one-dimensional and two-dimensional problems.
- To study possible mode-interactions and nonlinear bifurcations for the two dimensional problem.

- To investigate whether the bifurcation loci of nonlinear mode interactions encroach on the wavenumber restriction at higher  $\epsilon$ , both for the one-dimensional and two-dimensional problems.
- To investigate the gap in the Eckhaus instability region associated with mode interactions (see Figure 3.6).
- To extend the methods discussed in this thesis to the Boussinesq equations, enabling results such as the Eckhaus boundary and wavenumber restriction to be compared with those from experimental methods.

# Bibliography

- [1] G. Ahlers, D. S. Cannell, P. C. Hohenberg and V. Steinberg. Time-dependence of Flow Patterns Near the Convective Threshold in a Cylindrical Container. *Physical Review Letters*. Vol.54, pp.1373–1376, 1985.
- [2] E. J. Anderson. Application of Newton-Krylov Methods to a Biharmonic Model of Pattern Formation. *M.Sc. Thesis*. Department of Computer Science, Duke University, 1996.
- [3] H. Bénard. Les Tourbillons Cellulaires dans une Nappe Liquide. *Rev. Gén. Sciences Pure Appl.* Vol.11, pp.1261–1271, pp.1309–1328, 1900.
- [4] H. Bénard. Les Tourbillons Cellulaires dans une Nappe Liquide Transportant de la chaleur par Convection en Régime Permanent. *Ann. Chim. Phys.* Vol.147, pp.839–842, 1901.
- [5] P. Bjorstad. Fast Numerical Solution of the Biharmonic Dirichlet Problem on a Rectangle. *SIAM Journal on Numerical Analysis*. Vol.20, pp.59–71, 1983.
- [6] S. N. Brown and K. Stewartson. On Thermal Convection in a Large Rectangular Box. *Studies in Applied Mathematics*. Vol.57, pp.187–204, 1977.
- [7] A. R. Champneys. Homoclinic Orbits in Reversible Systems and their Applications in Mechanics, Fluids and Optics. *Physica D*. Vol.112, pp.158–186, 1998.
- [8] S. Chandrasekhar. *Hydrodynamic and Hydromagnetic Stability*. Clarendon Press, Oxford, 1961.
- [9] R. M. Clever and F. H. Busse. Transition to Time-dependent Convection . *Journal of Fluid Mechanics*. Vol.65, pp.625–645, 1974.

- [10] S. M. Cox. Mode Interactions in Rayleigh-Bénard Convection. *Physica D*. Vol.95, pp.50–61, 1996.
- [11] V. Croquette, M. Mory and F. Schosseler. Rayleigh-Bénard Convective Structures in a Cylindrical Container. *Journal de Physique*. Vol.44, pp.293–301, 1983.
- [12] M. C. Cross. Derivation of the Amplitude Equation at the Rayleigh-Bénard Instability. *Physics of Fluids*. Vol.23, No.9, pp.1727–1731, 1980.
- [13] M. C. Cross. Ingredients of a Theory of Convective Textures Close to Onset. *Physical Review A*. Vol.25, pp.1065–1076, 1982.
- [14] M. C. Cross, P. G. Daniels, P. C. Hohenberg and E. D. Siggia. Effect of Distant Sidewalls on Wave-number Selection in Rayleigh-Bénard Convection. *Physical Review Letters*. Vol.45, pp.898–902, 1980.
- [15] M. C. Cross, P. G. Daniels, P. C. Hohenberg and E. D. Siggia. Phase-Winding Solutions in a Finite Container Above the Convective Threshold. *Journal of Fluid Mechanics*. Vol.127, pp.155–183, 1983.
- [16] M. C. Cross and P. C. Hohenberg. Pattern Formation out of Equilibrium. *Rev. Mod. Phys.* Vol.65, pp.851–1112, 1993.
- [17] G. Dangelmayr. Steady-state Mode Interactions in the Presence of  $O(2)$ -Symmetry. *Dynamics and Stability of Systems*. Vol.1, pp.159–185, 1986.
- [18] G. Dangelmayr and E. Knobloch. Steady-state Mode Interactions in the Presence of  $O(2)$ -Symmetry and in Non-Flux Boundary-Value Problems. *Contemporary Mathematics*. Vol.56, pp.53–56, 1986.
- [19] P. G. Daniels. The Effect of Distant Sidewalls on the Transition to Finite Amplitude Bénard Convection. *Proc. Roy. Soc. London A*. Vol.358, No.1693, pp.173–197, 1977.
- [20] P. G. Daniels and M. Weinstein. On Finite-Amplitude Patterns of Convection Near a Lateral Boundary. *Quarterly Journal of Mechanics and Applied Mathematics*. Vol.45, pp.315–336, 1992.

- [21] P. G. Daniels and M. Weinstein. On Finite-Amplitude Patterns of Convection in a Rectangular-planform Container. *Journal of Fluid Mechanics*. Vol.317, pp.111–127, 1996.
- [22] R. P. Davies-Jones. Thermal Convection in an Infinite Channel with No-slip Sidewalls. *Journal of Fluid Mechanics*. Vol.44, pp.695, 1970.
- [23] S. H. Davis. Convection in a Box: Linear Theory. *Journal of Fluid Mechanics*. Vol.30, pp.465, 1967.
- [24] E. J. Doedel, A. R. Champneys, X. Wang, Y. A. Kuznetsov and T. Fairgrieve. AUTO 97: Continuation and Bifurcation Software for Ordinary Differential Equations (with HomCont). <ftp://ftp.cs.concordia.ca/pub/doedel/auto/>, 1997.
- [25] P. G. Drazin and W. H. Reid. *Hydrodynamic Stability*. Cambridge University Press, Cambridge, 1981.
- [26] V. Eckhaus. *Studies in Nonlinear Stability Theory*. Springer Tracts in Natural Philosophy, Vol.6, Springer, 1965.
- [27] M. Golubitsky and D. G. Schaeffer. *Singularities and Groups in Bifurcation Theory*. Vol I, Springer, 1985.
- [28] H. S. Greenside, W. M. Coughran Jr. and N. L. Schryer. Nonlinear Pattern Formation Near Onset of Rayleigh-Bénard Convection. *Physical Review Letters*. Vol.49, No.10, pp.726–729, 1982.
- [29] H. S. Greenside and W. M. Coughran Jr. Nonlinear Pattern Formation Near Onset of Rayleigh-Bénard Convection. *Physical Review A*. Vol.30, pp.398–427, 1984.
- [30] E. Hernández-García, M. San Miguel, R. Toral and J. Viñals. Noise and Pattern Selection in the One-Dimensional Swift-Hohenberg Equation. *Physica D*. Vol.61, pp.159–165, 1992.
- [31] E. L. Ince. *Ordinary Differential Equations*. Dover Publications, 1956.
- [32] E. L. Koschmieder. On Convection on a Uniformly Heated Plane. *Beitr. Phys. Atmos.* Vol.32, pp.1–11, 1966.

- [33] E. L. Koschmieder. *Bénard Cells and Taylor Vortices*. Cambridge University Press, 1993.
- [34] L. Kramer and P. C. Hohenberg. Effects of Boundary Conditions on Spatially Periodic States. *Physica D*. Vol.13, pp.357–369, 1984.
- [35] L. Kramer and W. Zimmerman. On the Eckhaus Instability for Spatially Periodic Patterns. *Physica D*. Vol.16, pp.221–232, 1985.
- [36] M. Kuwamura. The Stability of Roll Solutions of the Two-Dimensional Swift-Hohenberg Equation and the Phase-Diffusion Equation. *SIAM J. Math. Anal.*. Vol.27, pp.1311–1335, 1996.
- [37] M. Lowe and J. P. Gollub. Pattern Selection Near the Onset of Convection. *Physical Review Letters*. Vol.55, pp.2575–2578, 1985.
- [38] P. Manneville. *Dissipative Structures and Weak Turbulence*. Academic Press Limited, London, 1990.
- [39] S. W. Morris, E. Bodenschatz, D. S. Cannell and G. Ahlers. Spiral Defect Chaos in Large Aspect Ratio Rayleigh-Bénard Convection. *Physical Review Letters*. Vol.71, pp.2026–2029, 1993.
- [40] A. C. Newell and J. Whitehead. Finite Bandwidth, Finite Amplitude Convection. *Journal of Fluid Mechanics*. Vol.38, pp.279–303, 1969.
- [41] Y. Pomeau and P. Manneville. Wavelength Selection in Axisymmetric Cellular Structures. *Journal of Physics*. Vol.42, pp.1067–1074, 1981.
- [42] M. R. E. Proctor. Private Communication, 2000.
- [43] Lord Rayleigh. On Convection Currents in a Horizontal Layer of Fluid when the Higher Temperature is on the Underside. *Phil. Mag.* Vol.32, pp.529–546, 1916.
- [44] H. R. Schober, E. Allroth, K. Schroeder and H. Muller-Krumbhaar. Dynamics of Periodic Pattern Formation. *Physical Review A*. Vol.33, pp.567–575, 1986.
- [45] L. A. Segel. Distant Side-walls Cause Slow Amplitude Modulation of Cellular Convection. *Journal of Fluid Mechanics*. Vol.38, pp.203–224, 1969.

- [46] L. F. Shampine and M. W. Reichelt. The Matlab ODE Suite. <http://www.mathworks.com/odesuite.html>. The Math Works Inc. 1996.
- [47] L. F. Shampine and M. W. Reichelt. The MATLAB ODE Suite. *Rept. 94-6*. Math. Dept., SMU, Dallas, TX, 1994.
- [48] E. D. Siggia and A. Zippelius. Pattern Selection in Rayleigh-Bénard Convection Near Threshold. *Physical Review Letters*. Vol.47, pp.835–838, 1981.
- [49] J. Swift and P. C. Hohenberg. Hydrodynamic fluctuation at the Convective Instability. *Physical Review A*. Vol.15, pp.319–328, 1977.
- [50] K. Tsiveriotis and R. A. Brown. Bifurcation Structure and the Eckhaus Instability. *Physical Review Letters*. Vol.63, pp.2048–2051, 1989.
- [51] Waterloo Maple Inc. *Maple V Release 5*. Waterloo Maple Inc. 1998.